Doctoral theses at NTNU, 2021:52

Abel Assegid Taffese

Modeling, Analysis, and Control of MMC-Based HVDC Converters for Grid Services

Doctoral thesis

NTNU
Norwegian University of Science and Technology
Thesis for the Degree of Philosophiae Doctor

NTNU
Norwegian University of Science and Technology

Abel Assegid Taffese

Modeling, Analysis, and Control of MMC-Based HVDC Converters for Grid Services

Thesis for the Degree of Philosophiae Doctor

Trondheim, February 2021

Norwegian University of Science and Technology
Faculty of Information Technology and Electrical Engineering
Department of Electric Power Engineering

NTNU
Norwegian University of
Science and Technology

NTNU
Norwegian University of Science and Technology

Thesis for the Degree of Philosophiae Doctor

Faculty of Information Technology and Electrical Engineering
Department of Electric Power Engineering

ISBN 978-82-326-5425-3 (printed ver.)
ISBN 978-82-326-5262-4 (electronic ver.)
ISSN 1503-8181 (printed ver.)
ISSN 2703-8084 (online ver.)

Doctoral theses at NTNU, 2021:52

Printed by NTNU Grafisk senter

Abstract

The integration of large-scale, remote, renewable energy sources has led to the proliferation of HVDC converters in the power system. Following this proliferation, more and more ancillary services, such as Power Oscillation Damping (POD), that were traditionally provided by synchronous generators, are being demanded from the HVDC converters in order to support the power system. One challenge in this regard is that these services can require the manipulation of active power, which is taken from the dc side of the converter. This is undesirable because it propagates active power disturbances (oscillations) into other connected ac grids. With the dc side transitioning to meshed HVDC grids, which can interconnect several asynchronous ac grids, the propagations of such power disturbances become even more important. In addition to the propagation of the disturbance itself, a second problem is that the observability of an oscillation in another connected system can cause negative interaction among system-level controllers, such as Power System Stabilizers (PSSs), located in different systems. Both these problems can be avoided if the power needed for the service is obtained from a different source.

The Modular Multilevel Converter (MMC), which is currently the most attractive topology in HVDC applications, has a potential to provide a temporary energy storage capability that can be used for ancillary services. In addition to the ac-dc MMC, dc-dc converters based on the MMC, such as the Front-to-Front (F2F) topology, also offer such a capability. This thesis focuses on developing and testing methods to utilize the energy storage capability of these converters to source the power needed for the ancillary services, so that the other connected ac grids are not disturbed. The thesis provides contributions on the *modeling* and *control* of the aforementioned converters.

Modeling: MMC models of varying levels of detail are presented and compared. The levels of detail range from the most detailed models targeting fast transients studies to the simplified ones suitable for large-scale studies. Based on these models, new simplified models of the MMC-based Front-to-Front (F2F) dc-dc converter are also proposed in this thesis. The models aggregate the arm energy states of the converter in order to reduce the number of states, which is desired when performing large-scale studies. The proposed models were validated against detailed models, and the results showed that the simplified models can accurately represent the F2F converter in large-scale system studies.

Control: The thesis proposes control methods on two different levels. The first is at the arm energy control level, where an improved arm energy controller is proposed. The other is at a higher level, where different implementations of methods to utilize the arm energy are proposed and analyzed. The arm energy controller is instrumental for the effective implementation of the high-level controllers.

The proposed arm energy control is a complete approach for implementing a closed-loop compensated modulation based on estimated arm voltages without accurate knowledge of the system parameters. The arm capacitance and the time delay between the controller

and the converter are the parameters which are not known accurately or are assumed to change throughout the lifetime of the converter. The proposed method has been tested using both simulation and experimental tests with a strong correlation between the two results. The experimental tests have shown that the method can work in cases that are not ideal where the number of modules is as low as 18. The tests have also demonstrated that the method works effectively in the presence of noise and asymmetrical capacitance changes.

At a higher level, the thesis proposes two methods for utilizing the MMC energy for grid services, so that the power disturbance generated by the services is diverted into the submodule capacitors of the converter. These are the power cancellation method and Virtual Capacitance Support (VCS). The power cancellation method is a local implementation where active power disturbance due to the grid service is diverted into the arm energy. This method is local because it relies on the availability of the active power disturbance measurement. On the other hand, VCS requires measurement of the dc voltage variations which can be accessed by multiple converters. This enables a distributed implementation where the energy storage capability of multiple converters can be utilized. The methods have been shown to be effective in three applications: Power Oscillation Damping (POD), wind farm active power smoothening, and dc voltage dynamic support.

A detailed analysis and validation of the VCS scheme in a POD application is also presented. The effectiveness of the scheme was studied using modal analysis, time-domain simulation, and Power Hardware In The Loop (PHIL) tests. There is a strong correlation between the results from the three studies, and they all show that the scheme can effectively divert the active power disturbance (oscillation) into the arm capacitors. It was shown that the VCS method only affects the observability of the mode in other grids, not the damping or frequency, as expected. Additionally, the PHIL tests show that the scheme is practically applicable since it was implemented using a scaled 18-level MMC prototype under realistic conditions. A requirement for the scheme to work properly is that the converter be designed with a slightly higher storage capacity compared to nominal design, for example 15% increase in sub-module voltage was used in this study. The amount of additional capacity can be chosen depending on the desired level of participation of the converters in providing the service.

Acknowledgements

I would like to express my appreciation to all my colleagues, friends, and family who helped me thought out the study. Firstly, I would like to thank my main supervisor Prof. Elisabetta Tedeschi for her unwavering support and understanding. Her prompt and thorough feedback on my work has been instrumental in my learning path. I would also like to extend my deepest gratitude to my co-supervisor Prof. Erik de Jong, from the Electrical Energy Systems department at Eindhoven University of Technology, for his invaluable inputs and encouragement.

I would like to thank everyone from NTNU and SINTEF who helped me with my laboratory tests at the National Smart Grid Laboratory. I am particularly grateful to Salvatore and Atsede who found time to help me in preparing and reviewing my test setups.

I had a great pleasure of working with a very diverse group of colleagues during my stay at NTNU. I would like to thank everyone for the memorable time I spent at NTNU. I would like to thank Atsede for being such a great officemate in the early days of my study, where she helped me navigate those challenging first days. I have also had numerous technical discussions with Anirudh, for which I am very grateful. I finalized the thesis while working for Siemens Subsea. I would like to thank everyone at Siemens Subsea for their support and for accommodating me when I needed more time to work on my thesis.

Last, but not least, I am forever indebted to my wife and kids, Megi, Bona, and Meti, for their love, patience and support throughout the process.

Dedicated to Eiye (እዬ) and Abat (አባት).

Table of Contents

List of Tables

List of Figures

List of Abbreviations

ac	Alternating Current.
dc	Direct Current.
ADC	Analog to Digital Converter.
HVDC	High Voltage Direct Current.
MTDC	Multi-Terminal Direct Current.
RMS	Root Mean Square.
EMT	Electromagnetic Transient.
P2P	Point-to-Point.
POD	Power Oscillation Damping.
PSS	Power System Stabilizer.
MMC	Modular Multilevel Converter.
VSC	Voltage Source Converter.
LCC	Line Commutated Converter.
FCS	Fixed Capacitance Support.
M2DC	Modular Multilevel DC.
DC-MMC	DC Modular Multilevel Converter.
DAB	Daul Active Bridge.
AAC	Alternate Arm Converter.
SM	Submodule.
HB	Half-Bridge.
FB	Full-Bridge.
IGBT	Insulated Gate Bipolar Transistor.
PCC	Point of Common Coupling.
dq	Direct-Quadrature.
KVL	Kirchhoff's Voltage Law.
PWM	Pulse Width Modulation.
LTI	Linear Time Invariant.
pu	Per-unit.
PLL	Phase Locked Loop.
F2F	Front-to-Front.
SSTI	Steady-State Time Invariant.
SSTP	Steady-State Time Periodic.
CCSC	Circulating Current Suppression Controller.
PHIL	Power Hardware In The Loop.
VCS	Virtual Capacitance Support.
SEXS	Simplified Excitation System.
AVR	Automatic Voltage Regulator.
ITM	Ideal Transformer Model.
PI	Proportional Integral.
FPGA	Field Programmable Gate Array.
PR	Proportional Resonant.

FD-π	Frequency Dependent-π.
DAE	Differential Algebraic Equation.
TSO	Transmission System Operator.

1
Introduction

1.1 Background

The ever-increasing demand for energy and the shift toward renewable energy sources is driving the integration of remote and offshore power generation into the electric power system. High Voltage Direct Current (HVDC) has been the technology of choice for the transmission of such remote generations because of its controllability and flexibility [1], in addition to its lower cost beyond a break-even transmission distance, which is often in the order of several hundred kilometers. In long-distance submarine transmission cases, HVDC is the only viable option because the reactive power generated by the cables makes ac transmission impractical. The earliest HVDC converters were Line Commutated Converter (LCC) type, which offer very limited controllability compared to the Voltage Source Converters (VSCs). The main advantage of VSCs is the capability to reverse active power without reversing the dc voltage, and decoupled control of active and reactive powers [2]. Among the VSC topologies, the Modular Multilevel Converter (MMC) has emerged as the preferred choice owing to its modular and scalable design and its near-sinusoidal output voltages and currents without the need for harmonic filters [3].

Most of the existing HVDC converters in operation today are parts of Point-to-Point (P2P) schemes. As the number of P2P links grows, it makes sense in terms of economics and reliability to interconnect them to form a Multi-Terminal Direct Current (MTDC) system. The first VSC-MTDC system was commissioned in China in 2014 [2]. A defining feature of MTDC systems is that they do not include meshes [2], i.e. there is only one path between any two terminals in the system. When an MTDC system includes a mesh, it is known as a Meshed dc grid or HVDC grid [2], [4]. HVDC grids can be embedded into a single ac power system, or they can interconnect two asynchronous ac systems. In either case they are part of a hybrid ac/dc power system [5], where both ac and dc power systems co-exist and exchange the necessary ancillary services [6]. Ancillary services are defined differently by different Transmission System Operators (TSOs) and regulators [7], but they can be summarized as services needed for the orderly, secure, and reliable operation of the power system. These are functions or features other than the main purpose of units in a power system.

Ancillary services that have been traditionally provided by synchronous generators in ac power systems include Power Oscillation Damping (POD), frequency

regulation (balancing), and voltage regulation (reactive power support). The first two are connected to active power, while the last is related to reactive power. Synchronous generators can provide these services because the active power can be regulated by changing the mechanical power, and the reactive power can be controlled by changing the excitation. When providing ancillary services through HVDC converters, there is a difference in behavior, especially for services involving active power. While a converter can autonomously generate the reactive power needed for an ancillary service, it cannot provide the active power-based services on its own because it is not connected to a power source. The converter takes the active power needed for the service from its dc side, which is normally connected to other ac grids. This leads to a disturbance of other connected ac grids when providing active power-based services to one grid. Besides the propagation of the disturbance itself, the observability of a disturbance across the connected ac grids means that there exist dynamic couplings among system-level controllers located in different ac grids, leading to a negative interaction with reduced performance [5].

The Modular Multilevel Converter (MMC), which is the most popular choice in recent installations, offers a temporary energy storage capability distributed in its submodule capacitors. This thesis investigates ways to effectively utilize this storage capability to prevent the propagation of active power disturbances and avoid negative interactions among system-level controllers. The same principle can be extended to MMC-based dc-dc converters, which are being proposed with the main goals of voltage matching and power flow control in HVDC grids. The dc-dc converter is considered to be a key enabler of future HVDC grids. Being relatively new components with no commissioned converter yet, dc-dc converters have not been studied in detail, and they lack proper models needed to include them in HVDC grid studies. Thus, this thesis also addresses modeling and control of dc-dc converters.

1.2 Scope of the thesis

The focus of this thesis is to find ways to utilize the energy storage capability of the MMC to provide active power-based ancillary services without propagating disturbances across HVDC grids. This task was divided into four steps or phases as discussed in the following.

The first step was to study HVDC grids including MMCs in order to identify the effect of disturbances resulting from the provision of active power-based ancillary services. A key aspect in such studies is the availability of models having a level detail commensurate with the study. To this end, the thesis addresses the following research questions.

Research question 1

How can the components of an HVDC grid, including the emerging dc-dc converters, be modeled for system-level studies? What simplifications can be achieved depending on the type of control?

The second aspect is related to the control system. The MMC, being complex, needs several interdependent layers of control to work effectively. The aim of this step is to find arm energy control strategies that facilitate the provision of the aforementioned services as highlighted in the research question below.

Research question 2

How should the MMC energy be controlled to facilitate the energy-based services? What improvements are needed to address challenges arising from practical implementation of such control methods?

With the control system in place, the next step is to find the best way to utilize the MMC energy for active power-based ancillary services. This step involves higher level control strategies that manipulate the arm energy by setting the references to the controllers developed in the previous step. The main topics addressed in this step are given by the questions below.

Research question 3

What methods can be used to manipulate the MMC energy in order to provide energy-based services? How can the amount of energy available for such services be quantified based on the design parameters of the MMC (such as submodule capacitance and voltage)? How can the design of the MMC be modified to accommodate such services?

The last step is to validate the control methods, proposed as the outcome of the previous steps, using simulations and laboratory experiments. This step involves identification of analysis, simulation and testing methods that are suitable for the application at hand, followed by performing the detailed analysis and testing. The research questions addressed in this step are shown below.

Research question 4

How do the proposed methods perform when they are implemented in practice? What is the impact of the simplifying assumptions made in the derivation and analysis of the methods?

By addressing the above-mentioned questions, the thesis presents the complete process from modeling all the way to practical implementation and validation of

control strategies to utilize the energy storage capability of the MMC for ancillary services.

1.3 Contributions

The main contributions of this thesis are summarized in the following points.

- This thesis presents MMC models for different applications with varying levels of detail. Phasor-based modeling approach is employed to capture dynamics of the ac quantities at the fundamental frequency and the dominant harmonics. Several of the MMC models discussed in this thesis have already been proposed in the literature. However, this thesis contributes a simplified representation of the models using phasors to obtain Steady-State Time Invariant (SSTI) models. Furthermore, the models have been validated against experimental results. The thesis also proposes simplified modeling of MMC-based Front-to-Front (F2F) dc-dc converter.

- An improved MMC energy control with online parameter adjustment is proposed in this thesis. The proposed method removes the circulating current ripple and provides good dynamic performance to enable the energy-based services.

- Two methods for utilizing the MMC energy storage capability for power system services are proposed in this thesis. Applications include: Power Oscillation Damping (POD), wind power smoothening and dc voltage dynamic support. Effectiveness of the proposed methods is demonstrated by both simulation and experiments.

- The thesis also presents a detailed practical demonstration of the proposed methods using a Power Hardware In The Loop (PHIL) setup. The connection from modal analysis to time domain simulations, and later to PHIL tests, is used to highlight the interactions in the system and to show the effectiveness of the proposed methods.

1.4 List of publications

The following are the papers published as part of this work.

P1 A. A. Taffese, E. de Jong, and E. Tedeschi, "Modelling of DC-DC Converter for System Level Studies," English, in *Proceedings of the 8th IEEE Benelux Young Researchers Symposium in Electrical Power Engineering: YRS2016*, Eindhoven, The Netherlands: Technische Universiteit Eindhoven, May 2016, p. 6

P2 A. A. Taffese, E. Tedeschi, and E. C. W. de Jong, "Modelling of DC-DC converters based on front-to-front connected MMC for small signal studies," in *2016 IEEE 17th Workshop on Control and Modeling for Power Electronics (COMPEL)*, Jun. 2016, pp. 1–7

P3 A. A. Taffese, E. Tedeschi, and E. de Jong, "Arm voltage estimation method for compensated modulation of modular multilevel converters," in *2017 IEEE Manchester PowerTech*, Jun. 2017, pp. 1–6

P4 A. A. Taffese, E. Tedeschi, and E. de Jong, "A control scheme for utilizing energy storage of the modular multilevel converter for power oscillation damping," in *2017 IEEE 18th Workshop on Control and Modeling for Power Electronics (COMPEL)*, Stanford, CA, USA: IEEE, Jul. 2017, pp. 1–8

P5 A. A. Taffese and E. Tedeschi, "Coordination of Modular Multilevel Converter Based HVDC Terminals for Ancillary Services," in *2018 Power Systems Computation Conference (PSCC)*, Dublin, Ireland: IEEE, Jun. 2018, pp. 1–7

P6 A. A. Taffese and E. Tedeschi, "Simplified Modelling of the F2F MMC-Based High Power DC-DC Converter Including the Effect of Circulating Current Dynamics," in *2018 IEEE 19th Workshop on Control and Modeling for Power Electronics (COMPEL)*, Jun. 2018, pp. 1–6

P7 E. Tedeschi and A. A. Taffese, "Electrical power transmission and grid integration," en, *Renewable Energy from the Oceans: From wave, tidal and gradient systems to offshore wind and solar*, pp. 321–343, Jul. 2019

P8 A. A. Taffese, E. de Jong, S. D'Arco, *et al.*, "Online Parameter Adjustment Method for Arm Voltage Estimation of the Modular Multilevel Converter," *IEEE Transactions on Power Electronics*, vol. 34, no. 12, pp. 12 491–12 503, Dec. 2019, ISSN: 1941-0107

P9 A. A. Taffese, A. G. Endegnanew, S. D'Arco, *et al.*, "Power oscillation damping with virtual capacitance support from modular multilevel converters," eng, *IET Renewable Power Generation*, 2019, Accepted: 2020-01-28T12:53:16Z, ISSN: 1752-1416

The following papers are published within the period of this work, but not included in this thesis because they are not strictly related to the main topic.

P10 L. V. Costanzo, I. Zubimendi, A. A. Taffese, *et al.*, "Parallelization of Medium Voltage generator-side converters for Multi-MW wind turbines: Comparison of two topological alternatives," in *2015 International Conference on Renewable Energy Research and Applications (ICRERA)*, Nov. 2015, pp. 917–922

P11 A. A. Taffese and E. Tedeschi, "Harmonic Resonance Mode Analysis in dq Domain," eng, *Renewable Energy and Power Quality Journal*, vol. 15, 2017, Accepted: 2017-11-30T09:56:15Z, ISSN: 2172-038X

P12 S. Sanchez, D. T. Duong, A. A. Taffese, *et al.*, "Performance Evaluation of the Empirical Method for Online Detection of Power Oscillations: A Multiterminal HVDC Application," in *IECON 2018 - 44th Annual Conference of the IEEE Industrial Electronics Society*, Oct. 2018, pp. 6021–6025

The publications included in this thesis are related to the content of the chapters, as shown in Table 1.1.

Table 1.1: Mapping of publications to chapters.

Chapter	2	3	4	5	6	7	8
Publication	**P1**	**P2**, **P6**	**P2**, **P3**	**P6**	**P3**, **P8**	**P4**, **P5**, **P7**	**P9**

1.5 Outline of the thesis

Chapter 2 provides a review of the basic components of HVDC transmission systems. The principle of operation of an MMC converter is presented, followed by a discussion on the role of dc-dc converters in HVDC grids and a review of topologies proposed in the literature.

Chapter 3 deals with the modeling of HVDC components with varying levels of detail focusing on simplifications for large-scale studies. The main contributions in this chapter are the phasor-based models of the MMC and the MMC-based F2F dc-dc converter. The models developed in this chapter are used in the case studies presented in subsequent chapters.

Chapter 4 introduces a generic controller for an ac-dc MMC connected to an ac grid. The focus is on a hierarchical control arrangement with high-level power, current and voltage controllers, and mid-level energy and circulating current controllers. Low-level controllers, such as submodule voltage balancing controllers, are not covered in this thesis. The goal of the chapter is to provide a review of well-established control methods from literature. This is used as background information in the discussion of the control method proposed in this thesis in Chapter 6.

Simulation, analysis, and testing methodology adopted in this thesis are discussed in Chapter 5. The chapter provides an overview of the methods together with the necessary theoretical background. The methods discussed are time-domain simulation, small-signal (modal) analysis, and PHIL testing.

Chapter 6 presents an improved MMC arm energy control method proposed in this thesis. The proposed method consists of a closed-loop energy control com-

bined with compensated modulation using estimated arm voltages. Under ideal conditions, i.e. all parameters accurately known, compensated modulation eliminates the circulating current ripple without any additional control to suppress it. However, in practice the arm capacitance and the time delay in the measurement path are not known accurately, leading to a residual circulating current ripple. A method to correct for parameter errors is proposed in this chapter. The complete control method has been validated using both simulations and laboratory experiments. The parameter correction method is tested by removing capacitors from selected submodules. The complete control system forms the basis for the energy-based services presented in the next two chapters.

Two methods for utilizing the energy storage capability of the MMC for active power-based grid services are proposed in Chapter 7. These two methods are *power cancellation* and *Virtual Capacitance Support (VCS)*. The two methods are developed and analyzed in detail. Application case studies involving POD, wind farm active power smoothening, and dc voltage transient support are also presented. The chapter also discusses the energy storage requirement of these services with a special focus on POD.

Chapter 8 presents an extensive analysis and testing of the VCS method using a detailed multi-machine, multi-area, power system connected via a three-terminal dc grid. The system is analyzed using modal analysis to identify poorly damped modes. This is followed by design of a POD controller. Time domain simulations and tests using the PHIL setup involving one physical 18-level MMC are used to validate the VCS method. The analysis and test results show very good agreement.

Finally, the conclusions are presented in Chapter 9, where the main findings from the thesis are summarized.

2
Converters in HVDC Grids

This chapter introduces the Modular Multilevel Converter (MMC) topology together with its principle of operation and preliminary component sizing. It also discusses dc-dc converter topologies with a special focus on the Front-to-Front (F2F) dc-dc converter based on the MMC. The main goal of this chapter is to provide background information for the subsequent chapters. The discussion in this chapter is partially supported by the following contribution by the author.

> A. A. Taffese, E. de Jong, and E. Tedeschi, "Modelling of DC-DC Converter for System Level Studies," English, in *Proceedings of the 8th IEEE Benelux Young Researchers Symposium in Electrical Power Engineering: YRS2016*, Eindhoven, The Netherlands: Technische Universiteit Eindhoven, May 2016, p. 6

Chapter Outline

2.1 Introduction

HVDC grids are built by interconnecting converter stations, ac-dc and dc-dc, with cables and overhead lines. The main components of such an ac-dc HVDC station are shown in Fig. 2.1. On the ac side, a transformer is used to match the converter voltage to the ac grid voltage at the point of connection. The circuit breaker is responsible for clearing fault currents at the ac or dc terminals of the converter. Using an ac breaker to isolate dc-side faults leads to the disconnection of all the ac grids that feed into the fault, which is not desirable from an availability point of view. Circuit breakers on the dc side are under development in order to more selectively isolate faulty sections of the HVDC grid without powering down the whole system [4]. The dc inductor's purpose is to limit the rate of rise of dc current during faults and fast transients. The main component in Fig. 2.1 is the

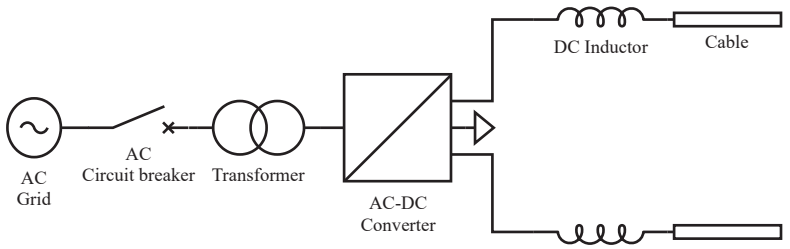

Figure 2.1: Main components of symmetric monopole HVDC station.

converter. HVDC converters have evolved all the way from the earliest (1950s) LCC type converters to the most modern MMC. Throughout this evolution, the converter topologies have changed significantly. Voltage source type converters were introduced in the 1990s. Ever since then the two-level converter topology has been adopted in many HVDC applications. But as the voltage level increased, there was a need for modular and scalable technology. Thanks to the introduction of the MMC, this was achieved in the early 2000s. The MMC has been very popular ever since, which is also part of the reason why it was adopted in this study. Apart from its scalability and modularity, the converter topology also has inherent energy storage capability which is not fully exploited as yet. In the development of an HVDC grid system, additional components are required. One of the new components that have not yet been commissioned are the dc-dc converters in HVDC system, which primarily play the role of transformers in dc grid in addition to other services. Despite their vital role, dc-dc converters have not received the same level of research focus as the other components in regard to integration into system-level studies. This thesis will address modeling of dc-dc converters that can be used in large-scale system studies in the next chapter. The purpose of this chapter is to introduce the main converter topologies, both ac-dc and dc-dc,

in HVDC grids. This chapter is organized as follows. It starts with an introduction to the MMC topology, which details the components of the converter and basic principle of operation. This is followed by an introduction of MMC-based dc-dc converter topologies with a focus on Front-to-Front (F2F) topology. This section will also provide a general overview of on the role of dc-dc converters in HVDC systems. The last section briefly introduces other components that have not been the main focus of the thesis, but are present in HVDC systems. These include transformers, cables, smoothing reactors, and circuit breakers.

2.2 Modular multilevel converters

The modular multilevel converter is composed of several interconnected power processing units, called Submodules (SMs), as shown in Fig. 2.2. They are also called cells in literature, for example in [20]. Each string of submodules is known as an *arm of the MMC*. A pair of arms connected in series form *a leg*. The two arms are called *upper* and *lower* arms of a leg. In an ac-dc MMC, the ac terminal is taken from the mid-point where the two arms are connected, while the dc terminal is formed by the two outermost nodes, as shown in Fig. 2.2. A three-phase MMC has three legs (six arms) which are connected to a common dc link. The arms are interconnected via inductors, called the *arm inductors*, whose purpose is to limit the magnitudes of fault currents and circulating currents.

2.2.1 Submodule topologies

Several submodule topologies have been proposed in the literature [20], [21]. Among these, the Half-Bridge (HB) and Full-Bridge (FB) topologies are the most common ones. The internal structures of these submodule topologies are shown in Fig. 2.3. Both topologies are equipped with a capacitor bank, which is the main energy storage element in the submodules. The output of the MMC is controlled by inserting and removing the submodule capacitors in the output current path. The capacitors are said to be inserted when they appear on the path from **(+)** terminal to **(–)** terminal of the submodules in Fig. 2.3.

In the case of half-bridge submodules, this is achieved by turning on the upper switch. In this case, either the IGBT Q_1 or the freewheeling diode D_1 conduct depending on the current polarity. The submodule is bypassed when the lower switch is turned on, which means that the current flow is through either Q_2 or D_2 depending on the current polarity. The HB submodule can produce only two voltage levels at the output; 0 or V_{sm}.

The FB submodule can produce one additional level ($-V_{sm}$), hence giving a three-level output. These three switching states are achieved as follows. Turning on Q_1 and Q_4 inserts the capacitor into the main power circuit with a positive polarity

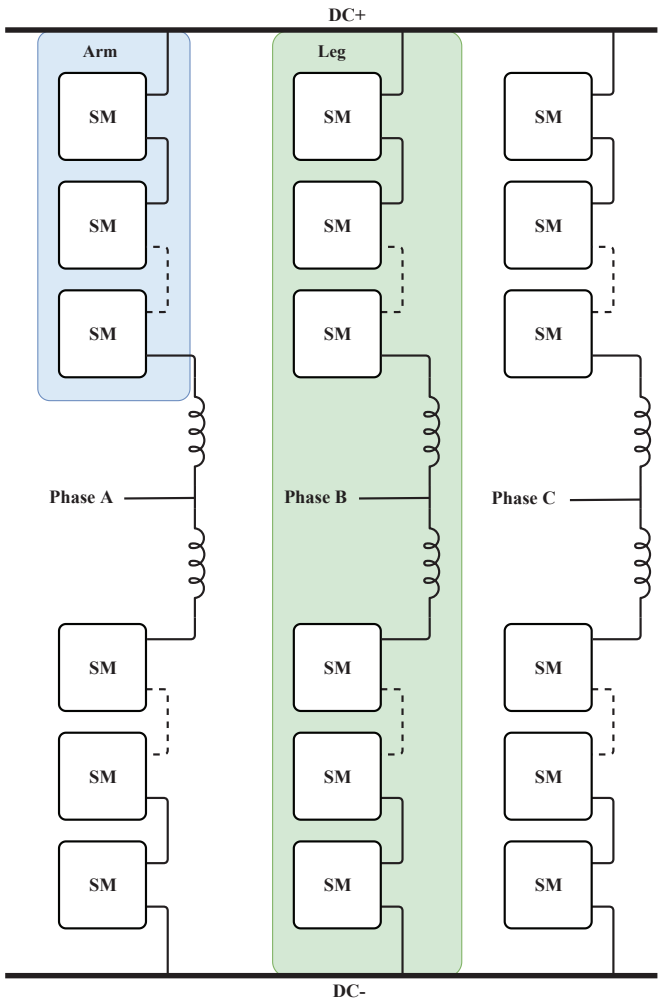

Figure 2.2: Topology of a three-phase MMC.

yielding $+V_{sm}$ at the output. The opposite polarity can be obtained when turning on Q_2 and Q_3. Similarly, the capacitor can be removed by turning on the two upper (or the two lower) switches at the same time. The current flows through the IGBTs or the freewheeling diodes depending on the current polarity. The switching states of the devices depending on current polarity are summarized in Table 2.1.

The commercially available MMC HVDC converters are all built using HB submodules [21]. The popularity of the HB submodule stems from its simplicity due to its low component count. However, the FB submodule has the capability to generate normal ac voltage with zero dc link, which is an enabling feature in

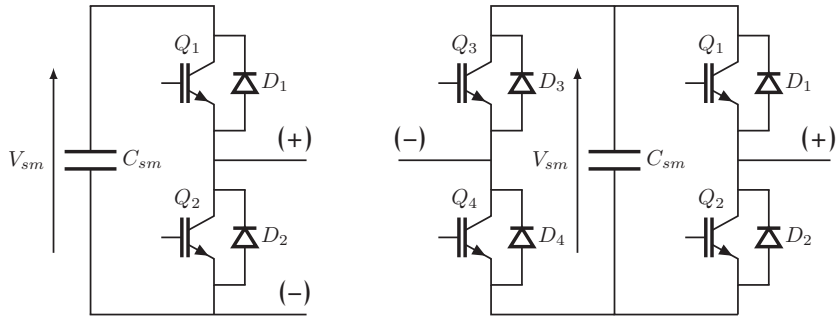

Figure 2.3: MMC submodules: half-bridge (left) and full-bridge (right).

Table 2.1: Submodule switching states.

Topology	Output voltage	Conducting devices ($I > 0$)*	Conducting devices ($I < 0$)*
Half-bridge	0	Q_2	D_2
	V_{sm}	D_1, C_{sm}	Q_1, C_{sm}
Full-bridge	0	D_1, Q_3	Q_1, D_3
	0	Q_2, D_4	D_2, Q_4
	V_{sm}	D_1, C_{sm}, D_4	Q_1, C_{sm}, Q_4
	$-V_{sm}$	Q_2, C_{sm}, Q_3	D_2, C_{sm}, D_3

*Current flowing from (+) terminal to (–) terminal is defined to be positive.

applications where dc side fault blocking is a requirement. It can also be used in applications where dc voltage reversal is required, like interoperability with LCC HVDC [21]. The main drawback of the FB submodule is that it has double the number of semiconductor components and drive circuitry than the HB. This can lead to higher cost, heavier converter, and increased losses. The choice of submodule topology is, therefore, a trade-off between the required features and the cost of implementation. More cost-effective approaches which combine the benefits of both topologies have been discussed in [22].

2.2.2 Principle of operation of the MMC

A HB-MMC arm can produce a voltage output between 0 and the sum of all the submodule voltages in the arm. The FB submodule can also produce a maximum voltage with negative polarity. Negative voltage generation at the output of an arm is not needed for normal operation of a three-phase MMC because the converter has to interface with both ac and dc sides. As mentioned earlier, the negative polarity output is beneficial when dc-side fault blocking is desired. Since fault blocking is not studied in this thesis, the modeling and analysis is henceforth focused on HB submodules with only positive voltage polarity to simplify the dis-

cussions. A staircase-like waveform can be produced by incrementally inserting submodules in an arm. There is considerable degree of freedom in choosing which modules are inserted at a given time. This fact is exploited to achieve balancing of the capacitor voltages across submodules in the same arm [23]. If N is defined as the number of submodules in an arm, the voltage output v of an arm is the sum of capacitor voltages of the submodules that are inserted, as given by (2.1).

$$v_u = \sum_{i=1}^{N_{ins\,u}} v_{smi\,u} \quad \text{and} \quad v_l = \sum_{i=1}^{N_{ins\,l}} v_{smi\,l} \tag{2.1}$$

where v_{smi} is the capacitor voltage of i^{th} submodule, N_{ins} is the number of inserted submodules. v_u and v_l are the upper and lower arm inserted voltages, respectively. For a given arm, the *insertion index*, n, is defined as the ratio of the inserted voltage to the sum of submodules capacitor voltages in an arm, which is approximately equal to the ratio of N_{ins} to N.

$$n_u \equiv \frac{\sum_{i=1}^{N_{ins\,u}} v_{smi\,u}}{\sum_{i=1}^{N} v_{smi\,u}} \approx \frac{N_{ins\,u}}{N} \quad \text{and} \quad n_l \equiv \frac{\sum_{i=1}^{N_{ins\,l}} v_{smi\,l}}{\sum_{i=1}^{N} v_{smi\,l}} \approx \frac{N_{ins\,l}}{N} \tag{2.2}$$

where n_u and n_l are the upper and lower arm insertion indexes, respectively. The insertion index is generally a discrete amplitude signal which can take one of the $N+1$ values between 0 and 1 with a step size of $1/N$. As the value of N increases, the step size decreases, and the insertion index can be assumed to be a continuous variable with negligible error. This assumption is valid even for the cases where N is as low as six if a PWM technique is applied to the last submodule to reduce the error in the output step.

The sum of capacitor voltages of all the submodules in a given arm is called *the arm voltage* or *the sum of capacitor voltages*, which is defined as shown in (2.3) for the upper and lower arms.

$$v_{cu} = \sum_{i=1}^{N} v_{smi\,u} \quad \text{and} \quad v_{cl} = \sum_{i=1}^{N} v_{smi\,l} \tag{2.3}$$

where v_{cu} and v_{cl} are the upper and lower arm voltages, respectively. By using the arm voltage definitions and assuming that the submodule voltages are balanced, the inserted voltages v_u and v_l can be written as shown in (2.4).

$$v_u = n_u v_{cu} \quad \text{and} \quad v_l = n_l v_{cl} \tag{2.4}$$

The equations presented so far are in the form of the upper and lower arms, which is an equivalent representation that reflects the physical structure of the converter. However, representation in terms of common-mode and differential terms

gives a model that is simpler for analysis and control design. The common-mode and differential parts correspond to the dc and ac sides, respectively. This implies that this approach to modeling gives a better separation between the control of the two sides. Therefore, the upper and lower arm variables are transformed into common-mode and differential terms. Transformation of the insertion indexes is shown in (2.5).

$$n_c = \frac{1}{2}(n_u + n_l) \quad \text{and} \quad n_{ac} = (-n_u + n_l) \tag{2.5}$$

where n_c and n_{ac} are the common-mode and differential insertion indexes, respectively. The arm currents can be transformed similarly, as shown in (2.6).

$$i_c = \frac{1}{2}(i_u + i_l) \quad \text{and} \quad i_{ac} = (i_u - i_l) \tag{2.6}$$

where i_c and i_{ac} are the common-mode and differential arm currents, respectively. Finally, the arm voltages are transformed as shown in (2.7)

$$v^{\Sigma} = \frac{1}{2}(v_{cu} + v_{cl}) \quad \text{and} \quad v^{\Delta} = \frac{1}{2}(v_{cu} - v_{cl}) \tag{2.7}$$

where Σ denotes the common-mode (average) arm energy and Δ represents the differential arm energy. These results will be used in the derivation of an average dynamics model of the MMC in Section 3.2. In ac-dc applications, each of the upper and lower arms produces the ac voltage with opposite polarity on top of a common mode voltage equal to half of the dc link voltage. Both the ac and dc currents flow through inserted submodules, which causes ripples in the capacitor voltages and circulating current between the legs. The magnitudes of these ripples depends on the value of the submodule capacitance and the arm inductance. The next section discusses considerations in the selection of the submodule capacitance and the arm inductance.

2.2.3 Component sizing considerations

Detailed design of an MMC has been addressed in detail in the literature [21], [24]. Therefore, the purpose of this section is to briefly discuss the design trade-offs involved in the selection of the most important components with respect to this thesis, i.e. the submodule capacitance and the arm inductance.

The submodule capacitance is chosen to minimize the ripple in the submodule voltage, and hence, the sum of capacitor voltages. Ideally the capacitor should be chosen to make the ripple as low as possible. This would, however, lead to high cost and possibly weight of the converter. Therefore, a ripple in the order of ±10% is specified to provide a good trade-off between the two requirements [21]. The

capacitor size is often specified as a ratio of how much energy it can store (in kJ) to the rating of the converter (in MVA) resulting in a unit of kJ/MVA. The size of the capacitor that results in the voltage ripple in the range of ±10% is in the range of 30 kJ/MVA to 40 kJ/MVA [21].

The arm inductors have a primary purpose of limiting circulating current between the legs of an MMC. The circulating currents originate from the voltage mismatch among the three legs which are connected in parallel. Without the arm inductors, the currents can change very rapidly even with small mismatches in the leg voltages because the rate of change of current is limited by only the parasitic inductance of the wires. This makes the task of the controller very difficult because it has to balance the legs instantaneously. Therefore, having the arm inductors lowers the rate of rise of current, which in turn, relaxes the requirement on the controller. Fault current limiting is a second function of the arm inductors which results in a higher inductance value than the one required for reducing circulating current ripples. Unless FB submodules are used, a dc-side short circuit results in the ac side feeding fault current via the freewheeling diodes of the MMC. The arm inductors reduce the fault current up to an acceptable level until it is cleared by the ac side circuit breaker. Typical impedance values for the arm inductors are in the range of 10% to 15% of the base impedance [21].

2.2.4 Summary

A brief introduction to the topology and principle of operation of the MMC was presented in this section together with some design considerations. Two of the popular submodule topologies were discussed and qualitatively compared. The principle of operation of MMC was explained with the help of simple equations describing the voltages and currents of an arm. The basic equations presented in this section are expanded in the next chapter where detailed dynamic models are derived.

A new component that plays a key role in enabling HVDC grids is the dc-dc converter, which is in the early stage where several topologies are being proposed. Some of these topologies have structures inspired by the modularity and scalability of the MMC. As highlighted in the research questions in Chapter 1, this thesis partly focuses on the modeling of a dc-dc converter topology. In light of this, the next section presents a brief review of dc-dc converter topologies proposed in literature.

2.3 DC-DC converters in HVDC grids

There are a number of technical choices in the implementation of an HVDC link. Among the choices are the converter technology, grounding scheme, and operat-

ing voltage. Converter technology is, currently, either LCC or VSC in its broadest sense. Grounding schemes include monopole, symmetric monopole, and bi-pole, which are further classified based on whether ground or metallic return is used. Several of the HVDC installations existing today have a wide variety of voltage levels because of the lack of standardized voltage levels. The combination of the aforementioned choices led to many possible end designs for Point-to-Point (P2P) links limited, currently, by the number of major players in the industry. A study exploring HVDC links in the North Sea showed that there is a possibility to connect the P2P links to form a meshed dc grid [25]. However, there are five different voltage levels, two grounding schemes and two different converter technologies in the area. This case is a good example of the challenges of interconnecting P2P links because it exhibits most of the possible combinations; it has converter technology incompatibility, dc voltage difference, and different grounding schemes. The dc-dc converter topologies are currently being studied and developed to enable such interconnections. The next few sections discuss some aspects of dc-dc converters for this application.

2.3.1 The role of dc-dc converters in HVDC grids

There are different sets of requirements placed on dc-dc converters for solving each of the challenges mentioned in the previous section. Ref. [26] addresses the requirements for dc-dc converters under different applications. The major requirements, which vary with the type of application, are input-output voltage ratio or stepping ratio, need of galvanic isolation, and bi-directional power flow capability. A stepping ratio is defined as low when it is below 1.5 and high when it is above 5 [26]. In order for the dc-dc converter to become economically sound, it also has to offer additional features such as fault blocking and isolation. This is very important since the current difficulty in the implementation of MTDC is partly due to the absence of dc circuit breakers at acceptable ratings and costs. High-level requirements for selected applications are presented in subsequent sections.

2.3.1.1 Power-flow control

Power flow controllers are required in a dc system with more lines than converters [6]. For this application, the primary role of the dc-dc converter is to adjust the dc voltage on the two sides in order to achieve the desired power flow on the link. The converter plays the role of phase angle regulators in ac systems. The stepping ratio is normally close to one unless the converter is also used for voltage matching. Therefore, a low-ratio converter with bi-direction power flow capability is required in this application.

2.3.1.2 Voltage level matching

If the sole purpose of the converter is to match the voltage on the two sides, the main requirements are to produce the proper voltage ratio and meet the isolation needs of the application. Bi-directional power flow might be required depending on the application.

2.3.1.3 Interconnection of different converter technologies

Interconnection of LCC and VSC technologies poses a special set of challenges because the converter on one side is a current source and on the other side is a voltage source [26]. The most important difficulty is handling power reversal. For LCC, power is reversed by reversing the voltage; while for the VSC, it is done by reversing the current. Therefore, the dc-dc converter should be able to emulate LCC behavior with bipolar voltage on the LCC side while maintaining VSC behavior with bipolar current on the VSC side.

2.3.2 A review of topologies

Over the past couple of years, a number of dc-dc converter topologies have been proposed for high voltage dc-dc converter. A comprehensive review of these topologies is given in [27]. They can be broadly grouped into two categories: single-stage converters and double-stage converters. These groups are described in the next sections.

2.3.2.1 Single-stage dc-dc topologies

Single-stage topologies convert a dc input to a dc output without an intermediate ac stage [28]–[30]. Although these topologies do not involve an ac stage, balancing of arm and sub-module energies is facilitated by an ac circulating current commonly known as the secondary current. The main advantage of these topologies is reduced component count, and hence footprint. These advantages, however, come at the expense of being limited low voltage ratio applications in order to have efficient and cost-effective operation. Some of the dc-dc topologies proposed in literature are the Modular Multilevel DC (M2DC) [28], the DC Modular Multilevel Converter (DC-MMC) [29], and the double-π topology [30].

2.3.2.2 Double-stage dc-dc topologies

This group of topologies has an ac intermediate stage linking the two dc sides. These can be with or without coupling transformer, (Fig. 2.4). The transformer's purpose is twofold, to provide additional voltage stepping, and galvanic isolation. The additional stepping makes these topologies suitable for high-ratio applications. Moreover, galvanic isolation helps stop dc faults from propagating to the

healthy side [26]. Additionally, having a transformer-isolated topology offers the possibility of extension to multiport operation with a modification to the transformer design. In the event of a dc short circuit on one of the sides, double-stage

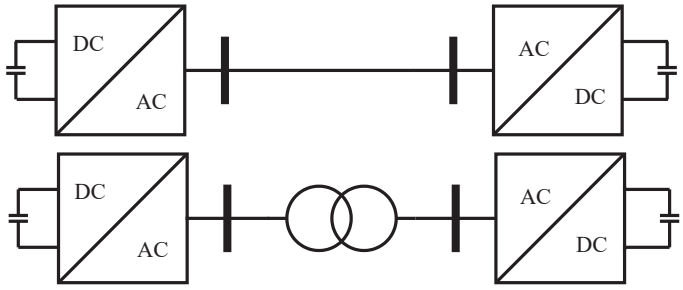

Figure 2.4: Double-stage dc-dc converter topology with and without transformer.

topologies can block the affected side while at the same time reducing the ac voltage to zero. This enables the healthy side to continue operating at normal voltage without exchanging power and to disconnect smoothly if necessary. This might be beneficial if the dc-dc converter is connected to multiple branches, in which case the other branches can continue exchanging power since the link is not affected. Among the isolated topologies presented in literature are the Front-to-Front (F2F) converter and Daul Active Bridge (DAB) converter [26], [31], [32]. Among these, the F2F converter is discussed in detail in the following section.

2.3.3 The Front-to-Front MMC topology

The F2F is composed of two full power ac-dc converters connected on their ac sides. A major difference from the back-to-back arrangement is that the ac side is internal, and its quantities can be optimized for cost, size, and efficiency. Operation frequency of 350 Hz was suggested in [31] as a result of a trade-off between size and efficiency. Different technologies can be used for each ac-dc converter depending on the application and voltage level. Candidate topologies include MMC, Alternate Arm Converter (AAC), and even passive rectifiers when bi-directional power flow is not required.

MMC-based F2F topology offers the flexibility and scalability of the MMC. Therefore, the F2F is well suited for bulk power applications at high voltages. The fact that is has a transformer isolation makes it a suitable candidate for dc hubs applications where the dc-dc converter acts as a hub for collection and distribution of power from offshore generation to onshore grids [4]. Moreover, the building block of the converter (the MMC) is well established, and hence minimal development is needed to get the MMC-based F2F ready for market, thus making it the most promising topology. The MMC-based F2F is, therefore, selected for further

modeling and simulation in the next chapter of this thesis.

Because of the higher frequency of operation, the submodule capacitance, the arm inductance, and the transformer can be designed to be considerably smaller than a 50/60 Hz MMC. For example, the arm inductance is chosen to be 10% to 15%. Since the frequency is increased by a factor of 7 (350 Hz), it means that the inductance value can be reduced by a factor of up to 7. This gives a good trade-off between the losses and footprint for offshore HVDC applications where space is at a premium [31].

2.4 Summary

This chapter presented an overview of converter topologies in HVDC grids. The MMC is the latest addition to the ac-dc converter topologies in HVDC applications. It has a modular structure consisting of low voltage power processing units (submodules) connected in series. It is the modularity and scalability of the MMC that made it popular in recent installations. Moreover, it has a short-term energy storage capability distributed in its submodules, which can be used to provide ancillary services to the ac power system, as discussed in Chapter 7. Principle of operation and basic design criteria for the MMC is presented in this chapter. Further dynamic modeling and detailed analysis of the MMC is presented in subsequent chapters.

Another key component in HVDC grids is the dc-dc converter, which plays a role equivalent to that of a transformer (voltage level matching) and power flow control devices in ac systems. It can also serve to interconnect technologies that are otherwise incompatible, like LCC and VSC technologies. The development of dc-dc converters is at an early stage where several topologies are being proposed. A high-level review of the proposed topologies is presented in this chapter. Among these topologies, the MMC-based F2F converter, which composed of two MMCs connected on the ac side, is considered to be promising because its building block, the MMC, is a proven technology. Despite its key role in future HVDC grids, the dc-dc converter is not well integrated into system-level studies mainly due to the lack of appropriate models. Modeling and analysis of the dc-dc converter is, therefore, covered in the next chapter to provide simplified models with a suitable level of detail for system-level studies. The modeling effort was limited to the F2F dc-dc converter because it is considered to be the most promising one.

3
Modeling of HVDC Grid Components

This chapter focuses on the modeling of HVDC grid components, particularly ac-dc MMC, MMC-based dc-dc converter, and power cables. Different studies require different levels of detail in the models, and hence different modeling approaches. The chapter presents several models suitable for different applications. In addition to a review of existing models, new models for the MMC-based Front-to-Front (F2F) dc-dc converter are proposed in this chapter. The models presented here form the basis for the analyses and discussions in the remainder of the thesis. The discussion in this chapter is partially supported by the following contributions by the author.

> A. A. Taffese and E. Tedeschi, "Simplified Modelling of the F2F MMC-Based High Power DC-DC Converter Including the Effect of Circulating Current Dynamics," in *2018 IEEE 19th Workshop on Control and Modeling for Power Electronics (COMPEL)*, Jun. 2018, pp. 1–6
>
> A. A. Taffese, E. Tedeschi, and E. C. W. de Jong, "Modelling of DC-DC converters based on front-to-front connected MMC for small signal studies," in *2016 IEEE 17th Workshop on Control and Modeling for Power Electronics (COMPEL)*, Jun. 2016, pp. 1–7

Chapter Outline

3.1 Overview of power system modeling requirements

Simulation models are used for a variety of purposes, ranging from detailed analysis at the component level all the way to large-scale system optimizations. Each of these use cases for the models places a constraint on how much detail should be included in the models. In power systems, the most common types of studies are steady-state analysis, small-signal stability analysis, Root Mean Square (RMS) simulation, and Electromagnetic Transient (EMT) simulation. Steady-state (load-flow) models are most commonly used for determining equipment ratings during the design stage and to optimize system performance during operation. These kinds of studies require the least amount of detail in the models often including only admittances, impedances, and slow outer controllers that define steady-state behavior of the system.

Small signal stability analysis offers a set of tools that can be used to analyze stability of a system subjected to small disturbances around a stable operating point. Such tools can be used to systematically identify, analyze, and solve stability problems, especially in situations where there are multiple controllers that can interact. The modeling detail required for small-signal studies depends on the objective of the study. For example, electromechanical interactions in the order of few hertz can be studied with much simpler models compared to current controller interactions that can be in the range of 100 Hz to few kHz. However, a requirement to perform small-signal studies is that all the quantities (state variables) need to be constants in steady state. Transformations, such as phasor-based modeling, are often used to achieve this.

RMS simulation is used extensively in large-scale power systems where time domain investigation of sub-synchronous frequency phenomena is performed. The models are represented in simplified phasor forms that result in fast simulations which scale very well for large system studies. EMT simulations require the most detailed models because the timescale of interest is in the range of μs to few ms. Depending on the scenario, distributed parameter (travelling wave) models might be needed to ensure accurate results. EMT simulations are very resource intensive and therefore, they are often limited to component level and small-scale system studies.

Every modeling approach gives a certain trade-off between accuracy and usability (time efficiency). It is up to the user to decide on the acceptable level of trade-off for the given application. It is also important that the modeling detail used for one component is commensurate with the rest of the system. Any mismatch can cause either loss of accuracy or an unnecessary increase in model complexity.

3.2 Average arm model of the MMC

There are different ways to model the MMC for different purposes [33]–[44]. For transients and fast dynamics study a detailed switching model is used. On the other hand, for system-level dynamics studies, which is the focus of this work, average models are sufficient. The average model can adequately capture dynamics of the MMC assuming that submodule-level imbalances are nullified by implementing appropriates control functions. This assumption does not introduce significant modeling error as discussed in [34] and also verified in this thesis as part of the experimental results. The main assumptions used to develop the average model are [34]:

1. the insertion indexes are continuous variables.
2. the submodule voltages in the same arm are balanced and the capacitances are the same.

From Fig. 3.1, two loops can be identified; ac and dc loops. The dc loop is formed by the dc voltage, the inserted voltages, and the arm inductances. Similarly, the ac loop contains the grid voltage, the transformer, the arm inductances and the internal ac voltage of the converter. Applying Kirchhoff's Voltage Law (KVL) on the dc loop gives (3.1).

$$v_{dc} - v_u - L_{arm}\frac{\mathrm{d}}{\mathrm{dt}}i_u - R_{arm}i_u - v_l - L_{arm}\frac{\mathrm{d}}{\mathrm{dt}}i_l - R_{arm}i_l = 0 \tag{3.1}$$

where L_{arm} and R_{arm} are the inductance and resistance, respectively. Grouping terms and simplifying yields (3.2).

$$\begin{aligned} v_{dc} - (v_u + v_l) - L_{arm}\frac{\mathrm{d}}{\mathrm{dt}}(i_u + i_l) - R_{arm}(i_u + i_l) &= 0 \\ v_{dc} - (v_u + v_l) - 2L_{arm}\frac{\mathrm{d}}{\mathrm{dt}}i_c - 2R_{arm}i_c &= 0 \\ v_{dc} - (n_u v_{cu} + n_l v_{cl}) - 2L_{arm}\frac{\mathrm{d}}{\mathrm{dt}}i_c - 2R_{arm}i_c &= 0 \end{aligned} \tag{3.2}$$

Substituting the definitions of the insertion indexes from (2.5) and the arm voltages from (2.7) into (3.2) gives (3.3).

$$L_{arm}\frac{\mathrm{d}}{\mathrm{dt}}i_c = \frac{1}{2}v_{dc} - n_c v^{\Sigma} - n_{ac} v^{\Delta} - R_{arm}i_c \tag{3.3}$$

Following similar steps, the ac side equations can be derived as follows:

$$L_{ac}\frac{\mathrm{d}}{\mathrm{dt}}i_{ac} = n_{ac} v^{\Sigma} - n_c v^{\Delta} - v_g - R_{ac}i_{ac} \tag{3.4}$$

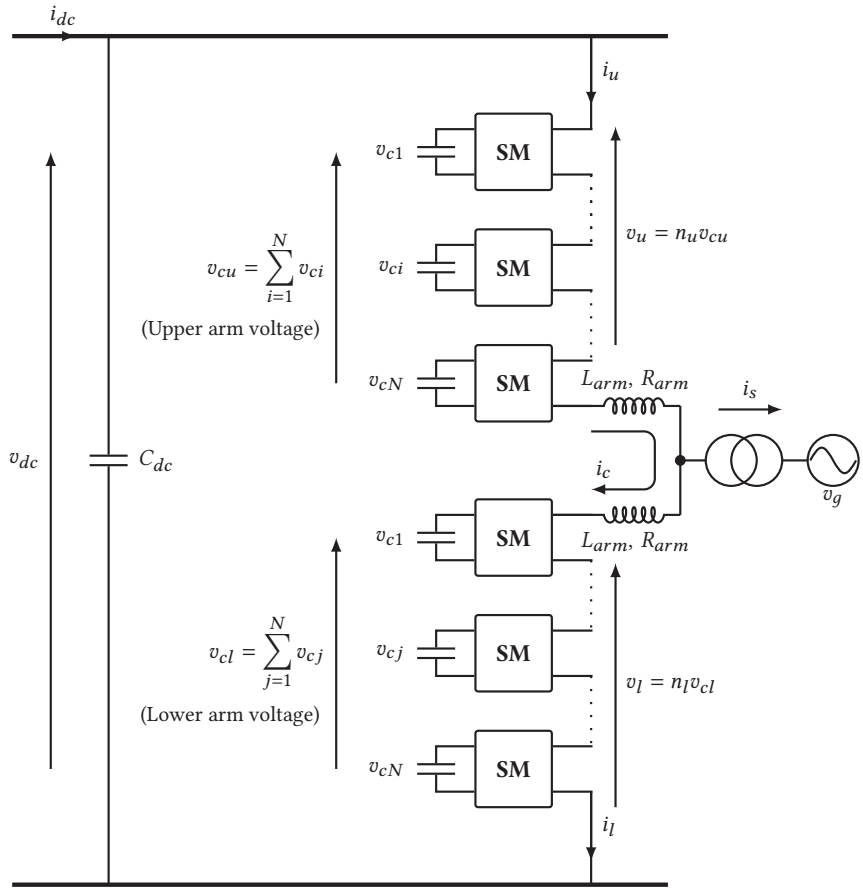

Figure 3.1: Per-phase circuit diagram of MMC.

$$\text{where} \quad L_{ac} = L_{arm} + \frac{1}{2}L_t \quad \text{and} \quad R_{ac} = R_{arm} + \frac{1}{2}R_t \tag{3.5}$$

where R_t and L_t are the resistance and inductance of the transformer, respectively.

Dynamic equations for the arm voltages can be derived by starting from dynamics of a single submodule. Equation (3.6) shows the equation for dynamics of a submodule in the upper arm. It can be noted that the same arm current flows through all the inserted submodules.

$$C_{sm}\frac{\mathrm{d}}{\mathrm{dt}}v_{sm\,u} = \begin{cases} i_u, & \text{inserted} \\ 0, & \text{bypassed} \end{cases} \tag{3.6}$$

Applying summation on (3.6) over the number of submodules N gives (3.7).

$$\sum_{i=1}^{N} C_{smi}\frac{\mathrm{d}}{\mathrm{dt}}v_{smi\,u} = N_{ins\,u}\,i_u \tag{3.7}$$

Assuming that the submodule capacitance values and voltages are the same across the submodules (as per assumption 2), (3.7) simplifies to (3.8).

$$\begin{aligned}
\sum_{i=1}^{N} C_{sm}\frac{\mathrm{d}}{\mathrm{dt}}Nv_{sm\,u} &= N_{ins\,u}i_u \\
C_{sm}\frac{\mathrm{d}}{\mathrm{dt}}v_{cu} &= N_{ins\,u}i_u \\
\frac{C_{sm}}{N}\frac{\mathrm{d}}{\mathrm{dt}}v_{cu} &= \frac{N_{ins\,u}}{N}i_u \\
C_{arm}\frac{\mathrm{d}}{\mathrm{dt}}v_{cu} &= n_u i_u
\end{aligned} \tag{3.8}$$

where $C_{arm} = C_{sm}/N$ is the equivalent arm capacitance. The lower arm voltage dynamics can be similarly derived to give (3.9).

$$C_{arm}\frac{\mathrm{d}}{\mathrm{dt}}v_{cl} = n_l i_l \tag{3.9}$$

Applying the transformations from (2.5) to (2.7), the common-mode and differential arm voltage dynamics can be written as shown in (3.10) and (3.11).

$$C_{arm}\frac{\mathrm{d}}{\mathrm{dt}}v^{\Sigma} = n_c i_c - \frac{1}{2}n_{ac}i_{ac} \tag{3.10}$$

$$C_{arm}\frac{\mathrm{d}}{\mathrm{dt}}v^{\Delta} = \frac{1}{2}n_c i_{ac} - n_{ac}i_c \tag{3.11}$$

The equations describing dynamics of the MMC are summarized in (3.12), which gives the complete average arm model for one leg of an MMC. Three sets of these equations, one for each phase, are needed to represent a three-phase MMC.

$$\begin{aligned}
L_{arm}\frac{\mathrm{d}}{\mathrm{dt}}i_c &= \frac{1}{2}v_{dc} - n_c v^{\Sigma} - n_{ac}v^{\Delta} - R_{arm}i_c \\
L_{ac}\frac{\mathrm{d}}{\mathrm{dt}}i_{ac} &= n_{ac}v^{\Sigma} - n_c v^{\Delta} - v_g - R_{ac}i_{ac} \\
C_{arm}\frac{\mathrm{d}}{\mathrm{dt}}v^{\Sigma} &= n_c i_c - \frac{1}{2}n_{ac}i_{ac} \\
C_{arm}\frac{\mathrm{d}}{\mathrm{dt}}v^{\Delta} &= \frac{1}{2}n_c i_{ac} - n_{ac}i_c
\end{aligned} \tag{3.12}$$

3.3 Phasor model

Equation (3.12) gives a Steady-State Time Periodic (SSTP) model of the MMC [39], which means that the ac quantities in the system have instantaneous values

that oscillate at a given frequency in steady state. In certain use cases, a Steady-State Time Invariant (SSTI) model, where all the states are constant in steady state, is also desired because it allows linearization and further analyses such as small-signal stability studies [39]. Dynamic phasor-based modeling [35] of the harmonic components can be used in order to obtain an SSTI model from (3.12). The following assumptions are made to simplify the modeling:

1. i_{ac}, n_{ac}, v^{Δ}, and v_g are assumed to have only a first harmonic component
2. i_c, n_c, and v^{Σ} are assumed to have dc and second harmonic components

Harmonic orders are defined with respect to the ac side fundamental frequency. The harmonic components will be substituted by *phasors* denoted by ***boldface*** letters with an arrow on top, and the harmonic orders are indicated by the *subscripts*.

$$\begin{aligned} i_c &= i_{c0} + i_{c2} \quad \text{and} \quad n_c = n_{c0} + n_{c2} \\ v^{\Sigma} &= v_0^{\Sigma} + v_2^{\Sigma} \quad \text{and} \quad v^{\Delta} = v_0^{\Delta} + v_1^{\Delta} \\ i_{ac} &= i_{ac1} \quad \text{and} \quad n_{ac} = n_{ac1} \end{aligned} \tag{3.13}$$

The subscript 1 is dropped from the ac quantities i_{ac1} and n_{ac1} for the sake of notation simplicity.

3.3.1 Phasor operations

Since the derivation involves transformation of time domain signals into phasors, a brief description of phasor operations, particularly product and derivative operations, is presented here. Given two signals x and y in (3.14),

$$x(t) = X\cos(k_x\omega t + \phi_x) \quad \text{and} \quad y(t) = Y\cos(k_y\omega t + \phi_y) \tag{3.14}$$

the corresponding phasors are $\vec{\mathbf{x}}$ and $\vec{\mathbf{y}}$ rotating at frequencies $k_x\omega$ and $k_y\omega$, respectively as shown in (3.15).

$$\vec{\mathbf{x}} = X\mathrm{e}^{j\phi_x} \quad \text{and} \quad \vec{\mathbf{y}} = Y\mathrm{e}^{j\phi_y} \tag{3.15}$$

According to the trigonometric angle addition formula, the product of x and y is given by (3.16).

$$\begin{aligned} x(t)y(t) = \frac{1}{2}XY\big[&\cos\left((k_x - k_y)\omega t + \phi_x - \phi_y\right) \\ &+ \cos\left((k_x + k_y)\omega t + \phi_x + \phi_y\right)\big] \end{aligned} \tag{3.16}$$

The right-hand side of (3.16) can be transformed into two phasor quantities $\frac{1}{2}\vec{\mathbf{x}}\vec{\mathbf{y}}^*$ and $\frac{1}{2}\vec{\mathbf{x}}\vec{\mathbf{y}}$ rotating at frequencies $(k_x - k_y)\omega$ and $(k_x + k_y)\omega$, respectively. The rotation frequency of a phasor is equal to the frequency of the sinusoid in time domain. $(\cdot)^*$ is the complex conjugate operator. If $k_x = k_y$, the real part of $\frac{1}{2}\vec{\mathbf{x}}\vec{\mathbf{y}}^*$ is a dc term.

Derivative of a phasor quantity with respect to time is defined by accounting for the time rotation. For example, time derivative of x is given as follows:

$$\frac{\mathrm{d}}{\mathrm{d}t}x \longrightarrow \left(\frac{\mathrm{d}}{\mathrm{d}t}\left(\vec{\mathbf{x}}\mathrm{e}^{j\omega t}\right)\mathrm{e}^{-j\omega t}\right) = \frac{\mathrm{d}}{\mathrm{d}t}\vec{\mathbf{x}} + \mathrm{j}\omega\vec{\mathbf{x}} \tag{3.17}$$

It is done in two-step process where the phasor is converted to time domain signal, where derivative is applied, and then the result is converted back to phasor.

3.3.2 Phasor model of the MMC

The dc (average) dynamic equations are transformed to phasor domain as given by (3.18), where only the terms resulting in a dc component are included.

$$\begin{aligned} C_{arm}\frac{\mathrm{d}}{\mathrm{d}t}v_0^{\Sigma} &= n_{c0}i_{c0} + \frac{1}{2}\Re\{\vec{\mathbf{n}}_{c2}\vec{\mathbf{i}}_{c2}^*\} - \frac{1}{4}\Re\{\vec{\mathbf{n}}_{ac}\vec{\mathbf{i}}_{ac}^*\} \\ L_{arm}\frac{\mathrm{d}}{\mathrm{d}t}i_{c0} &= \frac{1}{2}v_{dc} - n_{c0}v_0^{\Sigma} + \frac{1}{2}\Re\{\vec{\mathbf{n}}_{ac}\vec{\mathbf{v}}_1^{\Lambda *}\} - \frac{1}{2}\Re\{\vec{\mathbf{n}}_{c2}\vec{\mathbf{v}}_2^{\Sigma *}\} - R_{arm}i_{c0} \end{aligned} \tag{3.18}$$

where $\Re\{\cdot\}$ is the real part operator. Similarly, the first harmonic components are given by (3.19).

$$\begin{aligned} C_{arm}\frac{\mathrm{d}}{\mathrm{d}t}\vec{\mathbf{v}}_1^{\Lambda} &= \frac{1}{2}n_{c0}\vec{\mathbf{i}}_{ac} + \frac{1}{4}\vec{\mathbf{n}}_{c2}\vec{\mathbf{i}}_{ac}^* - \vec{\mathbf{n}}_{ac}i_{c0} - \frac{1}{2}\vec{\mathbf{n}}_{ac}^*\vec{\mathbf{i}}_{c2} - \mathrm{j}\omega C_{arm}\vec{\mathbf{v}}_1^{\Lambda} \\ L_{ac}\frac{\mathrm{d}}{\mathrm{d}t}\vec{\mathbf{i}}_{ac} &= \vec{\mathbf{n}}_{ac}v_0^{\Sigma} + \frac{1}{2}\vec{\mathbf{n}}_{ac}^*\vec{\mathbf{v}}_2^{\Sigma} - n_{c0}\vec{\mathbf{v}}_1^{\Lambda} - \frac{1}{2}\vec{\mathbf{n}}_{c2}\vec{\mathbf{v}}_1^{\Lambda *} - \vec{\mathbf{v}}_g - R_{ac}\vec{\mathbf{i}}_{ac} - \mathrm{j}\omega L_{ac}\vec{\mathbf{i}}_{ac} \end{aligned} \tag{3.19}$$

The second harmonic part is given by (3.20).

$$\begin{aligned} C_{arm}\frac{\mathrm{d}}{\mathrm{d}t}\vec{\mathbf{v}}_2^{\Sigma} &= n_{c0}\vec{\mathbf{i}}_{c2} + \vec{\mathbf{n}}_{c2}i_{c0} - \frac{1}{4}\vec{\mathbf{n}}_{ac}\vec{\mathbf{i}}_{ac} - 2\mathrm{j}\omega C_{arm}\vec{\mathbf{v}}_2^{\Sigma} \\ L_{arm}\frac{\mathrm{d}}{\mathrm{d}t}\vec{\mathbf{i}}_{c2} &= -n_{c0}\vec{\mathbf{v}}_2^{\Sigma} - \vec{\mathbf{n}}_{c2}v_0^{\Sigma} + \frac{1}{2}\vec{\mathbf{n}}_{ac}\vec{\mathbf{v}}_1^{\Lambda} - R_{arm}\vec{\mathbf{i}}_{c2} - 2\mathrm{j}\omega L_{arm}\vec{\mathbf{i}}_{c2} \end{aligned} \tag{3.20}$$

Equations (3.18) to (3.20) constitute a tenth-order dynamic phasor model of an MMC leg. Although the tenth-order model is strictly applicable to one phase leg of an MMC, the same model can also be applied to a balanced three-phase system in dq domain, where the d and q components are the real and imaginary parts of the corresponding phasor. Dynamics of the dc voltage are a part of the dc

grid dynamic model that includes the cables and dc filter inductances. The model described by (3.18) to (3.20) is a detailed phasor model with 10 states.

The average component of the differential arm voltage $\vec{\mathbf{v}}_0^{\Delta}$ is neglected in the above model. This is justified because the arm voltages are normally balanced on average due to controller actions. If, however, these effects are to be captured, (3.21) can be included in the model. It should be noted that $\vec{\mathbf{v}}_0^{\Delta}$ is accompanied by a first harmonic common mode current $\vec{\mathbf{i}}_{c1}$ as shown in (3.21).

$$\begin{aligned} C_{arm}\frac{\mathrm{d}}{\mathrm{d}t}\vec{\mathbf{v}}_0^{\Delta} &= -\frac{1}{2}\Re\{\vec{\mathbf{n}}_{ac}\vec{\mathbf{i}}_{c1}^{*}\} \\ L_{arm}\frac{\mathrm{d}}{\mathrm{d}t}\vec{\mathbf{i}}_{c1} &= -\vec{\mathbf{n}}_{ac}v_0^{\Sigma} - R_{arm}\vec{\mathbf{i}}_{c1} - \mathrm{j}\omega L_{arm}\vec{\mathbf{i}}_{c1} \end{aligned} \tag{3.21}$$

3.3.3 Implication of the modeling assumptions

An important limitation of the phasor model derived in this section is its lack of generality in terms of modulation techniques. This comes from the assumption that the ac insertion index has only a fundamental component and the common-mode component has only dc and second harmonic components. Such assumptions are valid for direct modulation case where the modulation does not introduce harmonics to the insertion indexes. A brief description of modulation techniques for MMC are presented here to support the explanation. This topic is covered in more detail in Chapter 4.

The insertion indexes are calculated from the voltage references coming from the high-level current controllers using the specified modulation. The reference are composed of an ac component v_{ac}^r and a common mode component v_c^r. v_{ac}^r is a fundamental component signal unless harmonic injection is employed, which is not considered in this thesis. v_c^r, on the other hand, has a dc component and a second harmonic. The second harmonic is not needed in applications where compensated modulation is used. Once the references are generated, they are sent to the modulator, which calculates the insertion indexes. Only the upper arm reference is discussed here for illustrative purposes. The upper arm reference voltage is given by (3.22).

$$v_u^r = v_c^r - v_{ac}^r \tag{3.22}$$

The insertion indexes are calculated as shown in

$$n_u = \frac{v_u^r}{\hat{v}_{cu}} \tag{3.23}$$

$\hat{v}_{cu}$ is a normalizing signal that is chosen differently depending on the adopted modulation technique. It is chosen to be equal to the nominal dc voltage for the

case of direct modulation. In this case, the division by $\hat{v}_{cu}$ does not introduce further harmonics to the insertion indexes, which means that the modeling assumptions in the previous section are valid.

On the other hand, the divider $\hat{v}_{cu} = v_{cu}$ in the case of compensated modulation. Now, the insertion indexes will have harmonics that are caused by a combination of ripples in the arm voltage and ac components in v_u^r. Thus, the model in the previous section becomes inaccurate.

One way to generalize this model is by accounting for all the possible harmonic combinations that can arise due to compensated modulation and then derive the equations for each harmonic component. Ref. [40] proposed a generalized model including up to the sixth harmonic. The generalized model can be used to simulate MMC under different control arrangements. However, both the model given in this section and in [40] give similar results for the case of direct modulation. Therefore, the approach chosen in this thesis is to use the model in this section for direct modulation, while energy-based models (see next section) are used for compensated modulation.

3.4 Energy-based model

Energy-based modeling approach is presented in this section. This type of model gives a simpler representation for MMCs controlled using compensated modulation. The derivation starts from the arm voltage dynamics. The arm voltage dynamics of the upper and lower arms are given by (3.24).

$$C_{arm}\frac{\mathrm{d}}{\mathrm{dt}}v_{cu} = n_u i_u \qquad \text{and} \qquad C_{arm}\frac{\mathrm{d}}{\mathrm{dt}}v_{cl} = n_l i_l \tag{3.24}$$

Multiplying both sides of the equations in (3.24) by the respective arm voltages gives (3.25), where the product of the arm voltage and the insertions indexes is replaced by the respective inserted voltage.

$$C_{arm}v_{cu}\frac{\mathrm{d}}{\mathrm{dt}}v_{cu} = v_u i_u \qquad \text{and} \qquad C_{arm}v_{cl}\frac{\mathrm{d}}{\mathrm{dt}}v_{cl} = v_l i_l \tag{3.25}$$

The energy stored in the arms w_u and w_l are defined, as shown in (3.26).

$$w_u = \frac{1}{2}C_{arm}v_{cu}^2 \qquad \text{and} \qquad w_l = \frac{1}{2}C_{arm}v_{cl}^2 \tag{3.26}$$

Derivative of w_u and w_l with respect to time is given in (3.27).

$$\frac{\mathrm{d}}{\mathrm{dt}}w_u = C_{arm}v_{cu}\frac{\mathrm{d}}{\mathrm{dt}}v_{cu} \qquad \text{and} \qquad \frac{\mathrm{d}}{\mathrm{dt}}w_l = C_{arm}v_{lu}\frac{\mathrm{d}}{\mathrm{dt}}v_{lu} \tag{3.27}$$

Combining (3.25) and (3.27), the equations describing the arm energy dynamics are given by (3.28).

$$\frac{\mathrm{d}}{\mathrm{d}t}w_u = v_u i_u \qquad \text{and} \qquad \frac{\mathrm{d}}{\mathrm{d}t}w_l = v_l i_l \tag{3.28}$$

Equation (3.29) is obtained by expanding the upper and lower arm currents and inserted voltages into ac and common mode terms.

$$\begin{aligned}\frac{\mathrm{d}}{\mathrm{d}t}w_u &= (v_c - v_{ac})\left(i_c + \frac{1}{2}i_{ac}\right)\\ \frac{\mathrm{d}}{\mathrm{d}t}w_l &= (v_c + v_{ac})\left(i_c - \frac{1}{2}i_{ac}\right)\end{aligned} \tag{3.29}$$

The arm energies are converted in to sum and difference energies in (3.30). Such a representation simplifies control of the arm energy.

$$\begin{aligned}\frac{\mathrm{d}}{\mathrm{d}t}w^{\Sigma} &= 2v_c i_c - v_{ac} i_{ac}\\ \frac{\mathrm{d}}{\mathrm{d}t}w^{\Delta} &= v_c i_{ac} - 2v_{ac} i_c\end{aligned} \tag{3.30}$$

The circulating current dynamics can be derived from (3.2) as shown in (3.31).

$$L_{arm}\frac{\mathrm{d}}{\mathrm{d}t}i_c = \frac{1}{2}v_{dc} - v_c - R_{arm}i_c \tag{3.31}$$

The ac current dynamics is similarly given by (3.32).

$$L_{ac}\frac{\mathrm{d}}{\mathrm{d}t}i_{ac} = v_g - v_{ac} - R_{ac}i_{ac} \tag{3.32}$$

Equations (3.30) to (3.32) constitute the energy-based dynamic model of the MMC. Unlike the voltage-based model presented in Section 3.2, insertion indexes do not appear explicitly in the energy-based model. The insertion indexes can be included by using the following relations.

$$\begin{aligned}v_c &= \frac{1}{2}(v_u + v_l) = \frac{1}{2}(n_u v_{cu} + n_l v_{cl})\\ v_{ac} &= \frac{1}{2}(v_l - v_u) = \frac{1}{2}(n_l v_{cl} - n_u v_{cu})\end{aligned} \tag{3.33}$$

These relations complicate the model and also result in mixing of voltage-based and energy-based variables. The latter introduces square-root relation in the dynamic equation, which is highly nonlinear. Fortunately, these relations do not need to be implemented for the cases where compensated modulation is used.

This is because compensated modulation can make the voltage reference independent of the arm voltages. Therefore, instead of the insertion indexes, the model uses the voltage references as inputs. This is illustrated by (3.34) where the inserted upper arm voltage is shown to be equal to its reference values. The same is true for the lower arm.

$$v_u = v_u^r \frac{v_{cu}}{\hat{v}_{cu}} = v_u^r \frac{v_{cu}}{v_{cu}} = v_u^r \tag{3.34}$$

Consequently, the voltages v_c and v_{ac} are equal to their respective references v_c^r and v_{ac}^r. Taking this into account, the equations for the final energy-based model are presented in (3.35).

$$\begin{aligned} \frac{\mathrm{d}}{\mathrm{dt}} w^{\Sigma} &= 2 v_c^r i_c - v_{ac}^r i_{ac} \\ \frac{\mathrm{d}}{\mathrm{dt}} w^{\Delta} &= v_c^r i_{ac} - 2 v_{ac}^r i_c \\ L_{arm} \frac{\mathrm{d}}{\mathrm{dt}} i_c &= \frac{1}{2} v_{dc} - v_c^r - R_{arm} i_c \\ L_{ac} \frac{\mathrm{d}}{\mathrm{dt}} i_{ac} &= v_{ac}^r - v_g - R_{ac} i_{ac} \end{aligned} \tag{3.35}$$

3.4.1 Energy-based phasor model

Conversion of (3.35) into phasor form is simpler compared to the voltage-based model because compensated modulation is assumed. Under this condition, the common mode current i_c has only a dc component, which also means that the controller only needs to generate a dc common mode reference voltage v_c^r. The ac currents and voltages have a fundamental frequency component. Thus, the harmonic contents of the different elements are summarized as follows (also shown in (3.36)).

1. i_{ac}, v_{ac}^r, w^{Δ}, and v_g are assumed to have only a 1$^{\text{st}}$ harmonic component
2. i_c and v_c^r are assumed to only have dc components
3. w^{Δ} has dc and 2$^{\text{nd}}$ harmonic components

$$\begin{aligned} i_c = i_{c0} \quad &\text{and} \quad n_c = n_{c0} \\ w^{\Sigma} = w_0^{\Sigma} + w_2^{\Sigma} \quad &\text{and} \quad w^{\Delta} = w_1^{\Delta} \end{aligned} \tag{3.36}$$

There might also be a dc component in w^{Δ} due to a first harmonic component i_c, and the controller, in this case, injects a first harmonic common mode reference.

This occurs when a closed-loop control is employed to balance the arm energies. However, these components are not included in the model because such a closed-loop arm balancing control is not used in this thesis.

With these components considered, the equations in (3.35) are transformed to the ones shown in (3.37).

$$\begin{aligned}
\frac{\mathrm{d}}{\mathrm{dt}} w_0^{\Sigma} &= 2 v_{c0}^{r} i_{c0} - \frac{1}{2} \Re\{\vec{\mathbf{v}}_{ac}^{r} \vec{\mathbf{i}}_{ac}^{*}\} \\
\frac{\mathrm{d}}{\mathrm{dt}} \vec{\mathbf{w}}_2^{\Sigma} &= -\frac{1}{2} \vec{\mathbf{v}}_{ac}^{r} \vec{\mathbf{i}}_{ac} - \mathrm{j}\omega \vec{\mathbf{w}}_2^{\Sigma} \\
\frac{\mathrm{d}}{\mathrm{dt}} \vec{\mathbf{w}}_1^{\Delta} &= v_{c0}^{r} \vec{\mathbf{i}}_{ac} - 2\vec{\mathbf{v}}_{ac}^{r} - \mathrm{j}\omega \vec{\mathbf{w}}_1^{\Delta} \\
L_{arm} \frac{\mathrm{d}}{\mathrm{dt}} i_{c0} &= \frac{1}{2} v_{dc} - v_{c0}^{r} - R_{arm} i_{c0} \\
L_{ac} \frac{\mathrm{d}}{\mathrm{dt}} \vec{\mathbf{i}}_{ac} &= \vec{\mathbf{v}}_{ac}^{r} - \vec{\mathbf{v}}_{g} - R_{ac} \vec{\mathbf{i}}_{ac} - \mathrm{j}\omega L_{ac} \vec{\mathbf{i}}_{ac}
\end{aligned} \tag{3.37}$$

It should be noted that the equations in (3.37) assume ideal compensated modulation. In practice, ideal performance is difficult to achieve because of measurement distortions, and time delays. This causes a second harmonic circulating current. An improved controller is proposed in this thesis that achieves close to ideal performance and eliminates the circulating current with the help of an online parameter adjustment method. This is discussed in Chapter 6. Additionally, the improved controller also results in balancing of the arms in the same leg, which means that the dynamics of the dc term in w^{Δ} can safely be neglected.

3.5 Simplifications

Both the voltage-based and energy-based phasor models presented so far are for one leg of the MMC. A model of a three-phase MMC requires three times the number of equations with the only difference being the circuit parameters and ±120° shifts. However, if the circuit parameters are the same across the legs (symmetric system), the leg model can be used to represent the three-phase MMC under balanced symmetric operation. This is one simplification that can reduce model complexity in large-scale system studies.

Another simplification presented in [33] goes one step further and neglects the

ripple components in w_2^{Σ} and w_1^{Δ}. The result is a fourth-order model given by (3.38)

$$\begin{aligned} \frac{\mathrm{d}}{\mathrm{dt}} w_0^{\Sigma} &= 2v_{c0}^{r} i_{c0} - \frac{1}{2}\Re\{\vec{\mathbf{v}}_{ac}^{r}\vec{\mathbf{i}}_{ac}^{*}\} \\ L_{arm}\frac{\mathrm{d}}{\mathrm{dt}} i_{c0} &= \frac{1}{2}v_{dc} - v_{c0}^{r} - R_{arm} i_{c0} \\ L_{ac}\frac{\mathrm{d}}{\mathrm{dt}}\vec{\mathbf{i}}_{ac} &= \vec{\mathbf{v}}_{ac}^{r} - \vec{\mathbf{v}}_{g} - R_{ac}\vec{\mathbf{i}}_{ac} - \mathrm{j}\omega L_{ac}\vec{\mathbf{i}}_{ac} \end{aligned} \tag{3.38}$$

Phasors are realized in dq domain where the d and q axes are the real and imaginary parts, respectively. Thus, two states are needed to represent each phasor. The model given by (3.38) was used on several occasions throughout the thesis and was found to be accurate in representing the MMC in system studies where compensated modulation is used. This model should, however, be used with caution when applied to cases with direct modulation since it does not represent the circulating current ripple dynamics.

3.6 Modeling of MMC-based F2F dc-dc converters

As introduced in Chapter 2, the F2F dc-dc converter is made up of two MMCs connected on their ac sides (Fig. 3.2). This section presents the modeling of this converter as an extension of the MMC models from the previous sections. An

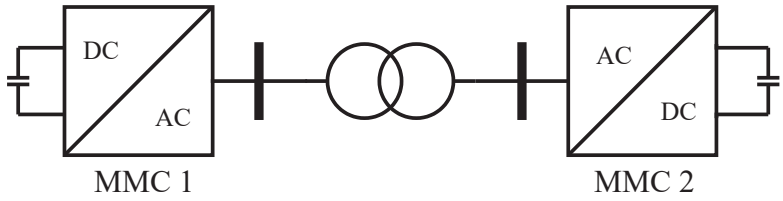

Figure 3.2: Topology of MMC-based F2F converter.

obvious option for modeling this topology is to put two MMC models and connect them on their ac sides. If the two MMCs are symmetrical and their operation is balanced, each side can be represented by 10 states, resulting in a total of 20 states. It can be challenging to include such a model in large-scale studies because the number of states (20 per converter excluding control states) is large. A simplified model suitable for large-scale studies is proposed in this section.

A first point of simplification is that the ac side is common to both MMCs, which means that the ac current dynamics can be represented by two states instead of four. The number of states decreased to 18 after this simplification. However, because of its symmetry, the F2F lends itself to further simplification. The following sections present two simplified models presented in [9] and [13].

3.6.1 Energy-based simplified model

Symmetry of the F2F dc-dc converter was utilized in [9] to develop a simple model of the converter with a single capacitor representing the arm energy dynamics. The derivation of this model starts from the simplified energy-based phasor model given by (3.38) as shown in (3.39). For the sake of simplicity, the two converters are assumed to have the same parameters in this derivation.

$$\begin{aligned}
\frac{\mathrm{d}}{\mathrm{d}t} w_{01}^{\Sigma} &= 2 v_{c01}^{r} i_{c01} - \frac{1}{2} \Re\{\vec{\mathbf{v}}_{ac1}^{r} \vec{\mathbf{i}}_{ac}^{*}\} \\
\frac{\mathrm{d}}{\mathrm{d}t} w_{02}^{\Sigma} &= 2 v_{c02}^{r} i_{c02} + \frac{1}{2} \Re\{\vec{\mathbf{v}}_{ac2}^{r} \vec{\mathbf{i}}_{ac}^{*}\} \\
L_{arm} \frac{\mathrm{d}}{\mathrm{d}t} i_{c01} &= \frac{1}{2} v_{dc1} - v_{c01}^{r} - R_{arm} i_{c01} \\
L_{arm} \frac{\mathrm{d}}{\mathrm{d}t} i_{c02} &= \frac{1}{2} v_{dc2} - v_{c02}^{r} - R_{arm} i_{c02} \\
L_{ac} \frac{\mathrm{d}}{\mathrm{d}t} \vec{\mathbf{i}}_{ac} &= \vec{\mathbf{v}}_{ac1}^{r} - \vec{\mathbf{v}}_{ac2}^{r} - R_{ac} \vec{\mathbf{i}}_{ac} - \mathrm{j}\omega L_{ac} \vec{\mathbf{i}}_{ac}
\end{aligned} \tag{3.39}$$

The extra subscripts 1 and 2 are for the two MMCs in Fig. 3.2. The ac current is defined as going out of the converters in the derivation of the MMC (see Fig. 3.1). Therefore, the current is multiplied by a negative sign for the second converter. Equation (3.38) captures the dynamics associated with energy exchange and power balance with good accuracy. Further simplification by aggregation of the two energy states w_{01}^{Σ} and w_{02}^{Σ} was proposed in [9]. This simplification was enabled by two main assumptions. The first consideration is that the ac current is completely internal to the converters, which means that it can be controlled with close to ideal performance. Dynamics of the ac current can, therefore, be neglected. The second assumption is that the losses in the ac side, primarily those of the isolating transformer, are negligible.

Taking these assumptions into account, the difference and the sum of the first two equations results in (3.40).

$$\begin{aligned}
\frac{\mathrm{d}}{\mathrm{d}t} w_{av} &= \frac{1}{2} \frac{\mathrm{d}}{\mathrm{d}t} \left(w_{01}^{\Sigma} + w_{02}^{\Sigma} \right) = v_{c01}^{r} i_{c01} + v_{c02}^{r} i_{c02} \\
\frac{\mathrm{d}}{\mathrm{d}t} w_{d} &= \frac{1}{2} \frac{\mathrm{d}}{\mathrm{d}t} \left(w_{01}^{\Sigma} - w_{02}^{\Sigma} \right) = v_{c01}^{r} i_{c01} - v_{c02}^{r} i_{c02} - \frac{1}{2} \Re\{\vec{\mathbf{v}}_{ac1}^{r} \vec{\mathbf{i}}_{ac}^{*}\}
\end{aligned} \tag{3.40}$$

w_d represents the dynamics associated with power transfer between the two sides via the ac side. The ac side quantities can be replaced by the per-phase active power reference since the dynamics are neglected. The average w_{av} is the average of the stored energy on the two sides. This average component is less relevant from a systems perspective because it is a result of internal variable interactions.

If it is controlled properly, it can be assumed to be equal to its reference value w_{av}^r. Individual energies w_{01}^Σ and w_{02}^Σ can then be calculated from the combination of w_{av}^r and w_d. The resulting equations describing the simplified F2F model are given in (3.41).

$$\begin{aligned} \frac{\mathrm{d}}{\mathrm{dt}} w_d &= \frac{1}{2}\frac{\mathrm{d}}{\mathrm{dt}}\left(w_{01}^\Sigma - w_{02}^\Sigma\right) = v_{c01}^r i_{c01} - v_{c02}^r i_{c02} - \frac{1}{3}p_{ac}^r \\ L_{arm}\frac{\mathrm{d}}{\mathrm{dt}} i_{c01} &= \frac{1}{2}v_{dc1} - v_{c01}^r - R_{arm} i_{c01} \\ L_{arm}\frac{\mathrm{d}}{\mathrm{dt}} i_{c02} &= \frac{1}{2}v_{dc2} - v_{c02}^r - R_{arm} i_{c02} \\ w_{01}^\Sigma &= w_{av}^r + w_d \quad w_{02}^\Sigma = w_{av}^r - w_d \end{aligned} \tag{3.41}$$

where p_{ac}^r is the ac power reference.

The simplified models of the F2F presented so far in this section (given by (3.39) to (3.41)) were compared and validated in [9]. The models compared in [9] are summarized in Table 3.1. *Model 4*, the last model, is a linearized version of *Model 3*, so the two models have the same level of detail. The linearized model is useful when performing small-signal analyses, as described in Chapter 5. The comparison of the models was made with the same controller parameters in all the cases and compensated modulation is implemented. The F2F dc-dc converter was used

Table 3.1: Summary of energy-based simplified models for the F2F dc-dc converter.

Model Name	Description	Equation number
Model 1	Full detail average model	-
Model 2	Single arm per MMC	(3.39)
Model 3	Single arm per F2F	(3.41)
Model 4	Linearized version of *Model 3*	-

to control power flow between the two dc sides, which is one of the main functions of a dc-dc converter in HVDC grids (see Section 2.3.1). The two MMCs are rated for 100 MVA at 100 kVdc and 50 kVac peak with an arm capacitance of 20 µF [9]. DC power of side 1 is plotted in Fig. 3.3 where a step change in active power was applied to excite the system response. The first two models have a very good match, which means that aggregation of the energy states into one arm energy state per converter does not introduce errors with respect to the full detail model. *Model 3* and *Model 4* have what appears an offset error compared to *Model 1* because the ac side losses are neglected. Other than that, all the models have the same response to the disturbance. The leg energy plot in Fig. 3.4 also shown that the simplified models give a very high level of accuracy. Therefore, the simplified

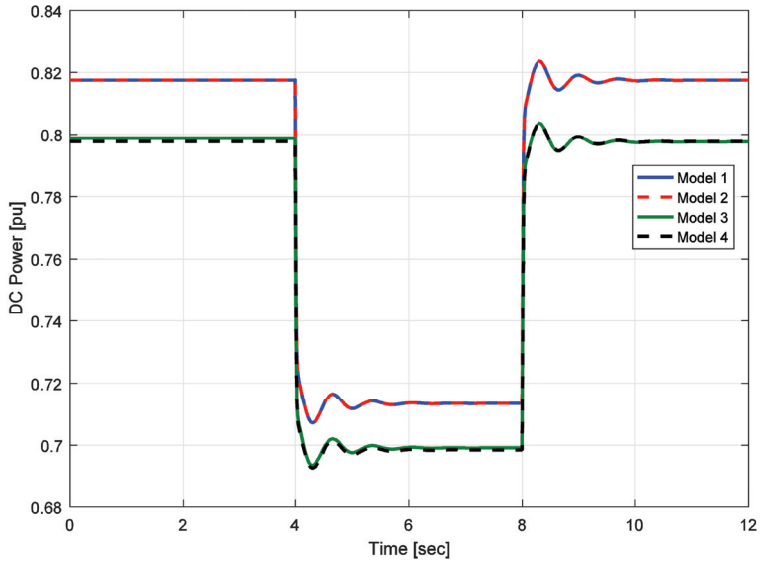

Figure 3.3: Comparison of simplified F2F models [9]: dc power of side 1, *Model numbers* defined in Table 3.1.

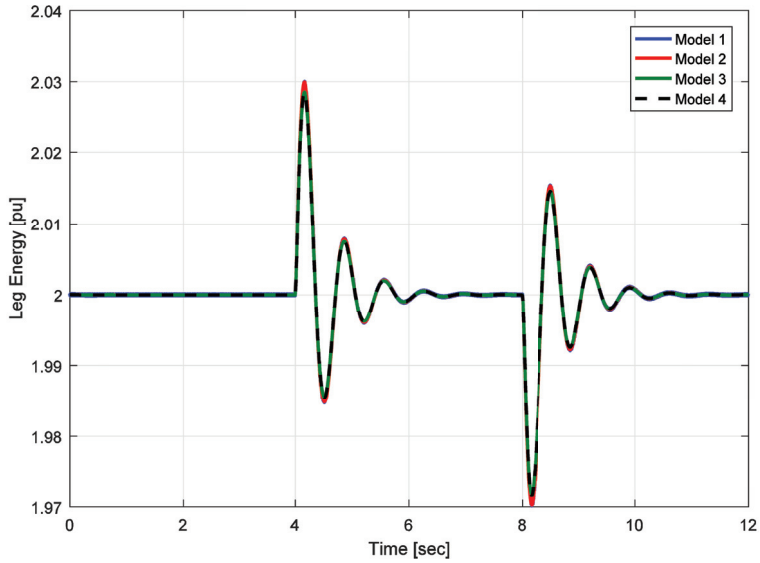

Figure 3.4: Comparison of simplified F2F models [9]: leg energy, *Model numbers* defined in Table 3.1.

model given by (3.41) can be used for system studies where the F2F was controlled using compensated modulation.

3.6.2 Voltage-based simplified model

When using other types of control, such as direct voltage control, there is an uncontrolled interaction between the different harmonic components in the converter, which leads to a poorly damped oscillation at the converter terminals [45]. The previous simplified model of the F2F in (3.41) (from [9]) fails to accurately capture such modes of oscillation. Additionally, the model neglects the effect of circulating current ripple and the associated suppression controllers. It has been shown that the effect of Circulating Current Suppression Controllers (CCSCs) cannot be neglected because they can interact with external systems [46]. Therefore, an improved simplification approach is proposed here [13].

The starting point for this model is the detailed voltage-based model Section 3.3.2. The approach exploits the symmetry of the converter in order to reduce the number of the ripple states instead of neglecting them altogether. The simplification is based on the assumption that the two MMCs have the same parameters in Per-unit. This is reasonable because the converters are normally designed with similar requirements. Additionally, it is assumed that the circulating current ripples flowing in the two sides, in Per-unit, are the same in magnitude but opposite in sign. This implies that $\vec{\mathbf{v}}_1^{\Delta}$, $\vec{\mathbf{v}}_2^{\Sigma}$, and $\vec{\mathbf{i}}_{c2}$ of the two sides can be computed using the values from only one side. Then, the computed values are applied to the two sides after being multiplied by the appropriate sign; this reduces the number of states by 6. Therefore, one of the sides is represented with a high level of accuracy while the second one suffers a slight approximation. The approximation is due to the fact that the local couplings between the ripples and the average dynamic states are neglected. The equations describing the improved model are given in (3.42).

$$
\begin{aligned}
C_{arm}\frac{\mathrm{d}}{\mathrm{d}t}v_{01}^{\Sigma} &= n_{c0}i_{c01} + \frac{1}{2}\Re\{\vec{\mathbf{n}}_{c2}\vec{\mathbf{i}}_{c2}^{*}\} - \frac{1}{4}\Re\{\vec{\mathbf{n}}_{ac1}\vec{\mathbf{i}}_{ac}^{*}\} \\
C_{arm}\frac{\mathrm{d}}{\mathrm{d}t}v_{02}^{\Sigma} &= n_{c02}i_{c02} + \frac{1}{2}\Re\{\vec{\mathbf{n}}_{c2}\vec{\mathbf{i}}_{c2}^{*}\} - \frac{1}{4}\Re\{\vec{\mathbf{n}}_{ac2}\vec{\mathbf{i}}_{ac}^{*}\} \\
L_{arm}\frac{\mathrm{d}}{\mathrm{d}t}i_{c01} &= \frac{1}{2}v_{dc1} - n_{c01}v_{01}^{\Sigma} + \frac{1}{2}\Re\{\vec{\mathbf{n}}_{ac1}\vec{\mathbf{v}}_1^{\Delta *}\} - \frac{1}{2}\Re\{\vec{\mathbf{n}}_{c2}\vec{\mathbf{v}}_2^{\Sigma *}\} - R_{arm}i_{c01} \\
L_{arm}\frac{\mathrm{d}}{\mathrm{d}t}i_{c02} &= \frac{1}{2}v_{dc2} - n_{c02}v_{02}^{\Sigma} + \frac{1}{2}\Re\{\vec{\mathbf{n}}_{ac2}\vec{\mathbf{v}}_1^{\Delta *}\} - \frac{1}{2}\Re\{\vec{\mathbf{n}}_{c2}\vec{\mathbf{v}}_2^{\Sigma *}\} - R_{arm}i_{c02} \\
C_{arm}\frac{\mathrm{d}}{\mathrm{d}t}\vec{\mathbf{v}}_1^{\Delta} &= \frac{1}{2}n_{c01}\vec{\mathbf{i}}_{ac} + \frac{1}{4}\vec{\mathbf{n}}_{c2}\vec{\mathbf{i}}_{ac}^{*} - \vec{\mathbf{n}}_{ac1}i_{c01} - \frac{1}{2}\vec{\mathbf{n}}_{ac}^{*}\vec{\mathbf{i}}_{c2} - \mathrm{j}\omega C_{arm}\vec{\mathbf{v}}_1^{\Delta} \\
L_{ac}\frac{\mathrm{d}}{\mathrm{d}t}\vec{\mathbf{i}}_{ac} &= \vec{\mathbf{n}}_{ac1}v_{01}^{\Sigma} + \frac{1}{2}\vec{\mathbf{n}}_{ac1}^{*}\vec{\mathbf{v}}_2^{\Sigma} - n_{c01}\vec{\mathbf{v}}_1^{\Delta} - \frac{1}{2}\vec{\mathbf{n}}_{c2}\vec{\mathbf{v}}_1^{\Delta *} - \vec{\mathbf{n}}_{ac2}v_{02}^{\Sigma} - R_{ac}\vec{\mathbf{i}}_{ac} - \mathrm{j}\omega L_{ac}\vec{\mathbf{i}}_{ac}
\end{aligned}
\tag{3.42}
$$

$$C_{arm}\frac{\mathrm{d}}{\mathrm{d}t}\vec{\mathbf{v}}_2^{\Sigma} = n_{c01}\vec{\mathbf{i}}_{c2} + \vec{\mathbf{n}}_{c2}i_{c01} - \frac{1}{4}\vec{\mathbf{n}}_{ac1}\vec{\mathbf{i}}_{ac} - 2\mathrm{j}\omega C_{arm}\vec{\mathbf{v}}_2^{\Sigma}$$

$$L_{arm}\frac{\mathrm{d}}{\mathrm{d}t}\vec{\mathbf{i}}_{c2} = -n_{c01}\vec{\mathbf{v}}_2^{\Sigma} - \vec{\mathbf{n}}_{c2}v_{01}^{\Sigma} + \frac{1}{2}\vec{\mathbf{n}}_{ac1}\vec{\mathbf{v}}_1^{\Delta} - R_{arm}\vec{\mathbf{i}}_{c2} - 2\mathrm{j}\omega L_{arm}\vec{\mathbf{i}}_{c2}$$

The last subscripts represent which dc side the variables are associated with. It should be noted that the variables $\vec{\mathbf{v}}_1^{\Delta}$, $\vec{\mathbf{v}}_2^{\Sigma}$, $\vec{\mathbf{i}}_{c2}$, $\vec{\mathbf{n}}_{c2}$, and $\vec{\mathbf{i}}_{ac}$ do not have the last subscript because they are common to both sides

The F2F models presented so far (listed in Table 3.2) were compared in a system controlled using direct modulation with CCSC [13]. The simulation model was for a 1000 MVA converter operating at ±320 kV, 50 Hz. A step change in active power was used to excite the system response. A plot of dc powers on both sides is depicted in Fig. 3.5. As expected, the simple model obtained based on the assumption of compensated modulation produced significant modeling error. The improved model gives an exact match on side *1* while some approximation errors are observed on side *2*. Overall, the improved model captures the general trend in the response.

Table 3.2: Summary of improved voltage-based simplified models for the F2F dc-dc converter.

Model Name	Description	Equation number
Detailed model	Full phasor model 2 MMCs	(3.18) to (3.20)
Simple model	Single arm per F2F (the same as *Model 2*)	(3.39)
Proposed model	Improved voltage-based model	(3.42)

In summary, this section presented the development, validation, and analysis of a simplified model of the MMC-based F2F dc-dc converter for system-level studies. The simplified energy-based model is applicable only when compensated modulation is used, which makes it possible to neglect the ripple dynamics. However, when direct voltage control is used, the ripples in the arm voltage and circulating current play an important role in the dynamics of the converter. This is because of the cross-coupling between harmonic components. The second approach is to utilize symmetry of the converter to reduce the number of states.

The improved model results in a reduction in the number of states by 8. This was achieved by eliminating the ripples and the CCSC from one of the converters. Simulation results comparing the proposed model with the detailed model revealed that the model is able to reproduce the signals from one of the sides with good accuracy, while a slight error is observed from the second side. This implies that the model correctly represents the effect of the controller. Therefore, the proposed model is suitable for representing an F2F, controlled using direct voltage

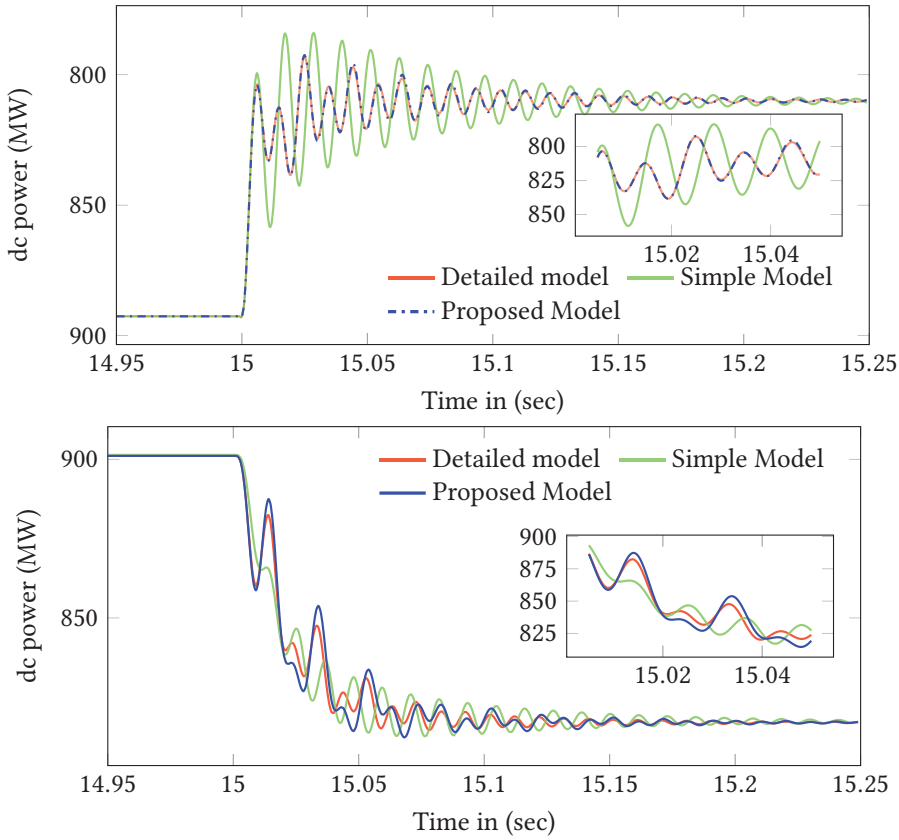

Figure 3.5: Comparison of simplified models: dc power of side *1* (top) and dc power of side *2* (bottom).

control with CCSC, for large-scale system studies where the focus is on controller interaction and stability. The simple energy-based model can still be used when compensated modulation is used because it can provide an even simpler model.

3.7 Per-unit conversion

The equations and parameter values presented so far are in physical units. In power systems, per-unit values are often used because they provide more intuitive interpretation of the results [47]. Per-unit conversion involves normalizing the physical quantities by the base (rated) values. The base values are chosen so that the per-unit values have intuitive interpretation. For example, the voltage base can be chosen to be the rated voltage of the converter, which implies that at one per-unit voltage the converter is operating at rated value. Moreover, per-unit representation removes the ratings from the equations and parameters. This enables a comparison of parameters and signals of converters with different ratings.

This section presents the per-unit system chosen in this thesis, followed by the conversion of the simplified MMC model into per-unit.

3.7.1 Choice of base values

In the process of per unit conversion, the base values for some of the quantities can be chosen freely, while the others follow from the equations relating the quantities [47]. Usually the base values for apparent power and voltage can be chosen freely. The current and impedance base values are computed from these freely chosen bases. For the case of the MMC, the base value for the arm energy is an additional base value that can be freely chosen.

The apparent power base value, S_b, is often chosen to be the rated power of the converter.

$$S_b = S_{rated} \tag{3.43}$$

The quantities are grouped into ac and dc because different base values are used for the ac and dc sides. The apparent power is common to both sides. For the MMC, the ac quantities include the ac voltages, the ac currents, and the ac side equivalent impedance. The dc side includes, the dc voltage, the dc current, the arm voltages, and the arm currents. In principle, the arm voltages and currents can be grouped with either side, but they are grouped with the dc side because their maximum values are closely related to the dc voltage.

The voltage bases are selected such that the dc base value of twice the ac peak voltage. This ensures that the voltages on both sides are close to one per-unit under nominal conditions.

$$V_b^{dc} = 2V_b^{ac} \tag{3.44}$$

Since the apparent power is common to both sides, the current base values are calculated as follows:

$$I_b^{ac} = \frac{2}{3}\frac{S_b}{V_b^{ac}} \quad \text{and} \quad I_b^{dc} = \frac{S_b}{V_b^{dc}} = \frac{3}{4}I_b^{ac} \tag{3.45}$$

The base values for impedance or resistance are derived by taking the ratio of the voltage and current base values.

$$Z_b^{ac} = \frac{V_b^{ac}}{I_b^{ac}} \quad \text{and} \quad Z_b^{dc} = \frac{V_b^{dc}}{I_b^{dc}} \tag{3.46}$$

The impedance base values are also used to normalize inductance and capacitance

values.

$$\begin{aligned} L_b^{ac} &= Z_b^{ac} \qquad C_b^{ac} = \frac{1}{Z_b^{ac}} \\ L_b^{dc} &= Z_b^{dc} \qquad C_b^{dc} = \frac{1}{Z_b^{dc}} \end{aligned} \tag{3.47}$$

This choice of base values for inductance and capacitance has two benefits:

1. The resulting dynamic equations in per-unit are the same in structure, i.e. no scaling factors. Other per-unit systems adopted in the literature [33], [47] use base values that give the same value for reactance and inductance. However, this introduces the fundamental frequency ω into the dynamic equations as a scaling factor. This can be counterintuitive, especially on the dc side.

2. The per-unit inductances and capacitance values are time constants which can provide physical insight into the system. For example, the per-unit capacitance is the amount of time it takes the capacitor to charge from zero to the base voltage (or discharge from base voltage to zero) given that one per-unit current is applied to it. This can be shown by considering the equation governing dynamics of a capacitor.

$$C\frac{\mathrm{d}}{\mathrm{d}t}v = i \implies C\mathrm{d}v = i\mathrm{d}t \tag{3.48}$$

where v and i are the voltage across and the current through the capacitor. Integrating the voltage from zero to the base voltage V_b, and the time from zero to the charging time τ gives the following relation.

$$\begin{aligned} C\int_0^{V_b} \mathrm{d}v &= I_b \int_0^{\tau} \mathrm{d}t \\ \tau &= C\frac{V_b}{I_b} = c_p \end{aligned} \tag{3.49}$$

where I_b is the base current and c_p is the per-unit capacitance value. Equation (3.49) shows that the per-unit capacitance is equal to the charging time of the capacitor from zero to the base voltage given that the base current is applied to it. A second interpretation of the per-unit capacitance is in terms of energy stored in the element. The capacitance value is twice the time it takes for its energy to dissipate given that it started from rated voltage and it is continuously supplying the rated power. This is also known as the energy-to-power ratio often presented as kJ/MVA for large systems.

Since the MMC is composed of six arms, the arm capacitance in per-unit is a third of the dissipation time. The relation between the dissipation time and the per-unit capacitance can be derived by multiplying both sides of (3.49) by the capacitor voltage and applying the rated power S_b instead of I_b. The same interpretations can also be applied to inductors.

Finally, the base value to the energy stored in the arm capacitors is selected so that a one per-unit voltage on the capacitors leads to a one per-unit energy [33].

$$W_b = \frac{1}{2} C_{arm} \left(V_b^{dc} \right)^2 \tag{3.50}$$

3.7.2 Calculation of per-unit parameters for MMC

By using the base values from the previous section, the main per-unit parameters of the MMC are calculated in this section. The first parameters are the ac side inductance and resistance, which are given in (3.51).

$$l_{ac} = \frac{1}{Z_b^{ac}} \left(L_t + \frac{1}{2} L_{arm} \right) \quad and \quad r_{ac} = \frac{1}{Z_b^{ac}} \left(R_t + \frac{1}{2} R_{arm} \right) \tag{3.51}$$

where L_t and R_t are the equivalent ac side gird inductance and resistance. The dc side per-unit inductance and resistance can be calculated in a similar way.

$$l_{dc} = \frac{L_{arm}}{Z_b^{dc}} \quad and \quad r_{dc} = \frac{R_{arm}}{Z_b^{dc}} \tag{3.52}$$

Since the arm quantities are grouped with the dc side, the arm capacitance is normalized to c_a as shown in (3.53).

$$c_a = C_{arm} Z_b^{dc} \tag{3.53}$$

The structure of the voltage and current dynamic equations is the same after conversion to per-unit with two exceptions. The first difference is that the inductance, resistance, and capacitance parameters are replaced by the corresponding values from (3.51) to (3.53). The second one is related to the convention of grouping quantities to the ac and dc sides. The ac voltage and current states should, therefore, be scaled by the base conversion ratios 4/3 and 2, respectively, every time they appear in connection with a dc dynamic equations. These conversion ratios have been defined in (3.44) and (3.45).

There is also a scaling factor introduced in equations representing energy dynamics with the selected base values. This is illustrated as follows. Recalling the upper

arm energy equation (3.28), the scaling factor is determined to be $c_a/2$ as shown in (3.54). This scaling factor is applied to all the arm energy states in per-unit.

$$\begin{aligned} \frac{\mathrm{d}}{\mathrm{dt}} w_u &= v_u i_u \\ \frac{\mathrm{d}}{\mathrm{dt}} \left(w_u^p W_b\right) &= \left(v_u^p V_b^{dc}\right)\left(i_u^p I_b^{dc}\right) \\ \frac{1}{2} C_{arm} \left(V_b^{dc}\right)^2 \frac{1}{V_b^{dc} I_b^{dc}} \frac{\mathrm{d}}{\mathrm{dt}} w_u^p &= v_u^p i_u^p \\ \frac{1}{2} c_a \frac{\mathrm{d}}{\mathrm{dt}} w_u^p &= v_u^p i_u^p \end{aligned} \tag{3.54}$$

where $(\cdot)^p$ is used to highlight the per-unit values. This notation is not adopted in the rest of the thesis because it complicates the equations. As an example case, the simplified energy-based model in (3.38) is converted into per-unit, as shown in (3.55). The rest of the models can be converted by following a similar approach.

$$\begin{aligned} \frac{c_a}{2} \frac{\mathrm{d}}{\mathrm{dt}} w_0^{\Sigma} &= 2 v_{c0}^r i_{c0} - \frac{1}{3} \Re\{\vec{\mathbf{v}}_{ac}^r \vec{\mathbf{i}}_{ac}^*\} \\ l_{dc} \frac{\mathrm{d}}{\mathrm{dt}} i_{c0} &= \frac{1}{2} v_{dc} - v_{c0}^r - r_{dc} i_{c0} \\ l_{ac} \frac{\mathrm{d}}{\mathrm{dt}} \vec{\mathbf{i}}_{ac} &= \vec{\mathbf{v}}_{ac}^r - \vec{\mathbf{v}}_g - r_{ac} \vec{\mathbf{i}}_{ac} - \mathrm{j}\omega l_{ac} \vec{\mathbf{i}}_{ac} \end{aligned} \tag{3.55}$$

3.8 Modeling of HVDC cables

This section presents a brief review of the models of power cables used in HVDC transmission systems. Cables are usually represented using simplified, lumped series impedance or π equivalent circuits, and these models are generally acceptable for a wide variety of studies. However, like any of the other HVDC components, the cables have to be represented differently for different study types. Five types of use cases for cable models were presented in [44]: steady-state simulation, transient stability simulation, EMT simulation, harmonic performance, and relay protection and control. The π model with parameters calculated at nominal frequency (50/60 Hz) is sufficient for the first two study types [44]. The last three studies require the models to capture frequency dependence of the cable parameters.

Cable parameters vary depending on frequency for two main reasons: skin effect and earth return path behavior [48]. These factors affect the series inductance and resistance of the cable, while the shunt capacitance is assumed to be independent of frequency. Travelling wave models are needed when the wavelength of the

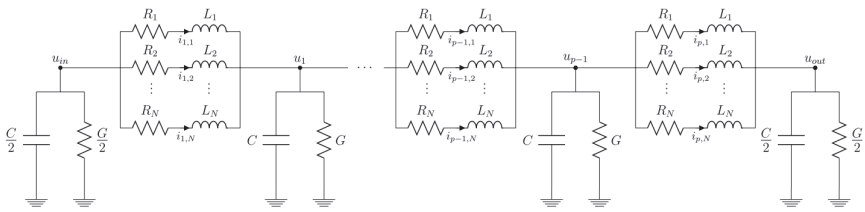

Figure 3.6: Frequency Dependent-π (FD-π) cable model [52].

voltage and current waves travelling along the cable is close to the length of the cable. This can happen either when the cable is of sufficient length, or when the frequency of interest is sufficiently high. For example, the wavelength at 50 Hz for a cable with propagation speed of 180 km/ms is 3600 km; for the same cable, the wavelength is 180 km at 1 kHz. Therefore, travelling wave models are necessary in EMT with frequency of interest in the range of kilohertz involving HVDC cables which are hundreds of kilometers long. It should be noted that a travelling wave model is not needed for harmonics studies; it is sufficient to use a π equivalent circuit with the series impedance and shunt admittance calculated for each harmonic frequency.

An advanced cable model called the *universal line model* was proposed in [49]. The approach uses *vector fitting* to capture frequency dependent parameters of power cables using a rational approximation [50]. While the *universal line model* is very accurate and widely accepted, it is computationally intensive, and also difficult to represent in small-signal (linear) studies. An approximate, state-space cable model valid over a specified frequency range was proposed to address these limitations [51]. The model is called Frequency Dependent-π (FD-π). As the name suggests, the model is composed of multiple π sections that are frequency dependent. The series impedance is vector fitted to obtain a rational approximation resulting in an equivalent circuit with several R-L branches connected in parallel, as shown in Fig. 3.6. The FD-π model gives very good accuracy if the number of sections and branches are appropriately chosen. Ref. [52] discusses several considerations that are involved in the selection of an *optimal* number of sections and branches. The main assumption in the FD-π model is that the cable sections are short enough to render lumped parameter representation feasible. Therefore, as the cable gets longer, the number of sections has to be increased to maintain accuracy. The number of branches is decided by the fitting of the series impedance of the cable over the frequency range of interest. Taking this fact into account and following the guideline from [52], an optimal model order can be selected.

This modeling approach was adopted in this thesis for most of the time domain

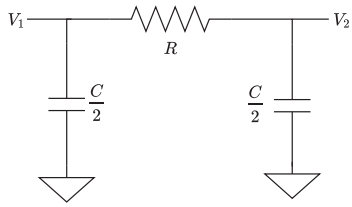

Figure 3.7: RC-π cable model.

simulations with the exception of phasor-based simulation, which focuses on electromechanical interactions in an ac/dc system. Since electromechanical studies focus on very low frequencies (0.2 Hz to 2 Hz [47]), the cable model does not need to capture the high-frequency behavior. Thus, a single π model is used in such cases. The selected π model does not include the series inductance of the cable, see Fig. 3.7. The choice to remove the inductance was based on the finding from [53], which stated that simplified π models including the series inductance can lead to incorrect conclusions about stability. If the inductance is removed, correct stability conclusions can be made. In summary, the FD-π model is used for time domain simulations in this thesis where fast dynamics interaction in the order of tens to hundreds of hertz is expected. The simple RC-π equivalent is used for slow dynamics investigations like electromechanical stability studies.

3.9 Summary

Models of varying levels of detail are needed for different power system studies. This chapter dealt with the review and development of models of the main components of an HVDC grid covered in this thesis. These components are the ac-dc MMC, the MMC based F2F dc-dc converter, and power cables.

Voltage and energy-based formulations of the average arm model of the MMC were presented. Phasor modeling approach was adopted to obtain SSTI models, which are models with constant states in steady state, making them suitable for small-signal analysis. The energy-based model can be simplified by removing the circulating current ripple if compensated modulation is used. This is possible because the circulating current is eliminated when compensated modulation is implemented.

The MMC models were then extended to model the F2F dc-dc converter. Further simplifications were proposed because of the symmetry of the converter. Simulation results validating the proposed simplifications were presented, which showed that these models can accurately represent the F2F converter in system-level studies.

Lastly, the modeling of HVDC cables was reviewed. Two model types were adopted in this thesis: the frequency dependent FD-π model and the simplified RC-π model. The FD-π is more detailed, and hence it is used for most of the time domain simulations in this thesis. The RC-π is used in Chapter 8, where the focus is on slow (electromechanical) dynamics.

4
Converter Control for Grid Applications

One of the most important components of an MMC HVDC converter is the control system. This chapter presents a review of the control layers needed for proper operation of such converters. The main goal of the chapter is to provide the necessary background information for the detailed discussion in later chapters. The discussion in this chapter is supported by the following contributions by the author.

> A. A. Taffese, E. Tedeschi, and E. C. W. de Jong, "Modelling of DC-DC converters based on front-to-front connected MMC for small signal studies," in *2016 IEEE 17th Workshop on Control and Modeling for Power Electronics (COMPEL)*, Jun. 2016, pp. 1–7
>
> A. A. Taffese, E. Tedeschi, and E. de Jong, "Arm voltage estimation method for compensated modulation of modular multilevel converters," in *2017 IEEE Manchester PowerTech*, Jun. 2017, pp. 1–6

Chapter Outline

4.1 Introduction

Proper control is essential for HVDC converters to be integrated into a power system. There are several requirements on the controllers originating from different stakeholders. The most basic control objective is for the converters to operate stably both in steady state and transient conditions over the expected range of operating points. This is essential because unstable converters cannot fulfill their other objectives. Another high-level objective common to all HVDC converters is that they should be able to reach and maintain desired setpoints; reaching setpoints is called a tracking (servo) objective, while maintaining the achieved setpoint is a regulation objective [54]. These objectives are very important to the system operator because variables such as active power, reactive power, and voltage need to be set to a desired value as per trading agreements, grid codes, and economic operation of the system. Article 13 of the EU commission regulation 2016/1447 [55] stipulates the requirements for such control functions.

In addition to the basic control functions introduced so far, grid codes also have requirements for other features or services. These include frequency support (regulation), voltage support, power quality improvement, and stability enhancement (oscillation damping). There are also low-level control requirements that do not directly affect the operator but are essential to the converter. These control requirements are tied to a specific converter topology unlike the high-level controllers, which are more general. For the case of MMC, a third level, called mid level, which represents the arm energy and circulating current, is introduced. The controllers in this level have strong coupling to the high-level controller, but they do not control terminal quantities like power and terminal voltage. A pictorial depiction of the different control layers for an MMC HVDC converter is shown in Fig. 4.1, which is an extended version of the control hierarchy diagram given in [44]. Each of the layers will be briefly discussed here.

Dispatch refers to the converter's interface that allows communication dispatch. Dispatch is the operator's interface which allows setting of the operating point of the converter in terms of ac and dc voltages and powers [44].

High-level controllers are located at the top of the control hierarchy because they are the least dependent on the topology. These controllers define the terminal characteristics of the converter. In other words, they are the ones that interact with the surrounding power system the most. Common controllers in this group include active and reactive power controllers, which can also be used to control dc and ac voltages, respectively.

Mid-level controllers are a group of controllers specific to the MMC topology. Al-

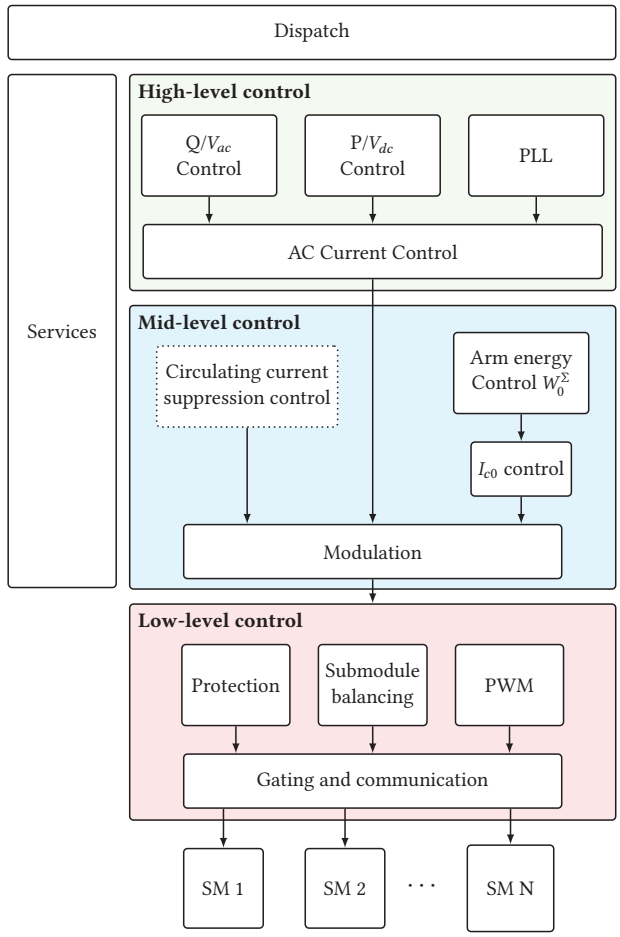

Figure 4.1: Layers of MMC control for HVDC applications.

though they are topology dependent, they also moderately interact with the system. They also define how the converter behaves as seen from high-level controllers. The arm energy and circulating current controllers fall into this group. The last element in this group is modulation. As described in the previous chapter, the term modulation is used to refer to how the arm voltage is varied (modulated) to give the desired inserted voltage. Detailed comparison of different control methods and a discussion on the design of the selected control topology will be presented later in this chapter.

Low-level controllers are the most topology-specific group of controllers. They include balancing submodules of the MMC, and generation of switching pattern. This thesis does not cover low-level controllers because they are outside the scope of this work. Their effect is neglected because it is assumed that they are well-

designed to close to ideal performance.

Service-level controllers are controllers that enable the provision of ancillary services from the converter. They interact with high- and mid-level controllers to achieve this. The main distinction between the service-level controllers and the others is due to the functions that are implemented in the service-level. While the other levels are strictly needed to provide the main functions of the converter, the service-level controllers are only there to provide additional functions which can be disabled without a major influence on normal operation. There can also be services that can be provided from low-level controllers, such as fault blocking, but they are not considered in this work.

4.2 Generic VSC HVDC high-level control

High-level control of a VSC HVDC includes controllers for ac current control, active power, reactive power, dc voltage, and ac voltage depending on the control mode. Such controllers are implemented in a cascaded approach with an inner current loop and outer power or voltage loops depending on the control mode. For a three-phase system, one of the most common control implementations in the literature is based on the synchronously rotating dq reference frame [44]. This implementation is adopted in this thesis. An essential component in such implementations is a PLL, which is responsible for obtaining the grid voltage angle at the Point of Common Coupling (PCC). The PCC is often located upstream of the converter transformer. The main components of the high-level controllers are discussed in the following sections starting with the PLL.

4.2.1 Phase locked loop

As mentioned, the main role of the PLL is to obtain the phase angle of the voltage at the PCC. The PLL angle can then be used to establish dq reference frame of the converter. This process can be explained by referring to Fig. 4.2. The dq reference frame for the system is shown in black, while the converter's internal reference is shown in blue. The figure also shows the PCC voltage in red together with its projections on the reference frames. Based on the notation in the figure, the objective of the PLL is to produce the angle θ_{PLL} which tracks the angle of the voltage at the PCC (θ_{PCC}), and thus forcing $\Delta\theta_{PCC}$ and v_q to zero. This can be achieved by using a closed-loop controller which uses v_q as feedback [21].

The implementation adopted in this thesis is shown in Fig. 4.3. The filter is used to prevent the PLL from tracking high-frequency noise and disturbances. The integrator is reset every time the angle exceeds $\pm 2\pi$. This is done to avoid numerical overflows due to continuous integration over an extended period of time. The PI controller can be tuned using symmetric optimum method [56]. Since the

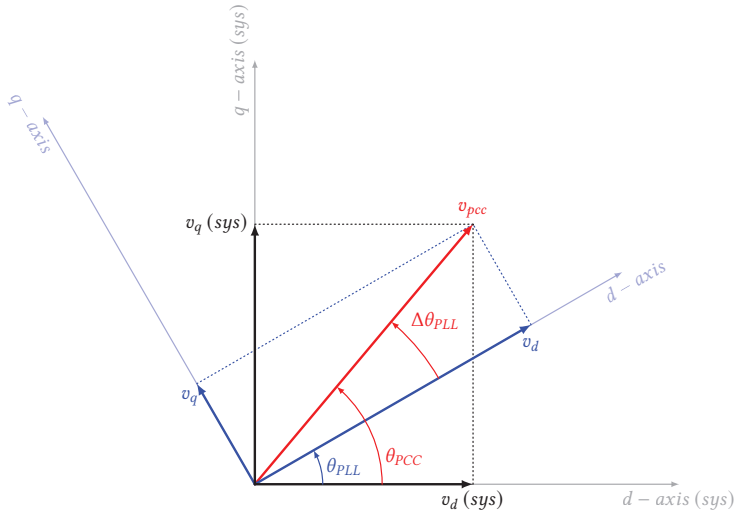

Figure 4.2: *dq*-axis transformation using a PLL.

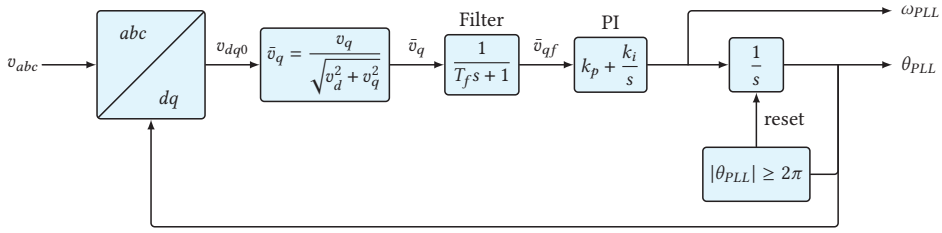

Figure 4.3: A block diagram of a PLL implementation in *dq* frame.

equivalent transfer function of the PLL is highly nonlinear, limits (saturations) should be applied to the output of the PI controller to avoid instability during large disturbance. The simulation should be started with an initial frequency in the vicinity of the steady-state frequency. Additionally, time delay compensation can be applied to θ_{PLL} to account for filtering and communication delays in the measurement circuit.

4.2.2 Current control

Outer control loops can accomplish the main control objective of the converter without current controllers. However, such implementations suffer from one major limitation: there is no direct way to enforce current limits. This is important because the semiconductor components (IGBTs) can be damaged due to overcurrent. In addition to current limiting, the use of inner current loop leads to performance improvement because the converter can be safely pushed to its limits to achieve a desired performance. A derivation of a *dq* frame current dynamic model and controller is presented in this section. Dynamic equation of the ac

current has already been presented in (3.55), but the final equation is repeated here in (4.1) for quick reference.

$$l_{ac}\frac{\mathrm{d}}{\mathrm{dt}}\vec{\mathbf{i}}_{ac} = \vec{\mathbf{v}}^{r}_{ac} - \vec{\mathbf{v}}_{g} - r_{ac}\vec{\mathbf{i}}_{ac} - \mathrm{j}\omega l_{ac}\vec{\mathbf{i}}_{ac} \tag{4.1}$$

where $\vec{\mathbf{v}}^{r}_{ac}$ is the ac voltage output of the converter, $\vec{\mathbf{i}}^{r}_{ac}$ is the ac current, $\vec{\mathbf{v}}^{r}_{g}$ is the grid voltage, l_{ac} is the per-unit inductance, and r_{ac} is the per-unit resistance. These phasor equations can be implemented in dq frame, where the real and imaginary parts are on the d and q axes, respectively as shown in (4.2).

$$\begin{aligned} & l_{ac}\frac{\mathrm{d}}{\mathrm{dt}}\mathbf{i}_{ac} = \mathbf{v}^{r}_{ac} - \mathbf{v}_{g} - r_{ac}\mathbf{i}_{ac} - \omega l_{ac}\mathbf{J}\mathbf{i}_{ac} \\ \text{where} \quad & \mathbf{i}_{ac} = \begin{bmatrix} i_d = \Re\{\vec{\mathbf{i}}_{ac}\} \\ i_q = \Im\{\vec{\mathbf{i}}_{ac}\} \end{bmatrix} \quad \mathbf{v}^{r}_{ac} = \begin{bmatrix} v^{r}_{d} = \Re\{\vec{\mathbf{v}}^{r}_{ac}\} \\ v^{r}_{q} = \Im\{\vec{\mathbf{v}}^{r}_{ac}\} \end{bmatrix} \\ & \mathbf{v}_{g} = \begin{bmatrix} v_{gd} = \Re\{\vec{\mathbf{v}}_{g}\} \\ v_{gq} = \Im\{\vec{\mathbf{v}}_{g}\} \end{bmatrix} \quad \mathbf{J} = \begin{bmatrix} 0 & -1 \\ 1 & 0 \end{bmatrix} \end{aligned} \tag{4.2}$$

The current $\mathbf{i}_{ac}$ can be controlled by using the $\mathbf{v}^{r}_{ac}$ as the actuator signal. The last term in (4.2) leads to coupling between the d and q axes, resulting in complications in the tuning process and reduced performance. Fortunately, the two axes can be decoupled by a simple change of variable, as shown in (4.3). The resulting transfer function is a simple first-order system.

$$\begin{aligned} & l_{ac}\frac{\mathrm{d}}{\mathrm{dt}}\mathbf{i}_{ac} = \bar{\mathbf{v}}^{r}_{ac} - r_{ac}\mathbf{i}_{ac} \\ & \text{where} \quad \mathbf{v}^{r}_{ac} = \bar{\mathbf{v}}^{r}_{ac} + \mathbf{v}_{g} + \omega l_{ac}\mathbf{J}\mathbf{i}_{ac} \end{aligned} \tag{4.3}$$

$\bar{\mathbf{v}}^{r}_{ac}$ is the output of the current controller which is modified according to (4.3) to obtain the voltage reference $\mathbf{v}^{r}_{ac}$ that is applied to the converter. Since both the measured current $\mathbf{i}_{ac}$ and the modified voltage reference $\bar{\mathbf{v}}^{r}_{ac}$ are available, the controller can perform the decoupling.

A current control scheme implementing the aforementioned decoupled current control is shown in Fig. 4.4. The block diagram also shows an equivalent model of the converter ac current dynamics given by (4.2) including time delay and filters. The time delay ($\mathrm{e}^{-s\tau_d}$ in Fig. 4.4) represents the total delay introduced by discretization of the voltage reference and delays due to communication latency. The filters remove sensor noise and high-frequency disturbances. The voltage references coming out of the controllers have to be limited in order to avoid overmodulation, which increases the harmonic distortion at the converter output. The limit enforces the voltage reference to be inside a circle whose radius is the magnitude of the maximum allowable reference voltage. The maximum voltage is

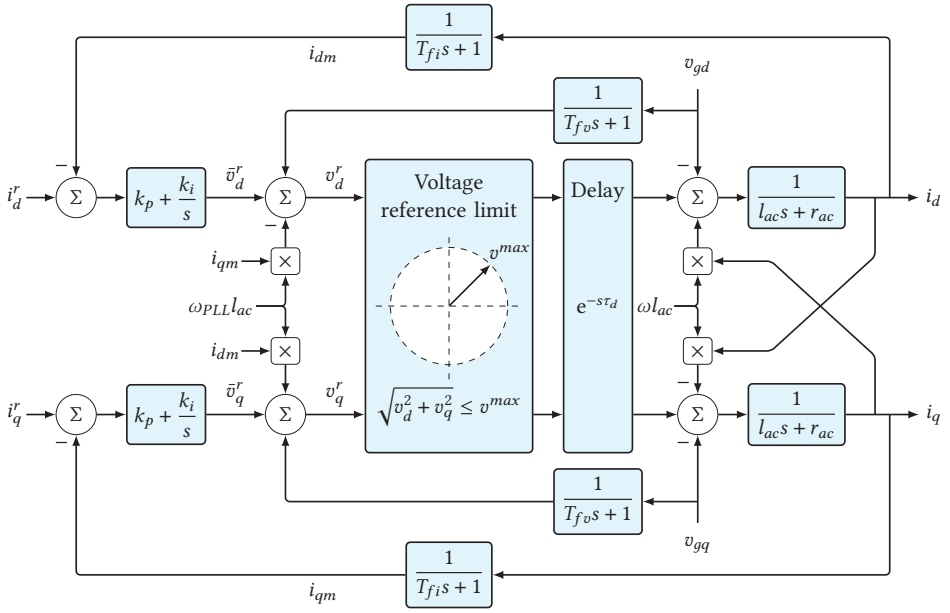

Figure 4.4: A block diagram of current control in dq frame with equivalent dynamics.

adjusted depending on the dc voltage for a two-level VSC, or the arm voltage for case of the MMC. It should be noted that the high-level controller presented here can be applied to any three-phase VSC irrespective of the number of levels. The resulting voltage references are then applied to the modulator after a dq to abc transformation with θ_{PLL}. The current controller was tuned using the modulus optimum technique [56], [57].

4.2.3 Outer control

Outer controllers are responsible for controlling terminal quantities such as active and reactive powers, and ac and dc voltages. Power at the PCC is given by (4.4).

$$\begin{aligned} p_{ac} &= v_{gd} i_d + v_{gq} i_g \\ q_{ac} &= v_{gq} i_d - v_{gd} i_g \end{aligned} \tag{4.4}$$

where p_{ac} and q_{ac} are the active and reactive powers, respectively, in per-unit. If the PLL is working properly, then $v_{gq} = 0$ which means that p_{ac} can be controlled using i_d and q_{ac} using i_q. In this thesis, power control is implemented using PI controllers, as shown in Fig. 4.5. The current references generated by the two PI controllers pass through current limiter block before being sent to the current controller. This prevents the outer controller from requesting current magnitudes that are above the converter's capability. The limit is applied by defining a circle of maximum current magnitude similar to the voltage reference limiter presented

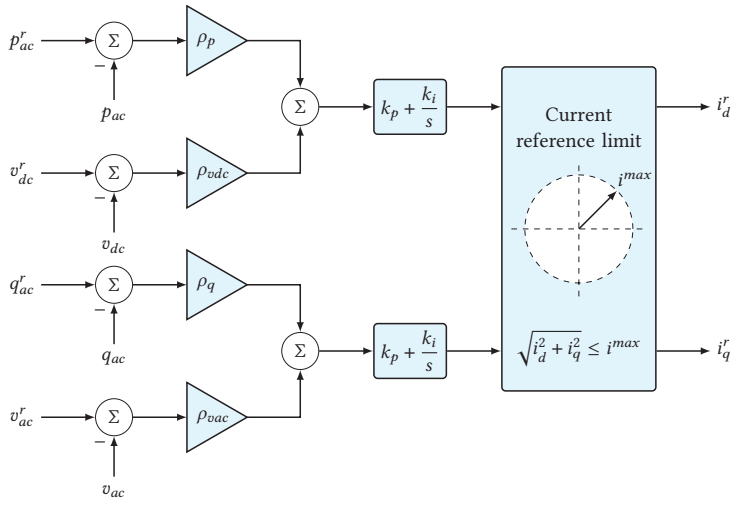

Figure 4.5: A block diagram of outer power and voltage control in dq frame.

in the previous section. Different strategies for prioritizing either the i_d^r or i_q^r can be implemented. In this thesis, the limit is implemented using a symmetric limiting strategy where both the d and q axis references are equally scaled, thus preserving the current angle [44]. The figure depicts several control modes depending on whether power control, voltage control or a combination is applied. The different control modes are realized by adapting the values of ρ_x where the subscript x represents the variable to be controlled. The dc voltage is closely coupled to active power balance in the converters, and thus it can be controlled using i_d as control input. Similarly, the ac side voltage can be controlled using reactive power (i_q). The different control modes are summarized in Table 4.1 along with the corresponding ρ_x values. In this thesis, P-V_{dc} droop mode and P-mode were

Table 4.1: Outer loop control modes.

Active power modes			Reactive power modes		
Mode	ρ_p	ρ_{vdc}	Mode	ρ_q	ρ_{vac}
P-mode	1	0	Q-mode	1	0
V_{dc}-mode	0	1	V_{ac}-mode	0	1
P-V_{dc} droop mode	1	*droop*	Q-V_{ac} droop mode	1	*droop*

used for the d-axis and Q-mode for the q-axis. A generic VSC-HVDC control is implemented using a cascaded control approach with an inner current control and outer power and voltage controls. A PLL is used to lock onto the rotating reference frame at the PCC. The control block and schemes presented in this sec-

tion will be used throughout this thesis with different mid-level controllers. The next section introduces the mid-level controllers needed for an MMC.

4.3 MMC control

Since the MMC, unlike the two-level VSCs, is composed of tens to hundreds of submodules, additional control layers are needed below the high-level controllers in order to regulate the energy exchange to and from the submodules; these controllers are called *mid-level* controllers in Fig. 4.1. Mid-level controllers include modulation, circulating current control, and arm energy control. This section presents a review of these controllers starting with modulation techniques. As mentioned earlier, low-level controllers, like submodule level balancing, are not included in this thesis, and it is assumed that they are properly implemented.

4.3.1 Modulation technique

Modulation technique in this context is used to refer to the method chosen for calculating the insertion indexes to achieve a desired voltage level on the inserted voltage. As explained in Chapter 2, the insertion indexes have values between 0 and 1, which equate to the ratio of the number of inserted submodules to the total number of submodules in the arm. Taking the upper arm as an example, if the desired inserted voltage reference is v_u^r, the insertion index n_u is calculated, as shown in (4.5).

$$n_u = \begin{cases} \dfrac{v_u^r}{\hat{v}_{cu}} & \text{for } 0 \leq v_u^r \leq \hat{v}_{cu} \\ 0 & \text{for } v_u^r < 0 \\ 1 & \text{for } v_u^r > \hat{v}_{cu} \end{cases} \tag{4.5}$$

where $\hat{v}_{cu}$ is the voltage used to normalize the arm voltage reference so that n_u is between 0 and 1. If the value of the reference v_u^r is negative or if it exceeds $\hat{v}_{cu}$, the output is saturated to 0 or 1, respectively. There are two different modulation techniques depending on the choice of $\hat{v}_{cu}$, which leads to two very different dynamics. These are direct modulation and compensated modulation, which are discussed in the following.

4.3.1.1 Direct modulation

Direct modulation is a special case of (4.5) where $\hat{v}_{cu} = V_{dc}$, where V_{dc} is the rated dc voltage. The measured dc voltage can also be used as a divider, leading to a slightly different dynamic. The resulting inserted voltage of the upper arm v_u can be calculated as shown in (4.6).

$$v_u = n_u v_{cu} = v_u^r \frac{v_{cu}}{V_{dc}} \tag{4.6}$$

The main advantage of direct modulation is its simplicity, because it is implemented by a single division (multiplication) operation per arm. However, this approach introduces a large circulating current ripple in the common mode current. The origin of the ripple can be analyzed by considering the fact that the arm voltage has ripples at the first and second harmonics with respect to the ac side, as shown in Fig. 4.6. The first harmonic is a differential component between the upper and lower arms, while the second harmonic is a common mode [58].

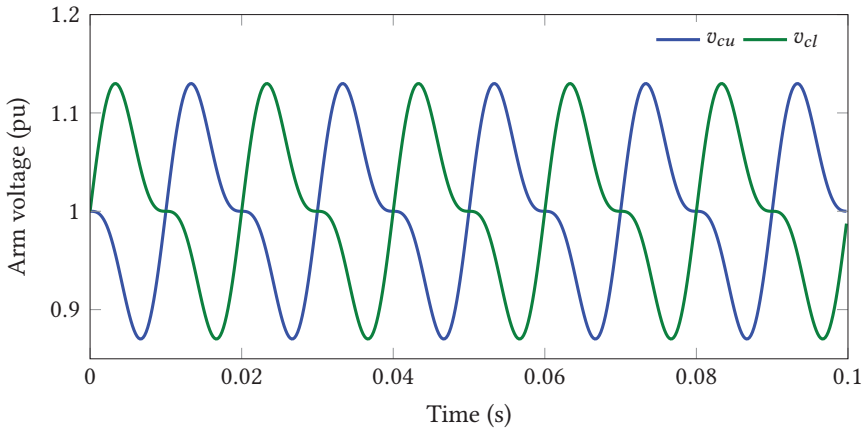

Figure 4.6: Example waveforms of the upper and lower arm voltages.

As per (4.6), the ripple components in Fig. 4.6 are multiplied to the inserted voltage reference v_u^r, which is composed of a fundamental frequency ac component and a dc component. Since V_{dc} is constant, it has no impact on the harmonic content of the inserted voltage. Consequently, v_u and v_l will have harmonics that were not

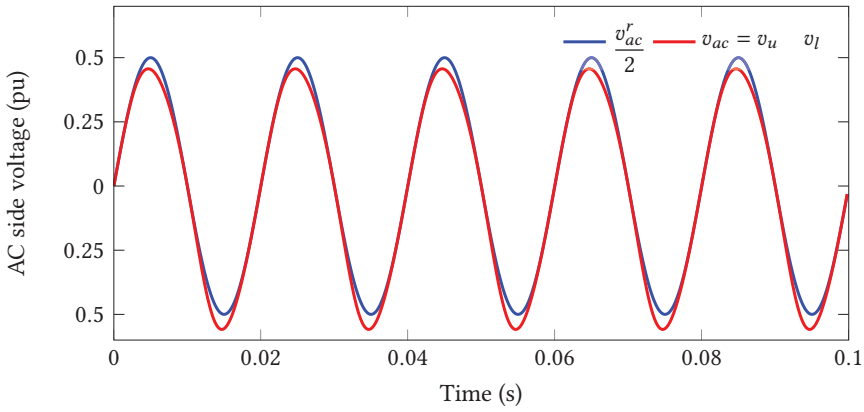

Figure 4.7: Comparison of the inserted voltage with its reference when using direct modulation.

present in v_u^r and v_l^r. This is demonstrated in Fig. 4.7, which shows a comparison of the inserted differential voltage (ac voltage) with the ac voltage reference, v_{ac}^r. There is a distortion in the ac voltage generated by the arm. The distortion has a dominant component at fundamental frequency and a lower magnitude second harmonic. The first harmonic distortion can be compensated by the ac current controller. The second harmonic is not compensated by the current controller, but its magnitude is low enough to be neglected. So, the effect of the ripples on the ac output voltage can be compensated without an additional controller. On the other hand, a second harmonic component in the common mode inserted voltage (see Fig. 4.8) creates a second harmonic circulating current. This circulating current component is suppressed by using controllers called Circulating Current Suppression Controllers (CCSCs) [59] to avoid unnecessary losses. The green trace in Fig. 4.8 shows the effect of such suppression controls, which effectively remove the second harmonic component. There is also a dc offset from 1 pu to 0.95 pu, but this can easily be handled by adjusting the dc component of the arm voltage reference. Although the examples shown in Figs. 4.6 to 4.8 are simplified, they show the most important features of direct modulation. In practice, there might be additional harmonic components that arise from the interaction between the harmonics in the voltages and the currents; the example case considered only the harmonics in the voltages.

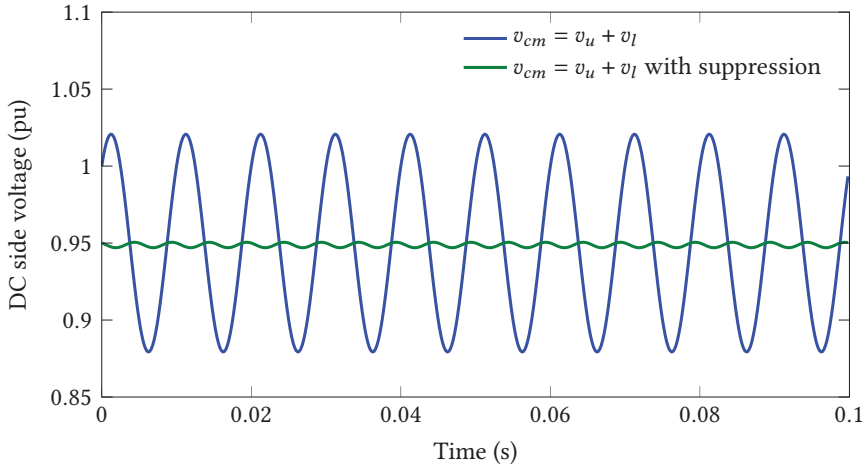

Figure 4.8: Harmonics in the arm voltage when using direct modulation with and without suppression.

CCSCs can be implemented either in Proportional Resonant (PR) form in *abc* domain [21], [60] or Proportional Integral (PI) form in *dq* domain [44], [61]. Both implementations can give a similar performance, but the advantage of the PR

approach is that it can handle imbalance among the phases because it is implemented per-phase. The proportional term in the PR controller influences both the dc component and the second harmonic ripple. It, in effect, adds a virtual resistance which increases the damping in the response of the controller. An additional controller is needed to achieve this in the case of PI implementation. However, this can be an advantage if there are different control objectives for the dc and second harmonic components.

4.3.1.2 Compensated modulation

Compensated modulation refers to methods of calculating the insertion indexes where the effect of the ripple in the arm voltages is pre-compensated. This avoids the ripples in the circulating current that arise when using direct modulation [33], [58]. Compensated modulation achieves this by dividing the reference voltages by the respective arm voltages during the calculation of the insertion indices [58]. Doing so prevents the arm voltage ripple from distorting the generated voltage, and thus the circulating current can be controlled to have only a dc component. This happens when the divider $\hat{v}_{cu} = v_{cu}$ in (4.5), and the resulting inserted voltage v_u is given by (4.7).

$$v_u = v_u^r \frac{v_{cu}}{v_{cu}} = v_u^r \tag{4.7}$$

Equation (4.7) shows that the inserted voltage can be controlled independently of the arm voltage with this type of modulation. In addition to this decoupling, there will be no ripple in the circulating current unless the controller is injecting it following a commanded reference. This implies that CCSCs are not required with compensated modulation. Moreover, compensated modulation leads to a more decoupled system which is easier to control. This is because the dynamic interaction between the ripples in the arm voltage and current state is minimized or eliminated in the ideal case. As a result of these advantages, compensated modulation is adopted in the remainder of this thesis.

However, there are two challenges with the implementation of compensated modulation: (1) distortion and delay in the arm voltage measurement, and (2) the loss of inherent stability of the arm energy[62]. The first limitation implies that there might still be circulating current ripple after implementing compensated modulation because of the mismatch between v_{cu} and $\hat{v}_{cu}$ caused by nonidealities in the measurement system. The second point relates to a property of direct modulation, which is not present in compensated modulation. This property is open-loop stability, which means that the upper and lower arm voltages converge to a common value without a closed-loop control. It has been shown in the literature [63] that this inherent stability is lost when compensated modulation is used.

Ref. [62] proposed an open-loop compensated modulation approach to overcome both of the aforementioned challenges. The main idea behind this type of compensated modulation is to use estimated versions of the arm voltages as dividers instead of the measured ones. The estimates are obtained by taking as input the measured currents, and voltage references coming from the controllers. This approach was proven to be globally asymptotically stable [64] and extended to include current control [65].

A shortcoming of the open-loop approach is that it relies on accurate knowledge of parameters, such as capacitance. Consequently, parameter errors can significantly affect its performance. An improved energy control which combines the benefits of the open-loop modulation with the dynamic performance of a closed-loop energy control is proposed in Chapter 6 of this thesis. The proposed method also includes an online parameter correction procedure to make it robust against parameter changes due to aging and configuration changes, such as bypassed submodules. Further discussion on modulation techniques is provided in Chapter 6.

4.3.2 Arm energy control

Depending on the type of modulation technique, the average arm energy might need to be closed-loop controlled. This is particularly true for the case of compensated modulation with measured arm voltages which makes the average arm energy open-loop unstable. Another reason to have a closed-loop control of the arm energy is in order to reduce the sensitivity of the arm energy to disturbances coming from other controllers and external sources. The purpose of this section is to provide an overview of a closed-loop arm energy controller. The arm energy is controlled in a cascaded control arrangement with an inner circulating current loop and an outer arm energy (voltage) loop. The dc (average) component of the circulating current is closed-loop controlled using a PI controller. The controller is derived based on the dynamics of the circulating current from Chapter 3, which is also repeated here in (4.8).

$$l_{dc}\frac{\mathrm{d}}{\mathrm{dt}}i_{c0} = \frac{1}{2}v_{dc} - v_{c0}^{r} - r_{dc}i_{c0} \tag{4.8}$$

where l_{dc} and r_{dc} are the arm inductance and resistance in per-unit on the dc side base value. On the right-hand side of (4.8), there is a voltage term, which is the difference between the dc link voltage v_{dc} and the common mode voltage reference v_{c0}^{r}. The current controller manipulates v_{c0}^{r} to control i_{c0}, while v_{dc} acts as an external disturbance. Therefore, the control objective is to track circulating current reference i_{c0}^{r} while rejecting disturbance from variations of v_{dc}.

One effect that is not included in (4.8) is the time delay between the generation of the reference v_{c0}^{r} and the time at which voltage is applied to the arms. Addition-

ally, there are filters placed at the measurement inputs of the controller in order to avoid aliasing and to limit noise content in the signals. These effects are included in the complete closed-loop diagram of the arm energy control in Fig. 4.9. Also

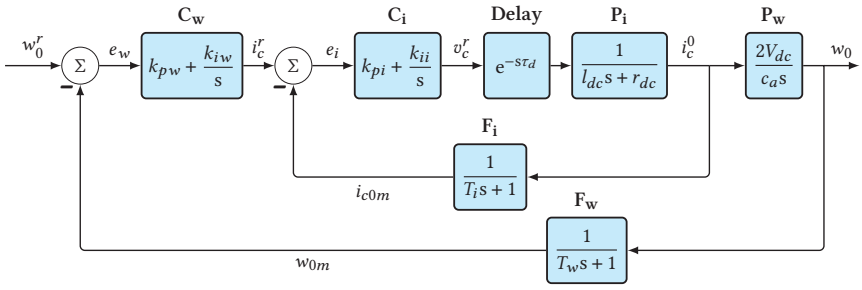

Figure 4.9: A block diagram of a cascaded arm energy control model.

shown in Fig. 4.9, is the outer energy loop, which is governed by the average arm energy dynamics derived in Chapter 3 (reproduced here in (4.9))

$$\frac{c_a}{2}\frac{\mathrm{d}}{\mathrm{dt}}w_0 = 2v_{c0}^r i_{c0} - \frac{1}{3}\Re\{\vec{\mathbf{v}}_{ac}^r \vec{\mathbf{i}}_{ac}^*\} \tag{4.9}$$

where c_a is the arm capacitance in per-unit. The $(\cdot)^{\Sigma}$ notation is dropped from the average energy for the sake of simplicity. The right-hand side of (4.9) represents power balance between the dc and ac sides. When the two sides are balanced, the arm energy stays constant. On the other hand, whenever there is a mismatch between the two powers, the arm energy either increases or decreases depending on the sign of the difference. The arm energy can, in principle, be controlled using either v_{c0}^r or i_{c0}. However, as mentioned earlier, v_{c0}^r is used to control i_{c0}, which means that v_{c0}^r is the only feasible choice that avoids strong coupling between the outer and inner loops. Direct control of the arm energy without the current loop is made possible by using v_{c0}^r. This, however, implies that the current is not controlled, which is major disadvantage because there is no direct way to implement current limiting.

Unlike (4.8), the right-hand side equation in (4.9) is nonlinear in the states because it involves the product $v_{c0}^r i_{c0}$. The ac side power also exhibits nonlinearity, but its nonlinearity is not important in this analysis because the ac power is considered as a disturbance. In order to linearize the dynamic model, a steady-state operating point for v_{c0}^r is identified first by setting the derivative to zero in (4.8). The resulting operating point V_{c0} in terms of the dc voltage at the operating point V_{dc} is given by (4.10).

$$V_{c0} = \frac{1}{2}V_{dc} - r_{dc}I_{c0} \approx \frac{1}{2}V_{dc} \tag{4.10}$$

The approximation on the right-hand side is possible because the value of r_{dc} is very small. Equation (4.9) can then be linearized to give the model shown in Fig. 4.9. More details on the linearization process are given in Chapter 5.

When considering Fig. 4.9, it can be noted that the structures of the control loops are suitable for tuning using symmetric and modulus optimum tuning techniques [56]. The inner loop plant model is a combination of first-order systems with a time delay, and hence the inner controller can be tuned using the modulus (magnitude) optimum criteria. On the other hand, the outer loop plant is composed of an integrator and a first-order transfer function. This is, however, not suitable for tuning using modulus optimum because of the integrator. Therefore, symmetric optimum technique is used to tune the outer controller.

4.4 F2F dc-dc converter control

This section briefly discusses specific control arrangements for an MMC-based Front-to-Front (F2F) dc-dc converter. Since the F2F converter consists of two MMCs connected on their ac sides, all the control structures discussed so far in this chapter are applicable to the F2F. The main difference compared to a single MMC control is in the way the high-level control responsibility is shared among the two MMCs. The first considerations relates to the ac voltages. Since there is no *grid voltage*, one of the converters has to provide a stiff voltage source [66]. This means that one of the MMCs does not need to have high-level controllers because it should only generate a constant ac voltage with the desired magnitude, frequency and phase. The second MMC can thus control its current and power by adjusting its ac voltage.

It is apparent that a PLL is not necessary because the ac voltage is internal to the converter, and the phase angle can be obtained directly from the controller which generates the reference for the ac voltage. The primary goal of the high-level control in an F2F converter is to control the power flow through the converter. This is achieved by controlling the ac power, which in turn controls the dc powers of the two sides of the converter [9]. A change in the ac power causes an imbalance between the ac and dc powers causing the arm energy to change. The arm energy controller intervenes by changing the dc power to keep the energy constant. The end result is that the dc powers on the two sides of the converter match the change in the ac power.

Similar to ac-dc HVDC converters, F2F dc-dc converters can be controlled in constant power mode, where the reference power is independent of the dc voltage. Alternatively, it can also include a dc voltage support scheme implemented in the form of droop. Ancillary services utilizing the energy storage capacity of the

F2F can also be implemented. In summary, the control arrangement needed in an MMC-based F2F dc-dc converter closely follows those of the ac-dc MMC controls with some peculiarities regarding the cooperation of the two MMCs that form the F2F converter.

4.5 Summary

An overview of control arrangements needed for an MMC bases HVDC converter was given in this chapter. Three layers of control are needed to meet these control objectives because of the complexity of the converter. At the highest level, there are the PLL, ac current control, and power or voltage control. These controllers are common to all VSC-HVDC converters. For the MMC case, these high-level controllers operate on top of the mid-level controller, whose task is to maintain energy balance of the floating submodules and to facilitate energy exchange between the ac and dc sides. At the lowest level, there are controllers responsible for interfacing with the converters at the submodule level. Low-level controllers are not covered in this thesis.

Controller structures for high- and mid-levels were presented. The modulation techniques and the arm energy control are particularly important in this thesis. Direct and compensated modulation schemes were presented. Despite its more complex implementation, compensated modulation is adopted in this work because it avoids the need for the circulating current suppression controllers. Moreover, the absence of the circulating current ripple reduces the interaction between the different ripple components, leading to a more decoupled system that is easy to control.

It was pointed out that the performance of compensated modulation can be significantly affected by the nonidealities of the measurement system, i.e. distortion and delay. A solution for this problem is to use the open-loop compensated modulation, which uses estimated arm voltages instead of the measured ones. The main challenge with this approach is that the estimation is heavily dependent on accurate knowledge of the converter parameters such as the arm capacitance, which can change over time. An improved control strategy which includes an online parameter adjustment algorithm is proposed in Chapter 6. The proposed control combines the benefits of the open-loop method with good dynamic performance of a closed-loop energy control. This proposed control forms the basis for energy-based services introduced in Chapter 7.

5
Simulation and Testing Methodology

This chapter discusses the methods chosen for the analyses and tests performed as part of this thesis. The methods can be categorized into time-domain simulations, small-signal analyses, and Power Hardware In The Loop (PHIL) testing. The theoretical background behind each method is presented together with some example of applications. Aspects regarding choice of software tools are also addressed in this chapter. The simulations were performed in a MATLAB®/Simulink®environment. The open source packages MATPOWER and MATACDC were used for loadflow calculations for the purpose of initialization. Small-signal analyses were also performed in MATLAB®by using Control System Toolbox™. Power hardware in the loop tests were performed using OPAL-RT real-time simulator with a grid emulator from EGSTON power. Background information on these analyses and test methods together with the implementation details are presented. The discussion in this chapter is supported by the following contribution by the author.

> A. A. Taffese and E. Tedeschi, "Simplified Modelling of the F2F MMC-Based High Power DC-DC Converter Including the Effect of Circulating Current Dynamics," in *2018 IEEE 19th Workshop on Control and Modeling for Power Electronics (COMPEL)*, Jun. 2018, pp. 1–6

Chapter Outline

5.1 Introduction

The method employed in the analysis and testing of a system significantly affects the quality of the results obtained. This chapter outlines the methods used in this thesis together with the background theory and justification for the choice of a given method. The methods presented here are time-domain simulations, small-signal analysis, and Power Hardware In The Loop (PHIL) testing. These methods are used in such a way that they complement each other. For instance, an oscillation observed in a time-domain simulation can be further investigated using small-signal analysis in order to identify its origin. The methods are discussed in the following sections. The challenges faced and the solutions applied when using each method are also highlighted.

5.2 Time domain simulation

Time domain simulation is the most used type of analysis or testing method in this thesis. It is relatively easy and straightforward to set up and run time-domain simulations depending on the selected modeling approach. Modeling approaches used for simulation can be broadly grouped into *causal* and *acausal* [67], [68]. These are also known as *signal-/block-based* and *physical* modeling approaches, respectively. Causal modeling has a signal flow direction from inputs to outputs, and hence enforces a cause and effect relation between the inputs and the outputs. This approach is the best fit for control systems which naturally have a sequential block diagram structure. However, causal modeling is not directly applicable to physical networks, like electrical circuits, because they do not have a causal nature. Instead, the variables such as voltage and current exist at the same time with neither of them being input or output. Acausal modeling enables such a modeling where all the variables are computed simultaneously. The main benefit of acausal modeling is re-usability of components to build large systems with ease. For example, once a resistor model is built, it can be used in any configuration irrespective of how it is connected. On the other hand, the equation for each network needs to be derived to causal modeling, which is somewhat cumbersome.

A combination of causal and acausal modeling approaches was adopted in this thesis. Causal modeling was applied to control system, while acausal modeling was used for the electrical networks. The most popular acausal modeling languages are Modelica and Simscape. These languages offer a very natural way of describing components using Differential Algebraic Equations (DAEs), which are later compiled and simulated in tools like OpenModelica and Simulink/Simscape. Simscape was chosen here because it has very good integration with the powerful control analysis tools available in MATLAB/Simulink.

Both instantaneous value (*abc* domain) and phasor simulations were performed using a custom-built library in Simscape. Instantaneous value simulations are more generally applicable, and they require the least amount of effort to develop. One challenge with such simulations is associated with small-signal analysis, which requires constant values in steady state to perform linearization as explained in Section 5.3. Phasor models are suitable in this case because they have constant values in steady state. Both approaches have been used in this thesis, and the following section gives an overview of the simulation library developed for both simulation types.

5.2.1 Instantaneous value simulation

Most of the components needed for instantaneous value simulations are already available from the standard Simscape library. The only custom components used are the MMC arm and the FD-π cable model. The dynamics of the MMC arm are governed by (5.1).

$$C_{arm}\frac{\mathrm{d}}{\mathrm{dt}}v_{cu} = n_u i_u \quad \text{and} \quad v_u = n_u v_{cu} \tag{5.1}$$

where n_u is the insertion index, i_u is the arm current, C_{arm} is the arm capacitance, and v_u is the inserted voltage of the upper arm. A similar equation applies to the lower arm. The code for an implementation of (5.1) in Simscape is shown in Listing 5.1. The code defines several sections named inputs, outputs, nodes, parameters, variables, and equations. The relation in (5.1) is implemented in the equations section. As can be seen from the *nodes* section, generic electrical nodes from the Simscape foundation library were used. The foundation library defines an electrical node with a current i as a *through* variable and voltage v as an *across* variable. More details on the terminology and syntax can be found from the Simscape documentation [69]. The code in Listing 5.1 generates a block/component with two electrical ports P and N, an input port for insertion index n, and an output port for arm voltage measurement $v_{c,meas}$. The cable model was developed in state-space form by following a similar approach. These components are then interconnected to complete the average MMC model. The resulting model was used in the majority of the simulation tasks in this thesis, and the simulation model was found to be robust (in terms of numerical issues) and accurate (validated against laboratory test results).

5.2.2 Phasor simulation

Unlike instantaneous values simulations, Simscape does not have a built-in library of components for phasor simulation. Therefore, a custom phasor library was developed. Since Simscape does not support complex numbers, the implementation was performed using a vector of two elements representing the real

Listing 5.1: A Simscape implementation of an average model for the MMC arm.

```
component MMC_arm
% MMC arm capacitor dynamice
% Models the voltage source in the average MMC model
  inputs % Insertion index input
        n = {0.5, '1'}; %n:left
  end
  outputs % Arm voltage measurement
        vc_meas = {0, 'V'}; %vc:left
  end
  nodes % Electrical ports: positive (P) and negative (N)
    P = foundation.electrical.electrical; % P:right
    N = foundation.electrical.electrical; % N:right
  end
  parameters
    Carm = { 29e-6, 'F' };   % Arm Capacitance
  end
  variables
    i  =  { 0, 'A' }; % Current through variable
    vc =  { 0, 'V' }; % Arm capacitor voltage
  end
  branches
    i : P.i -> N.i; % Current through from node p to node n
  end
  equations
   Carm*vc.der == n*i;         % Arm voltage differential equation
     P.v - N.v == vc*n;        % Inserted voltage relation
       vc_meas == vc;          % arm voltage measurement
  end
end
```

and imaginary part of each phasor. The real and imaginary parts are called the d and q components, respectively. This type of approach is used in RMS simulation in popular power system tools like PowerFactory [70].

One option to implement the phasor models is to use two nodes for each ac port (one for d and one for q) and run two wires between components to make a connection. This, however, leads to complex diagrams which also entail the possibility mistakes, such as interchanging the d and q components. A better solution is to create a new physical *domain* where each node has four variables: v_d, v_q, i_d, and i_q. Additionally, electrical frequency is also included in each node because electrical frequency is a global variable whose value is set by power balance and the interaction between governors of the generators in the system. It is set up such that one generator, preferably the largest one, will act as a swing machine (i.e. it sets the frequency) and the other generators will have small variations around this value during transients.

Since the dc sides have the same values in phasor form, the built-in library ele-

ments are used for resistors and capacitors on the dc side. Components for which custom phasor models were developed are: MMCs, ac transmission lines (series reactance), synchronous machines, transformers and loads. A sample implementation of an inductor, which is a building block for some of the other components, is shown in Listing 5.2. Only the *equations* section is presented for simplicity. The

Listing 5.2: A Simscape implementation of an inductor in *dq* domain.

```
1    equations
2        P.vd - N.vd == R*id - X*iq + X/P.omega_n*id.der;
3        P.vq - N.vq == R*iq + X*id + X/P.omega_n*iq.der ;
4    end
```

inductor in Listing 5.2 has two ports P and N with reactance X and resistance R. The grid frequency is ω_n. Models for remaining devices were also developed in the same manner. Each of these phasor components was validated against the ones present in PowerFactory.

One last important step in the process of phasor simulation is initialization. Load-flow programs MATPOWER [71] and MATACDC [72], [73] were used for this purpose. MATPOWER is a MATLAB-based load-flow program for ac systems. MATACDC an extension of MATPOWER to include both ac and dc systems. It solves the load-flow problem sequentially [72]. An interface script was written to read a Simulink phasor model and format it in a way that is understood by the load-flow programs. After the load-flow solution is obtained, the interface script initializes all the phasor blocks with the results so that the model starts the simulation from steady state. This section presented the simulation approach adopted in this thesis. Physical modeling was used because it enables the reuse of model components, which simplifies the process of building complex systems. Both instantaneous value and phasor simulation approaches were employed. Implementation of custom components in Simscape was also highlighted.

5.3 Small-signal analysis

Small-signal analysis refers to a set of tools used to analyze stability of linear systems. It can also be applied to nonlinear systems with an important constraint of validity over a small region around a stable equilibrium point, and hence the name *small-signal*. This type of analysis is also referred to as linear analysis, modal analysis, or eigenvalue analysis. This section provides a review of small-signal analysis with some implementation details and examples. The topics presented here are extensively covered in [47], [74]–[76].

5.3.1 Linear system representation

Linear systems, which satisfy scaling and superposition criteria [76], are represented in state-space form, as shown in (5.2), where $\mathbf{x}$ is a vector of n states, $\mathbf{u}$ is a vector of m inputs, and $\mathbf{y}$ is a vector of p outputs. States of a system are the minimum number of variables that are needed to fully describe the system [76].

$$\begin{aligned} \dot{\mathbf{x}} &= \mathbf{A}\mathbf{x} + \mathbf{B}\mathbf{u} \\ \mathbf{y} &= \mathbf{C}\mathbf{x} + \mathbf{D}\mathbf{u} \\ \mathbf{x} &= \begin{bmatrix} x_1 & x_2 & \dots & x_n \end{bmatrix}^T \\ \mathbf{u} &= \begin{bmatrix} u_1 & u_2 & \dots & u_m \end{bmatrix}^T \\ \mathbf{y} &= \begin{bmatrix} y_1 & y_2 & \dots & y_p \end{bmatrix}^T \end{aligned} \tag{5.2}$$

$\mathbf{A}$ is the state (system) matrix, $\mathbf{B}$ is the input (control) matrix, $\mathbf{C}$ is the output matrix, and $\mathbf{D}$ is the direct transmission (feedthrough) matrix [76]. When the matrices $\mathbf{A}$, $\mathbf{B}$, $\mathbf{C}$, and $\mathbf{D}$ are constants, the system is known as a Linear Time Invariant (LTI) system. Output of the system can be calculated at any given time based on the states, the inputs and the state-space matrices. Values of the states before the current time of computation are known as initial conditions. The state matrix $\mathbf{A}$ plays an important role in determining how the system responds to disturbances. The response can be computed from (5.2) by using the state transition matrix [76] or by numerical integration of (5.2), but these approaches do not provide useful insight into the system dynamics. A better approach using eigenvalues and eigenvectors is discussed in the next section.

5.3.2 Eigenvalues and eigenvectors

Geometrically, matrices rotate and scale the vectors they are multiplied to. However, when matrices are multiplied to some special vectors, the resulting vectors do not rotate (but stay on the same position), but they are scaled by a constant, as shown in (5.3). The special vector ϕ and the scaling λ are called the (right) eigenvector and eigenvalue of $\mathbf{A}$, respectively [77].

$$\mathbf{A}\boldsymbol{\phi} = \lambda\boldsymbol{\phi} \tag{5.3}$$

Since $\mathbf{A}$ is an $n \times n$ matrix, it has n eigenvalues and eigenvectors, which are written in matrix form in (5.4).

$$\mathbf{A}\boldsymbol{\Phi} = \boldsymbol{\Phi}\boldsymbol{\Lambda} = \begin{bmatrix} \boldsymbol{\phi}_1 & \boldsymbol{\phi}_2 & \dots & \boldsymbol{\phi}_n \end{bmatrix} \begin{bmatrix} \lambda_1 & & & \\ & \lambda_2 & & \\ & & \ddots & \\ & & & \lambda_n \end{bmatrix} \tag{5.4}$$

where $\mathbf{\Phi}$, whose columns $\boldsymbol{\phi}_i$ are eigenvectors of $\mathbf{A}$, is the eigenvector matrix and $\mathbf{\Lambda}$ is a diagonal matrix of the eigenvalues of $\mathbf{A}$. Multiplying both sides of (5.4) by $\mathbf{\Phi}^{-1}$ yields (5.5), which shows that the state matrix can be diagonalized by using a similarity transformation. The previous statement holds given that $\mathbf{A}$ has a linearly independent set of eigenvector so that $\mathbf{\Phi}$ is invertible [77].

$$\mathbf{\Phi}^{-1}\mathbf{A}\mathbf{\Phi} = \mathbf{\Lambda} \tag{5.5}$$

The transformation is performed by changing the state vector from $\mathbf{x}$ to $\mathbf{z}$, as given by (5.6).

$$\mathbf{x} = \mathbf{\Phi}\mathbf{z} \tag{5.6}$$

Substituting (5.6) into (5.2) gives the state-space equations in model (decoupled) form in (5.7).

$$\begin{aligned} \dot{\mathbf{z}} &= \mathbf{\Lambda}\mathbf{z} + \mathbf{\Phi}^{-1}\mathbf{B}\mathbf{u} \\ \mathbf{y} &= \mathbf{C}\mathbf{\Phi}\mathbf{z} + \mathbf{D}\mathbf{u} \end{aligned} \tag{5.7}$$

Diagonalization of $\mathbf{A}$ transforms the n^{th} order coupled differential equation in $\mathbf{x}$ into n first-order differential equations in $\mathbf{z}$, which have simple exponential solutions [47], [76]. The elements of $\mathbf{z}$ are called *modes* of the system. The modal responses depend on the eigenvalues which are, in general, in a complex form, as shown in (5.8).

$$\lambda_i = \alpha_i + j\beta_i \tag{5.8}$$

where α and β are the real and imaginary parts of the eigenvalue λ_i. Complex eigenvalues occur in conjugate pairs if the state matrix is real, which is true for systems in the scope of this thesis. This means that if λ_i is an eigenvalue, so is $\lambda_i^* = \alpha_i - j\beta_i$.

5.3.2.1 Time domain response

A complex conjugate eigenvalue pair $(\lambda_i\,,\ \lambda_i^*)$ leads to an oscillatory response with frequency of β_i and exponential decay (growth) rate of α_i shown in (5.9).

$$z_i(t) = k_i \mathrm{e}^{\alpha_i t} \cos\left(\beta_i t + \theta_i\right) \tag{5.9}$$

where k_i and θ_i are the gain and phase shift associated with the mode. A sample waveform showing the effect of α_i is depicted in Fig. 5.1. The waveform shows decaying oscillation when $\alpha_i < 0$, growing oscillation when $\alpha > 0$, and sustained oscillation when $\alpha_i = 0$. These cases correspond to *asymptotically stable*, *unstable*, and *marginally stable* conditions, respectively [76]. Another special case is when $\beta_i = 0$, which implies that the response will exhibit exponential decay or growth without oscillation.

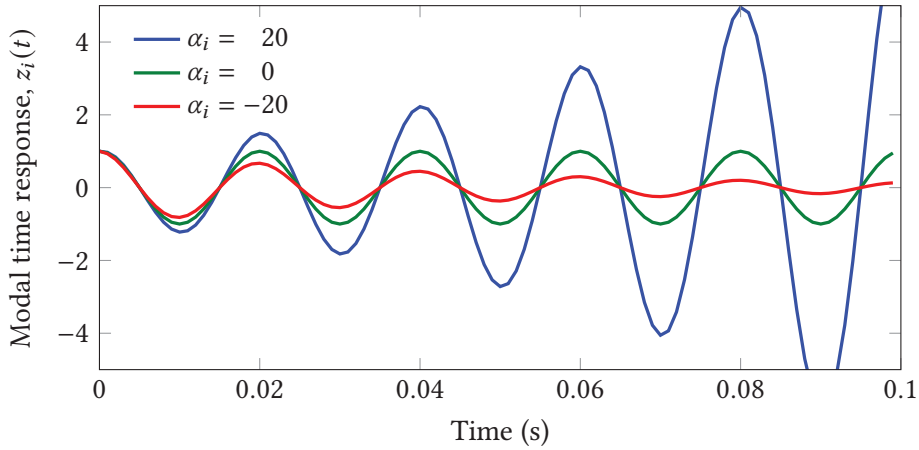

Figure 5.1: Time response of mode z_i with a complex eigenvalue $\lambda_i = \alpha_i \pm 2\pi 50$.

As it is evident from the example, the stability of the system is determined by the signs of the real parts of the eigenvalues. However, it is also important to have a measure of relative stability. Damping ratio ζ_i is one such measure which quantifies the rate of decay.

$$\zeta_i = -\frac{\alpha_i}{|\lambda_i|} = -\frac{\alpha_i}{\sqrt{\alpha_i^2 + \beta_i^2}} \tag{5.10}$$

Damping ratio is unitless and its value is between −1 and 1 (i.e. $|\zeta_i| \leq 1$). In the example of Fig. 5.1, the value of the damping ratio is ±0.048 (±4.8%). In power systems applications, damping ratio greater than 5% is considered to be acceptable [75], but higher damping might be needed in specific cases depending on the application. Second-order system response is characterized by using two parameters: natural frequency ω_{ni} and damping ζ_i. These parameters are related to the real and imaginary part of the eigenvalue, as shown in (5.11).

$$\begin{aligned} \alpha_i &= -\zeta_i \omega_{ni} \\ \beta_i &= \omega_{ni}\sqrt{1-\zeta_i^2} \end{aligned} \tag{5.11}$$

It should be noted that the relation in (5.11) and (5.10) for ζ_i are equivalent. Because of the relation with damping in (5.11), β_i is also known as the damped natural frequency [75].

5.3.2.2 Observability

After the properties of the modal responses (elements of $\mathbf{z}$) are computed as per the discussion so far, these properties have to be mapped to the original states $\mathbf{x}$

which is done by using the eigenvector matrix as shown in (5.6). This relation is discussed here in a greater detail because it reveals important properties that relate the modes to the states. Such properties can be used to decompose time-domain responses observed in the states into elementary responses containing exponentials and oscillations associated with individual modes. Equation (5.6) can be expanded column-wise, as shown in (5.12).

$$\begin{aligned} \mathbf{x} &= \boldsymbol{\phi}_1 z_1 + \boldsymbol{\phi}_2 z_2 + \cdots + \boldsymbol{\phi}_n z_n \\ \begin{bmatrix} x_1 \\ x_2 \\ \vdots \\ x_n \end{bmatrix} &= \begin{bmatrix} \phi_{11} \\ \phi_{21} \\ \vdots \\ \phi_{n1} \end{bmatrix} z_1 + \begin{bmatrix} \phi_{12} \\ \phi_{22} \\ \vdots \\ \phi_{n2} \end{bmatrix} z_2 + \cdots + \begin{bmatrix} \phi_{1n} \\ \phi_{2n} \\ \vdots \\ \phi_{nn} \end{bmatrix} z_n \end{aligned} \tag{5.12}$$

Each state is composed of a linear combination of the modes $\mathbf{z}$ scaled by the columns of the eigenvector matrix $\mathbf{\Phi}$. The elements of the right eigenvector ϕ_{i} show the contribution of mode z_i in all the states. This is known as *observability* or *mode shape* of mode z_i [47]. For example, ϕ_{21} is the observability of mode z_1 in state x_2.

The mode shapes are generally complex numbers with magnitude and phase angle in polar coordinated. As discussed earlier, the magnitudes are interpreted as the relative presence of a mode in the states. The phase angles give additional information which is useful when studying interaction between the states for the given mode. For instance, if two states have comparable mode shape but with an opposite directions (180° between them), it can be interpreted as the two states oscillating against each other when the mode is excited. This is often displayed using a mode phasor plot in the complex plane.

It should be noted that mode shape (observability) values should be compared for states with the same variable type. For example, it does not always make sense to compare mode shapes for voltage states to rotor angle states even after the units are removed by normalization (per-unit conversion). When such comparisons are made, the interpretation should be carefully analyzed. The discussion so far was focused on the observability of the modes in the states; however, in some cases it might be of interest to study the observability of the modes in the outputs, which are linear combinations of the states. In such cases, the same definitions in (5.12) apply with $\mathbf{\Phi}$ replaced by $\mathbf{C\Phi}$.

5.3.2.3 Controllability

The previous section discussed the mapping from the modes $\mathbf{z}$ to the states $\mathbf{x}$. The opposite mapping, known as *controllability*, is presented here. This is shown in

(5.13) where $\mathbf{\Psi}$ is the left eigenvector matrix.

$$\mathbf{z} = \mathbf{\Phi}^{-1}\mathbf{x} = \mathbf{\Psi}\mathbf{x} \tag{5.13}$$

The rows of $\mathbf{\Psi}$ are the left eigenvectors of $\mathbf{A}$. Each modal element can be written as a linear combination of the states weighted by the left eigenvectors as shown in (5.14).

$$\begin{bmatrix} z_1 \\ z_2 \\ \vdots \\ z_n \end{bmatrix} = \begin{bmatrix} \psi_{11}x_1 + \psi_{12}x_2 + \cdots + \psi_{1n}x_n \\ \psi_{21}x_1 + \psi_{22}x_2 + \cdots + \psi_{2n}x_n \\ \vdots \\ \psi_{n1}x_1 + \psi_{n2}x_2 + \cdots + \psi_{nn}x_n \end{bmatrix} \tag{5.14}$$

The elements of $\mathbf{\Psi}$ are the relative contributions of the states in each mode. Element ψ_{ik}, for instance, is the gain coupling state k to mode i. By inspecting the elements of the vector $\boldsymbol{\psi}_i$, which is the i^{th} row of $\mathbf{\Psi}$, the states which have the most or least influence on the mode can be identified. As was the case for observability in the previous section, comparison of controllability of states of different variable types should be taken with caution because there might be scaling mismatches.

Controllability is useful when identifying manipulated states (control inputs) to improve damping of a given mode. However, in practice not all states can be directly manipulated. The control inputs $\mathbf{u}$ are the ones that can be manipulated externally. In this case, the definition for controllability is that it is a measure of how controllable a mode is using a given set of inputs [47]. This controllability measure is calculated by replacing $\mathbf{x}$ by $\mathbf{Bu}$ in (5.13).

5.3.2.4 Participation factor

When the system under study becomes large, it is sometimes desirable to focus on specific modes of interest to simplify the analysis [74], [78]. It is thus important to identify which states have significant contributions/interaction with the selected modes. Observability and controllability values show how the states are related to the modes. However, comparison of these metrics across different types of states (voltage, current, rotor angles, etc.) is not useful since the states might have different units or scaling [47], [74], [75]. A dimensionless metric suitable for the aforementioned purpose is the *participation factor* [78], which is computed by

combining the observability and controllability metrics, as shown in (5.15).

$$\begin{aligned}\mathbf{P} &= \boldsymbol{\Phi} \circ \boldsymbol{\Psi}^T \\ &= \begin{bmatrix} \boldsymbol{\phi}_1 \circ \boldsymbol{\psi}_1^T & \boldsymbol{\phi}_2 \circ \boldsymbol{\psi}_2^T & \cdots & \boldsymbol{\phi}_n \circ \boldsymbol{\psi}_n^T \end{bmatrix} \\ &= \begin{bmatrix} \phi_{11}\psi_{11} & \phi_{12}\psi_{21} & \cdots & \phi_{1n}\psi_{n1} \\ \phi_{21}\psi_{12} & \phi_{22}\psi_{22} & \cdots & \phi_{2n}\psi_{n2} \\ \vdots & \vdots & \ddots & \vdots \\ \phi_{n1}\psi_{1n} & \phi_{n2}\psi_{2n} & \cdots & \phi_{nn}\psi_{nn} \end{bmatrix}\end{aligned} \tag{5.15}$$

where $(\circ)$ is an element-wise product operator which is also known as *Hadamard* or *Schur* product [79]. Each column of the $\mathbf{P}$ is normalized so that the sum of its elements is equal to 1. An alternative normalization is to divide the columns so that the largest element in the columns is 1. In either case, the participation factors are relative magnitudes along the columns, which means that comparison of the factors should be made along the columns not the rows. Participation factors also quantify the sensitivities of the eigenvalues to the diagonal elements of $\mathbf{A}$. The diagonal elements couple a state to its derivative, i.e. x_i to $\dot{x}_i$. Thus, it can be interpreted as the sensitivity of the eigenvalues to changes in a given state (5.16) [74].

$$p_{ik} = \frac{\partial \lambda_k}{\partial a_{ii}} \tag{5.16}$$

where p_{ik} is the i^{th} element in the k^{th} column of $\mathbf{P}$, a_{ii} is the i^{th} diagonal element of $\mathbf{A}$. Only the magnitudes of the eigenvectors $\boldsymbol{\phi}_i$ and $\boldsymbol{\psi}_i$ are used in the calculation of $\mathbf{P}$ in (5.15), so the elements of the participation factor matrix are real and positive.

5.3.2.5 Residues

Residues relate the inputs u to the outputs y for a given mode. They are the same as the residues obtained by partial fraction expansion of a transfer function [47], [76]. Residues are calculated by transforming the modal state-space equations in (5.7) into transfer function form with inputs $\mathbf{u}$ and outputs $\mathbf{y}$ [80]. After Laplace transformation and algebraic manipulations, the transfer function form of (5.7) is given in (5.17).

$$\mathbf{y} = \mathbf{C}\boldsymbol{\Phi}\left[s\mathbf{I} - \boldsymbol{\Lambda}\right]^{-1}\boldsymbol{\Psi}\mathbf{B}\mathbf{u} \tag{5.17}$$

Since $\boldsymbol{\Lambda}$ is diagonal, (5.17) can be expanded into the inverse of the contributions of the individual eigenvalues as shown in (5.18).

$$\mathbf{y} = \frac{\mathbf{R}_1}{s-\lambda_1}\mathbf{u} + \frac{\mathbf{R}_2}{s-\lambda_2}\mathbf{u} + \cdots + \frac{\mathbf{R}_n}{s-\lambda_n}\mathbf{u} \tag{5.18}$$

The elements of the residue matrices $\mathbf{R}_i$ are given by (5.19).

$$\mathbf{R}_i = \mathbf{C}\boldsymbol{\phi}_i\boldsymbol{\psi}_i\mathbf{B} \tag{5.19}$$

It can be noted that the residue matrices are rank-1 matrices resulting from a dyadic (outer) product of the left and right eigenvectors. One application of residues is in the identification of dominant modes in the outputs when a disturbance is applied to the inputs. This section introduced a set of tools, based on eigenvalues and eigenvectors, that give useful insight into a systems response and the various cross-couplings. These tools are used in different parts of the thesis to analyze stability of the test systems and to investigate the effectiveness of the proposed control schemes.

5.3.3 Linearization

The previous section introduced powerful tools that can be used to analyze linear systems. In practice, systems exhibit some level of nonlinearity, which limits the tools available for analyzing them. This can be rectified by linearization, which results in an approximate linear model for nonlinear systems around an equilibrium operating point $(\mathbf{x}_0, \mathbf{u}_0)$. By doing so, a nonlinear system can be analyzed using linear tools against the backdrop of validity around the operating point. Equations of nonlinear dynamic system are written in the form shown in (5.20).

$$\begin{aligned} \dot{\mathbf{x}} &= \mathbf{f}(\mathbf{x}, \mathbf{u}) \\ \mathbf{y} &= \mathbf{g}(\mathbf{x}, \mathbf{u}) \end{aligned} \tag{5.20}$$

where $\mathbf{f}$ and $\mathbf{g}$ are nonlinear vector valued functions. Linearization is performed by expanding (5.20) using a first-order Taylor series approximation, as given in (5.21).

$$\begin{aligned} \dot{\mathbf{x}} &= \mathbf{f}(\mathbf{x}_0, \mathbf{u}_0) + \nabla \mathbf{f}_x(\mathbf{x}_0, \mathbf{u}_0)\,(\mathbf{x} - \mathbf{x}_0) + \nabla \mathbf{f}_u(\mathbf{x}_0, \mathbf{u}_0)\,(\mathbf{u} - \mathbf{u}_0) \\ \mathbf{y} &= \mathbf{g}(\mathbf{x}_0, \mathbf{u}_0) + \nabla \mathbf{g}_x(\mathbf{x}_0, \mathbf{u}_0)\,(\mathbf{x} - \mathbf{x}_0) + \nabla \mathbf{g}_u(\mathbf{x}_0, \mathbf{u}_0)\,(\mathbf{u} - \mathbf{u}_0) \end{aligned} \tag{5.21}$$

where $\nabla \mathbf{f}(\mathbf{x}_0, \mathbf{u}_0)$ and $\nabla \mathbf{g}(\mathbf{x}_0, \mathbf{u}_0)$ are the *Jacobians* (vector partial derivatives) of $\mathbf{f}$ and $\mathbf{g}$ with respect to the states and inputs evaluated at the operating point. The subscripts x and u indicate the variables to which the derivatives are evaluated. Since linearization is performed at an equilibrium point, the state derivatives evaluated at the operating point are zero, i.e. $\mathbf{f}(\mathbf{x}_0, \mathbf{u}_0) = 0$. Taking this into account and changing variables, (5.21) can be simplified to (5.22).

$$\begin{aligned} \Delta\dot{\mathbf{x}} &= \nabla \mathbf{f}_x(\mathbf{x}_0, \mathbf{u}_0)\Delta\mathbf{x} + \nabla \mathbf{f}_u(\mathbf{x}_0, \mathbf{u}_0)\Delta\mathbf{u} \\ \Delta\mathbf{y} &= \nabla \mathbf{g}_x(\mathbf{x}_0, \mathbf{u}_0)\Delta\mathbf{x} + \nabla \mathbf{g}_u(\mathbf{x}_0, \mathbf{u}_0)\Delta\mathbf{u} \end{aligned} \tag{5.22}$$

where $\Delta\mathbf{x} = \mathbf{x} - \mathbf{x}_0$, $\Delta\mathbf{u} = \mathbf{u} - \mathbf{u}_0$, $\Delta\mathbf{y} = \mathbf{y} - \mathbf{y}_0$, and $\mathbf{y}_0 = \mathbf{g}(\mathbf{x}_0, \mathbf{u}_0)$. Equation (5.22) is already in linear form, but it can be converted into the conventional state-space form by substituting the Jacobians by the respective state-space matrices.

$$\begin{aligned} \Delta\dot{\mathbf{x}} &= \mathbf{A}\Delta\mathbf{x} + \mathbf{B}\Delta\mathbf{u} \\ \Delta\mathbf{y} &= \mathbf{C}\Delta\mathbf{x} + \mathbf{D}\Delta\mathbf{u} \end{aligned} \tag{5.23}$$

The Δ notation is dropped in further reference to linearized systems for the sake of simplicity, but it should be noted that all the variables are small deviations around an operating point. The state-space matrices are written in the form of the expanded Jacobians, as shown in (5.24) and (5.25). The derivative should be evaluated at $\mathbf{x} = \mathbf{x}_0$ and $\mathbf{u} = \mathbf{u}_0$.

$$\mathbf{A} = \begin{bmatrix} \frac{\partial f_1}{\partial x_1} & \frac{\partial f_1}{\partial x_2} & \cdots & \frac{\partial f_1}{\partial x_n} \\ \frac{\partial f_2}{\partial x_1} & \frac{\partial f_2}{\partial x_2} & \cdots & \frac{\partial f_2}{\partial x_n} \\ \vdots & \vdots & \ddots & \vdots \\ \frac{\partial f_n}{\partial x_1} & \frac{\partial f_n}{\partial x_2} & \cdots & \frac{\partial f_n}{\partial x_n} \end{bmatrix} \quad \text{and} \quad \mathbf{B} = \begin{bmatrix} \frac{\partial f_1}{\partial u_1} & \frac{\partial f_1}{\partial u_2} & \cdots & \frac{\partial f_1}{\partial u_n} \\ \frac{\partial f_2}{\partial u_1} & \frac{\partial f_2}{\partial u_2} & \cdots & \frac{\partial f_2}{\partial u_n} \\ \vdots & \vdots & \ddots & \vdots \\ \frac{\partial f_n}{\partial u_1} & \frac{\partial f_n}{\partial u_2} & \cdots & \frac{\partial f_n}{\partial u_n} \end{bmatrix} \tag{5.24}$$

$$\mathbf{C} = \begin{bmatrix} \frac{\partial g_1}{\partial x_1} & \frac{\partial g_1}{\partial x_2} & \cdots & \frac{\partial g_1}{\partial x_n} \\ \frac{\partial g_2}{\partial x_1} & \frac{\partial g_2}{\partial x_2} & \cdots & \frac{\partial g_2}{\partial x_n} \\ \vdots & \vdots & \ddots & \vdots \\ \frac{\partial g_n}{\partial x_1} & \frac{\partial g_n}{\partial x_2} & \cdots & \frac{\partial g_n}{\partial x_n} \end{bmatrix} \quad \text{and} \quad \mathbf{D} = \begin{bmatrix} \frac{\partial g_1}{\partial u_1} & \frac{\partial g_1}{\partial u_2} & \cdots & \frac{\partial g_1}{\partial u_n} \\ \frac{\partial g_2}{\partial u_1} & \frac{\partial g_2}{\partial u_2} & \cdots & \frac{\partial g_2}{\partial u_n} \\ \vdots & \vdots & \ddots & \vdots \\ \frac{\partial g_n}{\partial u_1} & \frac{\partial g_n}{\partial u_2} & \cdots & \frac{\partial g_n}{\partial u_n} \end{bmatrix} \tag{5.25}$$

There are some peculiarities associated with interpretation of results obtained using linearized nonlinear systems compared to linear systems. One of these differences is that any conclusion made based on the results applies to the operating point rather than the system. This is in contrast to linear systems where any stability conclusion applies to the system globally. Thus, an equilibrium point of a nonlinear system is *asymptotically stable* if all the eigenvalues of the linearized state matrix $\mathbf{A}$ have negative real parts [81]. Another point to be considered when studying linearized systems is that the models are valid in small regions around the operating point. The word *small* is subjective and it changes from system to system. So, the validity of the model should be verified against the nonlinear model for the largest expected magnitude of the disturbance applied to the system.

5.3.4 Analysis using software tools

The analysis of linear systems can be performed by using different tools which can be grouped into two categories: numerical and symbolic computation tools. Numerical tools, such as MATLAB®, perform all the calculations numerically to the machine's precision, while symbolic tools compute exact solutions [82], [83]. A downside of symbolic tools is that they tend to be slow when the system under study is large. However, they can have comparable performance to numerical

tools when performing large parameter sweep studies because the symbolic calculations do not need to be repeated for each iteration. So, a numerical approach is used in this thesis. In particular, the Control System Toolbox™, which is part of MATLAB®, is used. The choice was motivated by the fact that the toolbox integrates seamlessly with Simulink®. This allows the system to be constructed in a drawing-based environment, which is less prone to errors in the equations. The toolbox has function to linearize the model and also to perform parameter sweep analysis.

One challenge when using numerical methods in parameter sweep studies is eigenvalue switching, which means that the order of the eigenvalues changes during parameter sweep. This makes it difficult to track a given eigenvalue because the switching introduces jumps in the root locus. This issue can be addressed by sorting the eigenvalues based on the correlation between eigenvectors at the current and previous steps of the sweep [84]. The rationale behind the method is that if the parameter change is small, the eigenvectors do not exhibit a drastic change in direction, and hence there is a correlation between the eigenvectors. The correlation matrix is calculated as shown in (5.26).

$$\mathbf{Cor} = \mathbf{\Phi}_{new}^{H}\mathbf{\Phi}_{old} \tag{5.26}$$

where $(\cdot)^H$ is the Hermitian (complex conjugate transpose) of a matrix, $\mathbf{\Phi}_{old}$ and $\mathbf{\Phi}_{new}$ are the previous and current eigenvector matrices, respectively. Under the assumption of distinct eigenvalues, the eigenvectors are orthogonal to each other. Therefore, there will be one maximum value close to 1 in each row of **Cor** with the other elements being close to zero. The row number is the old location of the eigenvalue while the location of the maximum value (in each row) is the new location of the eigenvalue. For example, if the second row of **Cor** has 0.9 at position 4 and zeros everywhere else, it means that the second eigenvalue in the previous step has moved to the fourth position and this process can be repeated until the end of the parameter sweep. As a result, the mode can be moved back to its original location together with the corresponding eigenvectors. If **Cor** is an identity matrix, no action is necessary. By implementing this algorithm, a desired eigenvalue can be tracked during parameter sweeps. A sample implementation of this algorithm in MATLAB®is shown in Listing 5.3. It should be noted that the Control System Toolbox does not include implementation of this kind of mode-sorting algorithm. The listing is included to give a sample implementation that can work in MATLAB or OCTAVE.

The procedure followed in setting up a small-signal study in Simulink®is outlined as follows:

1. The system model is created as a Simulink®diagram. The model is checked for

Listing 5.3: Implementation of an eigenvalue-tracking algorithm in MATLAB.

```
function [Phi_new, Lambda_new] = eigen_track(Phi_prev, A)
%EIGEN_TRACK A function to track eigenvalues and eigenvector during
%sequential computation
% Syntax:  [Phi_new, Lambda_new] = eigen_track(Phi_prev, A)
%
% Inputs:
%    Phi_prev - Eigenvector matrix at the previous computation
%    A   - The matrix for which eigenvectors are computed
%
% Outputs:
%    Phi_new - Eigenvector matrix at the current computation
%    Lambda_new - Eigenvalue matrix at the current computation

%------------- BEGIN CODE --------------
% Compute the eigenvalues/vectors
[Phi_new, Lambda_new] = eig(A);
% Convert the diagonal eigenvalue matrix to a column vector
D = diag(Lambda_new);

% Compute the correlation between the current and the previous
    eigenvectors
Cor = abs(Phi_new'*Phi_prev);
% Find the location of the maximum in each row of Cor
[~, max_idx] = max(Cor, [], 2);
% Swap the columns of the new eigenvector
Phi_new(:,max_idx) = Phi_new;
% Swap the elements of the eigenvalue vector
D(max_idx) = D;
% Convert the eigenvalue vector to a diagonal matrix
Lambda_new = diag(D);

end
%------------- END OF CODE --------------
```

error and its response is verified by simulation.

2. Input and output points are specified in the model.

3. A steady-state operating point is identified either by running load-flow or by simulating the model until it reaches steady-state and capturing the final states.

4. Parameters are specified for sweep analysis.

5. State-space model of the system is extracted by linearizing around the specified operating point. If parameter sweep is specified, the operation results in multidimensional matrices for each parameter value.

6. Eigenvalues and eigenvector are calculated for detailed analysis. Eigenvalue tracking is used when parameter sweeps are studied.

5.3.5 Application - Small-signal analysis of an F2F dc-dc converter

This section presents an original application of the small-signal analysis method to an F2F dc-dc converter with the purpose of demonstrating the analysis methods and highlighting subtleties that can appear. The case is taken from [9], which presents a simplified model of an F2F converter for small-signal studies. The focus in this section is not on the development of the models or the controllers; these are presented in [9] and adopted here along with an explanation to give some context whenever necessary. The goal of this section is to demonstrate the use of the small-signal analysis method presented in the previous sections.

The system under study is composed of two MMCs connected on the ac side via a coupling transformer. The two dc sides are modeled as voltage sources behind a resistance to model the effect of the voltage drop on cables and the drop associated with dc voltage droop control on ac/dc converters. The MMCs are controlled using compensated modulation, which is explained in Chapter 4. As per the discussion in Chapter 3, simplified energy-based models are sufficient when compensated modulation is used. The ac side is controlled in *dq* domain with an inner current loop and outer power (*P,Q*) loop introduced in Chapter 4. Cascaded control is also applied on the dc side, where the inner loop is the dc circulating current controller and the outer loop is the leg energy controller.

The overall goal of the controller is to control power flow though the dc-dc converter, which is achieved by controlling the ac current. This creates a power imbalance which leads to a change in the average leg energy. The leg energy controller will then act to balance this power by adjusting the dc powers, which is the intended effect. For the purpose of this section, the focus is on the response of the system to a step change in ac active power reference from 0.8 pu to 0.7 pu and back.

A plot of active powers flows in the converter is shown in Fig. 5.2, where the step in the reference is applied at 4 s and 8 s. Positive power flow direction is from dc side 1 to dc side 2. It is expected that the powers are such that $p_{dc1} > p_{ac} > p_{dc2}$ because of the losses. This is, however, not the case in Fig. 5.2. The reason for this is that the model used for simulation is based on aggregation of the two MMC energy states which is developed by neglecting the losses in the converter [9]. The losses were not included because they have a negligible impact on the results of small-signal analyses. This was demonstrated in [9], where the simplified model is validated against more detailed models including the losses. The response in active power is generally smooth with slight oscillation at the beginning of the step changes. On the other hand, the leg energy states of the two sides (MMCs),

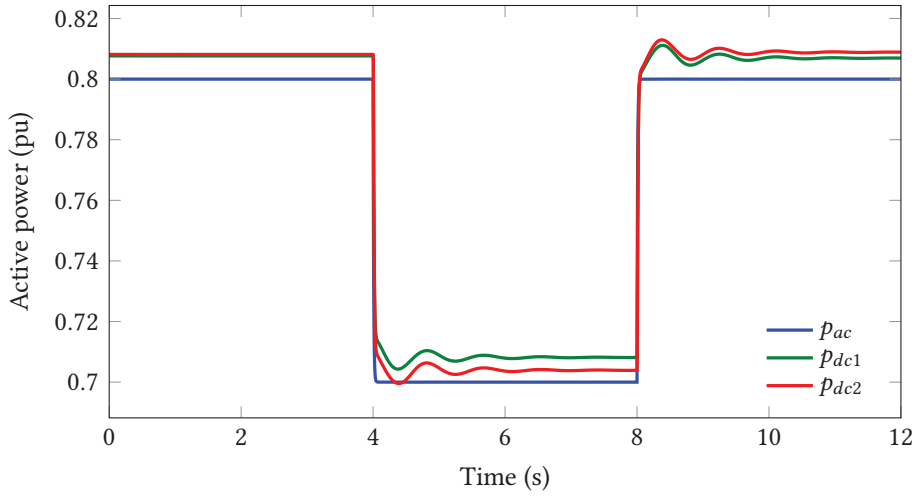

Figure 5.2: Active power response to a step change in the active power reference.

which are depicted in Fig. 5.3, exhibit significant levels of oscillation. The origin of these oscillations will be studied by using small-signal analysis in the following.

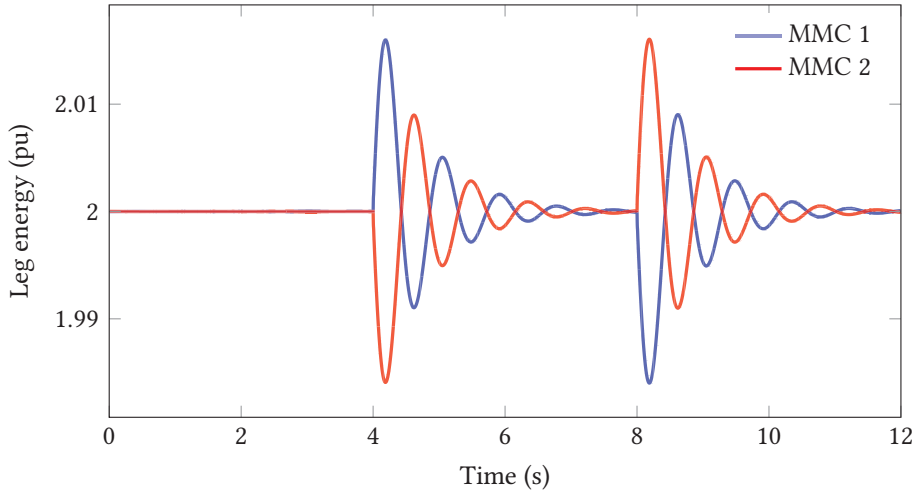

Figure 5.3: Leg energy response to a step change in active power.

5.3.5.1 Mode identification

To identify the origin of the oscillation in Fig. 5.3, a small-signal analysis was set up with the active power reference (p^r_{ac}) as *input* and the two aggregate leg energy states w^{Σ}_1 and w^{Σ}_2 as outputs. Then, a linearized model was generated followed by the calculation of the eigenvalues shown in Table 5.1. The first useful information

to link the oscillation in the time response to the eigenvalues is the frequency. The frequency of oscillation is roughly 1 Hz, as can be seen from Fig. 5.3. This correlates to eigenvalues 13 and 14 in Table 5.1. Identification of the mode is trivial in this case because there is only one mode with frequency close to the one observed in the plot. In a more general case with eigenvalues close to each

Table 5.1: Eigenvalues for the F2F small-signal study [9].

Mode No.	λ	ζ	$f_{osc} = \beta/(2\pi)\ (Hz)$
1	$-1970 + j5732$	0.33	912
2	$-1970 - j5732$	0.33	912
3	$-3128 + j3396$	0.68	540
4	$-3128 - j3396$	0.68	540
5	$-247 + j762$	0.31	121
6	$-247 - j762$	0.31	121
7	-827	1.0	-
8	$-183 + j81$	0.91	12.9
9	$-183 - j81$	0.91	12.9
10	-189	1.0	-
11	-192	1.0	-
12	-121	1.0	-
13	$-1.6 + j8$	0.2	1.3
14	$-1.6 - j8$	0.2	1.3
15	$0^{\dagger}$	-	-
16	$-610 + j263$	0.92	41.8
17	$-610 - j263$	0.92	41.8
18	-100	1.0	-

†The eigenvalue at the origin is related to power balance achieved by the leg energy controller. If it is uncontrolled, the average leg energy will drift in the events of power unbalance.

other, the dominant mode can be identified by computing the residue vector from the selected input (p^r_{ac}) to the output w^{Σ}_1 for all the modes. These values of the residues show the magnitudes the response from each mode. This information can be combined with the damping to a dominance factor η [9], as given in (5.27).

$$\eta = |\mathbf{r}| \oslash \boldsymbol{\zeta} \tag{5.27}$$

where $\oslash$ is the element-wise (Hadamard) division operator, $\mathbf{r}$ is a vector of residues for the selected input-output pair across all the modes, and $\boldsymbol{\zeta}$ is a vector of damping values (third column in Table 5.1). The value of η for modes with zero damping should be saturated to a maximum value to avoid infinite dominance factor. A high value of η shows that a mode has high presence and low damping, which

means that it is likely to dominate the time response. Fig. 5.4 shows η from p^r_{ac} to

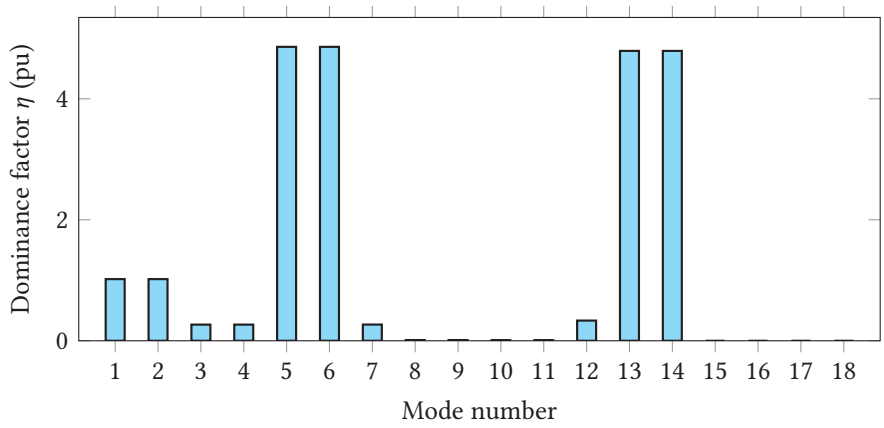

Figure 5.4: Mode dominance factors for the leg energy states [9].

w_1^Σ; a similar plot is obtained from w_2^Σ. Two pairs of complex conjugate eigenvalues (5, 6) and (13, 14) have high dominance value. The second pair is consistent with the earlier finding. The pair (5, 6), on the other hand, is not visible from the time domain response in Fig. 5.3. This is explained by considering the fact that the time response in Fig. 5.3 is excited by step changes in the input, while the residues calculated using the state matrices are applicable only when investigating the response of the system to an impulse input. The impulse response of the system, depicted in Fig. 5.5, exhibits the mode pair (5, 6) at the beginning of the response which matches the prediction made by the dominance factor.

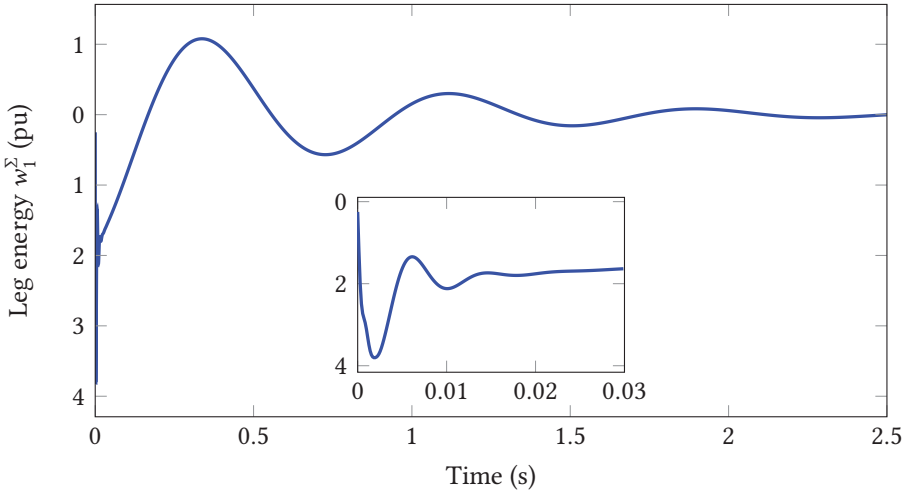

Figure 5.5: Leg energy response to an impulse in active power.

The effect of a step signal as opposed to an impulse can be studied by analyzing the system matrices. A step signal is effectively an impulse signal passed through an integrator [76]. This leads to one more state (for the case of single input) which modifies the state matrices as shown in (5.28).

$$\begin{aligned} \mathbf{A}_s &= \begin{bmatrix} \mathbf{A} & \mathbf{B} \\ \mathbf{0} & 0 \end{bmatrix} \quad \mathbf{B}_s = \begin{bmatrix} \mathbf{0} \\ 1 \end{bmatrix} \\ \mathbf{C}_s &= \begin{bmatrix} \mathbf{C} & \mathbf{D} \end{bmatrix} \quad \mathbf{D}_s = 0 \end{aligned} \tag{5.28}$$

where the subscript s indicates the matrices for the case of a step input and the ones without the subscript are the original state-space matrices. The dominance factors computed with the modified model of (5.28) are shown in Fig. 5.6, which clearly shows a single pair of eigenvalues that are consistent with the initial findings. The main observation from this example is that the type of the excitation plays an important role in the interpretation of the residues and the dominance factor.

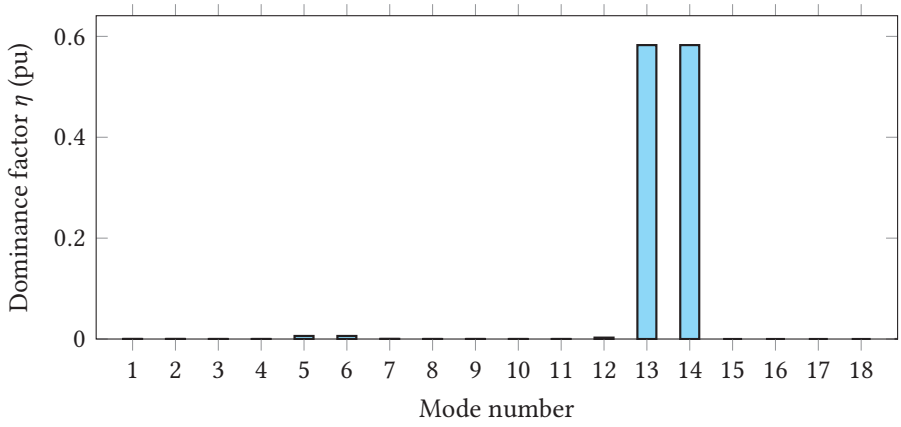

Figure 5.6: Mode dominance factors for the leg energy states (step input).

5.3.5.2 Modal properties

Since the mode of interest was identified in the previous steps, the modal properties such as observability and participation factors are computed next in order to gain a better insight into the system response. It is of interest to identify which states the mode is associated with. This is best revealed by the participation factors, which are shown in Fig. 5.7. There are 18 states in total including the dc voltages (v_{dc1} and v_{dc2}), the ac currents (i_d and i_q), the dc circulating currents (i_{c1} and i_{c2}), the leg energies (w_1^{Σ} and w_2^{Σ}), and other states associated with filters (δ's) and control states (γ's). The measurement filters are used in the feedback path for the control of the current, voltage, and leg energy states. Modes 13 and 14

have strong participation factors associated with the leg energy states of the two sides and their corresponding controllers. This implies that the modes can be significantly influenced by the energy controllers. In addition to this information, observability (mode shapes) can be used to make the connection between the modal results and the observations from the time domain data.

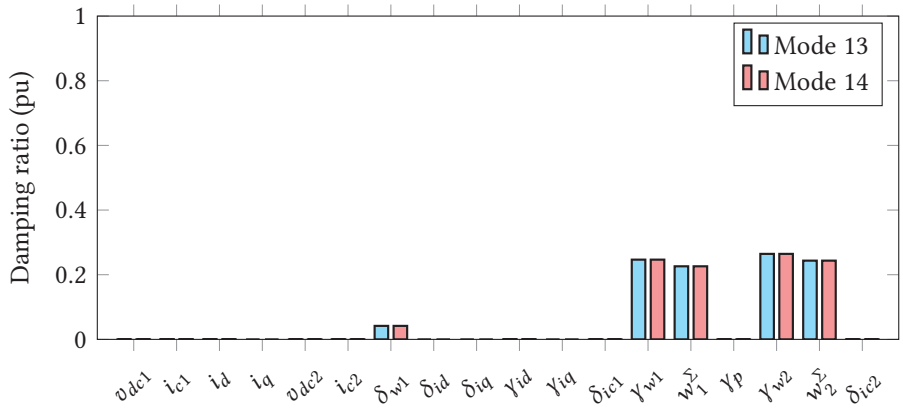

Figure 5.7: Participation factors for modes 13 and 14. γ's are control integrator states, and δ's are measurement filter states.

Observability of mode 13 in the leg energy states and the associated control states are shown in the mode phasor plot in Fig. 5.8. Since the selected mode is a complex conjugate pair, the observability values are also complex with both magnitude and angle in the polar coordinates. It can be clearly seen that the observabilities (mode shapes) of the two leg energy states are in phase opposition to each other with similar magnitudes. This implies that the oscillation associated with this mode will appear in the two states with opposite polarity. This can be confirmed by inspecting the time domain plot in Fig. 5.3. The same observation applies to the controller states. This can be interpreted as the two MMC energy states oscillating against each other.

5.3.5.3 Parameter sweep

In Fig. 5.7, the eigenvalue pair (13, 14) are related to the energy control states. This section shows an attempt to improve the controller response by changing the proportional gain of the circulating current controllers. Since the circulating current control is the inner loop for energy control, this will have a direct impact on the energy controller response. The parameter was varied from the base value of $k_p = 0.0038$ all the way to 0.038 ($10 \times k_p$). A linearized model of the system is generated numerically for each value of k_p. The eigenvalues are then calculated from the state matrix **A**. Fig. 5.9 shows mode 13 on the complex plane as a function

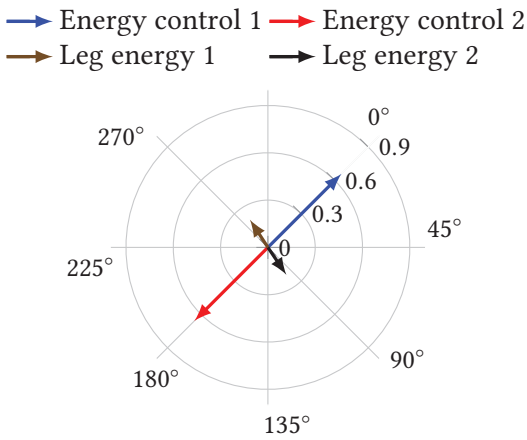

Figure 5.8: Observability of mode 13 in energy states of an F2F converter [9].

of the parameter k_p. The plot shows several discontinuities caused by eigenvalue switching, which is explained in the previous section. The eigenvalue tracking algorithm given in Listing 5.3 can be used to rectify this problem; the result is shown in Fig. 5.10, which is free from the discontinuities observed in Fig. 5.9.

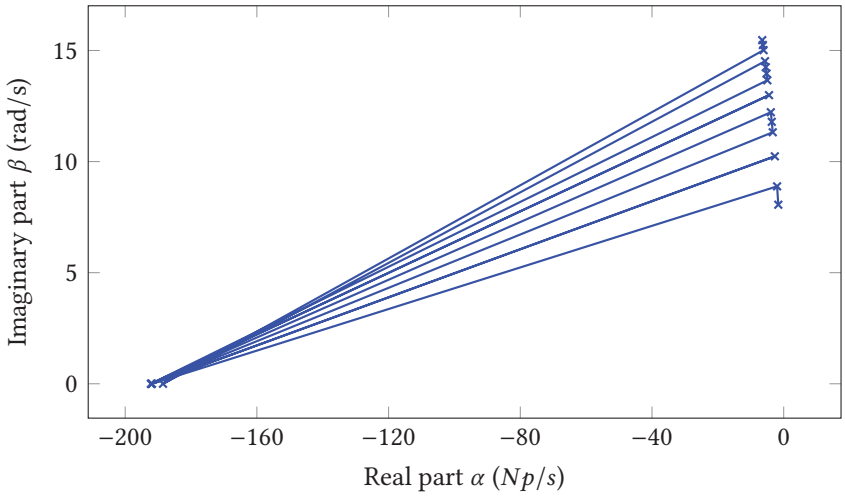

Figure 5.9: Mode 13 during parameter sweep without eigenvalue tracking.

It can be seen from Fig. 5.10 that the eigenvalue moves to the left, which results in a higher damping. However, the mode also moves upwards (increase in frequency), which reduces the damping. Ideally, it is desired that the mode moves only to the left side (without any increase in frequency) in order to achieve maximum damping for a given change in the parameter. In this particular case, the

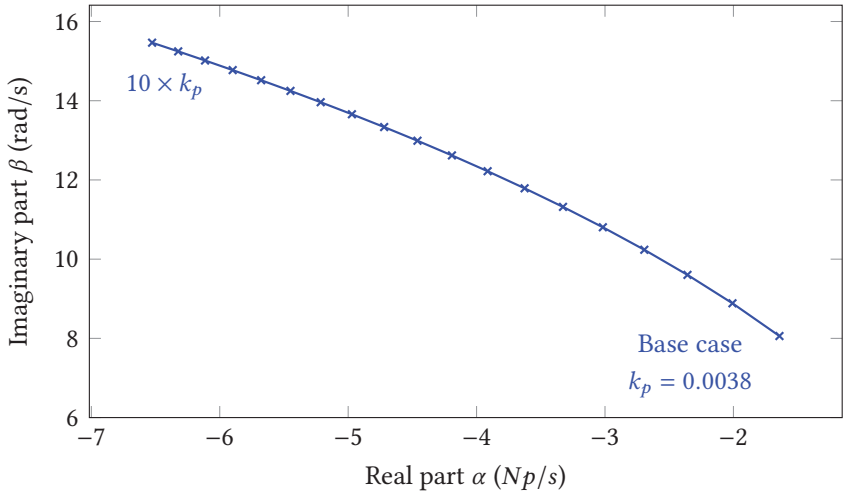

Figure 5.10: Mode 13 during parameter (k_p) sweep with eigenvalue tracking.

mode moved more to the left than upwards, leading to an effective increase in damping from 0.2 to 0.39. The damping improvement is evident in the time domain plot comparing the response for different values of k_p shown in Fig. 5.11. In addition to the increase in damping, an increase in k_p leads to an increase in the oscillation frequency (shrinking of the oscillation in Fig. 5.11) consistent with the upward movement of the eigenvalue in Fig. 5.10. This section presented a review

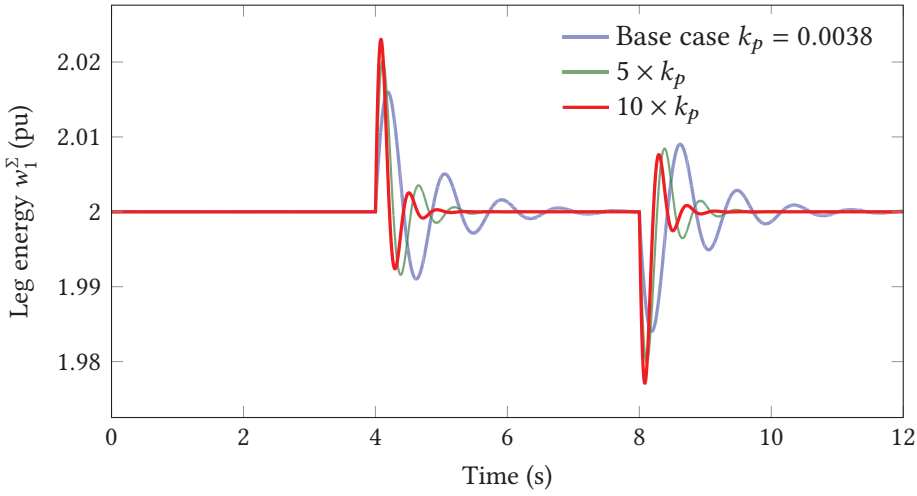

Figure 5.11: Leg energy response to a step change in power for different values of k_p

of the theoretical background for small-signal analysis setup and the implementation details in a numerical software package such as MATLAB®. Application

of the method was demonstrated using an example to highlight a typical analysis process while also showing numerical computation challenges like eigenvalue switching. The method discussed in this section is applied in different parts of this thesis with a goal of model validation and evaluation of controller performance. The latter applies to the validation of a power oscillation damping controller using the energy storage capability of the MMC, which is presented in Chapter 8.

5.4 Power hardware in the loop testing

Performance of a system can be evaluated by using either simulations or laboratory tests. Simulations provide a very flexible, low-risk environment for evaluating different configurations. Laboratory tests, on the other hand, offer exact representation of the system under test, which is modeled with varying levels of approximations in simulations. However, the advantage of accuracy comes at the expense of cost and a reduced degree of freedom in the changing the system configuration. It is, in particular, a challenge to test systems consisting of several components, as is the case in ac/dc grids. Power Hardware In The Loop (PHIL) tests offer a good trade-off between simulations and laboratory tests. Such setups include part of the system (e.g. a converter) as physical equipment, while the remaining part is simulated using a real-time simulator. A brief overview of the basic principle of PHIL testing is presented in the following sections. The PHIL setup used in this thesis is also introduced.

5.4.1 Basic principle

The principle behind PHIL can be demonstrated by taking a simple example of a voltage divider circuit shown in Fig. 5.12. The circuit is split into two parts by the switch S_1. As soon as S_1 closes, the two parts of the circuit become *electrically connected*. The two nodes a and b are said to be *electrically connected* when the voltages at and currents through the points are the same. This is shown mathematically in (5.29).

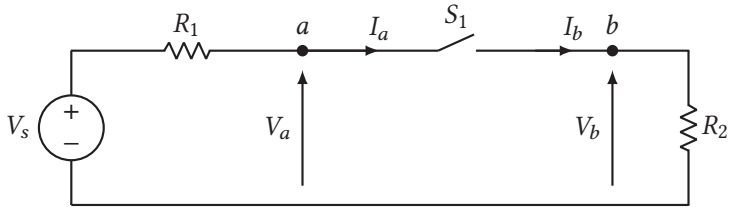

Figure 5.12: A simple voltage divider circuit to illustrate PHIL.

$$V_a = V_b \quad \text{and} \quad I_a = I_b \tag{5.29}$$

The basic idea behind PHIL is that a and b will still be *electrically connected* as

long as (5.29) is satisfied even though there is no physical wire connecting the two points. This implies that the circuit in Fig. 5.13 is equivalent to the one in Fig. 5.12, given that $\bar{I}_b = I_b$ and $\bar{V}_a = V_a$. One of the two parts is often simulated in real-time, while the other one is physically available. For example, V_s and R_1 can be part of the simulated circuit and R_2 is a physical resistor. The voltage at node a in the simulation has to be applied to R_2. This is accomplished by using a power amplifier, which has to be large enough to supply the current $I_b = V_b/R_2$. The current flowing through R_2 is then measured and injected in the simulated circuit. The scaling factors k_a and k_b are used to normalize the data transferred between the simulated and the physical systems in such a way that the two systems can operate at a different voltage and current. Under ideal conditions, this setup will work without any problems. However, there are some practical limitations that introduce challenges in PHIL setups related to instability and loss of accuracy [85]. The main nonidealities are:

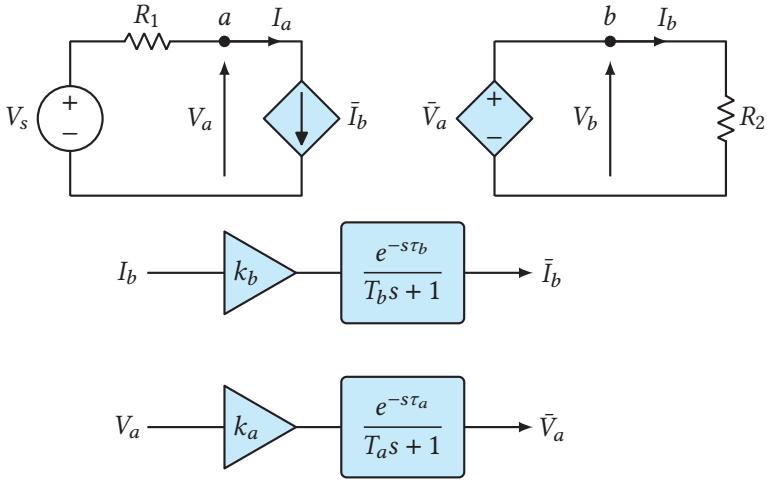

Figure 5.13: Transformation of a voltage divider circuit into a PHIL setup.

1. The power amplifier has limited bandwidth and resolution in terms of magnitude. This introduces distortion on the voltage applied to the physical circuit. This effect is represented by T_a in Fig. 5.13.
2. The measurement system has associated filtering lag (T_b in Fig. 5.13) and distortion due to noise. Additional distortion is introduced by the Analog to Digital Converters (ADCs) used to convert measured signals into digital values that can be processed by the real-time simulator.
3. There are delays due to real-time simulation time step and communication latency. Real-time simulation has a constraint to read its inputs and write to its outputs in synchronism with the external system. These read and write operations are per-

formed within each simulation time step. A consequence of this is the presence of one time step delay between the reading of the measurements to the time when reference voltage is sent to the power amplifier. When the simulated system becomes complex, the simulation time step has to be increased to avoid overrun. Therefore, the effect of the simulation time step delay is more severe when simulating large systems. Communication delays can often be neglected unless the physical distance between the simulator and the physical system is large, leading to time delays in the same order as the simulation time step. The effect of time delays is captured by τ_a and τ_b in Fig. 5.13.

A combination the above-mentioned factors can lead to a loss of accuracy and stability. The accuracy can be checked by comparing against an offline simulation with a much smaller time step. A method for performing stability analysis is presented in the [85].

The dependent current and voltage sources in Fig. 5.13 form a type of interface algorithm called Ideal Transformer Model (ITM) [85]. Several other interface algorithms have been discussed in the literature with the aim of improving accuracy and stability properties [85], [86]. However, the ITM was found to be adequate for the tasks performed in this thesis. Since instability can lead to equipment damage, it is important to perform analyses and simulations at several levels before implementing the PHIL setup. The workflow followed during this thesis is as follows:

Offline simulation: Perform offline simulation with the whole system without including the interface algorithm.

Stability analysis: Analyze stability of the system including the interface algorithm effects.

Offline simulation with non-ideal interface: Perform simulations including the effect of the non-ideal power amplifier and measurement system. The simulation is also run in fixed steps with the target time step to be used in the real-time simulation.

Real-time simulation: Perform real-time simulation using the model obtained from the previous steps. The partitioning of the model should reflect the final partitioning between the simulation and physical systems. The aim of this step is to check stability and to test whether the target time step is large enough for simulation without overrun. If the real-time simulator has multiple cores, the system can be further partitioned into smaller sections that can be run with smaller time steps. If the selected time step is not sufficiently large, a larger time step is selected and the previous two steps are repeated.

PHIL testing: Prepare the hardware setup and perform PHIL test. Soft energization and de-energization procedures should be in place to avoid transient stress on the test system.

5.4.2 PHIL setup

This section discusses the PHIL setup used in this thesis. All the tests were performed in the National Smart Grid Laboratory of Norway [87], which is run jointly by NTNU and SINTEF. The laboratory has a wider array of equipment targeted at several smart grid applications. Of particular interest in this thesis are the real-time simulators, the MMCs, and the power amplifier. Each of these is briefly discussed in the following.

The **real-time simulator** lies at the heart of a PHIL setup, where it facilitates communication between the different components as shown in Fig. 5.14. **OPAL-RT** real-time simulators with several processor cores were available in the lab. One of the cores is dedicated to user interaction, i.e. command interface and plotting, while the others can run parts of a partitioned system or several independent simulations at the same time. The models are built in the MATLAB/Simulink environment, and later compiled in RT-Lab, which is an integrated development environment from OPAL-RT.

Three **MMC** converters with 6 half-bridge, 12 full-bridge, and 18 half-bridge submodules per arm, were available in the laboratory. Each of these converters was rated for 60 kW, 700 Vdc, and 400 Vac. The MMCs also include a three-phase, 400 V:400 V, 50 Hz coupling transformer. The low-level controllers for the MMCs were implemented on Field Programmable Gate Array (FPGA) boards, while the mid- and high-level controllers were run on one of the cores of the real-time simulator. Therefore, the real-time simulator sends insertion indexes over the communication line. Measured voltages and currents are sent in the opposite direction over the link. As mentioned in Chapter 4, the scope of this thesis is limited to mid- and high-level controllers, and hence all the controllers discussed in this thesis are implemented in the real-time simulator.

The **power amplifier** has 6 outputs rated for 700 V which can be configured as either ac or dc. The amplifier has a total capacity of 200 kVA and bandwidth of up to 5 kHz. The real-time simulator sends voltage references to each of the amplifier outputs over the communication line, and in return, the amplifier reports its voltage and current measurement at its outputs. The output configuration used in this thesis is shown in Fig. 5.14.

In summary, the PHIL setup used in this thesis is introduced in this section together with basic theoretical details. The simplest interface algorithm, i.e. ITM, is used because it showed a good performance for the test cases in this thesis. The test setup was used in Chapters 6 and 8 to test control methods at the converter and system levels, respectively.

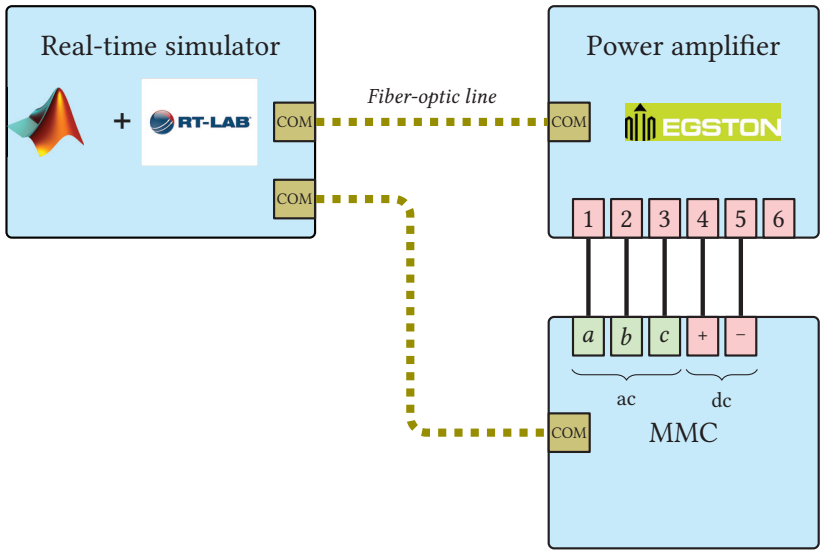

Figure 5.14: Functional block diagram of the laboratory setup for PHIL testing.

5.5 Summary

This chapter presented the methods used in the thesis for analysis and testing. The methods are categorized into three: time-domain simulations, small-signal analysis, and PHIL testing. Each of these categories is presented in detail including a review of the background theory and some practical aspects that might be encountered during the analysis and testing. Time-domain simulation offers a quick way to get test a system both in steady state and transient conditions. Small-signal analysis offers an intuitive way to analyze and understand dynamics of even the most complex systems. Finally, PHIL testing gives a close-to-reality testing environment to validated control algorithms or to analyze the stability of systems when the complete system is either too expensive or too large to realize in the setup. A custom simulation library, suitable for each of the methods, was developed in Simscape. The methods are used in the next chapters of this thesis in a complementary manner where the output of one type of analysis provides information that is not obtained from the others or where one is used as a validation reference for the other.

6
Improved MMC Energy Control

This chapter presents an improved energy control scheme combining the open-loop compensated modulation with closed-loop control of the average energy. In the open-loop compensated modulation, the arm voltages are estimated from the measured currents and the voltage reference coming from the controllers. In the proposed scheme, the estimation is complemented by an online parameter adjustment method which addresses the main limitation of the open-loop method: poor performance due to parameter errors. Detailed development of the method together with validation using both simulations and experimental testing is presented in this chapter. This controller provides the mid-level control which is needed to enable the energy-based services presented in the next two chapters. The discussion in this chapter is supported by the following contributions by the author.

> A. A. Taffese, E. Tedeschi, and E. de Jong, "Arm voltage estimation method for compensated modulation of modular multilevel converters," in *2017 IEEE Manchester PowerTech*, Jun. 2017, pp. 1–6
>
> A. A. Taffese, E. de Jong, S. D'Arco, *et al.*, "Online Parameter Adjustment Method for Arm Voltage Estimation of the Modular Multilevel Converter," *IEEE Transactions on Power Electronics*, vol. 34, no. 12, pp. 12 491–12 503, Dec. 2019, ISSN: 1941-0107

Chapter Outline

6.1 Introduction

The Modular Multilevel Converter (MMC) has a complex structure with large number of Submodules (SMs) and interconnections [20], [23]. Thus, it requires a number of additional controllers [59], [88], [89] compared to the two-level Voltage Source Converter (VSC). As highlighted in Chapter 4, one of these added controllers is responsible for the calculation of insertion indexes, which are signals that dictate the percentage of submodules inserted in a given arm at a given time. Several methods to calculate these indexes have been described in the literature [10], [21], [40], [62], [90], [91] (see Section 4.3.1), each one leading to a different trade-off between simplicity and performance. The simplest option is the direct voltage control (a subset of uncompensated modulation techniques [40]), which assumes that the arm capacitor voltages are ripple-free, and hence, it generates the ac and common-mode references without applying any compensation. This leads to a significant amount of second harmonic ripple in the circulating current, resulting in an increased power loss [58]. Moreover, direct voltage control leads to an uncontrolled coupling between the different harmonic components, which can lead to oscillations during transients [45]. Circulating current suppression controllers [21], [92]–[95] have been proposed to suppress the ripple, but the oscillation problem [45] is not solved by such controllers. Furthermore, it was found that these controllers can negatively interact with other higher-level controllers [46].

Compensated modulation [40] (also referred to as indirect modulation [59]) solves the aforementioned problems by avoiding the need for a circulating current suppression controller. This is achieved by dividing the voltage references, generated by the high-level controllers, by the respective arm voltages to generate the insertion indexes. By doing so, the circulating current ripple can be effectively suppressed without any additional controllers [58]. Applying compensated modulation also limits the coupling among the internal variables of the MMC [40], avoiding the undesired oscillations reported in [45]. The arm voltage can be either measured (closed-loop [58]) or estimated (open-loop [62]) for the purpose of compensated modulation.

The main drawbacks of compensated modulation using measured arm voltages are that the system becomes open-loop unstable [96], and that ideal measurement of the arm voltage is required to achieve effective suppression of the ripple. The first drawback can be overcome by implementing closed-loop control of the sum and difference energy components in a leg. However, the second problem is difficult to address because measurement systems will inevitably exhibit distortion and delay. The open-loop method solves these two problems by using estimated

values of the arm voltages. Furthermore, it has been shown in [64], [65] that the open-loop approach is globally asymptotically stable without a closed-loop arm voltage controller. However, it requires accurate knowledge of the parameters, particularly the arm capacitance and time delay due to measurement and communication. Such a requirement is not easy to satisfy because, even if the parameters are accurately known in the beginning, their values are likely to change as the components age and as the environmental conditions change. For example, capacitance of capacitors can drop by up to 20% over their lifetime [97], [98]. This leads to a mismatch between the actual parameters and the ones known to the arm voltage estimator. Such a mismatch will be referred to as *'parameter error'* henceforth.

The effect of parameter errors is twofold: 1) the average arm energy deviates from the desired reference because of capacitance error, and 2) the ripples in the arm energy are phase shifted and scaled due to capacitance and time delay errors, leading to circulating current ripple. The first effect, in the extreme case, causes the converter to go into over-modulation, even when the value set by the open-loop modulator is within the normal operation range. Ref. [10] overcomes this problem by controlling the average arm energy using the average value of the measured arm voltage, while the ripples are estimated using measured currents and references from high-level controllers. This is possible because the average part is not significantly affected by distortion and delay of the measurement path. Although the method in [10] makes the average part insensitive to parameter errors, effective removal of the circulating current ripple still requires accurate knowledge of the arm capacitance value and of the time delay in the measurement and control path.

This chapter proposes a complete scheme, based on [10] and [15], that includes a method for correcting parameter errors online. The proposed method includes closed-loop control of the average arm energy, and compensated modulation using estimated arm voltages with parameter error correction. The parameter correction method uses the first and second harmonic components (with respect to the fundamental ac side frequency) of the circulating current ripple as feedback. These current components should not be present if the parameters are accurately known. Therefore, the proposed method is a feedback controller that adjusts the estimated parameters to force these two circulating current components to zero. Unlike circulating current suppression controllers, this controller is activated only when the circulating current ripple magnitude exceeds a preset threshold and then deactivated once the parameter correction process is complete. Additionally, the proposed controller can be designed to be significantly slower (10 to 100 times) compared to other controllers leading to sufficient fre-

quency decoupling. This frequency separation is not applicable in circulating current suppression controllers because they have be tuned to be sufficiently fast to keep the circulating current ripple close to zero by actively rejecting disturbances coming from other controllers and changes in operating point. Consequently, the proposed controller can be designed in such a way that it does not negatively interact with other controllers in the system. A similar scheme using closed-loop controllers to compensate for arm inductor parameter variation in the energy balancing of the alternate arm converter has been reported in [99].

The main contributions of this chapter are: 1) development of a complete control scheme for the average arm energy, 2) mathematical derivation of the relation between the parameter errors and the circulating current ripples, 3) development of a method to correct the errors online using a feedback controller, and 4) validation of the proposed scheme using simulations and laboratory experiments. The remainder of this chapter is organized as follows. Section 6.2 presents an average model of the MMC. The arm voltage estimation method adopted in this chapter is dealt with in Section 6.3. Section 6.4 presents design and analysis of the closed-loop control of the average arm energy. Simulation results showing the performance of the basic implementation of the control scheme without parameter correction are presented in Section 6.5. The effect of parameter errors, together with the proposed parameter correction method, is discussed in Section 6.6. Simulation and experimental results are addressed in Section 6.7, followed by conclusion in Section 6.8.

6.2 Average model of the MMC

The MMC can be modeled with different levels of detail depending on the type of study and size of the system [34], [37]–[42], as discussed in Chapter 3. This chapter focuses on the dynamics and the parameter variation effects at the arm-level, which are shown to be adequately represented by average models [33], [34]. Submodule level individual parameter variations are not considered because the collective effect of such variations is captured by an aggregate arm-level variation, which is sufficient for the purpose of the analysis in this chapter. Therefore, an average modeling approach is adopted in this chapter. The circuit diagram of a leg of an MMC given in Fig. 3.1 is repeated here in Fig. 6.1 for quick reference. The figure shows the MMC topology together with the relevant variable definitions and the assumed polarities. All the quantities in this chapter are in Per-unit (pu) with respect to the base values given in Table 6.1 (see Chapter 3 for detailed discussion in per-unit values), where the ac base values are applied to the quantities along the ac loop while the dc ones are used for variables in the dc loop. The arm voltages and currents are considered to be dc side quantities.

The pu base value for the energy, W_b in Table 6.1, is chosen such that the relation between voltage across an arm, v, and energy of the arm, w, becomes $w = v^2$ in per-unit [33]. The model presented in this chapter closely follows the derivation of the energy-based model in Chapter 3 with some differences in the simplifying assumptions. Some of the steps in the derivation are repeated here for quick reference.

The upper and lower arm insertion indexes, n_u and n_l are calculated as depicted in (6.1). The sub-scripts u and l denote the upper and lower arms, respectively. The superscript $(\cdot)^r$ indicates reference values generated by the controllers.

$$n_u = \frac{1}{\hat{v}_{cu}}\left(\frac{1}{2}v_{dc}^r - v_c^r - \frac{1}{2}v_s^r\right) \quad \text{and} \quad n_l = \frac{1}{\hat{v}_{cl}}\left(\frac{1}{2}v_{dc}^r - v_c^r + \frac{1}{2}v_s^r\right) \tag{6.1}$$

where v_{dc}^r is the dc voltage reference (typically set to 1.0 pu), v_c^r is a control signal used to shape the circulating current, and v_s^r is the ac voltage reference. $\hat{v}_{cu}$ and $\hat{v}_{cl}$ are estimates of the arm voltages whose values are selected based on the method used for calculating the insertion indexes. For example, the dc voltage is used in the case of direct voltage control [58] while measured arm voltages (sum of capacitor voltages) are used in compensated modulation [40].

Table 6.1: Per-unit base values.

Description	Value
power	S_b
dc voltage	V_b^{dc}
ac voltage	$V_b^{ac} = \frac{1}{2}V_b^{dc}$
dc current	$I_b^{dc} = S_b/V_b^{dc}$
ac current	$I_b^{ac} = \frac{2}{3}S_b/V_b^{ac}$
dc resistance	$R_b^{dc} = V_b^{dc}/I_b^{dc}$
ac resistance	$Z_b^{ac} = V_b^{dc}/I_b^{dc}$
dc inductance	$L_b^{dc} = R_b^{dc}$
dc capacitance	$C_b^{dc} = 1/R_b^{dc}$
arm energy	$W_b = \frac{1}{2}\frac{C_{SM}}{N}\left(V_b^{dc}\right)^2$

$$l_{dc} = \frac{L_{arm}}{L_b^{dc}} \quad r_{dc} = \frac{R_{arm}}{Z_b^{dc}} \quad C_{arm} = c_a C_b^{dc} = \frac{C_{SM}}{N}$$

Estimates of the arm voltages [62] are used in this chapter. The upper and lower arm currents (Fig. 6.1) can be decomposed into common mode, i_c, and differential mode, i_s, components as shown in (6.2). This decomposition helps in separating

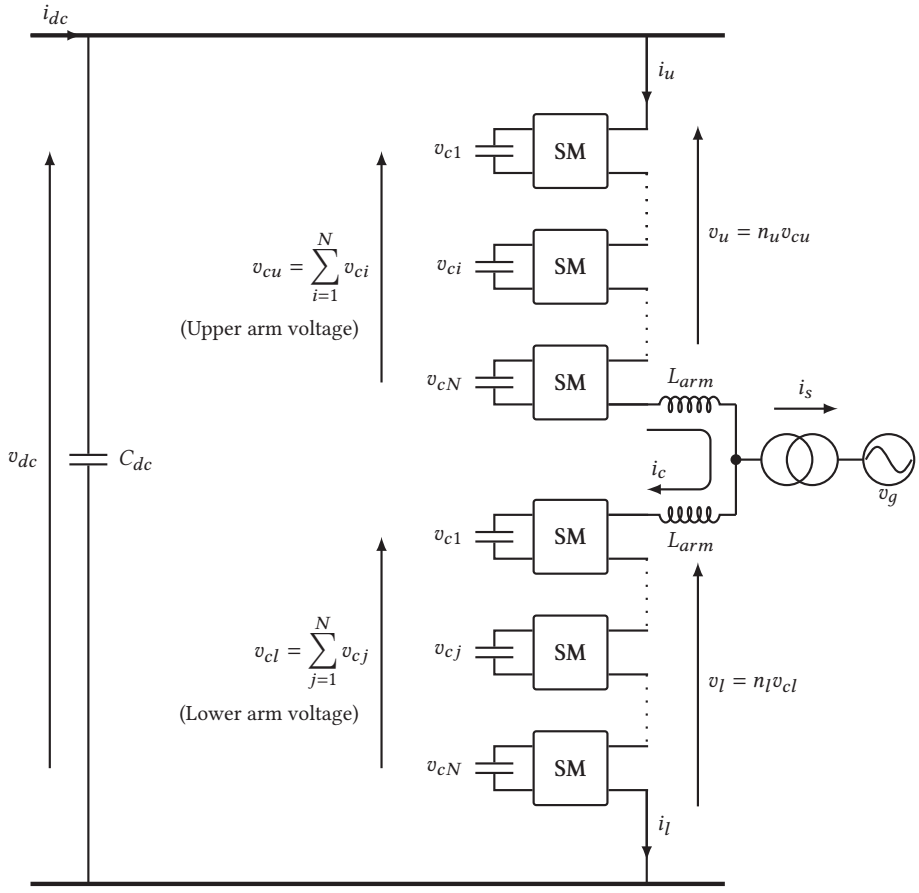

Figure 6.1: Per phase MMC circuit.

the controllers of the ac side from those of the dc side.

$$i_u = i_c + \frac{2}{3} i_s \quad \text{and} \quad i_l = i_c - \frac{2}{3} i_s \tag{6.2}$$

The factor 2/3 is a result of the selected Per-unit conversion (Table 6.4). The energy in the upper and lower arms, w_u and w_l, are governed by (6.3).

$$\begin{aligned} \frac{c_u}{2} \frac{\mathrm{d}}{\mathrm{dt}} w_u &= v_{cu} \cdot n_u \cdot i_u = \frac{v_{cu}}{\hat{v}_{cu}} \left(\frac{1}{2} v_{dc}^r - v_c^r - \frac{1}{2} v_s^r \right) \left(i_c + \frac{2}{3} i_s \right) \\ \frac{c_l}{2} \frac{\mathrm{d}}{\mathrm{dt}} w_l &= v_{cl} \cdot n_l \cdot i_l = \frac{v_{cl}}{\hat{v}_{cl}} \left(\frac{1}{2} v_{dc}^r - v_c^r + \frac{1}{2} v_s^r \right) \left(i_c - \frac{2}{3} i_s \right) \end{aligned} \tag{6.3}$$

where c_u and c_l are the upper and lower arm capacitances in pu. In Chapter 3, the arm capacitors of the upper and lower arms were assumed to be equal. Equation (6.3) can be transformed into the form shown in (6.4) where the upper and lower energy terms are replaced by their sum, $w^\Sigma = w_u + w_l$, and difference, $w^\Delta = w_u - w_l$, and the common mode voltage is defined as $v_{cm}^r = (v_{dc}^r - 2v_c^r)/2$.

$$\begin{aligned} \frac{1}{2} \frac{\mathrm{d}}{\mathrm{dt}} w^\Sigma &= \left(\frac{v_{cu}}{c_u \hat{v}_{cu}} + \frac{v_{cl}}{c_l \hat{v}_{cl}} \right) \left(v_{cm}^r i_c - \frac{1}{3} v_s^r i_s \right) + \left(\frac{v_{cu}}{c_u \hat{v}_{cu}} - \frac{v_{cl}}{c_l \hat{v}_{cl}} \right) \left(\frac{2}{3} v_{cm}^r i_s - \frac{1}{2} v_s^r i_c \right) \\ \frac{1}{2} \frac{\mathrm{d}}{\mathrm{dt}} w^\Delta &= \left(\frac{v_{cu}}{c_u \hat{v}_{cu}} - \frac{v_{cl}}{c_l \hat{v}_{cl}} \right) \left(v_{cm}^r i_c - \frac{1}{3} v_s^r i_s \right) + \left(\frac{v_{cu}}{c_u \hat{v}_{cu}} + \frac{v_{cl}}{c_l \hat{v}_{cl}} \right) \left(\frac{2}{3} v_{cm}^r i_s - \frac{1}{2} v_s^r i_c \right) \end{aligned} \tag{6.4}$$

Dynamics of the circulating current can similarly be derived as shown in (6.5).

$$l_{dc} \frac{\mathrm{d}}{\mathrm{dt}} i_c = \frac{1}{2} v_{dc} - \frac{1}{2} \left(\frac{v_{cu}}{\hat{v}_{cu}} + \frac{v_{cl}}{\hat{v}_{cl}} \right) v_{cm}^r + \frac{1}{4} \left(\frac{v_{cu}}{\hat{v}_{cu}} - \frac{v_{cl}}{\hat{v}_{cl}} \right) v_s^r - r_{dc} i_c \tag{6.5}$$

where l_{dc} and r_{dc} are the arm inductance, L_{arm}, and resistance, R_{arm}, in pu with the dc base values in Table 6.1. Equations (6.4) and (6.5) constitute a third-order dynamic arm model that will be used in this chapter.

6.3 Estimation of the arm voltages

The ripple in the arm voltages can be estimated from the measured currents, and reference voltages obtained from the controllers. The implementation presented in [34] uses closed-form expressions of per-phase ripple estimates. Alternative methods have been presented in [21], [100], which include a method that extracts the ripples from the measured arm voltages using band-pass filters [21]. This approach is attractive from the perspective of minimizing computation and avoiding nonlinear operations [21]. The implementation in this chapter is based on the closed-form expressions [34] because the same equations will be used in the derivation of the algorithm for parameter error correction in Section 6.6. However, the results obtained in this chapter are equally applicable to the band-pass

filter approach. The following assumptions [62] are made to simplify the derivation:

A.1 The ac voltages and currents are purely sinusoidal waveforms at fundamental frequency. Additionally, the grid frequency is assumed to be constant over time, which implies that all the harmonic components are also constant frequency.

A.2 The dc quantities and peak values of the ac quantities change slowly compared to the fundamental period. Consequently, they are treated as constants in the derivation.

A.3 The estimated arm capacitor voltages converge to the actual values in steady-state (i.e. $\hat{v}_{cu,l} = v_{cu,l}$).

Assumption **A.1** is reasonable because the MMC is capable of producing near-sinusoidal waveforms. Moreover, it can be shown that the impact of harmonics in the ac quantities on the arm voltage estimator is negligible under normal operating conditions where the THD is low (for example below 1.5% according to IEEE 519 [101]). The second assumption is not valid during fast transients, but this does not have a significant impact; its effect will be shown using simulation and experimental results in Section 6.7. Assumption **A.2** is acceptable because the grid quantities are assumed not to change abruptly under normal operation. Assumption **A.3** is affected by the presence of parameter errors and will be discussed in Section 6.6. The phase voltage reference and the phase current are given by (6.6) where V_s^r and I_s are peak values of the phase voltage reference and phase current, respectively. The quantities ϕ_v and ϕ_i are phase angle offsets of the voltage and current, respectively, with respect to a common angle reference. For the case of a balanced three-phase system, phases b and c would have additional phase shifts of $-2\pi/3$ and $2\pi/3$, respectively.

$$v_s^r = V_s^r \cos(\omega t + \phi_v) \quad \text{and} \quad i_s = I_s \cos(\omega t + \phi_i) \tag{6.6}$$

Since all the ac components in the system have constant frequency and amplitude in steady state (Assumptions **A.1** and **A.2**), they can be converted into complex constants, at their respective frequencies, in phasor domain. Phasor form is chosen because it makes the derivation applicable to both single-phase and balanced three-phase systems. For balanced three-phase systems, these phasors correspond to the dq values where the d and q components are the real and imaginary parts, respectively. The phasors will be denoted by boldface capital letters with arrows on top.

Because of Assumption **A.3**, the energy dynamics given by (6.4) simplify to (6.7).

$$\begin{aligned}\frac{\mathrm{d}}{\mathrm{dt}}w^{\Sigma} &= 2b^{\Sigma}\left(v_{cm}^{r}i_{c} - \frac{1}{3}v_{s}^{r}i_{s}\right) + 2b^{\Delta}\left(\frac{2}{3}v_{cm}^{r}i_{s} - \frac{1}{2}v_{s}^{r}i_{c}\right)\\ \frac{\mathrm{d}}{\mathrm{dt}}w^{\Delta} &= 2b^{\Delta}\left(v_{cm}^{r}i_{c} - \frac{1}{3}v_{s}^{r}i_{s}\right) + 2b^{\Sigma}\left(\frac{2}{3}v_{cm}^{r}i_{s} - \frac{1}{2}v_{s}^{r}i_{c}\right)\end{aligned} \tag{6.7}$$

where $b^{\Sigma} = \left(\frac{1}{c_u} + \frac{1}{c_l}\right)$ and $b^{\Delta} = \left(\frac{1}{c_u} - \frac{1}{c_l}\right)$. It should be noted that (6.7) is still valid when there are parameter errors, because the effect of the mismatch between the estimates, $\hat{v}_{cu,l}$, and the actual arm voltages, $v_{cu,l}$, has a negligible impact on the energy dynamic equations. This can be verified by linearizing the divisions in (6.4) and evaluating the contribution of the mismatches. Consequently, (6.7) is used in the remainder of this chapter. Depending on the harmonic content in i_c, different components appear in w^{Σ} and w^{Δ}. In this chapter the circulating current is assumed to have a dc component, i_{c0}, a first harmonic, i_{c1}, and a second harmonic, i_{c2}. The other harmonic components are not included because their magnitudes are assumed to be negligible compared to the aforementioned components. As a result, w^{Σ} and w^{Δ} can be written in the form shown in (6.8) by expanding the ac components in (6.7).

$$\begin{aligned}w^{\Sigma} &= 2b^{\Sigma}\Big(h_{20} + h_{11} + h_{22}\Big) + 2b^{\Delta}\Big(h_{10} + h_{12} + h_{21} + h_{32}\Big) + 2w^{0}\\ w^{\Delta} &= 2b^{\Delta}\Big(h_{20} + h_{11} + h_{22}\Big) + 2b^{\Sigma}\Big(h_{10} + h_{12} + h_{21} + h_{32}\Big)\end{aligned} \tag{6.8}$$

where h_{kp} is the k^{th} harmonic energy component caused by the p^{th} harmonic of i_c. For instance, h_{21} is a second harmonic component due to the first harmonic of i_c (i_{c1}). Table 6.2 shows the definitions of the harmonic components together with their corresponding phasors. $\vec{\mathbf{V}}_s^r$ and $\vec{\mathbf{I}}_s$ are the ac voltage reference and ac current in phasor form. v_{cm}^r and i_{c0} are assumed to be dc quantities, so the notation for these quantities does not change when transforming to phasor form. The phasor equations in Table 6.2 are obtained by transforming the terms in the brackets of (6.7) into phasor form followed by time-integration, which, in phasor domain, is equivalent to division by $jk\omega$ where k is the harmonic order. Products of two time-domain sinusoids such as $v_s^r i_s$ are expanded using the trigonometric angle addition formula before conversion to phasor form (i.e. $v_s^r i_s = \frac{1}{2}V_s^r I_s\left(\cos(\phi_v - \phi_i) + \cos(2\omega t + \phi_v + \phi_i)\right)$, which translates to a dc component, $\frac{1}{2}\Re\{\vec{\mathbf{V}}_s^r\vec{\mathbf{I}}_s^*\}$, and a second harmonic phasor, $\frac{1}{2}\vec{\mathbf{V}}_s^r\vec{\mathbf{I}}_s$). Equation (6.8) and Table 6.2 describe a general case where the circulating current has non-zero ripple, which happens only when there are parameter errors. This will be revisited in Section 6.6. However, for the purpose of deriving the arm voltage estimator

Table 6.2: Definition of harmonic components.

Time Domain	Phasor
$h_{10} = \int \left(\frac{2}{3} v_{cm}^r i_s - \frac{1}{2} v_s^r i_{c0}\right) \mathrm{d}t$	$\vec{\mathbf{H}}_{10} = \frac{2}{j3\omega} v_{cm}^r \vec{\mathbf{I}}_s - \frac{1}{j2\omega} \vec{\mathbf{V}}_s^r i_{c0}$
$h_{20} = -\frac{1}{3} \int v_s^r i_s \, \mathrm{d}t$	$\vec{\mathbf{H}}_{20} = -\frac{1}{j12\omega} \vec{\mathbf{V}}_s^r \vec{\mathbf{I}}_s$
$h_{11} = \int v_{cm}^r i_{c1} \, \mathrm{d}t$	$\vec{\mathbf{H}}_{11} = \frac{1}{j\omega} v_{cm}^r \vec{\mathbf{I}}_1$
$h_{21} = -\frac{1}{2} \int v_s^r i_{c1} \, \mathrm{d}t$	$\vec{\mathbf{H}}_{21} = -\frac{1}{j8\omega} \vec{\mathbf{V}}_s^r \vec{\mathbf{I}}_1$
$h_{12} = -\frac{1}{2} \int v_s^r i_{c2} \, \mathrm{d}t$	$\vec{\mathbf{H}}_{12} = -\frac{1}{j4\omega} \vec{\mathbf{V}}_s^{r*} \vec{\mathbf{I}}_2$
$h_{22} = \int v_{cm}^r i_{c2} \, \mathrm{d}t$	$\vec{\mathbf{H}}_{22} = \frac{1}{j2\omega} v_{cm}^r \vec{\mathbf{I}}_2$
$h_{32} = -\frac{1}{2} \int v_s^r i_{c2} \, \mathrm{d}t$	$\vec{\mathbf{H}}_{32} = -\frac{1}{j12\omega} \vec{\mathbf{V}}_s^r \vec{\mathbf{I}}_2$

equations, the parameters are assumed to be known, which means that there is no circulating current ripple. This implies that all the harmonics due to the first and second harmonic components of the circulating current are zero (i.e. $h_{11} = h_{21} = h_{12} = h_{22} = h_{32} = 0$). Hence, the estimates of the sum and difference energies, $\hat{w}^{\Sigma}$ and $\hat{w}^{\Delta}$, can be written in the form shown in (6.9).

$$\hat{w}^{\Sigma} = 2w_0 + 2\hat{b}^{\Sigma}\hat{h}_{20} + 2\hat{b}^{\Delta}\hat{h}_{10} \quad \text{and} \quad \hat{w}^{\Delta} = 2\hat{b}^{\Sigma}\hat{h}_{10} + 2\hat{b}^{\Delta}\hat{h}_{20} \tag{6.9}$$

where $\hat{h}_{10}$ and $\hat{h}_{20}$ are the first and second harmonic components, respectively, in time domain. w_0 is the average (dc) component, $\hat{b}^{\Sigma}$ and $\hat{b}^{\Delta}$ the arm capacitance parameters known to the estimator. Phasor domain representation of $\hat{h}_{10}$ and $\hat{h}_{20}$ are $\hat{\vec{\mathbf{H}}}_{10}$ and $\hat{\vec{\mathbf{H}}}_{20}$, respectively, which are defined in (6.10).

$$\hat{\vec{\mathbf{H}}}_{10} = \frac{1}{j\omega}\left(\frac{2}{3} v_{cm}^r \vec{\mathbf{I}}_s - \frac{1}{2} i_{c0} \vec{\mathbf{V}}_s^r\right) \quad \text{and} \quad \hat{\vec{\mathbf{H}}}_{20} = \frac{-1}{12j\omega} \vec{\mathbf{V}}_s^r \vec{\mathbf{I}}_s \tag{6.10}$$

The corresponding time-domain ripples, $\hat{h}_{10}$ and $\hat{h}_{20}$, are obtained by inverse transforming (6.10). For the case of balanced three-phase systems, this is done by applying *dq* to *abc* transformations at fundamental frequency for $\hat{\vec{\mathbf{H}}}_{10}$, and at second harmonic for $\hat{\vec{\mathbf{H}}}_{20}$. Since $\hat{\vec{\mathbf{H}}}_{20}$ is a negative sequence signal, phases *b* and *c* of the output of the second harmonic transformation should be swapped. Then, the sum and difference energies are computed using (6.9). Finally, the arm voltages are computed from the corresponding energy term as shown in (6.11). The complete structure of the arm voltage estimator, together with the average energy controller, for a balanced three-phase system is shown in Fig. 6.2. Although the system is balanced with respect to the ac current and voltages, the estimator parameters, $\hat{b}^{\Sigma}$ and $\hat{b}^{\Delta}$, should be computed per phase since the capacitance of the

arms can be different because of tolerance values.

$$\hat{v}_{cu} = \sqrt{\hat{w}_u} = \sqrt{\frac{\hat{w}^{\Sigma} + \hat{w}^{\Delta}}{2}} \qquad \hat{v}_{cl} = \sqrt{\hat{w}_l} = \sqrt{\frac{\hat{w}^{\Sigma} - \hat{w}^{\Delta}}{2}} \tag{6.11}$$

The average (dc) component of $\hat{w}^{\Sigma}$ can be obtained by averaging of the arm voltages at the leg level (per-phase) or converter level. Since the converter is assumed to be symmetric, converter level averaging is used. Therefore, the measured dc energy, w_m^0 in Fig. 6.2, is obtained by averaging the six arm energies as given by (6.12). This effectively extracts the average value from the measurement. Then a low-pass filter is applied to the signal to remove noise, distortion, and fast transients. The measured dc circulating current, i_{c0m} in Fig. 6.2, is obtained by averaging the arm current as shown in (6.12).

$$w_{0m} = \frac{1}{6}\sum_{x,y} v_{cxy}^2 \quad i_{c0m} = \frac{1}{6}\sum_{x,y} i_{xy} \tag{6.12}$$

$$\text{where} \quad x \in \{u, l\} \quad \textit{and} \quad y \in \{a, b, c\} \tag{6.13}$$

The average energy is controlled in closed-loop using cascaded controllers with an inner current-loop. More details on this are given in the next section. There are some implementation aspects that affect the performance of the arm voltage estimator. These aspects are discussed in the following.

Under ideal conditions, i.e. all the parameters are accurately known and all the signals are instantaneously available, the arm energies can be perfectly estimated using (6.9) to (6.11) as was shown in [34], [62], [64]. However, there will inevitably be parameter errors and measurement lags in practical systems. Sensitivity of the average energy to parameter variations is reduced by employing closed-loop energy control. Another effect that can be easily compensated for is distortion of the ac signals by the measurement filters.

First-order measurement filters are included in the block diagram, (Fig. 6.2), to represent anti-aliasing and noise smoothing filters that are present in practical implementations. These filters result in phase and gain change in the ac signals. Under steady state and slowly changing conditions, these can be compensated for by simple gain and phase compensation, as shown in (6.14) and (6.15), respectively. A similar approach can be applied to compensate for communications delays on the signals.

$$G_{comp} = \sqrt{(\omega T_x)^2 + 1} \tag{6.14}$$

$$\phi_{comp} = \arctan(\omega T_x) \tag{6.15}$$

where T_x is the filter time constant and ω is the ac frequency. G_{comp} multiplies the signal magnitude after the filter and ϕ_{comp} gets added to the phase angle.

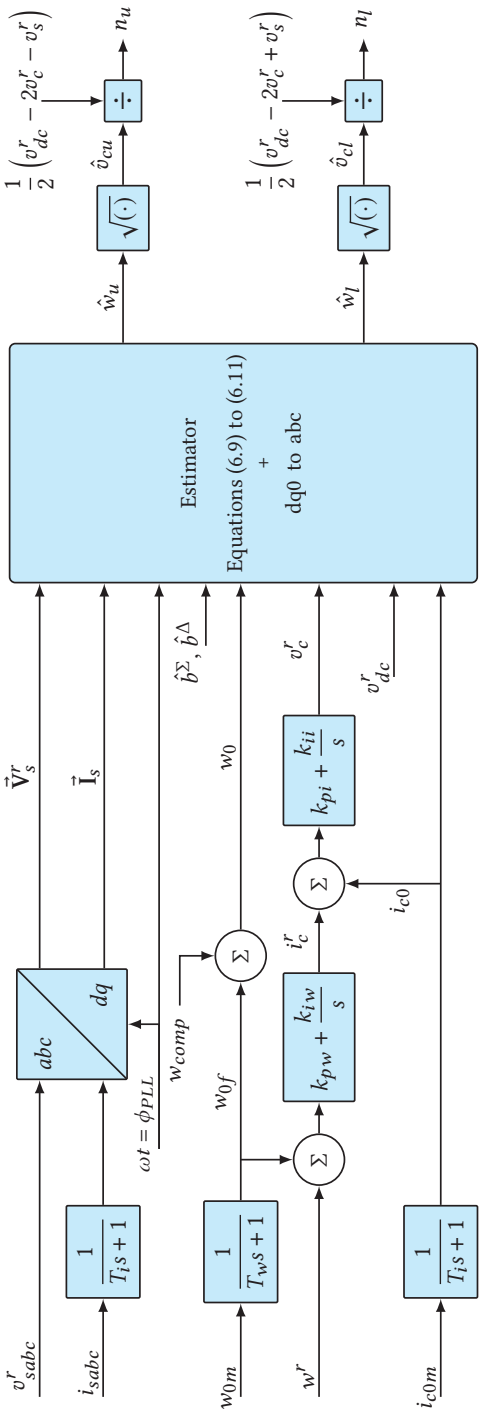

Figure 6.2: Block diagram of the arm voltage estimation method with average energy control.

Uncertainty in T_x and ω might prevent prefect compensation. However, as will be shown using simulations in Section 6.5, its impact is not significant.

6.4 Average energy control

This section deals with the average arm control design. This is an extension of the arm energy control method presented in Chapter 4. A linearized analysis is used to identify and mitigate the negative effect of the filter used to extract the average energy.

6.4.1 Control design

A simplified model shown in Fig. 6.3, based on the assumptions in Section 6.3 and the equations (6.3) to (6.5), is used for control design. It is assumed that $\left(v_d^r - 2v_c^r\right) \approx V_{dc}$, which is reasonable under normal operation. Moreover, the capacitances of the upper and lower arms are assumed to be equal to c_a. The boldface letters above the blocks will be used to refer to the transfer functions. This structure is well suited for Modulus and Symmetric optimum tuning techniques [56]. $\mathbf{C_i}$ is tuned using modulus optimum while $\mathbf{C_w}$ is designed using symmetric optimum method. The impact of the simplifying assumptions will be investigated using simulations in Section 6.5.

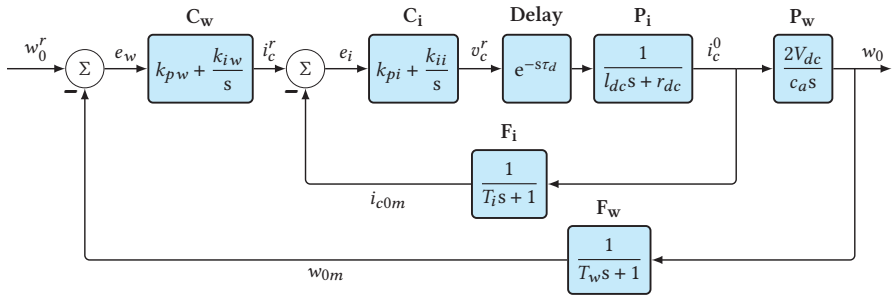

Figure 6.3: A block diagram of a cascaded arm energy control model.

6.4.2 Analysis

The analysis in this section is performed to study the effect of assuming that the estimator is ideal (Assumption **A.3** in Section 6.3). In order to simplify the analysis, only the average components will be considered. Furthermore, the difference in average energies between the upper and lower arms is considered to be zero following a similar argument as [34]. This permits the simplification in (6.16).

$$\frac{v_{cu}}{\hat{v}_{cu}} \approx \frac{v_0}{\hat{v}_0} \approx \frac{v_{cl}}{\hat{v}_{cl}} \tag{6.16}$$

where v_0 and $\hat{v}_0$ are average components of the actual and estimated voltages. Taking this into consideration and averaging the arm energies results in (6.17) and (6.18) where w_0 is the average energy.

$$\frac{\mathrm{d}}{\mathrm{dt}} w_0 = \frac{2}{c_a} \frac{v_0}{\hat{v}_0} \left[\left(\frac{1}{2} v_{dc}^r - v_c^r \right) i_{c0} - \frac{1}{6} \Re\{ \vec{\mathbf{v}}_s^r \vec{\mathbf{i}}_s^* \} \right] \tag{6.17}$$

$$l_{dc} \frac{\mathrm{d}}{\mathrm{dt}} i_{c0} = \frac{1}{2} v_{dc} - \frac{1}{2} \frac{v_0}{\hat{v}_0} v_{dc}^r + \frac{v_0}{\hat{v}_0} v_c^r - r_{dc} i_{c0} \tag{6.18}$$

Substituting the arm voltages, v_0 and $\hat{v}_0$ with the corresponding energies, $\sqrt{w_0}$ and $\sqrt{\hat{w}_0}$, and linearizing (6.17) and (6.18) around a steady-state operating point gives (6.19) and (6.20).

$$\frac{\mathrm{d}}{\mathrm{dt}} w_0 = \frac{2}{c_a} \left[\left(\frac{1}{2} v_{dc}^r - v_c^r \right) i_{c0} - \frac{1}{6} \Re\{ \vec{\mathbf{v}}_s^r \vec{\mathbf{i}}_s^* \} \right] \tag{6.19}$$

$$l_{dc} \frac{\mathrm{d}}{\mathrm{dt}} i_{c0} = v_c^r - r_{dc} i_{c0} - k \left(w_0 - \hat{w}_0 \right) \tag{6.20}$$

where k is a positive linearization constant. It can be seen that there is an equivalent proportional energy controller with gain k inherently in the system. This fact is the foundation of the open-loop approach. The parameter k is a function of system parameters and initial conditions. Therefore, the convergence speed cannot be controlled. To solve this problem, a closed-loop control is needed. First, the current controller, $\mathbf{C}_i$ from Fig. 6.3, is incorporated into the linear model of (6.19) and (6.20). In doing so, the transfer function from current reference, i_c^r to the average energy, w_0, becomes:

$$\frac{w_0}{i_c^r} = \frac{v_{dc} \mathbf{P}_i \mathbf{C}_i}{c_a s \left(1 + \mathbf{P}_i \mathbf{C}_i \mathbf{F}_i \right) + k \left(1 - \mathbf{G} \right) \mathbf{P}_i} \tag{6.21}$$

where $\mathbf{G}$ is a transfer function relating $\hat{w}_0$ to w_0, i.e. $\hat{w}_0 = \mathbf{G} w_0$. When $\mathbf{G} = 1$, (6.21) reduces to the transfer function obtained from the block diagram of Fig. 6.3. Therefore, the controller design presented in Section 6.4.1 is valid only when $\mathbf{G} = 1$. This will affect the controller performance and will be addressed here. From (Fig. 6.2) and definition of $\mathbf{G}$, the relation in (6.22) can be found.

$$\hat{w}_0 = \mathbf{F}_w w_0 + w_{comp} = \mathbf{G} w_0 \tag{6.22}$$

where w_{comp} is the compensation signal to improve the controller performance. $\mathbf{F}_w$ is the energy filter transfer function, (Fig. 6.3). The value of w_{comp} that will result in $\mathbf{G} = 1$ is given in (6.23). This is equivalent to computing the derivative of w_0, multiplying it by the energy filter time constant, T_w, and passing it through the energy filter.

$$w_{comp} = \left(1 - \mathbf{F}_w \right) w_0 = T_w s w_0 \mathbf{F}_w \tag{6.23}$$

However, computing direct derivative leads to noise amplification. So a better alternative is to estimate the derivative using the measurements that are already available. In such a way the complete compensation signal is given by (6.24).

$$w_{comp} = \frac{2T_w}{c_a}\left[\left(\frac{1}{2}v_{dc}^r - v_c^r\right) i_{c0} - \frac{1}{6}\Re\{\vec{\mathbf{v}}_s^r \vec{\mathbf{i}}_s^*\}\right] \cdot \mathbf{F}_w \tag{6.24}$$

This value of w_{comp} will cancel the effect of the energy filter and improve the performance of the controller. The next section will present simulation results that support this analysis.

In summary, the analysis in this section has revealed that the energy filter can affect dynamic performance of the average energy controller. The main purpose of the filter is to remove noise and distortion from the measured arm energy. It also decouples the average energy from the measured one at high frequencies, because the filter has high attenuation at high frequencies. Thus, the proposed method appears as a closed-loop controller at low frequencies, while it behaves like the open-loop method at high frequencies, which is proven to be asymptotically stable [64]. Therefore, the filter plays an important role in the determining the behavior of the system, and it cannot be removed to improve the dynamic performance at low frequencies. A compensation term based on estimated derivative is proposed in this section to reduce the effect of the filter on the dynamic performance.

6.5 Simulation results

Simulation results showing the performance of the proposed arm voltage estimation and control method are presented in this section. The system under test is a three-phase MMC HVDC terminal connected to a droop (1%) controlled dc bus and a strong ac grid via a transformer. The simulation is performed in Matlab/SIMULINK environment. The parameters, Table 6.3, and the modeling approach are adopted from [102]. The dc voltage reference is set at $v_{dc}^r = 1.0$. The average arm voltage is set to 15% above the nominal dc voltage to account for redundant submodules. The results show the effect of: (1) energy filter compensation, (2) ac filter lag compensation, and (3) parameter error in capacitance value. The simulation includes two disturbances: (1) a step change in energy reference from $w^r \approx 1.31$ to $w^r \approx 1.18$ pu at $t = 2$ sec, and (2) a step change in ac power from 0.89 pu (800 MW) to 0.45 pu (400 MW) at $t = 7$ sec.

Fig. 6.4 shows a result of the basic implementation by using (6.9) to (6.11) directly. The average energy exhibits poorly damped oscillation. As discussed in Section 6.4.2, this is caused by the lag in the energy filter, T_w. It can be effectively

Table 6.3: Parameters used for simulation.

Parameter	Value
Base apparent power, S_b	900 MVA
Base dc voltage, V_b^{dc}	640 kV
Frequency, ω	$2\pi 50$ rad/s
Arm capacitance, C_{arm}	29 μF
Arm inductance, L_{arm}	84 mH
Arm resistance, R_{arm}	0.885 Ω
Transformer reactance, X_t	17.7 Ω
Transformer resistance, R_t	1.77 Ω
Voltage filter time constant, T_v	500 μs
Current filter time constant, T_i	500 μs
Energy filter time constant, T_w	10 ms
Energy controller proportional constant, k_{pw}	13.6
Energy controller integral constant, k_{iw}	0.6
Circ. current controller proportional constant, k_{pcc}	0.046
Circ. current controller integral constant, k_{icc}	0.486
Simulation time step, T_{sim}	100 μs
Controller sampling time, T_s	200 μs

*Circ. = Circulating.

damped by applying the proposed energy filter compensation, see Fig. 6.5. As can be seen from the insets of Figs. 6.4 and 6.5 there is a clearly visible time delay in the estimated signal which is caused by the ac filters, T_i and T_v. As proposed in Section 6.3, a steady-state compensation for the filter gains and phases is applied to obtain the result in Fig. 6.6 where the measured and estimated values are well-matched.

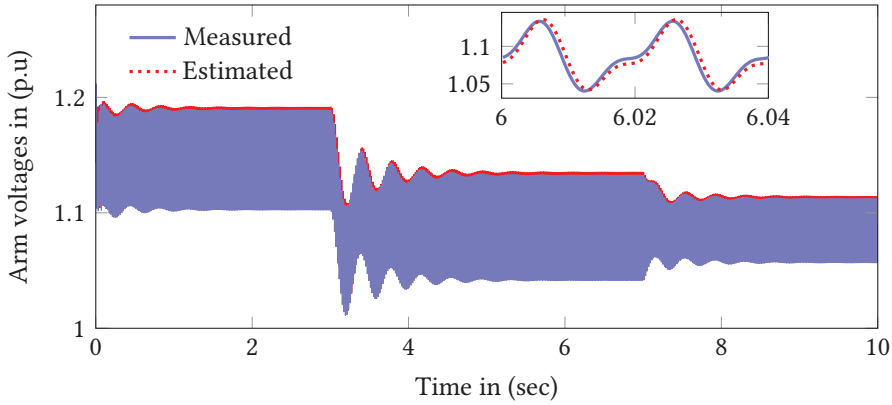

Figure 6.4: Arm voltage using the basic implementation of the estimation using (6.9) to (6.11).

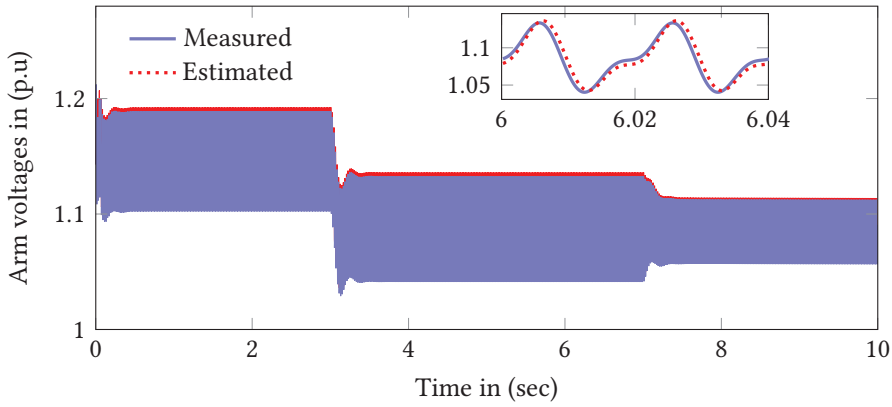

Figure 6.5: Arm voltage after applying energy filter compensation.

The effect of error in capacitance value is displayed in Figs. 6.7 and 6.8, where the considered value is 20% lower than the actual one. Despite a slight reduction in damping, the average energy is not affected by the parameter error, (Fig. 6.8). The effect is visible on the circulating current, Fig. 6.9. The error has caused as second harmonic circulating current with a magnitude approximately 30% of the dc value. The ripple is also present when the ac filter delays are not compensated,

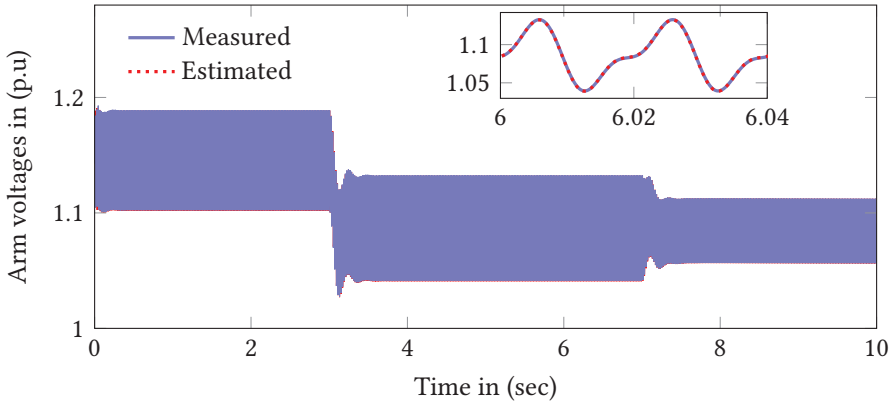

Figure 6.6: Arm voltage after applying both energy and ac filter compensations.

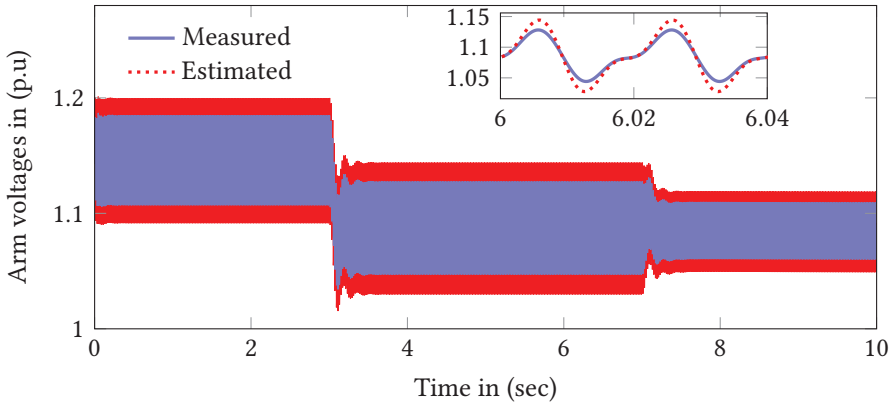

Figure 6.7: Arm voltage after applying both energy and ac filter compensations and 20% parameter error in capacitance.

Fig. 6.9. The 80% compensation case shows the impact of uncertainty in T_i when it is known within ±20%. The result shows ±20% that uncertainty in time constant does not significantly affect the ripple in the circulating current. However, ignoring delays caused significant ripple in the circulating current. Fig. 6.10 shows ac power and dc voltage signal when there is parameter error. This confirms that the converter continues to operate normally when parameter errors occur.

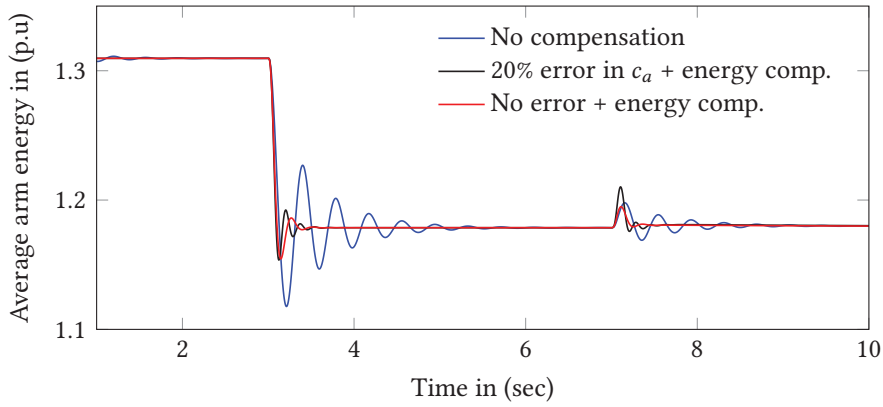

Figure 6.8: Impact of compensation and parameter error on average arm energy.

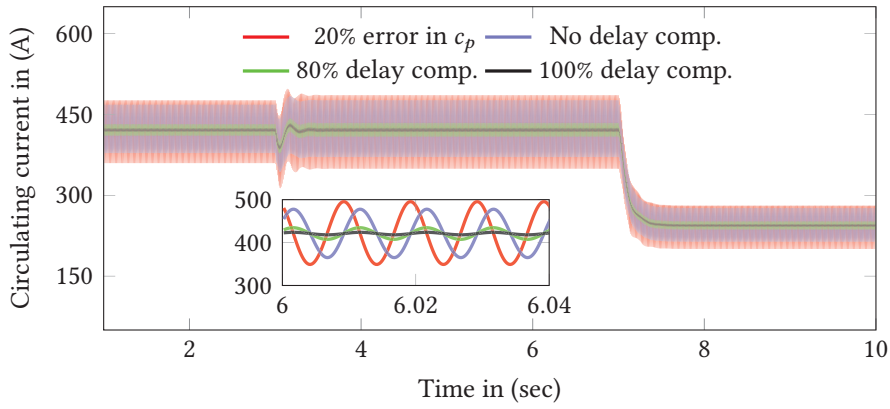

Figure 6.9: Circulating current under 20% parameter error in capacitance and different levels of delay compensation.

The simulation results have shown that the arm voltage estimation and control method proposed in Sections 6.3 and 6.4 have good performance when the parameters, such as capacitance and delay, are accurately known. Parameter errors cause circulating current ripple, which would otherwise be zero. It was also shown that the average energy controller response is less sensitive to parameter

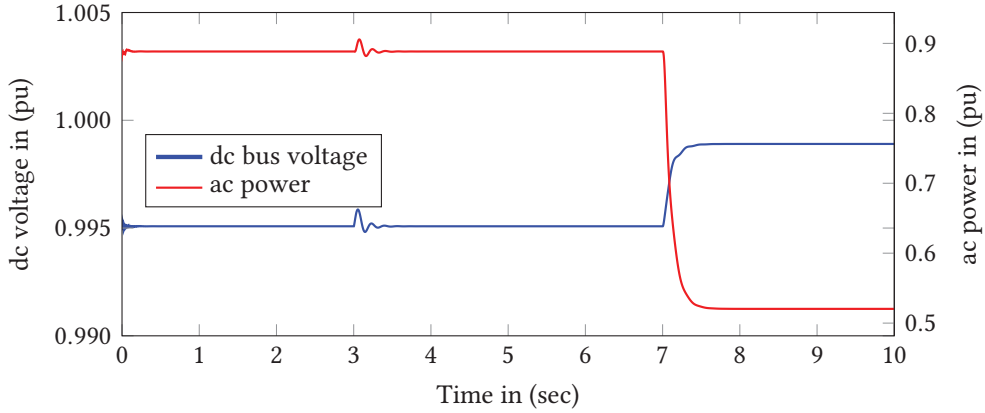

Figure 6.10: dc voltage and ac power when operating with 20% parameter error in capacitance.

errors. The energy filter lag causes an oscillatory response even when the controller is designed considering the effect of the filter. This is rectified by using the energy filter compensation proposed in Section 6.4. In practical applications, parameter errors are inevitable, which means that the basic implementation of the estimator will suffer from low performance in terms of eliminating the circulating current ripple. The next section is dedicated to the development of a method to identify the parameters by using the circulating current ripple as feedback. The resulting complete system will then be robust to parameter variations due to aging and change in operating points.

6.6 Parameter error correction

This section presents a method that automatically corrects parameter errors, capacitance and time delay, by monitoring the second harmonic ripple in the circulating current. First, the derivation of the relation between the circulating current and the parameter errors will be presented. Capacitance values change over time because of environmental stress and aging [97]. The time delay, denoted by t_d, accounts for communication delays, filter lags, and any delay introduced when sampling analog signals. The derivation will be based on the circulating current dynamic equation, (6.5). Any difference between the estimated and the actual arm voltages results in circulating current ripples. The right-hand side of (6.5) is a nonlinear function of the arm voltages because of the divisions of the arm voltages by their respective estimates. In order to simplify the analysis, these equations can be linearized assuming that the ripple is a small percentage of the average arm voltage. This is achieved by using (6.25), which is derived by assuming that the upper and lower arm energies are balanced at a steady-state operating

point ($W^0 = \hat{W}^0$).

$$\frac{v_{cu/l}}{\hat{v}_{cu/l}} = \sqrt{\frac{w_{u/l}}{\hat{w}_{u/l}}} \approx \frac{1}{2W^0}\left[w_{u/l} - \hat{w}_{u/l}\right] + 1 \tag{6.25}$$

After substituting (6.25) into (6.5) and transforming to the Σ and Δ energy terms, the circulating current dynamics become the one given by (6.26).

$$l_{dc}\frac{\mathrm{d}}{\mathrm{dt}}i_c = \frac{1}{2}v_{dc} - v_{cm}^r - \frac{1}{4W^0}\left[\left(w^\Sigma - \hat{w}^\Sigma\right)v_{cm}^r - \frac{1}{2}\left(w^\Delta - \hat{w}^\Delta\right)v_s^r\right] - r_{dc}i_c \tag{6.26}$$

Equation (6.26) shows that i_c can be split into two components: a component purely due to the control signal v_{cm}^r, and a component also influenced by estimation errors, $w^\Sigma - \hat{w}^\Sigma$ and $w^\Delta - \hat{w}^\Delta$. The control signal v_{cm}^r does not normally include harmonics; therefore, any harmonic component in i_c is due to the estimator error. The first and second harmonics of i_c will be derived in this section. Since the procedure is similar for both harmonics, the derivation of the second harmonic is presented, while the results are summarized for the first harmonic. The second harmonic component of i_c, i.e. i_{c2}, is related to the second harmonic of the sum energies, and the first and third harmonics of the difference energies. This can be confirmed by substituting these values in (6.26). The dynamics of i_{c2} are given by (6.27), which is obtained by substituting the arm energies from (6.8) and (6.9) into (6.26).

$$\begin{aligned} l_{dc}\frac{\mathrm{d}}{\mathrm{dt}}i_{c2} + r_{dc}i_{c2} = -\frac{1}{2W^0}\Bigg[&v_{cm}^r\left(b^\Sigma h_{20} + b^\Sigma h_{22} + b^\Delta h_{21} - \hat{b}^\Sigma\hat{h}_{20}\right) \\ &- \frac{1}{2}v_s^r\left(b^\Delta h_{11} + b^\Sigma h_{10} + b^\Sigma h_{12} + b^\Sigma h_{32} - \hat{b}^\Sigma\hat{h}_{10}\right)\Bigg] \end{aligned} \tag{6.27}$$

Grouping the terms common to both the estimator and the actual values, leads to (6.28).

$$\begin{aligned} l_{dc}\frac{\mathrm{d}}{\mathrm{dt}}i_{c2} + r_{dc}i_{c2} = -\frac{1}{2W^0}\Bigg[&b^\Delta\left(v_{cm}^r h_{21} - \frac{1}{2}v_s^r h_{11}\right) + b^\Sigma\left(v_{cm}^r h_{22} - \frac{1}{2}v_s^r(h_{12} + h_{32})\right) \\ &+ v_{cm}^r\left(b^\Sigma h_{20} - \hat{b}^\Sigma\hat{h}_{20}\right) - \frac{1}{2}v_s^r\left(b^\Sigma h_{10} - \hat{b}^\Sigma\hat{h}_{10}\right)\Bigg] \end{aligned} \tag{6.28}$$

The second line of (6.28) is related to the estimation errors while the first part is due to a combination of the harmonics in the actual values. After converting (6.28) into phasor form, substituting the harmonic values from Table 6.2, and grouping

like terms, (6.29) is obtained.

$$-(R+jX_2)\,\vec{\mathbf{I}}_2 = v_{cm}^r\left(b^{\Sigma}\vec{\mathbf{H}}_{20} - \hat{b}^{\Sigma}\hat{\vec{\mathbf{H}}}_{20}\right) - \frac{1}{4}\vec{\mathbf{V}}_s^r\left(b^{\Sigma}\vec{\mathbf{H}}_{10} - \hat{b}^{\Sigma}\hat{\vec{\mathbf{H}}}_{10}\right) - jG_{22}\vec{\mathbf{I}}_2 + j\vec{\mathbf{G}}_{21}\vec{\mathbf{I}}_1$$
$$\text{where}\quad G_{22} = \frac{b^{\Sigma}}{\omega}\left[\frac{1}{2}(v_{cm}^r)^2 + \frac{1}{12}\|\vec{\mathbf{V}}_s^r\|^2\right]\quad\text{and}\quad \vec{\mathbf{G}}_{21} = \frac{3b^{\Delta}}{8\omega}v_{cm}^r\vec{\mathbf{V}}_s^r \tag{6.29}$$

where $R = 2W^0 r_{dc}$ and $X_2 = 4W^0\omega l_{dc}$. $\|\cdot\|$ is the magnitude (norm) operator. A similar equation for the first harmonic component, i_{c1}, is derived by following the same reasoning and approach, as shown in (6.30). The relevant energy harmonics, for the first harmonic current, are the first harmonic components of the sum energies and the second harmonic components of the difference energies.

$$-(R+jX_1)\,\vec{\mathbf{I}}_1 = v_{cm}^r\left(b^{\Delta}\vec{\mathbf{H}}_{10} - \hat{b}^{\Delta}\hat{\vec{\mathbf{H}}}_{10}\right) - \frac{1}{4}\vec{\mathbf{V}}_s^{r*}\left(b^{\Delta}\vec{\mathbf{H}}_{20} - \hat{b}^{\Delta}\hat{\vec{\mathbf{H}}}_{20}\right) - jG_{11}\vec{\mathbf{I}}_1 + j\vec{\mathbf{G}}_{12}\vec{\mathbf{I}}_2$$
$$\text{where}\quad G_{11} = \frac{b^{\Sigma}}{\omega}\left[(v_{cm}^r)^2 + \frac{1}{32}\|\vec{\mathbf{V}}_s^r\|^2\right]\quad\text{and}\quad \vec{\mathbf{G}}_{12} = \frac{3b^{\Delta}}{8\omega}v_{cm}^r\vec{\mathbf{V}}_s^{r*} \tag{6.30}$$

where $R = 2W^0 r_{dc}$ and $X_1 = 2W^0\omega l_{dc}$. Comparing (6.29) and (6.30), it can be noted that $\vec{\mathbf{I}}_2$ is related to the mismatch between b^{Σ} and $\hat{b}^{\Sigma}$, while $\vec{\mathbf{I}}_1$ is related to the mismatch between b^{Δ} and $\hat{b}^{\Delta}$. For example, with the parameters used in this chapter (Table 6.4), and at full load condition, a 10% deviation common to both the upper and lower arms leads to $||\vec{\mathbf{I}}_2|| = 5.4\,\text{A}$ (6.3% in pu) and $||\vec{\mathbf{I}}_1|| = 0.09\,\text{A}$ (0.01% in pu). Similarly, a 10% differential deviation between the upper and lower arms leads to $||\vec{\mathbf{I}}_2|| = 0.15\,\text{A}$ (0.18% in pu) and $||\vec{\mathbf{I}}_1|| = 3.8\,\text{A}$ (4.4% in pu).

6.6.1 The effect of time delay

Time delay affects the actual and estimated phasor quantities differently. The actual values are affected through the ac reference v_s^r (see (6.7)), which is delayed by t_d before reaching the arms. The estimator, on the other hand, accesses the references without delay since it resides in the controller, but the estimates themselves, $\hat{v}_{cu}$ and $\hat{v}_{cl}$, are delayed by t_d when they propagate as part of the insertion indexes. Therefore, the delay is applied to only v_s^r for the actual values while it is applied to all the quantities in the estimates. The time delay in phasor domain is represented by multiplication with $\mathrm{e}^{-jk\phi_d}$ where k is the harmonic order and $\phi_d = \omega t_d$ is the phase shift at fundamental frequency. The phasor quantities on the right-hand side of (6.29) and (6.30) can, therefore, be expanded as shown in (6.31) for the actual values and in (6.32) for the estimates.

$$\vec{\mathbf{H}}_{10} = \frac{1}{j\omega}\left[\frac{2}{3}v_{cm}^r\vec{\mathbf{I}}_s - \frac{1}{2}i_c^0\vec{\mathbf{V}}_s^r\mathrm{e}^{-j\phi_d}\right]\qquad \vec{\mathbf{H}}_{20} = -\frac{1}{j12\omega}\vec{\mathbf{I}}_s\vec{\mathbf{V}}_s^r\mathrm{e}^{-j\phi_d} \tag{6.31}$$

$$\hat{\vec{\mathbf{H}}}_{10} = \frac{1}{j\omega}\left[\frac{2}{3}v_{cm}^{r}\vec{\mathbf{I}}_s - \frac{1}{2}i_c^0\vec{\mathbf{V}}_s^r\right]\mathrm{e}^{-j\phi_d} \qquad \hat{\vec{\mathbf{H}}}_{20} = -\frac{1}{j12\omega}\vec{\mathbf{I}}_s\vec{\mathbf{V}}_s^r\mathrm{e}^{-2j\phi_d} \tag{6.32}$$

After substituting these phasor quantities into (6.29) and (6.30) and simplifying, (6.33) and (6.34) are obtained.

$$\begin{aligned} -(R+jX_2)\vec{\mathbf{I}}_2 =& \frac{j}{4\omega}\left[v_{cm}^{r}\vec{\mathbf{I}}_s\left(b^{\Sigma}\mathrm{e}^{j\phi_d} - \hat{b}^{\Sigma}\right) - \frac{1}{2}i_{c0}\vec{\mathbf{V}}_s^r\left(b^{\Sigma} - \hat{b}^{\Sigma}\right)\right]\vec{\mathbf{V}}_s^r\mathrm{e}^{-2j\phi_d} \\ & - jG_{22}\vec{\mathbf{I}}_2 + j\mathrm{e}^{-j\phi_d}\vec{\mathbf{G}}_{21}\vec{\mathbf{I}}_1 \end{aligned} \tag{6.33}$$

$$\begin{aligned} -(R+jX_1)\vec{\mathbf{I}}_1 =& -\frac{j}{\omega}\left[\left(\frac{2}{3}(v_{cm}^{r})^2 + \frac{1}{48}\|\vec{\mathbf{V}}_s^r\|^2\right)\vec{\mathbf{I}}_s\left(b^{\Delta}\mathrm{e}^{j\phi_d} - \hat{b}^{\Delta}\right)\right. \\ & \left. - \frac{1}{2}v_{cm}^{r}i_{c0}\vec{\mathbf{V}}_s^r\left(b^{\Delta} - \hat{b}^{\Delta}\right)\right]\mathrm{e}^{-j\phi_d} - jG_{11}\vec{\mathbf{I}}_1 + j\mathrm{e}^{j\phi_d}\vec{\mathbf{G}}_{12}\vec{\mathbf{I}}_2 \end{aligned} \tag{6.34}$$

Equations (6.33) and (6.34) show the effect of phase and capacitance errors on the first and second harmonic circulating currents. This information enables the correction of the parameter errors by using current measurements as feedback.

6.6.2 Proposed parameter correction method

Referring to (6.33) and (6.34), it can be observed that $\vec{\mathbf{I}}_2$ and $\vec{\mathbf{I}}_1$ can be forced to zero by adjusting the capacitance parameters, $\hat{b}^{\Sigma}$ and $\hat{b}^{\Delta}$, respectively. This procedure results in the elimination of the parameter errors. A feedback controller is proposed in this chapter in order to achieve such parameter correction online. However, direct implementation of feedback control based on (6.33) and (6.34) results in difficulties because the dc gains of the resulting transfer functions, from $\hat{b}^{\Sigma}$ to $\vec{\mathbf{I}}_2$ and from $\hat{b}^{\Delta}$ to $\vec{\mathbf{I}}_1$, are dependent on the operating point of the system. This means that a controller designed for one operating point might lead to positive feedback at another point, causing instability. The proposed solution overcomes this challenge by transforming $\vec{\mathbf{I}}_2$ and $\vec{\mathbf{I}}_1$ such that the transfer function gains do not change sign over the whole operation range. Such a transformation is derived by first ignoring the time delays such that (6.33) and (6.34) simplify to (6.35) and (6.36).

$$\begin{aligned} -(R+jX_2)\vec{\mathbf{I}}_2 &= j\left(b^{\Sigma} - \hat{b}^{\Sigma}\right)\vec{\mathbf{G}}_{20} - jG_{22}\vec{\mathbf{I}}_2 + j\vec{\mathbf{G}}_{21}\vec{\mathbf{I}}_1 \\ \text{where} \quad \vec{\mathbf{G}}_{20} &= \frac{1}{4\omega}\left[v_{cm}^{r}\vec{\mathbf{I}}_s - \frac{1}{2}i_c^0\vec{\mathbf{V}}_s^r\right]\vec{\mathbf{V}}_s^r \end{aligned} \tag{6.35}$$

$$\begin{aligned} -(R+jX)\vec{\mathbf{I}}_1 &= -j\left(b^{\Delta} - \hat{b}^{\Delta}\right)\vec{\mathbf{G}}_{10} - jG_{11}\vec{\mathbf{I}}_1 + j\vec{\mathbf{G}}_{12}\vec{\mathbf{I}}_2 \\ \text{where} \quad \vec{\mathbf{G}}_{10} &= \frac{1}{\omega}\left[\left(\frac{2}{3}(v_{cm}^{r})^2 + \frac{1}{48}\|\vec{\mathbf{V}}_s^r\|^2\right)\vec{\mathbf{I}}_s - \frac{1}{2}v_{cm}^{r}i_{c0}\vec{\mathbf{V}}_s^r\right] \end{aligned} \tag{6.36}$$

The proposed transformations are then given by (6.37).

$$\vec{\mathbf{T}}_2 = \frac{\vec{\mathbf{G}}_{20}^*}{\|\vec{\mathbf{G}}_{20}\|^2} \quad \text{and} \quad \vec{\mathbf{T}}_1 = \frac{\vec{\mathbf{G}}_{10}^*}{\|\vec{\mathbf{G}}_{10}\|^2} \tag{6.37}$$

Application of these transformations on both sides of (6.35) and (6.36) makes the coefficients of $\hat{b}^{\Sigma}$ and $\hat{b}^{\Delta}$ real constants irrespective of the operating point. Therefore, controllers designed for the transformed currents, $\vec{\mathbf{I}}_{2T} = \vec{\mathbf{T}}_2\vec{\mathbf{I}}_2$ and $\vec{\mathbf{I}}_{1T} = \vec{\mathbf{T}}_1\vec{\mathbf{I}}_1$, will be stable for the whole range of operating points without requiring re-tuning. The benefit of applying such a transformation will be shown by using simulation results. Since the effect is the same for both harmonic components, only $\vec{\mathbf{I}}_2$ will be covered in this section. Figure 6.11 compares the circulating current, $\vec{\mathbf{I}}_2$, with the transformed version, $\vec{\mathbf{I}}_{2T}$, under different operating points. The test was started with both the active and reactive power references set to 0.707 pu (OP1 in Fig. 6.11). Then, the active and reactive powers were reversed in polarity at $t = 7$ s, (OP2), and $t = 15$ s, (OP3), respectively. The currents are normalized by dividing them by their maximum value so that they can be plotted together. The shaded regions in the time plot and the diamond marks in the phasor plot show steady-state operating points. It is evident that both the real and imaginary parts of the circulating current ripple exhibit a sign change over the course of the simulation. This is particularly clear from the phasor plot where the current changes quadrant as the operating point changes. The change in quadrant makes the controllers designed for one operating point unstable at another. The transformed current ($\vec{\mathbf{I}}_{2T}$) does not exhibit the change in quadrant and, therefore, is suitable for the controllers. The movement of the transformed current within the third quadrant is due to the presence of delay error.

The same transformation helps in separating the effect of time delay from capacitance errors. This can be seen by applying $\vec{\mathbf{T}}_2$ and $\vec{\mathbf{T}}_1$ in the presence of time delay, i.e. to (6.33) and (6.34). Presence of the delay introduces an imaginary part to the coefficients of $\hat{b}^{\Sigma}$ and $\hat{b}^{\Delta}$ which in turn leads to an imaginary part in the transformed currents, $\vec{\mathbf{I}}_{2T}$ and $\vec{\mathbf{I}}_{1T}$. It can be shown, by linearizing (6.33) for small phase shift (around $\phi_d = 0$), that the imaginary part is proportional to the time delay and the corresponding transfer function gain does not change sign with operating point. The real part, on the other hand, is a function of both parameter errors. The same is true for the first harmonic part in (6.34). The controller implementation can be simplified if the phase error is corrected first. At the end of phase error correction, the resulting current is a function of only capacitance error as depicted in (6.35) and (6.36). Hence, the proposed implementation is performed in two steps as shown in Fig. 6.12.

The phase error can be corrected using the imaginary part of either $\vec{\mathbf{I}}_{2T}$ or $\vec{\mathbf{I}}_{1T}$.

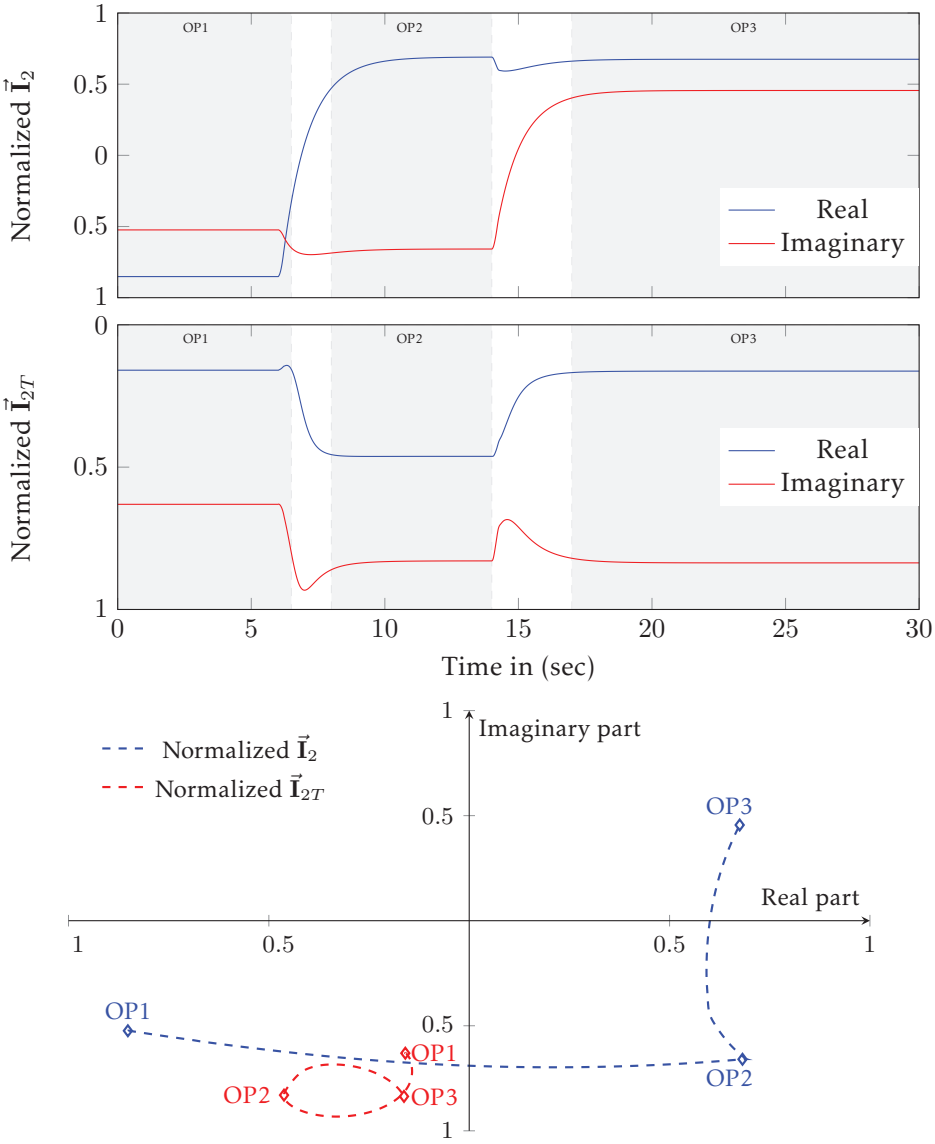

Figure 6.11: Effect of the current transformation under different operating points: normalized $\vec{\mathbf{I}}_2$ time plot (top), normalized transformed $\vec{\mathbf{I}}_{2T}$ time plot (middle), and phasor plot (bottom).

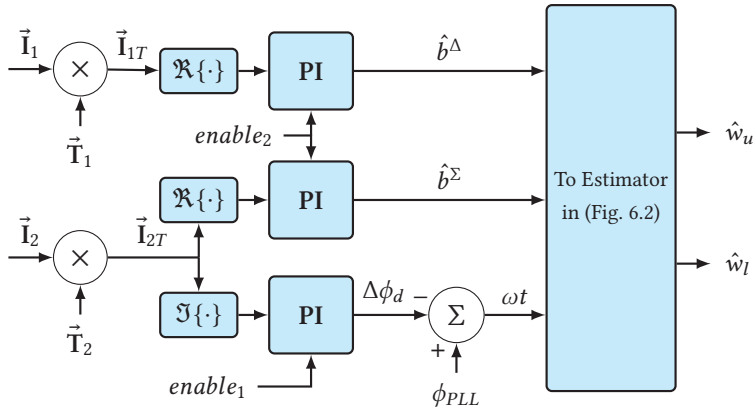

Figure 6.12: Implementation of the proposed parameter correction method.

$\vec{I}_{2T}$ is chosen in this chapter because it is more sensitive to delay changes. Each controller is activated by the enable signals where the subscripts show the sequence of activation. ϕ_{PLL} is the angle obtained from a PLL or other means of acquiring phase angle of the grid voltage. The parameter correction controllers are not required to always be active. The enable signals can be generated by a supervisory logic controller that monitors peak value of the circulating current ripple. The controllers can be enabled when a pre-specified upper threshold is exceeded (e.g 0.1 pu) and then disabled once the parameters are corrected, which can be indicated by the ripple being below a lower threshold (e.g. 0.01 pu). Another alternative is to run the parameter correction algorithm at regular intervals or during scheduled maintenance times. The parameter correction is implemented per-phase in order to identify each of the six arm capacitances individually. The phasors $\vec{I}_2$ and $\vec{I}_1$ are obtained by applying a method to extract phasors from single-phase time domain signals, such as the one presented in [103]. The remaining phasors are obtained from a balanced three-phase *abc* to *dq0* transformation. The next section presents simulation and experimental results validating the proposed method.

6.7 Simulation and experimental results

The proposed scheme is verified by simulations and experimental tests using the test setup shown in Fig. 6.13. An overview of the laboratory setup is given in Section 5.4.2. Both the ac and dc sides of the MMC are connected to a 200 kVA grid emulator with a 5 kHz bandwidth. The ac grid is emulated by a voltage source behind an impedance while the dc side is represented by an ideal dc voltage source. The experiment was performed on three MMCs with 6, 12, and 18 submodules per arm. The results obtained from the three tests are similar, and hence, only

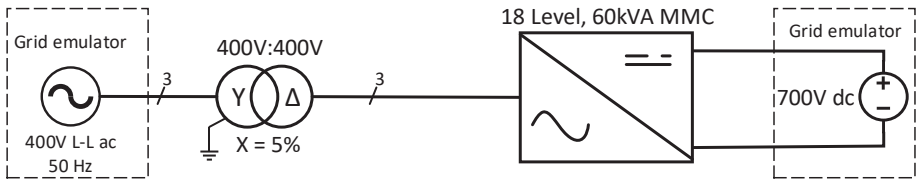

Figure 6.13: Experimental test setup.

Table 6.4: Test system parameters.

Symbol	Value	Symbol	Value
S_b	60 kVA	C_{arm}	1110 µF
V_b^{dc}	700 V	L_{arm}	1.4 mH
V_b^{ac}	350 V	No. of submodules	12
k_{pw}	0.4	k_{pi}	0.1
k_{iw}	7.6	k_{ii}	6.9
T_w	10 ms	T_i	0.5 ms

the ones from the 12 level MMC will be presented in this chapter. All the tests are performed at 500 V dc, 225 V ac peak, and 10 kW active power being injected into the ac grid.

6.7.1 Test cases

Table 6.5 displays the test cases covered in this chapter. The first case is a base case, where the parameter correction is disabled, and demonstrates the performance of the estimator, and the higher-level controllers under normal conditions with nominal parameters. Case 2 deals with the correction of parameter errors, where the initial values for the estimator are obtained from the nameplates of the components (i.e. nominal values). This test case demonstrates the application of the proposed method for commissioning purposes, where the exact values of the parameters are not known. Cases 3 to 5 test how well the proposed method captures changes in arm capacitance. This was achieved by removing up to 2 capacitors from 4 (out of the 18) selected submodules of the three arms shown in Table 6.5. Each submodule is composed of 6 capacitors connected in parallel. The arms are selected in such a way that the change introduced is unsymmetrical. The capacitor removals were done step-by-step, where the capacitors from Phase *a* upper arm were removed first, followed by Phase *b* lower arm, and finally, Phase *c* upper arm. The capacitors removed before the start of each test are not replaced until the end of the last case. Therefore, at the start of case 5, a total of 21 capacitors were removed from the converter.

Table 6.5: Test Cases.

Case No.	Arm	No. of SMs Modified	No. of Caps removed out of 6				Change in arm Capacitance (Δ)**	Parameter correction
			SM1	SM2	SM3	SM4*		
1	-	0	0	0	0	0	0%	No
2	-	0	0	0	0	0	0%	Yes
3	Phase *a* upper	4	2	2	2	1	-8.6%	Yes
4	Phase *b* lower	4	2	2	2	2	-10%	Yes
5	Phase *c* upper	4	2	1	2	1	-7.2%	Yes

*The remaining 14 submodules are not modified in any of the cases.

**These values are approximations, calculated based on nominal values of the capacitors

6.7.2 Base case (Case 1)

This case presents the basic implementation of the estimator with nominal capacitances, and no time delay. In order to show the performance of the estimator during transients, a 20% step change in the average arm voltage reference is applied at 10 s and then reversed at 20 s. The simulation and experimental results for the base case are displayed side-by-side in Figs. 6.14 and 6.15. It can be seen from Fig. 6.14 that the estimator displays a good performance in simulation. This is because the parameters are accurately known. The experimental results resemble the ones from the simulations confirming accuracy of the models used for simulation. The estimated and measured arm voltages from the experimental test in Fig. 6.14 seem to be well aligned. This, however, does not necessarily mean that the estimator is performing well because the measured arm voltage is different from the actual one due to distortion and delay in the measurement system. In simulation, the actual arm voltage is measured without distortion, and hence, good alignment means good performance. Therefore, the presence of circulating current ripple is used as an indicator of performance, where it is clear, (Fig. 6.15), that the estimator performs poorly in the experimental tests. This is attributed to the mismatch between the parameters assumed by the estimator and the actual parameters in the system. It can be seen from Fig. 6.14 that the estimator performance slightly degrades during transient at 10 s. This is because the ac peaks and the dc signals are changing faster than has been specified in Assumption **A.2**. As a consequence, the circulating current from the simulation displays ripple during transients, as can be seen from the inset in Fig. 6.15. Magnitude of the resulting circulating current is negligible and only occurs during fast transients.

6.7.3 Parameter error correction

As identified in the base case, the converter parameters are different from their nominal values assumed by the estimator, which led to the circulating current ripple. In this section, the proposed method is used to remove this mismatch between the estimator and actual parameters. Figure 6.16 depicts the parameter correction controllers' output during the process of parameter correction. It can be seen that phase correction is applied first. Capacitance correction is enabled around t =10 s, where the phase correction is expected to have reached steady state. The values shown in Fig. 6.16 at the end of this test (at t =40 s) are the mismatches between the parameters, the arm capacitances and ϕ_d, known to the estimator and those of the actual converter. Therefore, if the estimator parameters are adjusted by these values, the circulating current ripple can be eliminated. This is shown in Fig. 6.17, where the magnitude of the circulating current ripple progressively decreases when the correction is activated. The phase adjustment experiences a deviation when the capacitance correction is enabled around 10 s.

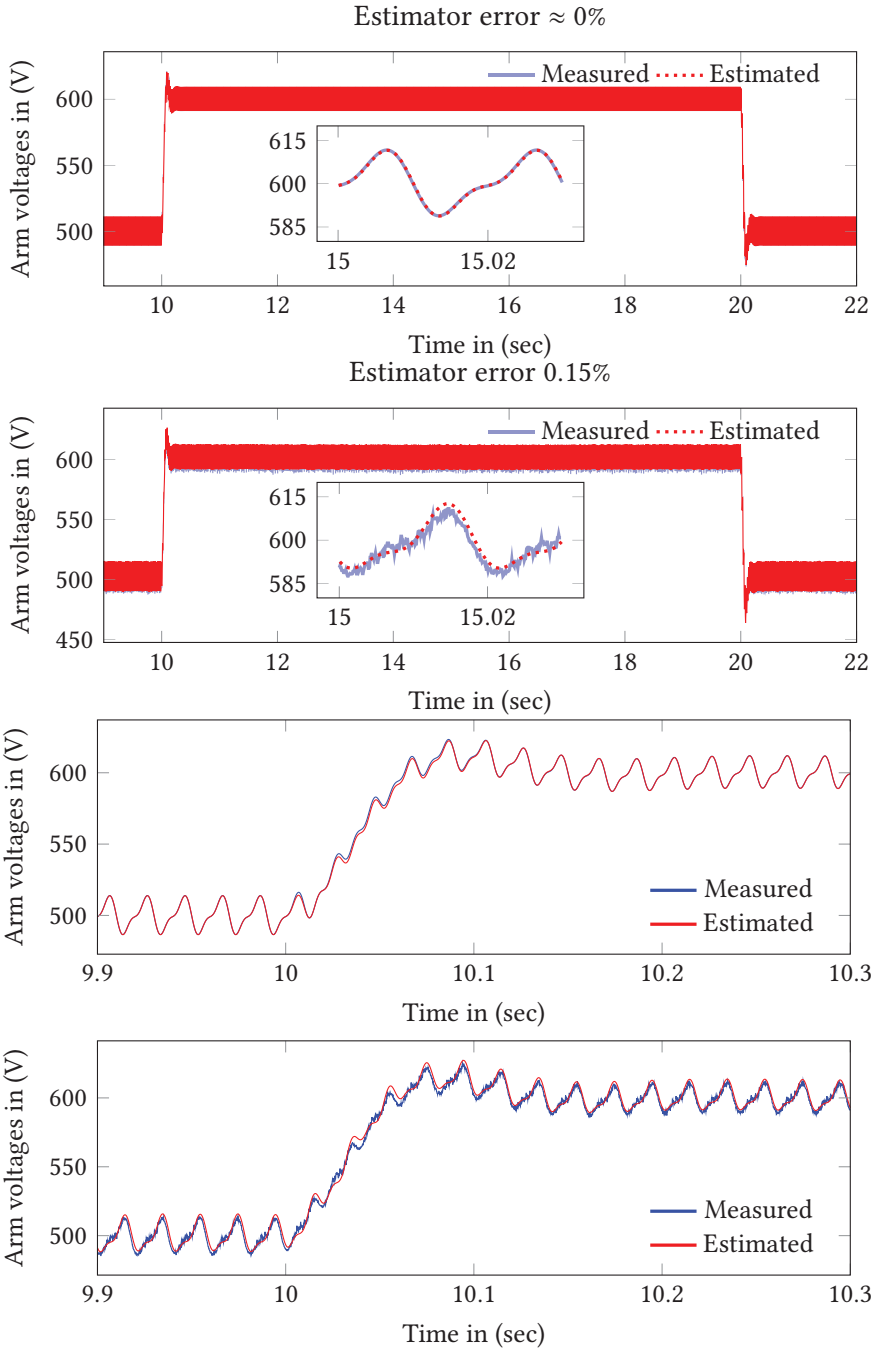

Figure 6.14: Base case arm voltages in response to step in the arm energy reference: (1) simulation, (2) experimental, (3) zoomed simulation, and (4) zoomed experimental.

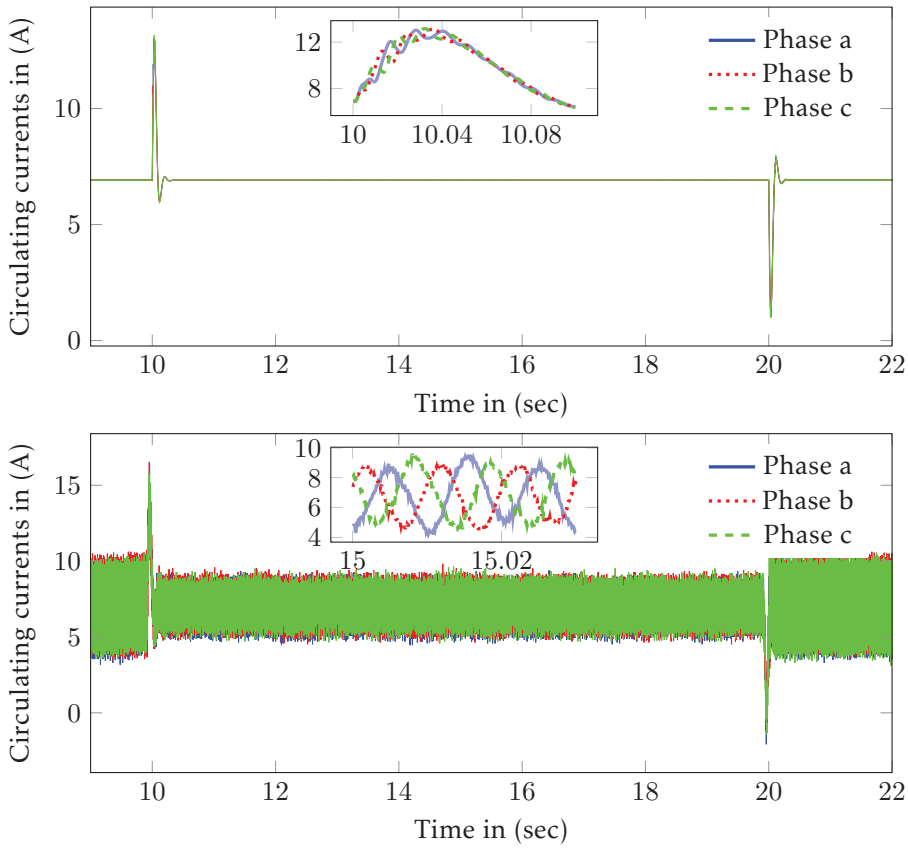

Figure 6.15: Base case circulating currents in response to step in the arm energy reference: simulation (top) and experimental (bottom).

This is because of the removal of harmonic cross-coupling terms, derived in Section 6.6, which bias the relation between $\vec{\mathbf{I}}_{2T}$ and phase angle error. The remaining current ripple, at the end of the correction is measurement noise, harmonic distortion, and high-frequency components due to switching of the submodules, which are not captured by average models. The upper and lower arm capacitance deviations (Fig. 6.16) for each phase are calculated from $\hat{b}^{\Sigma}$ and $\hat{b}^{\Delta}$ as given by (6.38).

$$\Delta c_u = \left(\frac{1}{c_a}\frac{1}{\hat{b}^{\Sigma}+\hat{b}^{\Delta}} - 1\right) \times 100\% \quad \text{and} \quad \Delta c_l = \left(\frac{1}{c_a}\frac{1}{\hat{b}^{\Sigma}-\hat{b}^{\Delta}} - 1\right) \times 100\% \tag{6.38}$$

where c_a is the nominal arm capacitance in Per-unit. The controllers are not affected by the parameter correction since the correction scheme is disabled under normal operation. This can be asserted by observing the circulating current response to step changes in the arm energy, which is plotted in Fig. 6.18. This shows

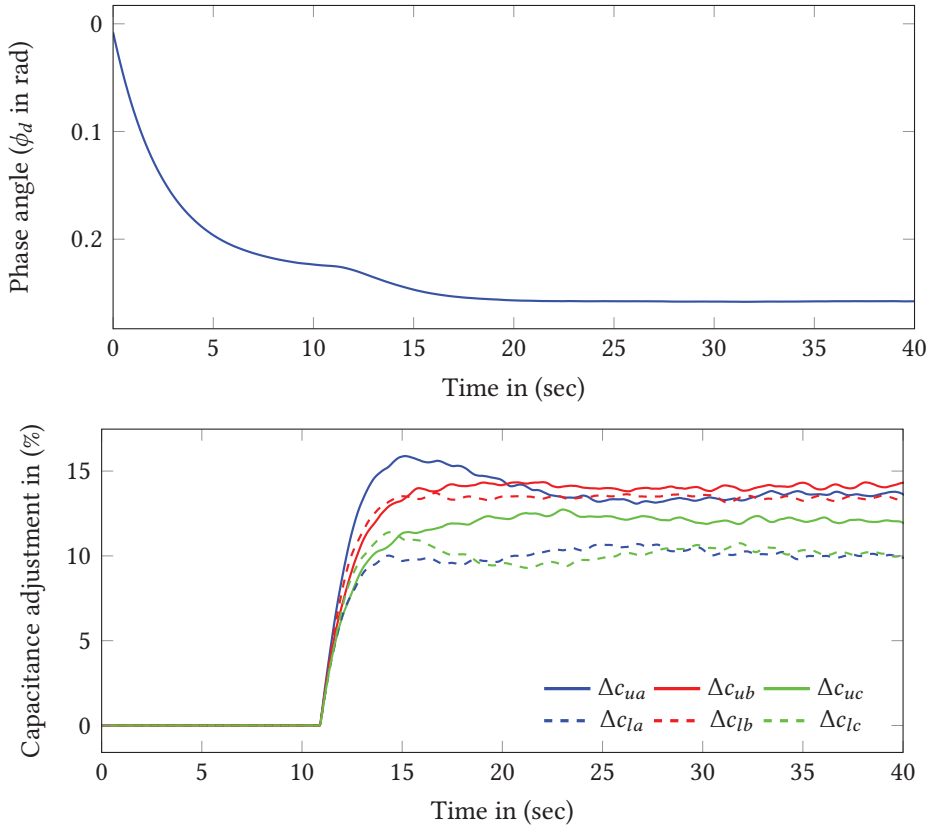

Figure 6.16: Parameters during the process of correction (Case 2): phase angle (top) and capacitance (bottom).

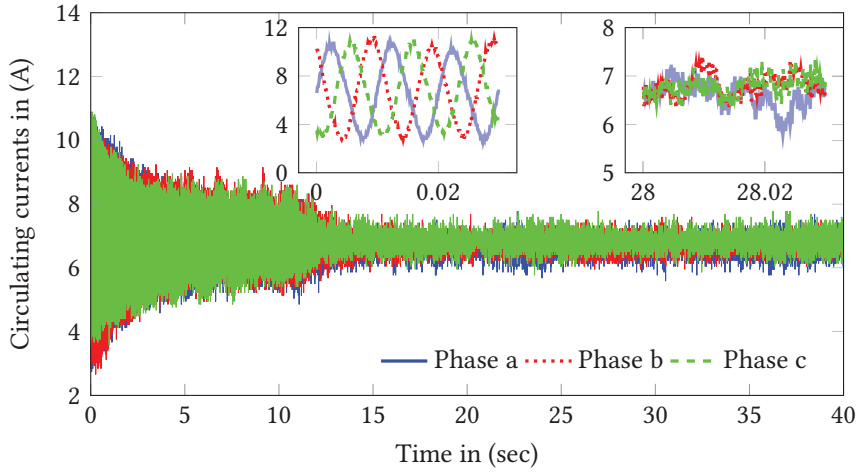

Figure 6.17: Circulating current during parameter correction (experimental).

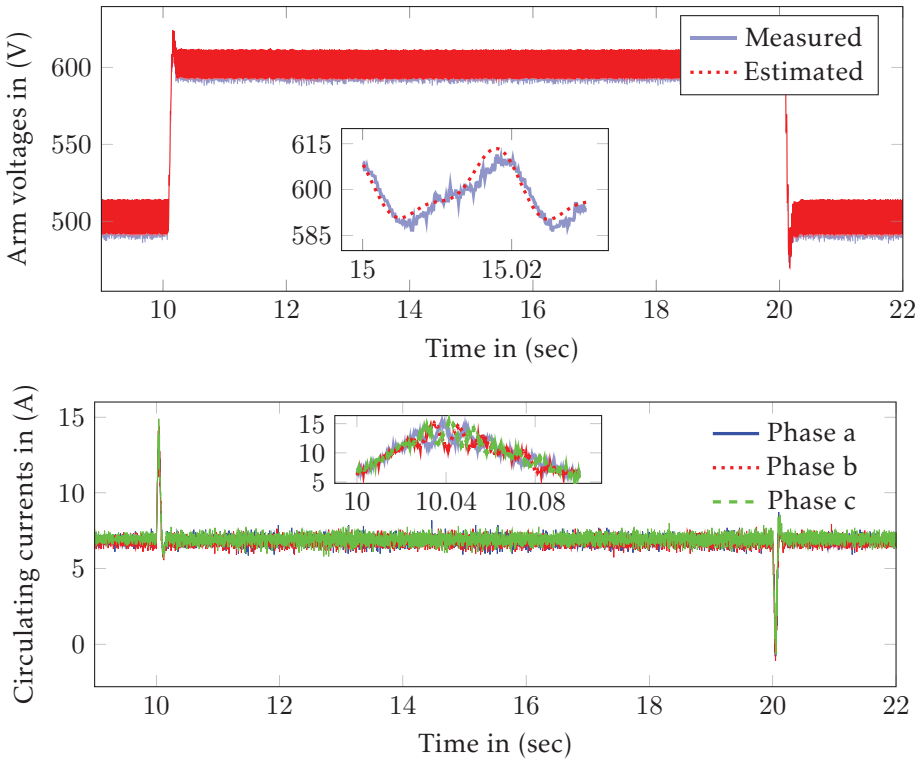

Figure 6.18: Arm voltage and circulating current after parameter error correction (experimental).

that, in comparison to Figs. 6.14 and 6.15, the correction reduces the current ripple without affecting the controller performance. This is an advantage compared to other approaches which use circulating current suppressors that are always active and can negatively interact with higher level controllers [45].

6.7.4 Changes in the arm capacitances

The parameter correction is also applied to cases 3 to 5, where the arm capacitances were modified. The resulting parameter adjustments are compared to those of case 2 in order to show how well the correction method copes with capacitance changes. Figure 6.19 depicts the upper and lower arm capacitance adjustments, which are calculated using (6.38). Each test was run similar to case 2 where the estimator is started with nominal values of the arm capacitances and no delay. Only the test cases relevant to the respective phases are shown in the figure in order to provide a clear comparison of the deviations. For instance, since Phase *a* upper arm is modified in case 3, the result in Fig. 6.19 compares case 3 to case 2 in order to show the change in capacitance. The unmodified arm in the same phase is also displayed to show that it is not affected by the removal of the capacitors. It can be seen that the proposed method correctly captures the capacitance modifications. Figure 6.19 also shows the percentage difference between the adjustments of case 2 and cases 3 to 5, where it can be seen that the adjustments are in close agreement with the values shown in Table 6.5. The mismatch between the deviations in Table 6.5 and Fig. 6.19 can be attributed to two reasons: 1) the capacitance tolerances, which change the deviations in Table 6.5, and 2) the presence of measurement noise, which prevents ideal operation of the correction method. The noise problem can be overcome by running the correction at higher currents where signal-to-noise ratio is higher. It should be noted, however, that the method performs well in removing the ripples, even in the presence of noise. The other option to minimize the impact of noise is to apply filtering to the current measurements and tune the correction controllers to be slower.

6.7.5 Discussion

The simulations and experimental results demonstrated that the proposed parameter adjustment method effectively eliminated circulating current ripple arising from parameter errors in the arm voltage estimator. This solves the main limitation of methods implementing compensated modulation using estimated arm voltages, such as the open-loop method. The method was derived under a steady-state assumption such that the ac quantities can be represented by complex phasors (Assumption **A.2**). The impact of violating this assumption, as shown in Fig. 6.14, is a slight degradation in the arm voltage estimator accuracy, which leads to ripple in the circulating current (Figs. 6.15 and 6.18). However, the esti-

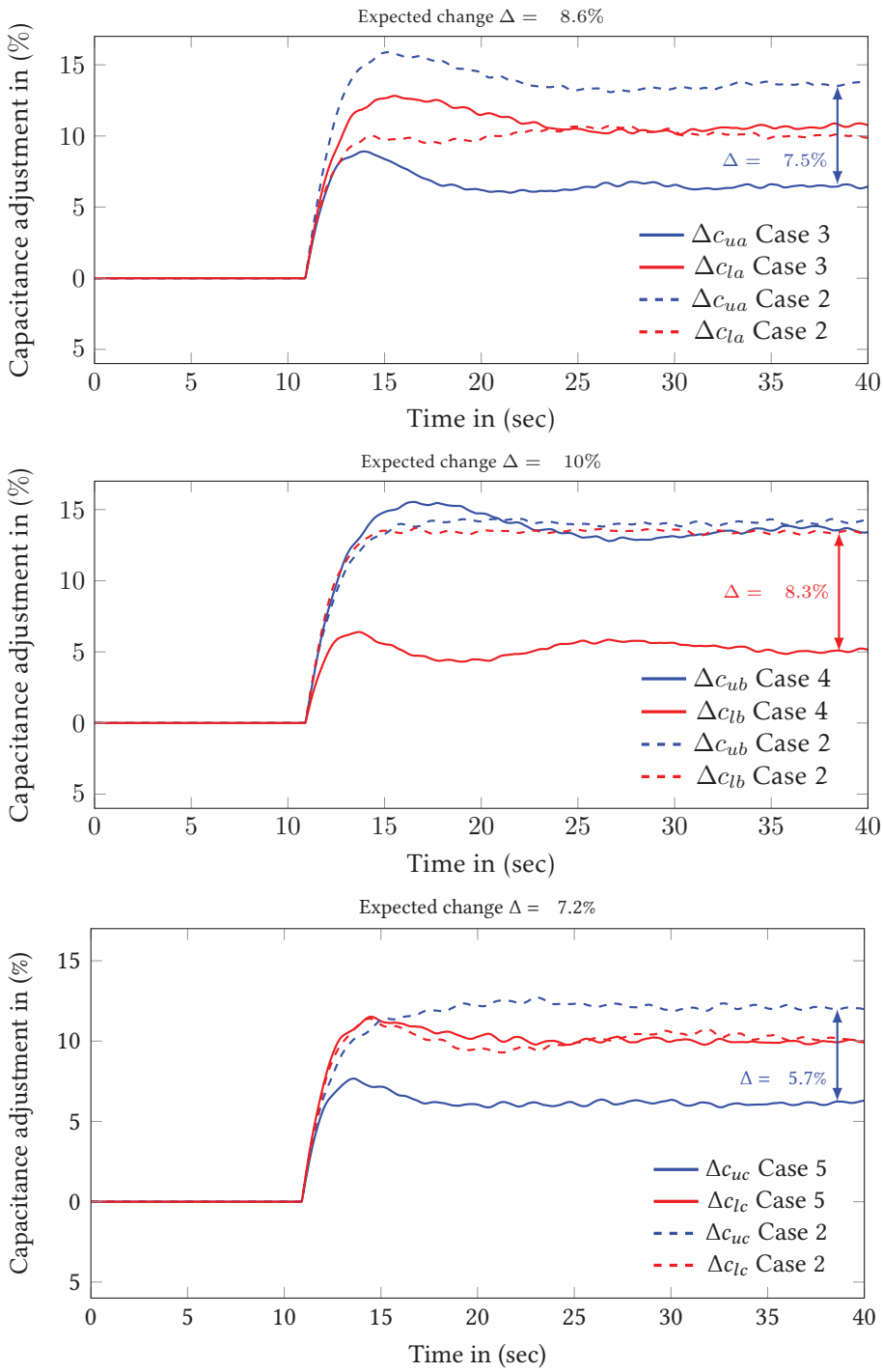

Figure 6.19: Capacitance adjustments before and after capacitor removals: Phase *a* (top), Phase *b* (middle), and Phase *c* (bottom).

mator error, and hence, the ripple in the circulating currents observed from both simulations and experiments, can be considered negligible. Another factor that can affect the performance of the arm voltage estimator is the presence of harmonics in the ac voltages and currents (violation of Assumption **A.1**). Harmonics cause additional ripple components in the arm voltages and the circulating currents. These new ripple components in the circulating current can be eliminated by including the harmonics in the derivation of the arm voltage estimator. However, this is not generally necessary since most grid codes and standards set a low limit on the THD at connection points (for example 1.5% in IEEE 519 [101]), in which case the estimator error introduced by harmonics in the grid becomes negligible.

A second effect of harmonics is on the parameter adjustment method. Since the method uses the first and second harmonic components in the circulating current ripple as feedback, it is only affected by harmonics whose combinations result in first and second harmonics in the circulating current. Such harmonic combination involves product of two harmonics, which are usually below 1% of the fundamental quantities [101]. Thus, the end effect of harmonics on the parameter correction can be neglected.

6.8 Conclusion

This chapter presents a complete approach for implementing compensated modulation without accurate knowledge of system parameters. Parameter errors lead to two types of problems: drifting of the average (dc) component of the arm energy away from the desired one, and increase in the circulating current ripple. This chapter addresses these two issues separately. As a first part, the average part is decoupled from the errors by using the measured average value. This is acceptable because the average part is assumed to change slowly enough that it is not affected by the measurement system. Additionally, the average part is controlled in closed-loop in order to provide good dynamic performance and disturbance rejection. The second part concerns the correction of parameter errors to reduce or eliminate the circulating current ripple.

The parameters considered in this chapter are the arm capacitance and time delay between the controller and the converter. The detailed derivation has shown that these quantities are related to the first and second harmonic ripples in the circulating current. A transformation is applied to the second harmonic current in order to make its imaginary part, in phasor domain, a function of only the phase error. This enables a two-step correction of the two errors: phase correction using the imaginary part of the second harmonic, followed by sum and difference capacitance corrections using the real parts of the second and first harmonic pha-

sors, respectively. It can be observed that, despite its rather long analytic derivation, the final result is simple and easy to implement (Fig. 6.12). The corrections are implemented using two PI controllers per leg that are enabled on-demand. Moreover, the controllers are designed to be slower than higher level controllers, which results in time-scale separation. This enables the removal of the circulating current ripple without potential negative interactions with the higher-level controllers.

The proposed method has been tested using both simulation and experimental tests with a strong correlation between the two results. The experimental tests have shown that the method can work in cases that are not ideal where the number of modules is as low as 18. The tests have also demonstrated that the method works well in the presence of noise and unsymmetrical capacitance changes. In summary, the proposed method gives a complete solution for implementing compensated modulation under changing system parameters. Moreover, the application of the method is not limited to the correction of parameter changes due to environmental conditions; it can also be used to identify the parameters during commissioning where they are not accurately known.

The complete control system proposed in this chapter gives a good dynamic performance which enables the implementation of the energy-based services presented in the next two chapters.

7

Methods of Utilizing the MMC Energy Storage

This chapter proposes control methods that enable the utilization of the energy storage capability of the MMC for active power-based ancillary services. Conventional implementations of such services on converters lead to the propagation of active power disturbance across the dc grid and into other connected ac power systems, which is undesirable. The proposed methods prevent such propagations by diverting the disturbance into the submodule capacitors of the MMC. An aggregate dc grid model is used to derive the proposed methods and to analyze the propagations of the disturbances. The proposed methods are verified using time-domain simulations focusing on different application cases. Finally, quantification of the amount of extra energy storage required to provide the aforementioned services is discussed, together with potential ways to obtain such extra storage. The discussion in this chapter is supported by the following contributions by the author.

> A. A. Taffese, E. Tedeschi, and E. de Jong, "A control scheme for utilizing energy storage of the modular multilevel converter for power oscillation damping," in *2017 IEEE 18th Workshop on Control and Modeling for Power Electronics (COMPEL)*, Stanford, CA, USA: IEEE, Jul. 2017, pp. 1–8
>
> A. A. Taffese and E. Tedeschi, "Coordination of Modular Multilevel Converter Based HVDC Terminals for Ancillary Services," in *2018 Power Systems Computation Conference (PSCC)*, Dublin, Ireland: IEEE, Jun. 2018, pp. 1–7
>
> E. Tedeschi and A. A. Taffese, "Electrical power transmission and grid integration," en, *Renewable Energy from the Oceans: From wave, tidal and gradient systems to offshore wind and solar*, pp. 321–343, Jul. 2019

Chapter Outline

7.1 Introduction

An increasing number of grid codes require HVDC converters to contribute more towards enhancing stability and power quality of the ac grid [104]. The contributions can be in the form of frequency regulation [105], Power Oscillation Damping (POD) [106], or ac voltage support. The first two services require manipulation of active power, which results in distortion on the dc voltage in the form of sags, swells, and oscillations. This causes converters terminals that participate in dc voltage regulation to provide the required active power in order to keep the dc voltage variations to a minimum. The dc voltage distortion by itself is not a major problem; it is the propagation of the distorted active power that poses power quality challenges to the other connected ac grids. Another side effect of this is that there is a strong dynamic coupling between ac grids across the terminals, which can lead to negative interactions among multiple POD controllers acting on different ac grids, potentially reducing their performance [5]. Energy storage capacity inherently available in the HVDC converters, particularly the Modular Multilevel Converters (MMCs), can be used to mitigate this problem.

One of the differences between the MMC and the two-level VSC is that the MMC has energy storage capability in its arms. In the two-level VSC, semiconductor switches take the place of the arms, which implies that the only major energy storage capability is in the dc link capacitance. This means that the energy stored by the converter cannot be utilized for other services without affecting other components connected to the dc side because the capacitance is directly inserted into the dc side.

The MMC offers more flexibility in manipulating its stored energy because the submodule capacitors, which make up the arm capacitance, are not directly inserted into the dc link. The degree of flexibility depends on the type of modulation scheme used and the availability of extra energy storage capability. As discussed in Chapter 4, there are two modulation techniques: direct modulation and compensated modulation. The arm voltage is equal to the dc voltage when direct modulation is used, which makes the MMC appear like a two-level VSC with the arm capacitors inserted into the dc link, and hence results in the loss of flexibility in using the arm energy. This is not desirable because the stored energy can be used to provide ancillary services to the connected power system. The use of compensated modulation provides better flexibility by decoupling the arm voltage from the dc voltage.

This chapter discusses the different ways in which the MMC energy storage capability can be used. A simplified aggregate model of a dc grid is presented first. This model is used to derive and analyze the different ways of arm energy utiliza-

tion. Two methods of utilizing the stored energy of the MMC, i.e. power cancellation and Virtual Capacitance Support (VCS), are presented next. The methods are studied using simulation case studies involving POD, wind power smoothening, and dc voltage support services. Finally, the extra energy storage requirement needed to utilize the arm energy for grid services is discussed.

7.2 Aggregate dc grid model

Performing analysis using a simplified aggregate model of a dc grid gives better insight into how the stored energy in the arms of the MMCs can be used for different services. The analysis will focus on slow dynamics (in the range of a few hertz), so all the MMC controllers are assumed to be ideal. Hence, each controlled signal is set to be equal to the respective reference value. The equation relating the arm energy to the dc and ac sides is given by (7.1). This is based on the energy dynamics, which were derived as part of the MMC model in Chapter 3. The original equation (first line of (7.1)) can be simplified by ignoring the losses inside the converter as shown in the second and third lines of (7.1).

$$\begin{aligned}\frac{\mathrm{d}}{\mathrm{d}t}w &= \frac{2}{c_a}\left[\frac{1}{2}\left(v_{dc}^r - 2v_c^r\right)i_c - \frac{1}{6}v_{dq}^r \cdot i_{dq}\right] \\ &\approx \frac{1}{c_a}\left[v_{dc}i_c - \frac{1}{3}\left(v_d^r i_d + v_q^r i_q\right)\right] \\ &= \frac{1}{3}\frac{1}{c_a}\left(p_{dc} - p_{ac}\right)\end{aligned} \tag{7.1}$$

Solving for i_c from (7.1), the following equation is obtained.

$$i_c = \frac{1}{v_{dc}}\left(c_a\frac{\mathrm{d}}{\mathrm{d}t}w + \frac{1}{3}p_{ac}\right) \tag{7.2}$$

p_{ac} can be substituted by the ac power reference including the droop, as shown in (7.3). Other dc voltage regulation methods, like master-slave or voltage-ration control [3], can also be represented in this way but this work focuses on droop because it is more popular due to the fact that it can distribute the voltage regulation responsibility among multiple converters without requiring communication. Therefore, only droop control is discussed further.

$$i_c = \frac{1}{v_{dc}}\left[c_a\frac{\mathrm{d}}{\mathrm{d}t}w + \frac{1}{3}\left(p_{ac}^r - \frac{1}{\rho}\left(v_{dc}^r - v_{dc}\right)\right)\right] \tag{7.3}$$

The next step is to incorporate i_c into the dc link dynamic equation. The dc grid consists of cables and pole capacitors. The cable capacitance is distributed along the length of the cable. For the purpose of aggregation, the losses and dynamics

introduced by the cable are ignored, which enables the dc grid to be represented by one lumped capacitor. This is equivalent to neglecting the inductance and resistance of the cables. Such a simplification is justified because the cable dynamics is significantly faster than the frequency of interest. This implies that the dc link voltage at each terminal is approximately the same and its dynamics are governed by (7.4).

$$c_g \frac{\mathrm{d}}{\mathrm{dt}} v_{dc} = -3 \sum_{j=1}^{m} i_{cj} \tag{7.4}$$

where c_g is the equivalent grid capacitance, m is the number of converters, and i_{cj} is the dc common-mode current of converter j. Substituting the values of i_{cj} from (7.3) yields,

$$c_g \frac{\mathrm{d}}{\mathrm{dt}} v_{dc} = -\sum_{j=1}^{m} \left[\frac{3c_{aj}}{v_{dc}} \frac{\mathrm{d}}{\mathrm{dt}} w_j + \frac{p^r_{acj}}{v_{dc}} - \frac{1}{\rho_j} \left(\frac{v^r_{dcj}}{v_{dc}} - 1 \right) \right] \tag{7.5}$$

where c_{aj}, w_j, p^r_{acj}, v^r_{dcj}, and ρ_j are the arm capacitance, the arm energy, the ac power reference, the dc voltage reference and the droop constant of converter j, respectively.

Equation (7.5) will be linearized around an equilibrium point in order to analyze the effect of the power variations. Since the losses are neglected, the following condition holds at a steady state operating point. Additionally, the derivative of the arm energy is also zero at steady-state.

$$\sum_{j=1}^{m} p^r_{acj} - \frac{1}{\rho_j} \left(v^r_{dcj} - v_{dc} \right) = 0 \tag{7.6}$$

A linearized version of (7.5) around the aforementioned operating point is given by (7.7).

$$c_g \frac{\mathrm{d}}{\mathrm{dt}} \Delta v_{dc} = -\sum_{j=1}^{m} \left[\frac{3c_{aj}}{V_{dc0}} \frac{\mathrm{d}}{\mathrm{dt}} \Delta w_j + \frac{\Delta p^r_{acj}}{V_{dc0}} - \frac{1}{\rho_j V_{dc0}} \left(\Delta v^r_{dcj} - \Delta v_{dc} \right) \right] \tag{7.7}$$

where V_{dc0} is the dc voltage at the operating point. All the variables are prefixed with Δ to signify that they are referring to deviations with respect to the operating point. Equation (7.7) can be further simplified by taking into account that the dc voltage is common to all the converters because the dc grid losses and dynamics are neglected. Furthermore, it can be assumed that the dc voltage references are constants (i.e. $\Delta v^r_{dc} = 0$), which is acceptable because the main focus here is the response to active power variations. The simplified equation is shown in (7.8).

$$c_g \frac{\mathrm{d}}{\mathrm{dt}} \Delta v_{dc} + \frac{\Delta v_{dc}}{V_{dc0}} \sum_{j=1}^{m} \frac{1}{\rho_j} = -\frac{1}{V_{dc0}} \sum_{j=1}^{m} \left[3c_{aj} \frac{\mathrm{d}}{\mathrm{dt}} \Delta w_j + \Delta p^r_{acj} \right] \tag{7.8}$$

Since the dc voltage dynamics given by (7.8) is a first-order, it can be characterized by two parameters: a gain and a time-constant. The gain is equal to the aggregate (equivalent) droop constant ρ_{eq} which is given by (7.9).

$$\rho_{eq} = \left(\sum_{j=1}^{m} \frac{1}{\rho_j} \right)^{-1} \tag{7.9}$$

The time constant T_{eq} is calculated from the droop constants and the equivalent grid capacitance as shown in (7.10).

$$T_{eq} = c_g \rho_{eq} V_{dc0} \tag{7.10}$$

Substituting these values into (7.8) and rearranging the terms yields (7.11).

$$T_{eq} \frac{\mathrm{d}}{\mathrm{dt}} \Delta v_{dc} + \Delta v_{dc} = -\rho_{eq} \sum_{j=1}^{m} \left[3c_{pj} \frac{\mathrm{d}}{\mathrm{dt}} \Delta w_j + \Delta p_{acj}^{r} \right] \tag{7.11}$$

Equations (7.5) and (7.11) give an aggregate model of a dc grid and its linearized version, which capture the relation between the dc voltage, the arm energy, and the ac active power. These relations will be used to analyze the effectiveness of the energy utilization methods presented in the next section.

7.3 The impact of active power-based services

When providing services that manipulate active power, a converter injects a time-varying active power Δp_{ac}, which is superimposed on the steady-state power command. The nature of this time-varying component is determined by the type of service provided. It exhibits oscillatory behavior in the case of POD, and a random fluctuation in the case of active power smoothening service, which is a service that filters out rapid power fluctuations coming from wind farms. In any case, these components cause an undesirable time variation in the dc voltage. When the converter arm energy is controlled to be constant (i.e. not participating in grid support), the dc voltage variation can be approximately quantified using the transfer function of the aggregate dc grid given by (7.11), as shown in (7.12). In order to simplify the analysis, it is assumed that only one converter (i.e. converter j) is providing the service by injecting the power variation Δp_{acj}.

$$\Delta v_{dc} = -\frac{\rho_{eq}}{T_{eq} s + 1} \Delta p_{acj} \tag{7.12}$$

This voltage variation is seen as a disturbance by the dc voltage regulating nodes, which try to keep the dc voltage constant by injecting a counter active power drawn from their respective ac sides. As a result, the fluctuation or oscillation

propagate across the dc grid and into other connected ac systems. The amount of power absorbed by each node can be found from the droop equations as shown by (7.13).

$$\Delta p_{acx} = -\frac{\rho_{eq}}{\rho_x}\frac{1}{T_{eq}s+1}\Delta p_{acj} \tag{7.13}$$

where Δp_{acx} is the net power absorbed by node x when node j injects the power variation Δp_{acj}. If converter j is also participating in voltage regulation, there will be a reduction in the amount of active power available for the service. In other words, the voltage regulation opposes the change in active power introduced by the service leading to a lower power available for the service. This reduction can be quantified using (7.14).

$$\Delta \hat{p}_{acj} = \left(1 - \frac{\rho_{eq}}{\rho_j}\frac{1}{T_{eq}s+1}\right)\Delta p_{acj} \tag{7.14}$$

where $\Delta \hat{p}_{acj}$ is the net varying power injected to provide the service. A numerical calculation using a simple system demonstrating the equations is presented in the next section.

7.3.1 Analysis of a POD case: simplified calculations

This section demonstrates the calculation of the propagation of active power through a dc grid when one of the terminals is providing POD service to its ac grid. The test case is a three-terminal dc grid where all the converters are rated for 900 MW, and where the first two of the three converters are operated in droop mode with $\rho = 0.05$. The third converter is operated in constant power mode and is providing POD with peak power 0.05 pu (45 MW) at 1 Hz. The dc grid equivalent capacitance is 100 ms and the dc voltage at the operating point is 1 pu (640 kV).
This gives:

$$\rho_{eq} = 0.025 \quad \text{and} \quad T_{eq} = 0.025 \times 0.1 = 2.5\,\text{ms}$$

It can be seen from the bode diagram in Fig. 7.1 that the first-order time constant has only a negligible impact at the oscillation frequency (the gain is 0.248 and the phase shift is −0.9° at 1 Hz). By combining the bode plot with the parameters given, the peak voltage variation can be calculated as follows:

$$\Delta v_{dc}^{max} = 0.0248 \times 0.05 = 1.2 \times 10^{-3}\,\text{pu} = 0.12\%$$

The peak power absorbed by each of the voltage regulating nodes can be calculated using (7.13) as shown below:

$$\Delta p_{1,2}^{max} = -\frac{0.0248}{0.05} \times 0.05 = -0.0248\,\text{pu}$$

This shows that each of the voltage-regulating terminals take approximately half of the power variation because they have the same droop value. The dc voltage shows very little change because almost all of the power fluctuation is absorbed by the droop-controlled terminals. The dc grid absorbs only 4×10^{-4} pu power, which explains why it is showing an insignificant amount of change.

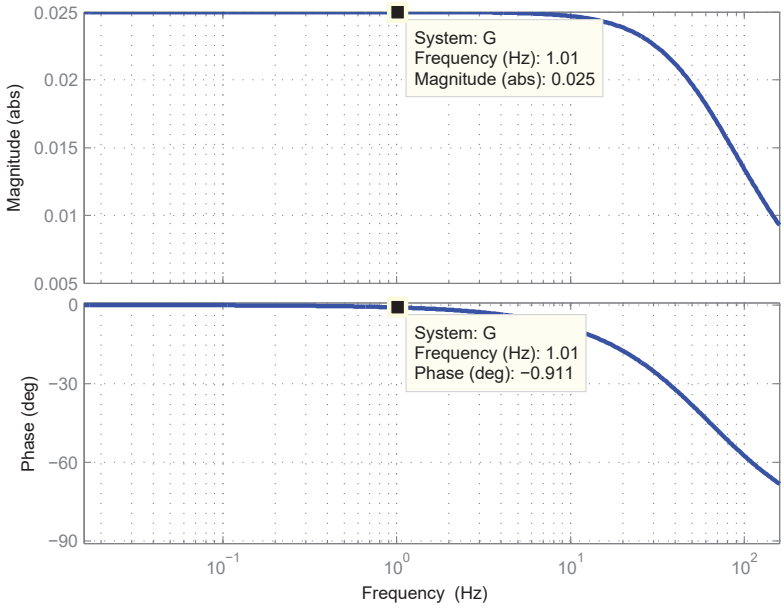

Figure 7.1: Bode plot of the aggregate dc voltage transfer function.

In a second case, the third terminal is also participating in voltage regulation with droop constant of $\rho = 0.075$, while at the same time injecting the power variation.

$$\rho_{eq} = 0.0187 \quad \text{and} \quad T_{eq} = 0.0187 \times 0.1 = 1.87\,\text{ms}$$

The resulting maximum voltage variation is:

$$\Delta v_{dc}^{max} = 0.0186 \times 0.05 = 9.3 \times 10^{-4}\,\text{pu} = 0.093\%$$

The power absorbed by the first two terminals is given by:

$$\Delta p_{1,2}^{max} = -\frac{0.0187}{0.05} \times 0.05 = -0.0187\,\text{pu}$$

The last converter also has to absorb some power because it is now participating in voltage regulation. The amount of power is:

$$\Delta p_{3}^{max} = -\frac{0.0187}{0.075} \times 0.05 = -0.0125\,\text{pu}$$

The amount of power injected for the service is thus reduced by Δp_3^{max}, i.e. only $0.05 - 0.0125 = 0.0475$ pu power is available for the service. This can reduce the effectiveness of the service. In this case, the damping capability is proportional to the available power until maximum possible damping is achieved. Thus, reducing the available power can reduce the damping of the oscillation.

7.3.2 Simulation of a POD case

This case study presents analysis and simulation results demonstrating the propagation of active power variations due to POD. Simplified calculations are presented first, followed by time-domain simulation results. The study, presented in [11], was performed using time domain simulation on a test system shown in Fig. 7.2 [11]. Parameters associated with the four converters in the test system are given in Table 7.1.

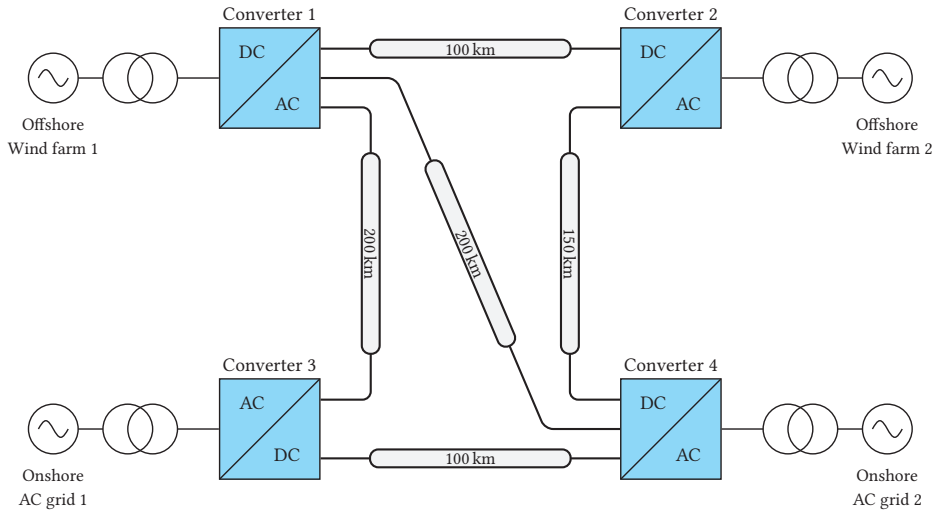

Figure 7.2: A four-terminal test grid [102].

The system consists of two offshore wind farms connected to converters 1 and 2, and two onshore grids connected to converters 3 and 4. All the four converters are MMCs, and they are controlled using the energy control method proposed in Chapter 4. The outer loop for the offshore wind farms is in constant power mode, while the onshore converters are controlled in droop mode with droop constant of 5%. The simulation models are built using a detailed average model in *abc* domain. Frequency Dependent-π (FD-π) [51] models were used to represent the dc cables. Calculation of the equivalent aggregate grid parameters is presented first.

Table 7.1: HVDC converter parameters for the four-terminal test system [102].

Parameter	Converters 1, 2, and 3	Converter 4
Base apparent power, S_b	900 MVA	1200 MVA
Base dc voltage, V_b^{dc}	640 kV	640 kV
AC Frequency, f	50 Hz	50 Hz
Arm capacitance, C_{arm}	29.3 µF	39 µF
Arm inductance, L_{arm}	84.8 mH	63.6 mH
Arm resistance, R_{arm}	0.885 Ω	0.67 Ω
Transformer reactance, X_t	17.7 Ω	13.4 Ω
Transformer resistance, R_t	1.77 Ω	1.34 Ω

7.3.2.1 Calculation of voltage variation

Since the converters have two different power ratings, system-level base values have to defined to convert the parameters to a common base. In this case, the base power is chosen to be 900 MW. Thus, the droop constant for Converter 4 has to be adapted to the new base as shown below:

$$\rho_4 = 0.05 \frac{900\,\text{MVA}}{1200\,\text{MVA}} = 0.0375\,\text{pu}$$

The equivalent droop is then calculated as

$$\rho_{eq} = \left(\frac{1}{0.05} + \frac{1}{0.0375} \right)^{-1} = 0.02143$$

The grid capacitance is calculated to be 142 µF by adding all the cable capacitances. In per-unit, this gives $c_g = 0.064$ pu. The equivalent time-constant is then calculated as follows:

$$T_{eq} = c_g \rho_{eq} V_{dc0} = 1.37\,\text{ms}$$

where V_{dc0} is assumed to be 1 pu. Since T_{eq} is small compared to the frequency of oscillation (1 Hz), its effect can be neglected in the calculation of the expected dc voltage variation as shown here.

$$\Delta v_{dc} \approx -\rho_{eq} \Delta p_{ac3} = -0.02143 \Delta p_{ac3}$$

Since Converter 3 is also participating in voltage droop control, Δp_{ac3} should be adjusted as explained in (7.14).

$$\Delta p_{ac3} = \left(1 - \frac{\rho_{eq}}{\rho_3} \right)^{-1} \Delta \hat{p}_{ac3}$$

where $\Delta\hat{p}_{ac3}$ is the net active power variation injected by converter 3. In other words, $\Delta\hat{p}_{ac3}$ is what the converter is requested to generate, but $\Delta\hat{p}_{ac3}$ is what it actually can inject into the system because of droop action. Incorporating the adjusted power variation, the voltage variation can be calculated as shown in (7.15).

$$\Delta v_{dc} \approx -\rho_{eq}\left(1-\frac{\rho_{eq}}{\rho_3}\right)^{-1}\Delta\hat{p}_{acj} = -\frac{\rho_{eq}\rho_3}{\rho_3-\rho_{eq}}\Delta\hat{p}_{ac3} = -0.0375\,\Delta\hat{p}_{ac3} \tag{7.15}$$

This equation will be used in the simulation results to show how these simplified calculations compare to simulations using detailed models.

7.3.2.2 Simulation results

Two test cases will be presented: a base case showing response of the system under normal conditions, and a case involving POD power injection by converter 3 with frequency of 1 Hz. The results are displayed in Figs. 7.3 to 7.5. From the base case (Fig. 7.3), it can be seen that the system exhibits a stable operation under normal conditions. Two reference changes were applied to represent changes in power production from the offshore wind farms (Converters 1 and 2): active power of converter 2 is increased by 120 MW (0.13 pu) at 2 s, while active power of converter 1 is reduced by 120 MW (0.133 pu) at 15 s. All the reference signals are rate-limited by using first-order low-pass filters. It can be noted that the dc voltage increases when the power production from the wind farms is increased. The reverse happened when total power is reduced at 15 s. Since the increase and decrease in power have the same magnitude, the dc voltage is the same before and after the power changes. The change in voltage can be estimated by using the equivalent droop, i.e. $\Delta v_{dc} = \rho_{eq} \times \Delta p_{ac} = 0.0214 \times 0.133 = 0.0028$ pu, which is very close to the one obtained from the simulation (Fig. 7.3).

The effect of a POD controller in converter 3 is emulated by injecting oscillating active power with frequency of 1 Hz and damping of 5%. A more realistic case including electromechanical dynamics of synchronous machines and an implementation a POD controller is presented in Chapter 8. Fig. 7.4 shows the result, which compares the dc and ac powers of converter 3. The difference between the ac and dc powers is because of the losses in the converter. The peak oscillating power $\Delta\hat{p}_{ac3}$ is 0.054 pu, which results in a dc voltage variation of $\Delta v_{dc} = -0.0375 \times 0.054 = -0.002$ pu according to (7.15). This can be compared to the simulation result given in Fig. 7.5, which shows a peak dc voltage variation of −0.0021 pu. The small difference is primarily due to the losses in the system which are neglected in the simplified calculations.

Because of its participation in droop control, converter 4 picks up the power os-

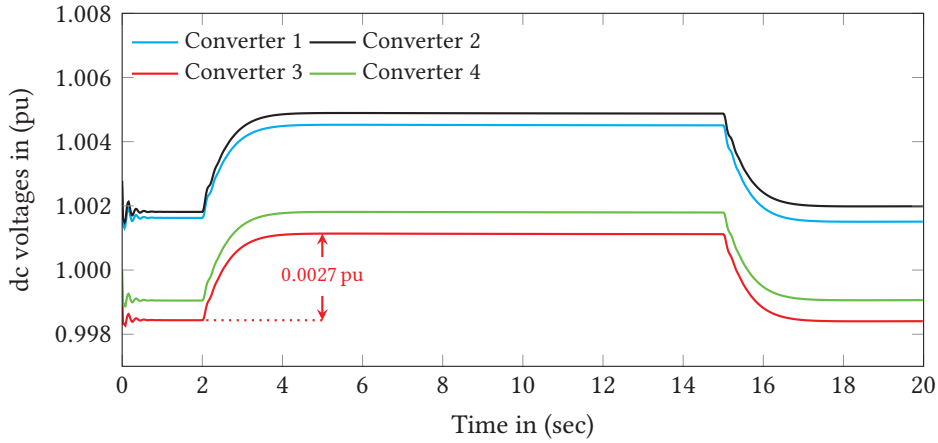

Figure 7.3: Base case performance of the dc grid in Section 7.3.2 during step changes in active power reference.

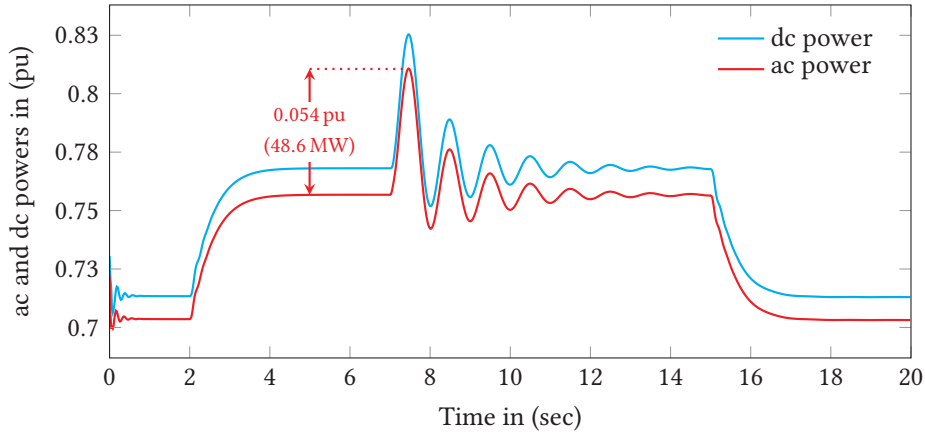

Figure 7.4: Variation of ac and dc powers of converter 3 due to POD.

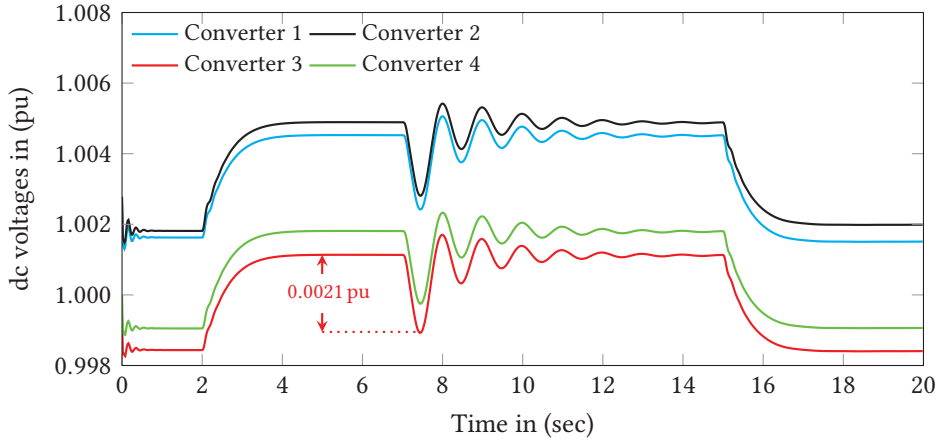

Figure 7.5: Variation of dc voltages due to POD.

cillation $\Delta p_{ac4} = \Delta v_{dc}/\rho_4 = -0.0021/0.0375 = -0.056$. This value is in good agreement with the simulation result in Fig. 7.6.

One important observation is that the oscillating power injected by converter 3 is, in effect, taken from the ac grid connected to converter 4. This means that active power services provided by one terminal in a dc grid can propagate to and disturb other connected ac grids whose interfacing converters are participating in dc voltage regulation. Looking at just the dc voltage, it might seem that the effect of the disturbance is negligible. However, these small variations (−0.002 pu) in the dc voltage cause significant amounts of power variations (−49.8 MW), which can have a considerable impact on the power system.

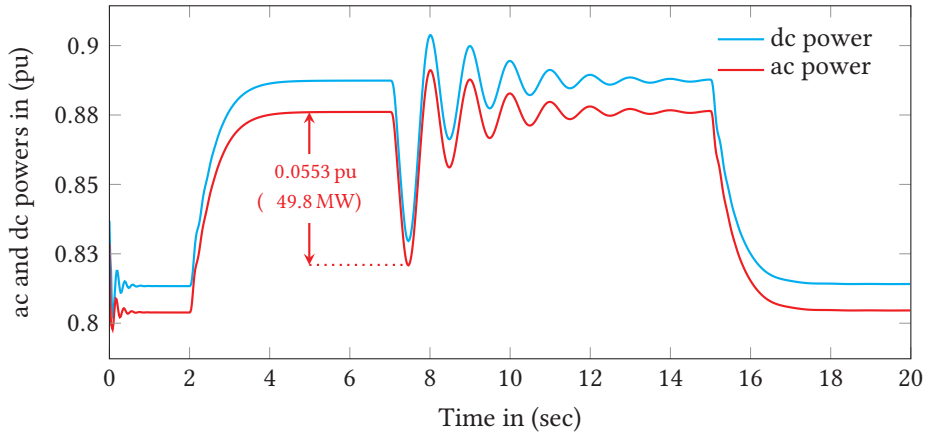

Figure 7.6: Variation of ac and dc powers of converter 4 due to POD in converter 3.

The discussion in this section, together with the analysis and simulation examples, highlighted that ancillary services involving active power can cause dc voltage variations. This, in turn, leads to the propagation of the problem into other connected ac grids that participate in dc voltage regulation. Furthermore, it was also shown that if droop voltage control is enabled on the converter providing the service, there is a reduction in the active power available for the service because the droop controller tries to oppose the changes in dc voltage. The next section presents two methods to utilize the energy stored in the arms of the MMC to avoid or minimize the propagation of active power variations via the dc grid. As will be shown later, this will also solve the second problem where the droop controllers counter the active power injected to provide the services.

7.4 Methods of utilizing the arm energy

Two types of methods for utilizing the arm energy will be presented in this section. The first type involves using the stored energy to counter power variations introduced by services, which is called *Power cancellation*. The second type uses the stored energy to emulate a virtual capacitance that is larger than the physical arm capacitance. This method will be referred to as *Virtual Capacitance Support (VCS)*.

7.4.1 Power cancellation

This method is derived by analyzing the relation between active power balance and the arm energy given by (7.11), which is rewritten as shown in (7.16).

$$\Delta v_{dc} = -\frac{\rho_{eq}}{T_{eq}\mathrm{s}+1}\sum_{j=1}^{m}\left[3c_{aj}\frac{\mathrm{d}}{\mathrm{dt}}\Delta w_j + \Delta p^r_{acj}\right] \tag{7.16}$$

where c_{aj} is the arm capacitance of converter j. Referring to (7.16), it can be seen that the effect of the active power variation Δp_{acj} can be compensated for by varying the derivative of the arm energy with the same magnitude but opposite in sign to Δp_{acj}. The compensation is done locally at terminal j by varying the energy reference as given in (7.17).

$$\Delta w^r_j = -\frac{1}{3c_{aj}}\int \Delta p_{acj}\mathrm{d}t \tag{7.17}$$

Substituting (7.17) in (7.16), it can be seen that the effect of Δp_{acj} can be canceled and the oscillation does not appear in the dc voltage. This is the approach followed in [11]. If $\Delta w^r_j = 0$, the energy controller balances the ac and dc powers of the converter in order to keep the energy constant. However, if the energy reference is varied according to (7.17), the ac power variations are not transferred

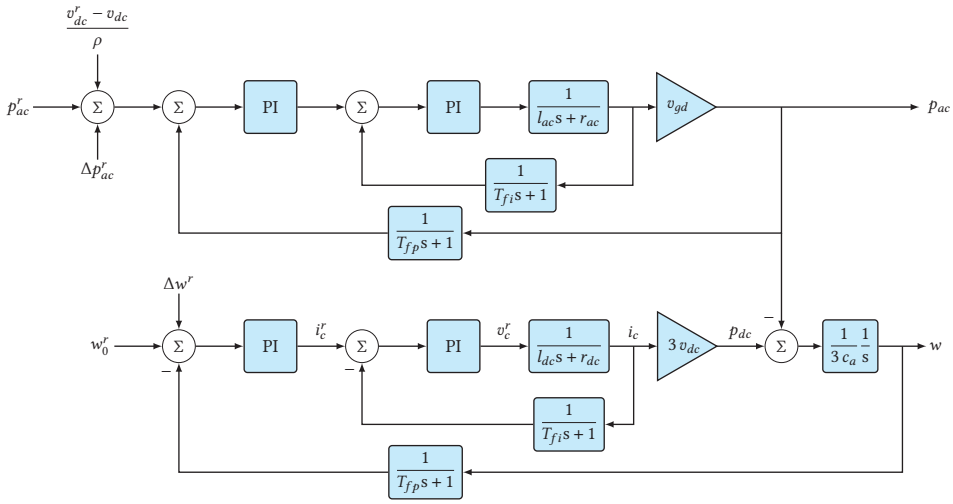

Figure 7.7: Block diagram of power and energy control loops.

to the dc side. Another interpretation is that the contribution of Δp_{ac} is removed from the energy measurement, so the energy controller does not see it, and hence it will not act to balance it to the dc side.

Fig. 7.7 shows a functional block diagram of a controller which implements the power cancellation method. It shows the relevant control loops involved in power balance. The POD controller, not shown in Fig. 7.7, is responsible for calculating the oscillating power (ΔP_{ac}^r) injected into the ac grid to improve the damping of electromechanical modes. The main goal of the controller is to extract the oscillating part of the ac power and feed it to the energy controller as a reference.

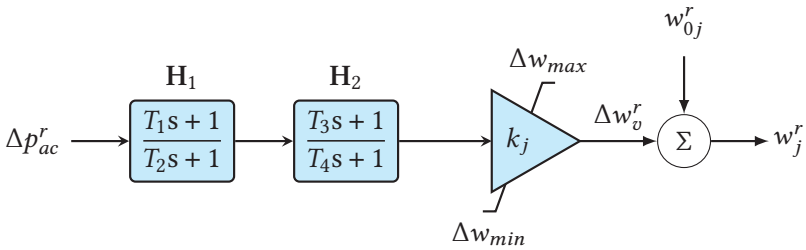

Figure 7.8: Block diagram of the power cancellation scheme [11].

Since the power variation is already available as the output of the POD block, the power cancellation scheme can be implemented by integrating and scaling Δp_{ac} as given in (7.17). However, direct integration is susceptible to drifting (accumulation of static offset over time), which leads to errors. The approach chosen

here is implementations using equivalent transfer functions $\mathbf{H}_1$ and $\mathbf{H}_2$, which are the equivalent transfer functions from P_{ac}^r to P_{ac} and from P_{ac} to W_m, respectively. The term equivalent is used to indicate that these transfer functions represent the gain and phase responses of the complete transfer functions at the oscillation frequency in the form of gain and lead-lag blocks. Such an implementation assumes that the system parameters are accurately known and there is only one mode of oscillation. These assumptions are made to simplify the initial implementation. If the parameters are not accurately known, the gains and phase angles can be tuned by performing tests. The effect of parameter errors will be shown by simulation in the next section.

The limit on the energy variation Δw is placed to avoid large variations in energy (arm voltage) which lead to the disturbance of normal operation if the arm voltage goes too low or stress to the submodules of the arm voltage goes too high. Section 7.5 presents a detailed discussion on how much energy variation is tolerated. A simulation case study demonstrating the effectiveness of the power cancellation method is presented in the next section.

7.4.1.1 Simulation case study

A POD simulation case implementing the power cancellation method using the test system in Fig. 7.2 is presented here. The results here build upon the ones presented in Section 7.3.2. It was shown in Figs. 7.4 to 7.6 that the oscillating power due to POD propagates through the dc grid. When the power cancellation controller is enabled, the POD power is diverted into the arm capacitors instead of the dc side, as is evident from Fig. 7.9. In doing so, the controller can effectively remove the oscillation from the dc side, (see Figs. 7.9 and 7.10). Compared to Fig. 7.4, the peak of the oscillating power has increased by ≈ 17 MW (see Fig. 7.9) when power cancellation is employed. This is because the dc voltage has a negligible amount of oscillation, which means that the droop control does not inject power to counter the power oscillation.

Because of the power taken from the capacitors, the average stored energy exhibits oscillatory response, (Fig. 7.11). This confirms that the oscillation is supplied from the arm capacitors instead of the dc side. Then nominal arm energy is set to $w_0 = 1.31 = 1.15^2$, which gives enough headroom to accommodate the change in energy without going into over-modulation. The requirement behind this headroom is discussed in more detail in Section 7.5. In order to investigate the correlation between energy deviation and oscillation frequency, POD at different frequencies was also simulated. Fig. 7.12 shows the arm energy of converter 2 with the power cancellation controller enabled. It can clearly be seen that the deviation grows with decrease in frequency. This is expected because the arm en-

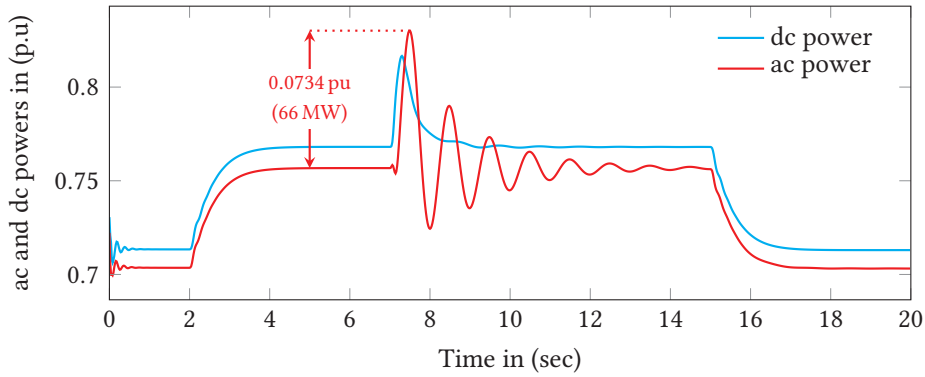

Figure 7.9: AC and dc powers of converter 3 with POD when power cancellation is applied.

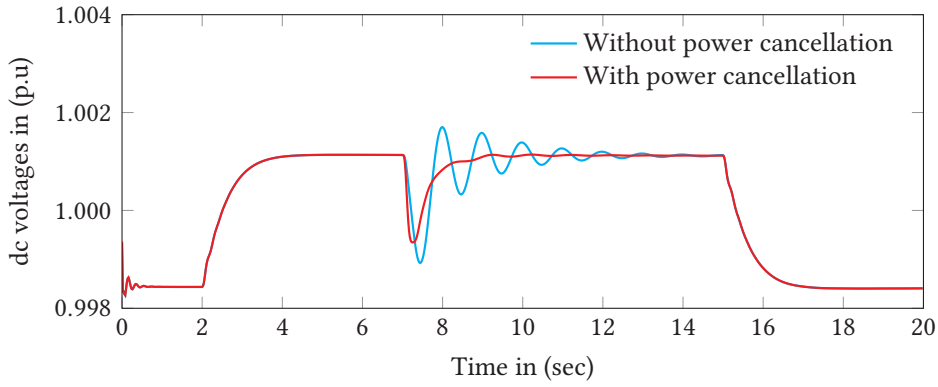

Figure 7.10: DC voltage at converter 3 without and with power cancellation.

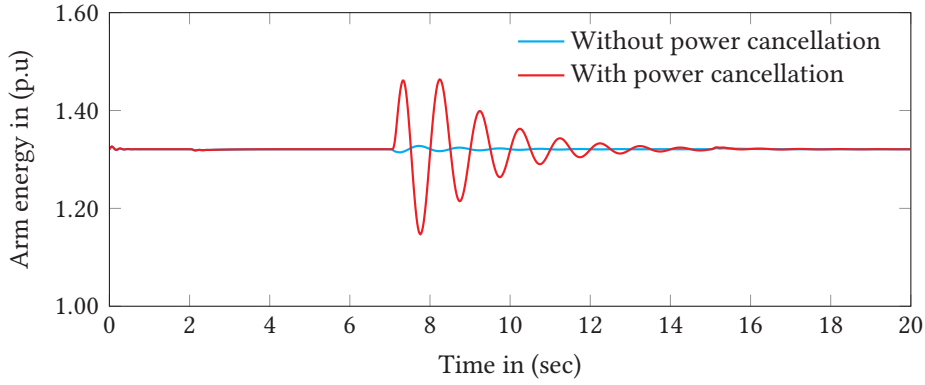

Figure 7.11: Arm energy of converter 3 without and with power cancellation.

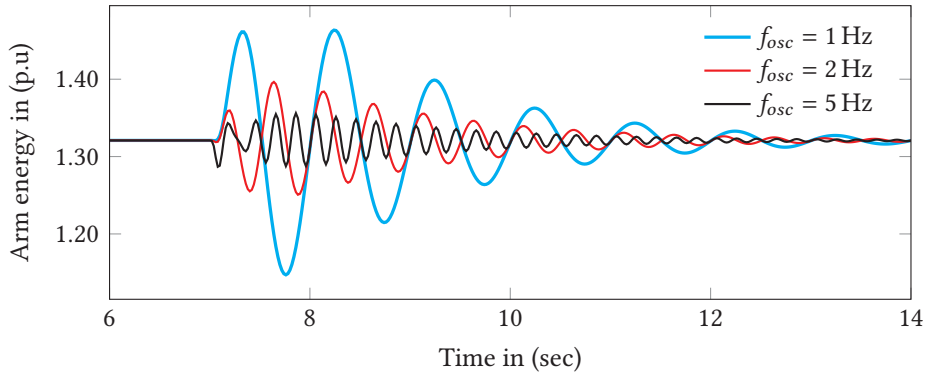

Figure 7.12: Arm energy of converter 3 with power cancellation at different oscillation frequencies.

ergy deviation is the integral of the power oscillation. The corresponding power injections are depicted in Fig. 7.13, where it can be seen that the magnitudes are the same in all the cases.

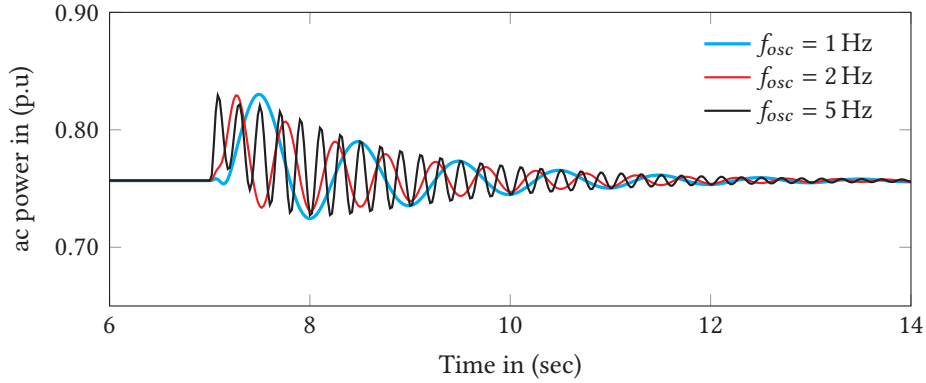

Figure 7.13: ac power of converter 3 with power cancellation at different oscillation frequencies.

The power cancellation controller block output is limited to $\approx \pm 0.32\ pu$, which is equivalent to ±0.15 pu limit on the arm voltage. These values are chosen to keep the arm energy above 1 pu in all cases. Fig. 7.14 shows how the system responds when the energy deviation is larger than the limits. It can be seen that the simple limiter (which is a simple clamping limiter) is able to keep the energy deviation within the specified limits. However, the dc voltage (Fig. 7.15 exhibits a larger magnitude distortion during the period when the output is limited. The second option to limit the output is to reduce gain of the power cancellation controller, which in effect reduces the amount of power diverted into the capacitors. This

results in a smoother limit but at the cost of some oscillation in the dc voltage, (Fig. 7.15). Combining the two approaches, dynamic adjustment of the gain with simple limiter on the output can give better results.

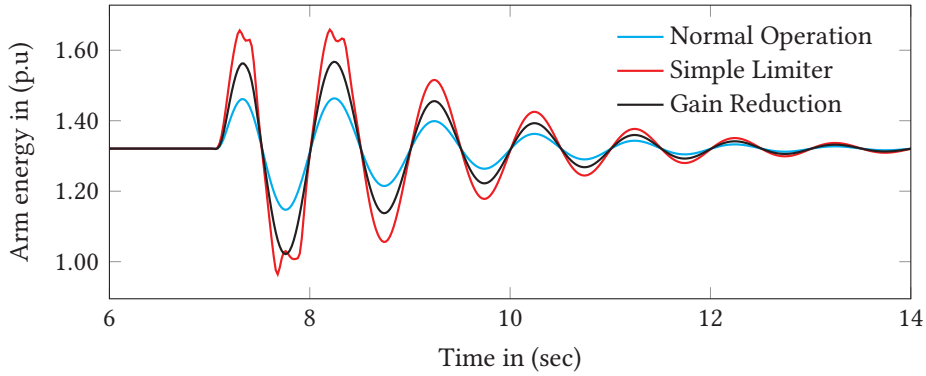

Figure 7.14: Effect of output limit on power cancellation: arm voltage of converter 3.

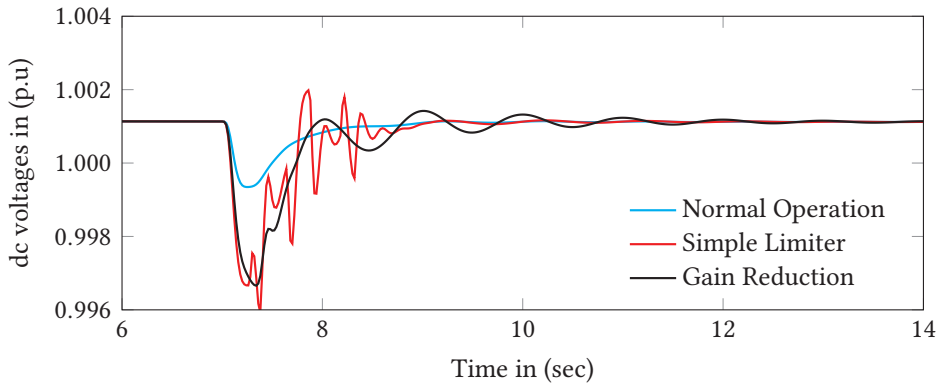

Figure 7.15: Effect of output limit on power cancellation: dc voltage at converter 3.

Finally, the effect of parameter inaccuracies is studied. Parameter errors result in either gain or phase error in the oscillation. The effect of phase angle error is shown in Fig. 7.16. The effect of gain error is similar to the gain reduction case in Fig. 7.14. The main consequence is that some of the oscillating power is taken from the dc side, thus resulting in dc voltage oscillation, Fig. 7.17. This implies that the proposed scheme can work well even with significant parameters errors. Further improvement can be gained by tuning the parameters from test results.

7.4.2 Virtual capacitance support

It was shown in the previous section that the power cancellation method can effectively divert power distortions associated with the ac side services into the

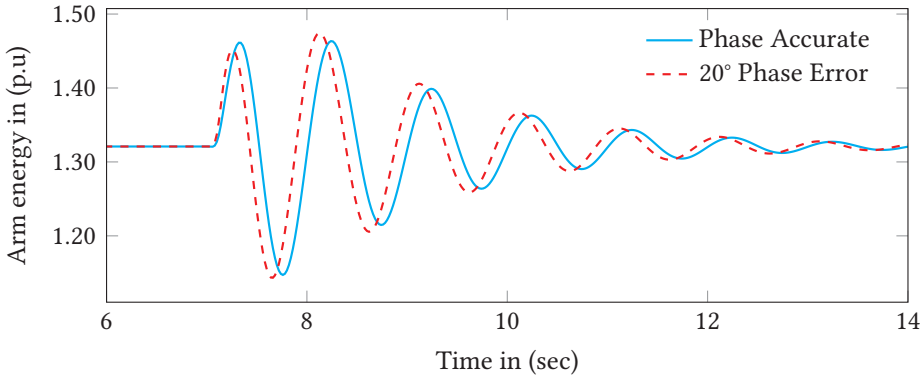

Figure 7.16: Effect of phase angle error: : arm voltage of converter 3.

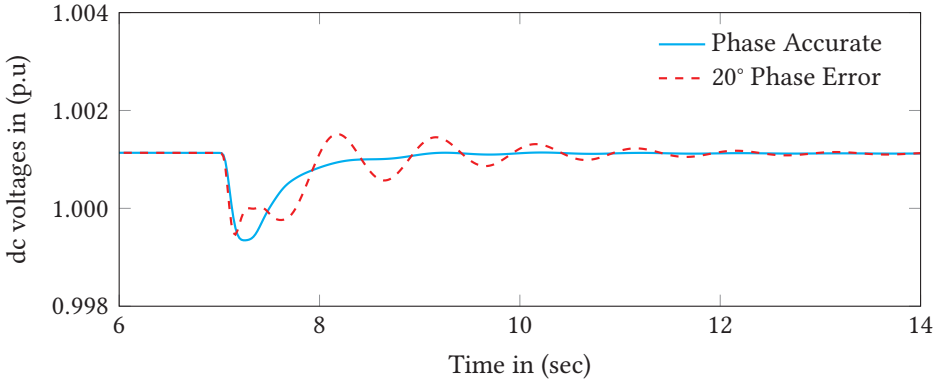

Figure 7.17: Effect of phase angle error: dc voltage at converter 3.

submodule capacitors of the MMC. It is a localized solution which acts at the source to prevent the distortion from entering the dc side. While this is an advantage in terms of solving the problem at the source, the localized nature of the method can also be a shortcoming in a dc gird where multiple converters can be coordinated to provide a larger energy storage capability. It is difficult to implement such a distributed approach using the power cancellation method because it is heavily reliant on local measurements. This means that the measured signals have to be communicated among the converters, which leads to significant delays depending on the distance. Therefore, an alternative approach is considered here. Instead of canceling the effect of the disturbances, this method works on strengthening the dc grid by increasing the effective dc capacitance.

Ref. [107] presents one such approach where the arm energy reference is varied proportionally to the stored energy in the dc grid. This virtually connects the arm capacitance in parallel with the grid capacitance. This approach will subsequently be referred to as Fixed Capacitance Support (FCS), since it increases the grid capacitance by a fixed amount (i.e. the arm capacitance). The per-unit implementation of this approach is given by (7.18) where k is a control parameter deciding the amount of additional capacitance obtained. Selection of the value of k is discussed in the following sections.

$$w_j^r = k_j \cdot v_{dc}^2 = w_j \tag{7.18}$$

$$\frac{\mathrm{d}}{\mathrm{dt}} w_j = 2 \cdot k_j \cdot v_{dc} \frac{\mathrm{d}}{\mathrm{dt}} v_{dc} \tag{7.19}$$

The aggregate dc grid dynamics are given by (7.5), which is repeated here in (7.20) for quick reference.

$$c_g \frac{\mathrm{d}}{\mathrm{dt}} v_{dc} = -\sum_{j=1}^{m} \left[\frac{3c_{aj}}{v_{dc}} \frac{\mathrm{d}}{\mathrm{dt}} w_j + \frac{p_{acj}^r}{v_{dc}} - \frac{1}{\rho_j} \left(\frac{v_{dcj}^r}{v_{dc}} - 1 \right) \right] \tag{7.20}$$

After substituting (7.19) in (7.20) and rearranging the terms, (7.21) is obtained.

$$c_{eq} \frac{\mathrm{d}}{\mathrm{dt}} v_{dc} = -\sum_{j=1}^{m} \left[\frac{p_{acj}^r}{v_{dc}} - \frac{1}{\rho_j} \left(\frac{v_{dc}^r}{v_{dc}} - 1 \right) \right] \tag{7.21}$$

$$where \quad c_{eq} = c_g + \sum_{j=1}^{m} 6 \cdot k_j \cdot c_{aj}$$

From (7.21), it can be seen that the grid capacitance is effectively increased. Each MMC contributes by inserting 6 of its arm capacitors scaled by the respective k_j. In order to analyze the method, (7.21) is linearized around an operating point

where the sum of active power references, p^r_{acj} is 0 and $v^r_{dc} = v_{dc} = v_{dc0}$. Following the procedure in Section 7.2, the transfer function from Δp_{acj} to Δv_{dc} can be calculated as given in (7.22).

$$\Delta v_{dc} = -\frac{\rho_{eq}}{T_{eq}s + 1} \sum_{j=1}^{m} \Delta p^r_{acj} \tag{7.22}$$

$$\text{where} \quad \rho_{eq} = \left(\sum_{j=1}^{m} \frac{1}{\rho_j} \right)^{-1} \quad \text{and} \quad T_{eq} = c_{eq} \cdot \rho_{eq} \cdot v_{dc0}$$

Equation (7.22) indicates that any disturbance in the active power passes through an equivalent low-pass filter with time-constant T_{eq} before appearing on the dc voltage. Therefore, a large value of T_{eq} (in the order of seconds) is desirable in order to achieve good attenuation in the frequency range of interest. For example, to ensure more than a factor 5 attenuation at 1 Hz, T_{eq} has to be greater than 800 ms. This requires the gains k_j to be in the order of hundreds since the capacitances, in pu, are in the order of a few milliseconds (≈70 ms for the test system) and ρ_{eq} is in the order of few percent (1% to 5%). However, this is unrealistic because the average arm voltage will be equal to $\sqrt{k} \times v_{dc}$. This fact restricts the value of k to be close to 1, which makes the FCS ineffective for this application. The next section discusses an alternative approach which offers better performance.

7.4.2.1 Emulation of virtual capacitance

The main limitation of the FCS scheme is that the gain has to be close to 1. This limitation can be avoided by applying the amplification gain k_j to the deviation in dc voltage, Δv_{dcf}, over a desired frequency range (0.2 Hz to 2 Hz) instead of the complete signal. The energy reference is then modified as shown in (7.23).

$$w^r_j = w^r_{0j} + k_j \cdot \Delta v^2_{dcf} \tag{7.23}$$

where w^r_{0j} is a reference related to the average arm voltage, which is constrained such that the arm voltage is close to v_{dc}. The scheme creates the same effect as the FCS, but now there is less restriction on the gain. It provides capacitance support only during transients over a desired frequency range. This method is referred to as VCS. The term virtual is used because this method does not just insert the arm capacitance like the FCS method, but rather provides an equivalent capacitance which is considerably larger than the physical arm capacitance over the frequency range of interest.

This method requires separation of the desired frequency components, Δv_{dcf}, from the measured signal, v_{dc}. This can be achieved by using the proposed scheme shown in Fig. 7.18. The first stage is a washout filter to remove the dc components followed by a low-pass filter to limit the gain at high frequencies. The

overall transfer function resembles a band-pass filter. It is important to have low phase shift in the pass band. Therefore, the filters are designed to give zero phase shift at 1 Hz i.e. the middle of the desired interval (0.2 Hz to 2 Hz). In addition, phase adjustment can be made by using lead-lag filters.

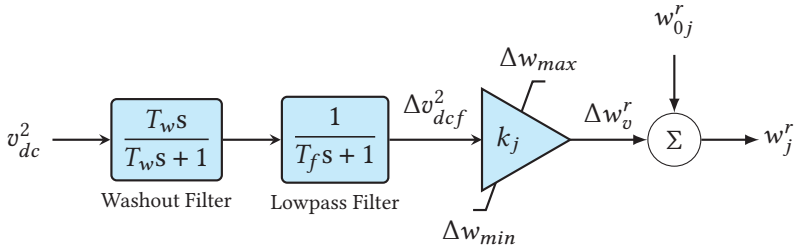

Figure 7.18: Block diagram of the VCS scheme [12].

The upper limit on the gain is due to the output saturation in Fig. 7.18. Once the output saturates, the converter immediately stops providing the capacitance support. This is because the current injection is proportional to the derivative of the stored energy, (see (7.3)). Since the stored energy is related to the arm voltage ($w = v^2$), the limits are coupled to the design of the converter. The upper limit is defined by the maximum voltage at which the arms can be operated, which is, in turn, defined by the maximum continuous submodule voltage rating. The lower limit, on the other hand, is constrained by the lowest possible arm voltage without causing over-modulation. Over-modulation occurs when the reference inserted voltage is greater than the sum of capacitor voltages. In order to accommodate downward changes in the stored energy without causing over-modulation, the arm voltage should be operated with a headroom above the dc voltage. The MMC is normally designed such that the average arm voltage equals the dc voltage. Therefore, the headroom requires either additional submodules or operation of each module at a higher voltage. The first option can be more attractive in some cases because most MMCs are equipped with redundant sub-modules. However, as the number of modules increases, the capacitance decreases because of the series connection. So, the second option offers a higher gain for the same percentage increase [11]. Section 7.5 discusses the required amount of additional energy storage and the two ways of obtaining this extra storage.

The implementation of the VSC shown in Fig. 7.18 introduces additional transfer functions, which can change the response. The effect of these transfer functions is analyzed in the next section.

7.4.2.2 Frequency response analysis

The filter stage in Fig. 7.18, which is used to extract the dc voltage variation Δv_{dc}, introduces additional dynamics in the response of the dc grid with VCS. Under ideal conditions where Δv_{dc} is extracted without any additional dynamics, the dc grid will have a first-order response with time-constant T_{eq}. The effect of the gain and filter parameters of VCS on the frequency response of the grid are analyzed in this section. The four-terminal test grid introduced in Section 7.3.1 (Fig. 7.2) is used in the analysis.

As discussed in the previous section, the time-constants of the filter stage are chosen to minimize the gain reduction and phase shift in the frequency range of interest (0.2 Hz to 2 Hz). The low-pass filter attenuates the output of the VCS scheme for high-frequencies outside the range of interest. This upper limit is defined such that the VCS scheme does not affect stable operation of other controllers in the system. In light of this, the time-constant of the low-pass filter is chosen to be $T_f = 100$ ms. The washout filter time-constant is chosen to be $T_w = 2$ s so that the low-frequency (close to dc) components are removed and the phase shift in the frequency range of interest is minimized. Figure 7.19 shows the transfer function of the filter stage with the chosen parameters. It can be noted that the transfer function has a significant phase variation around the center frequency. This variation can be flattened by using lead-lag phase compensation as shown in Fig. 7.20, which is achieved by applying a phase boost of 30° at 1 Hz and a phase reduction of 30° at 0.1 Hz. Higher-order filters with better behavior both in the pass-band and stop-band can be designed to improve the system response. This is not covered in this thesis because the purpose here is to introduce the concept, and the filter arrangement in the VCS scheme suffices for this purpose.

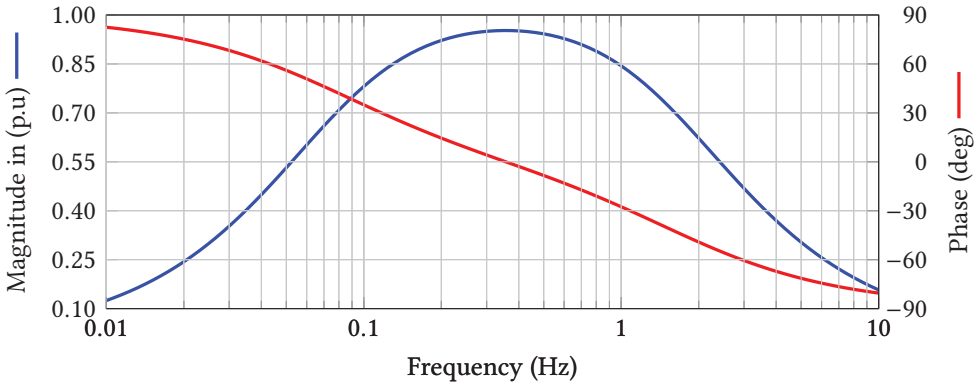

Figure 7.19: Bode plot of the filter stage in the VCS scheme with $T_w = 5$ s and $T_f = 20$ ms.

The transfer function from Δp^r_{acj} to Δv_{dc} (given by (7.22)) is calculated for the four-

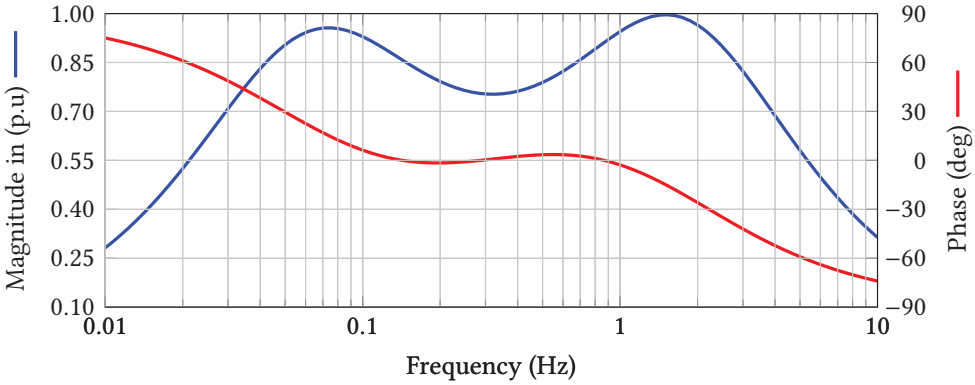

Figure 7.20: Bode plot of the filter stage in the VCS scheme after phase compensation.

terminal test system (Fig. 7.2) by taking the filter stage into account. Figure 7.21 shows the frequency response of the dc grid for different filter parameters with the gain set to $k_j = 100$. It is assumed that all the four converters are participating in the VCS scheme. The dc grid has an equivalent dominant second-order low-pass transfer function when the filter stage is taken into account. It can be seen that higher values of T_w give better performance in terms of attenuation. It should be noted, however, that higher values of T_w also mean that the VCS responds to lower frequencies (close to dc), which is not desired because the energy storage requirement is significantly increased. Therefore, $T_w = 2\,\text{s}$ is chosen to give a good compromise between the two requirements.

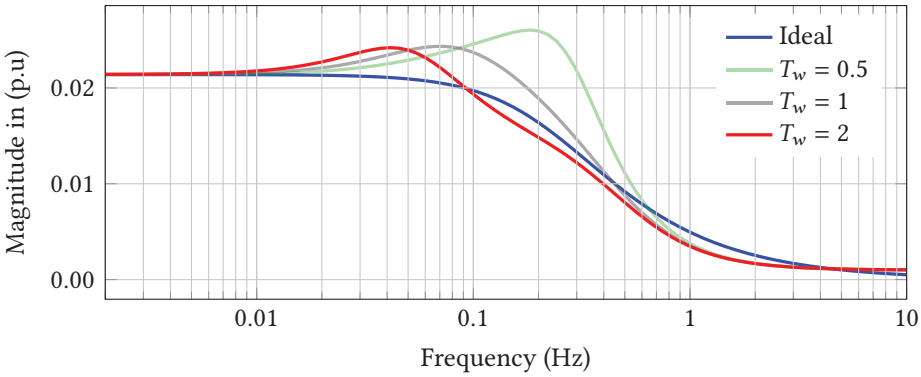

Figure 7.21: The effect of the washout filter time-constant T_w on the frequency response of the VCS scheme with $k_j = 100$.

The last parameter in the VCS scheme is the gain k_j which determines how much virtual capacitance is provided by each converter. When $k_j = 0$ (i.e. base case), there is negligible attenuation in the frequency range 0.2 Hz to 2 Hz. The same

observation applies to the FCS scheme ($k_j = 1.15$), which makes it ineffective for the application. A considerable amount of attenuation is achieved with higher gain values of $k_j = 100$.

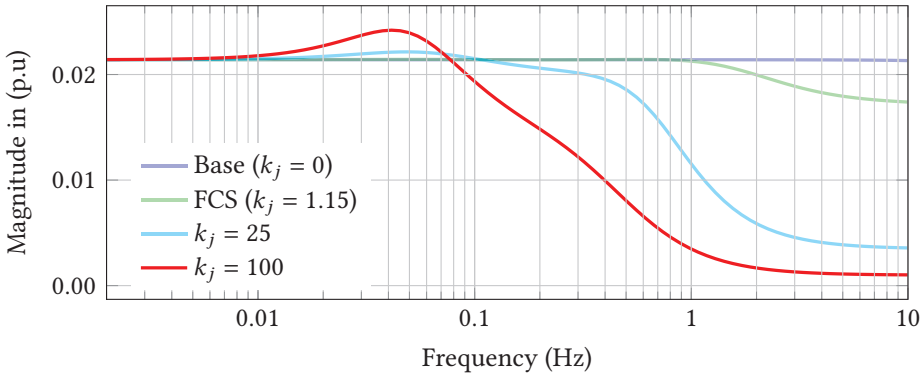

Figure 7.22: The effect of the gain k_j on the frequency response of the VCS scheme.

As demonstrated in this section, the response of the dc grid to power variations is greatly influenced by the parameters of the VCS scheme. It is also dependent on the grid parameters (cable lengths, arm capacitance values) and the number of converters participating in the scheme. It is, therefore, important that analyses similar to the one presented in this section be performed before selecting the parameters. The next section presents simulation case studies for different applications using the same test system and the parameters selected in this section.

7.4.2.3 Simulation case study: POD

In this section, the VCS method is applied to a POD case study using the four-terminal test grid (Fig. 7.2). The converters are controlled using compensated modulation, which is discussed in Chapter 4. The effect of the POD controller is emulated by injecting oscillating active power into the ac side of converter 3. The goal of the case study is to demonstrate the effectiveness of the VCS method. As explained in earlier sections, the arm energy (voltage) exhibits oscillation when it absorbs the POD power. Consequently, the arm energy must have a headroom above the dc voltage in order to accommodate the downward variations in energy. In this case study, the headroom is chosen to be 15% giving an arm voltage 1.15 pu, which gives a nominal arm energy of $1.15^2 = 1.31$ pu. Section 7.5 discusses how this headroom is sized and how it can be realized.

Converters 1 and 2 are connected to offshore wind farms, while converters 3 and 4 are connected to onshore ac grids. The power-flow condition is such that the wind farms are producing 800 MW and 600 MW, and the onshore grids are absorbing

650 MW and 746 MW. Power flow from the dc side into the ac side is positive by convention. The offshore converters are controlled in constant power mode, while the onshore converters are participating in dc voltage droop regulation with a droop constant of 5%.

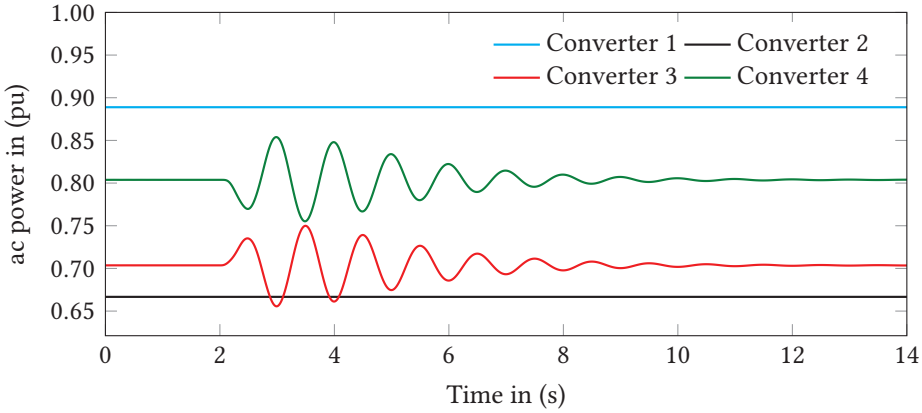

Figure 7.23: AC powers of the four converters during POD injection at converter 3. The sign of powers at converters 1 and 2 are inverted.

Per-unit powers of the four converters are shown in Fig. 7.23, where the signs of the powers at the offshore converters have been inverted to fit them in the same scale as those of the onshore converters. The POD power injection is enabled at $t = 2\,\mathrm{s}$ at converter 3. Since the offshore converters are participating in neither dc voltage regulation nor POD, their power flows are constant throughout the simulation period. Therefore, the oscillating power injected by converter 3 is taken from the ac grid of converter 4.

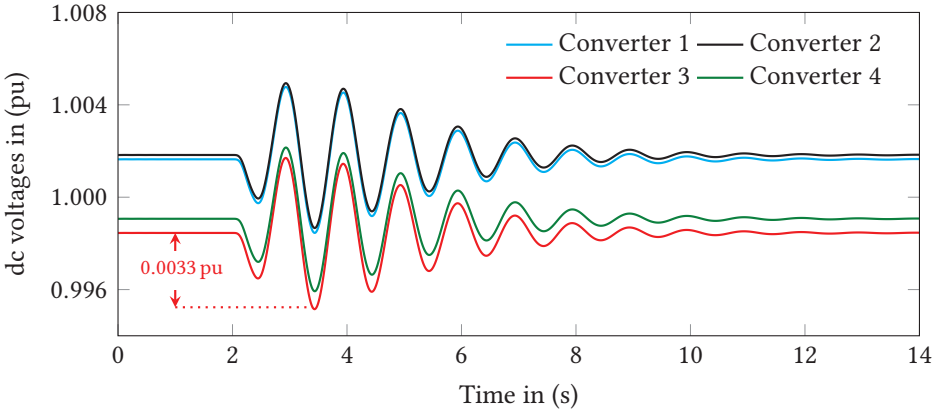

Figure 7.24: DC voltages during POD injection at converter 3.

Fig. 7.24 shows the corresponding dc voltages, which exhibit oscillation with magnitudes of upto 0.33%. It is this voltage oscillation that results in the propagation of the power oscillation to converter 4. This can be reduced by implementing the capacitance support methods, FCS and VCS. Comparison of these capacitance support methods using the dc voltages is given in Fig. 7.25. It can be seen that the FCS method has only a negligible effect on the dc voltage variation. In contrast, the oscillation is significantly attenuated when VCS is used. This is in agreement with the frequency domain analysis in Section 7.4.2.2. The ac powers at convert-

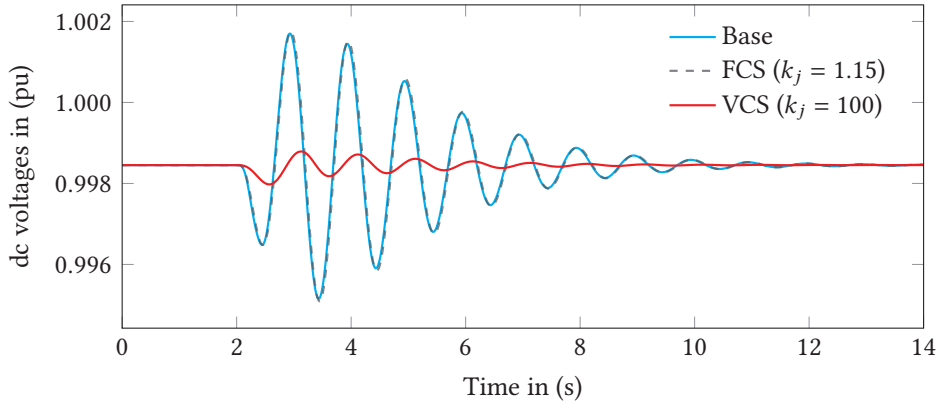

Figure 7.25: Comparison of capacitance support methods: dc voltage during POD injection at converter 3.

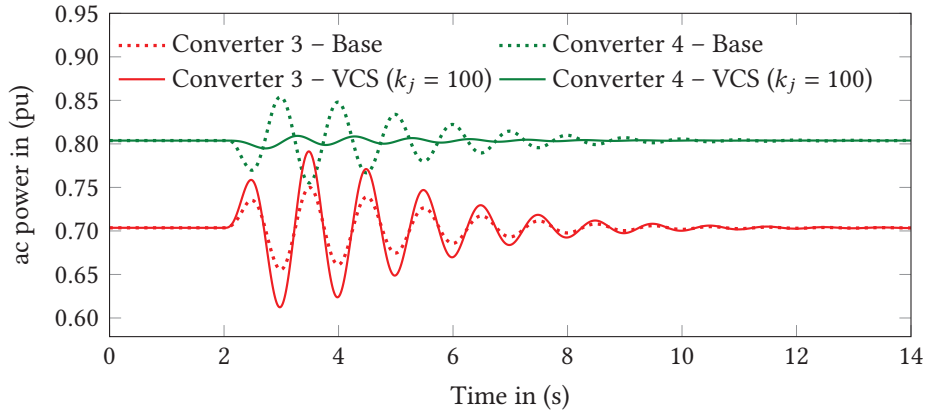

Figure 7.26: AC powers of converters 3 and 4 during POD injection at converter 3 without and with VCS.

ers 3 and 4 are shown in Fig. 7.26, which shows that VCS significantly reduces the amount of oscillating power that propagates toward the ac side of converter 4. The oscillation is diverted into the arm energy which shows increased oscilla-

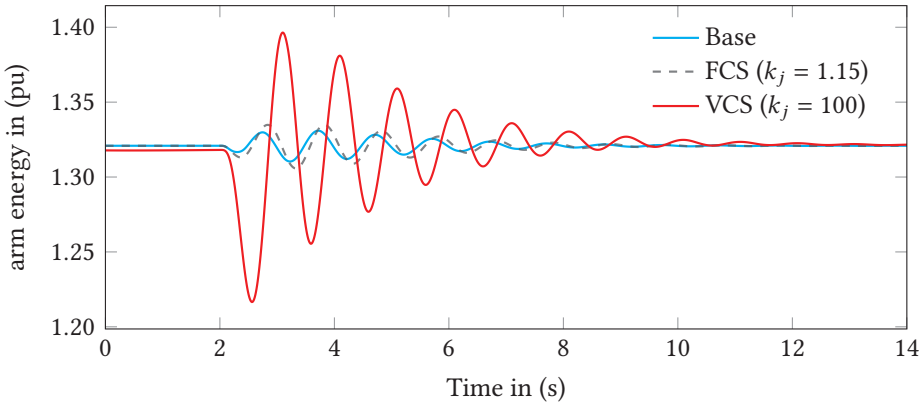

Figure 7.27: Comparison of capacitance support methods: arm energy during POD injection at converter 3.

tion when VCS is applied, as can be seen in Fig. 7.27. The ac power at converter 3 increases when VCS is enabled because the power reduction due to droop action is lower since the dc voltage variation is reduced.

Distribution of the arm energy utilization among the four converters can be highlighted by examining the variations in dc power without and with VCS in Fig. 7.28 and Fig. 7.29, respectively. The steady-state values are removed from the dc powers in order to emphasize the relation between the power variations. In the base case, Fig. 7.28, the oscillating power is exchanged between converters 3 and 4 as pointed out earlier.

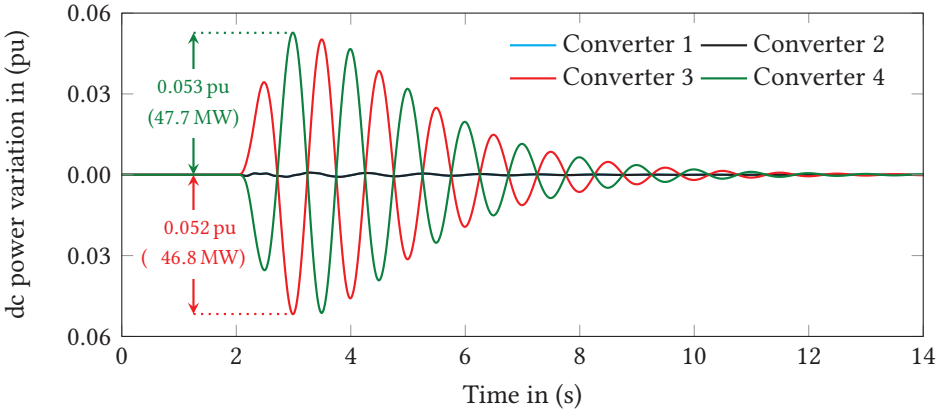

Figure 7.28: DC power variations of the four converters during POD injection without VCS.

When VCS is enabled, all the converters contribute in supplying the oscillating

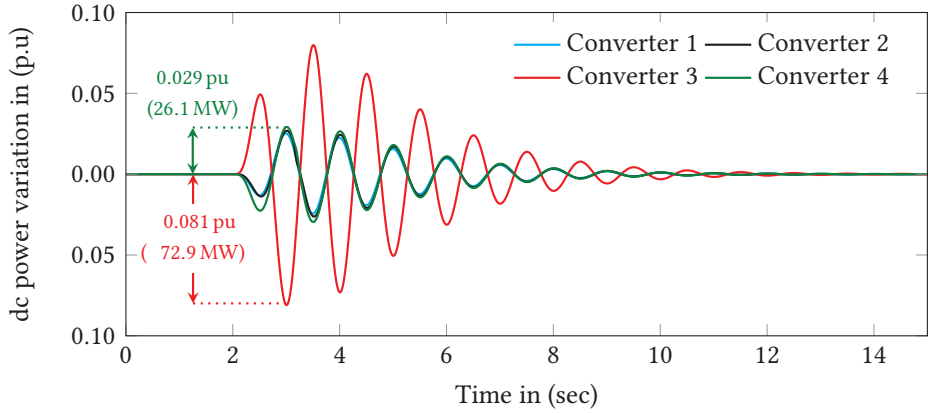

Figure 7.29: DC power variations of the four converters during POD injection with VCS.

power, see Fig. 7.29. Converters 1, 2, and 4 provide approximately a third of the dc power at converter 3. The differences are primarily due to transmission losses. The capacitors of converter 3 cover the remaining part of the ac power. Because of the interaction between droop control and POD, the power contribution at converter 3 is different from the others. This is clearly visible in the arm energy plot (Fig. 7.30), which shows that arm energy variation in converter 3 is shifted and has lower magnitude. Approximately equal energy variations are observed when the POD power is injected by a converter which is not participating in dc voltage droop control.

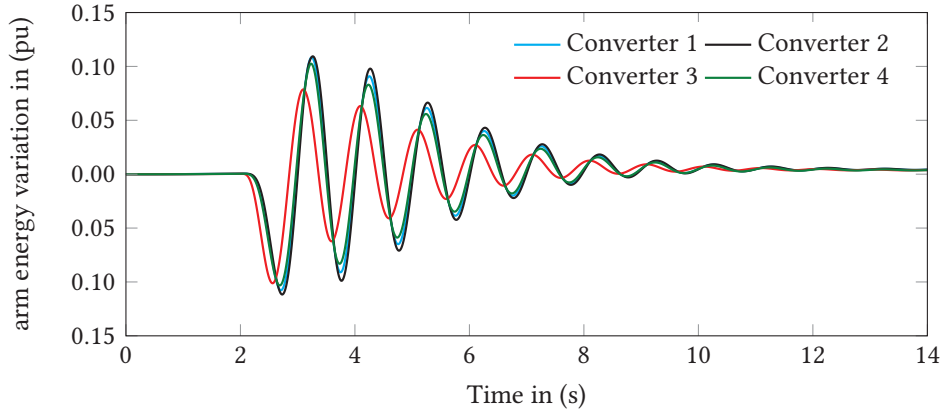

Figure 7.30: Arm energy variations of the four converters during POD injection with VCS.

In summary, this case study has demonstrated that VCS can be effectively used to

absorb power oscillations arising from a POD service. This prevents the oscillation from propagating to the other connected grids, where they can cause power quality issues or excite electromechanical oscillations of similar frequencies. The VCS is a distributed approach where all capable terminals can participate in the support. Consequently, higher power levels can be absorbed by using this approach compared to the power cancellation method.

7.4.2.4 Simulation case study: wind farm power smoothening

Wind power has taken an increasing share of the total energy production mix over the past few decades and has brought forth several challenges in grid operation and planning. One such challenge is the variability of wind, which translates into power fluctuations [108]. These fluctuations can be studied in three time-scales: long-term, short-term variations, and rapid variations. Long-term variations refer to diurnal and seasonal variations in wind speed, which are relatively predictable [109]. Short-term refers to time-scales in the order of minutes to a few hours. They cause challenges related to power balancing and frequency regulation. Rapid changes, on the other hand, refer to fast variations within a second to a few seconds. Such variations can be attributed to wind gusts, tower shadow, and fast transients in the collection grid.

These variations pose different power quality challenges in the grid; such as rapid voltage and frequency variations. Since short-term and rapid changes are difficult to predict, energy storage solutions are being proposed to smoothen the variations out [110]. As large, far-offshore wind farms are usually connected to the grid using an HVDC transmission system, the energy storage capability of the MMC can be considered for such applications. This section presents a case study which deals with reducing rapid variations in wind power using the VCS method. The simulation results are performed using the four-terminal dc grid [102] that has been used throughout this chapter.

A random power fluctuation, representing rapid wind power variations, is superimposed on the ac power of Converter 2 to emulate the rapid power variations. Fig. 7.31 depicts the ac powers at the four converters. The rapid power variations are introduced at 2 s. Converters 3 and 4 also exhibits the variation because they are participating in dc voltage regulation. The power variations cause a corresponding variation in the dc voltages, as shown in Fig. 7.32.

It can be seen from Fig. 7.33 that the rapid power fluctuation is significantly reduced when VCS is enabled. Consequently, the ac powers of converters 3 and 4 are much smoother with VCS (see Fig. 7.34). The fluctuation is averaged by the arm capacitors, which absorb the fast variations and release a smoother power. This

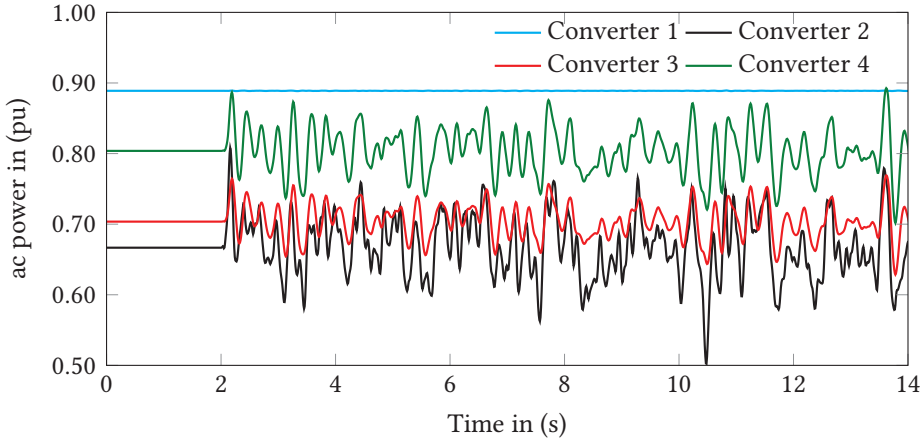

Figure 7.31: AC power variations due to wind farm power fluctuation at converter 2.

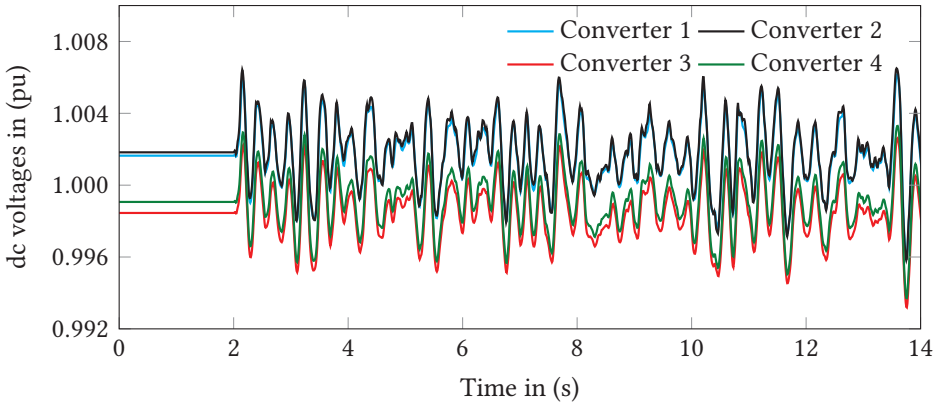

Figure 7.32: DC voltage variations due to wind farm power fluctuation at converter 2.

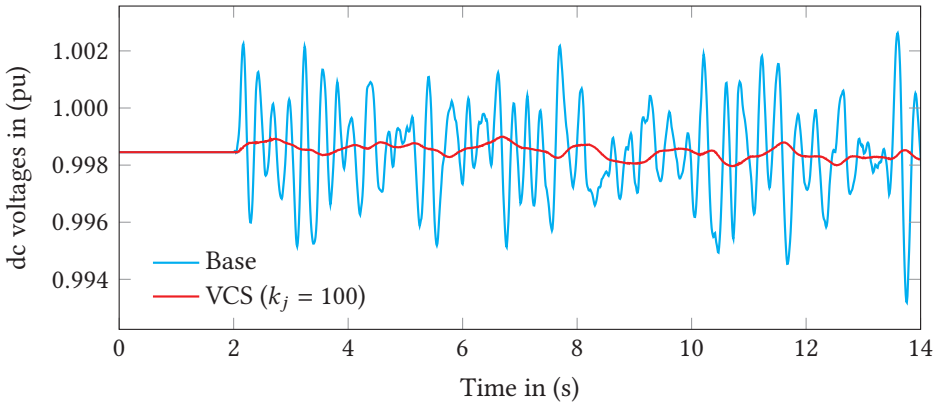

Figure 7.33: DC voltage variation due to wind farm power fluctuation at converter 2 without and with VCS.

can maximize production because the wind farm can generate active power-based on the available wind speed without attempting to maintain a smooth power flow. The arm energy variations due to the rapid power fluctuations are shown in Fig. 7.35.

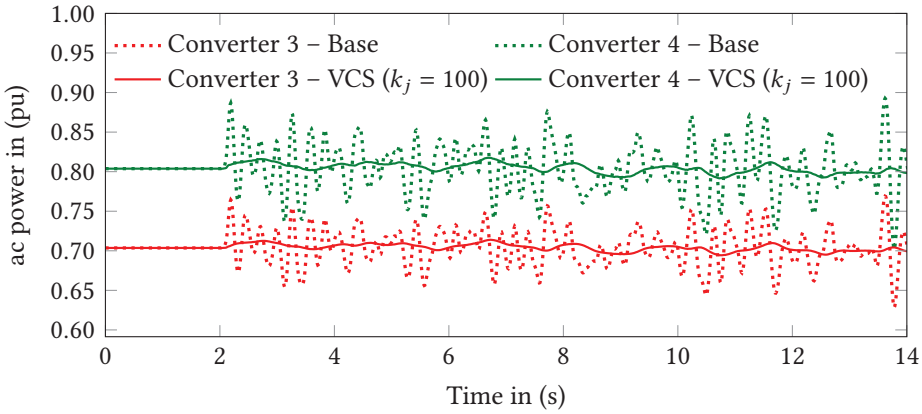

Figure 7.34: AC powers of converters 3 and 4 during POD injection at converter 3 without and with VCS.

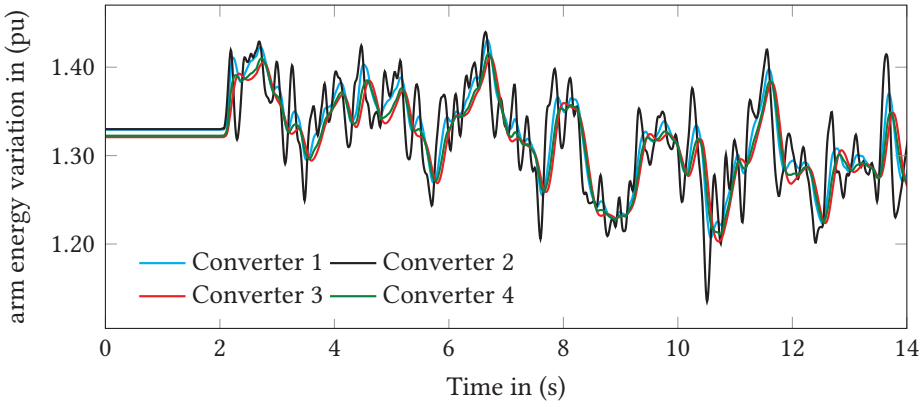

Figure 7.35: Arm energy variations of the four converters due to wind farm power fluctuation with VCS.

The simulation results demonstrated that the VCS can be applied to smoothen active power fluctuations coming from wind farms. VCS can be implemented independently with a focus on rapid variations, or it can complement slower and longer duration energy storage technologies (like batteries) to offer a solution that addresses both rapid and slow power fluctuations.

7.4.2.5 Simulation case study: dc voltage support

Sudden jumps in active power can occur in a dc grid due to a contingency involving the disconnection of several wind turbines at the same time. The purpose of this case study is to investigate how VCS can improve the rate of change of dc voltage when such a contingency occurs. This can be compared with inertia support in an ac system, which controls the rate of change of frequency. The contingency is emulated by step decrease in the active power of converter 1. Two cases are considered based on the amount of power generation lost: −7.5% and −15%.

Active powers during a −7.5% power drop are shown in Fig. 7.36. The power drop is balanced by a reduction in the powers of converters 3 and 4. Converter 4 takes a bigger share because it has a higher power rating and both the converters have the same droop constant of 5%.

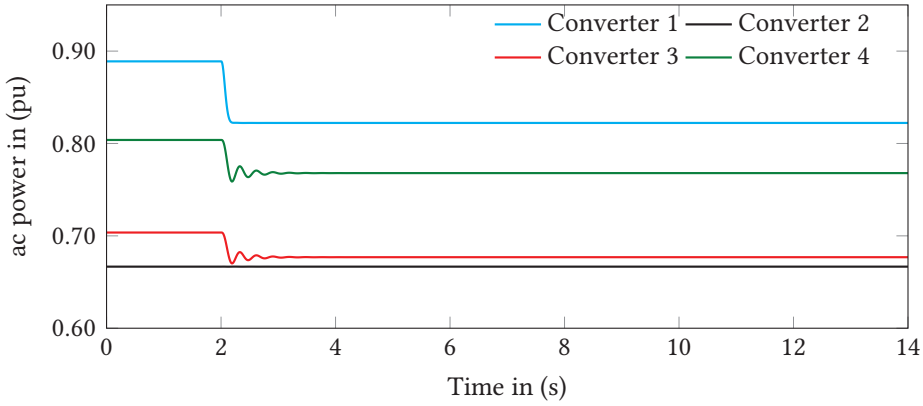

Figure 7.36: AC power variations due to a sudden 7.5% loss of generation at converter 2.

The rate at which the dc voltage drops is determined by the equivalent dc grid capacitance, response time of the converters participating in dc voltage regulation, and the steepness of the drop in power. VCS reduces the rate of change of dc voltage since it increases the dc grid capacitance as shown in Fig. 7.37. Compared to the previous two applications (POD and power smoothening), dc voltage support involves much lower frequencies, which leads to a severe constraint on the amount of power available to provide dc voltage support, particularly during larger power changes. When the change in power is increased from 7.5% to 15%, the available energy for VCS is exceeded midway through the transient as shown in Fig. 7.38. This leads to the reduction of the effective capacitance, which in turn results in an increased rate of change in the dc voltage. The same fig-

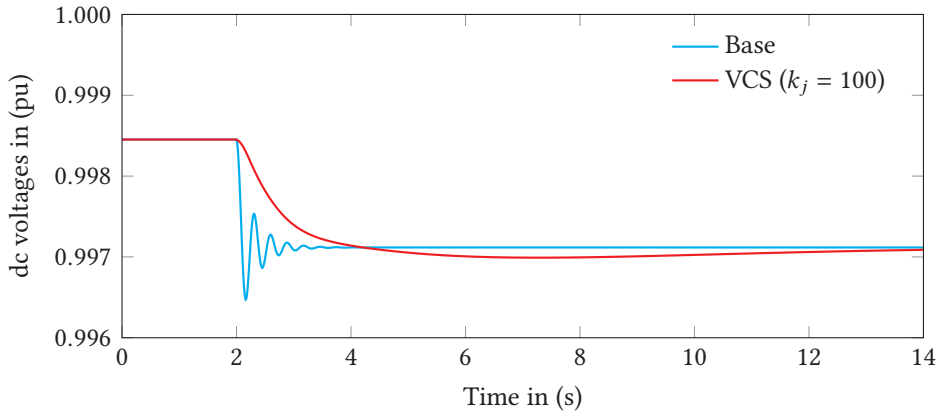

Figure 7.37: The effect of VCS on the rate of change of dc voltage due to a sudden 7.5% loss of generation at converter 2.

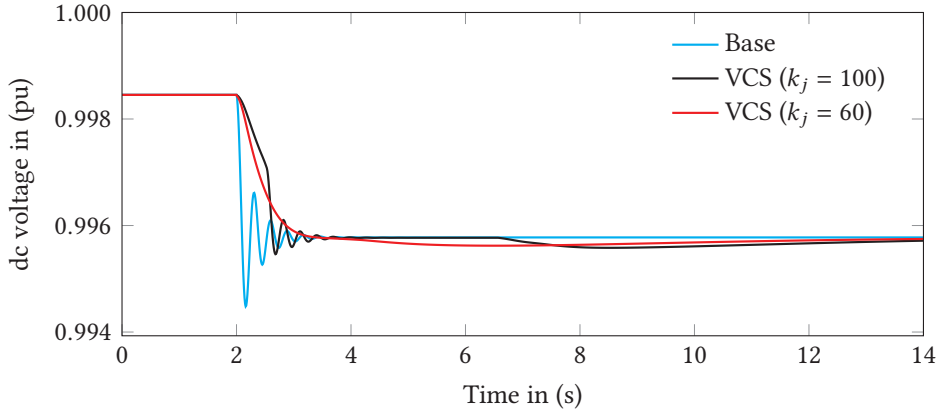

Figure 7.38: The effect of VCS on the rate of change of dc voltage due to a sudden 15% loss of generation at converter 2.

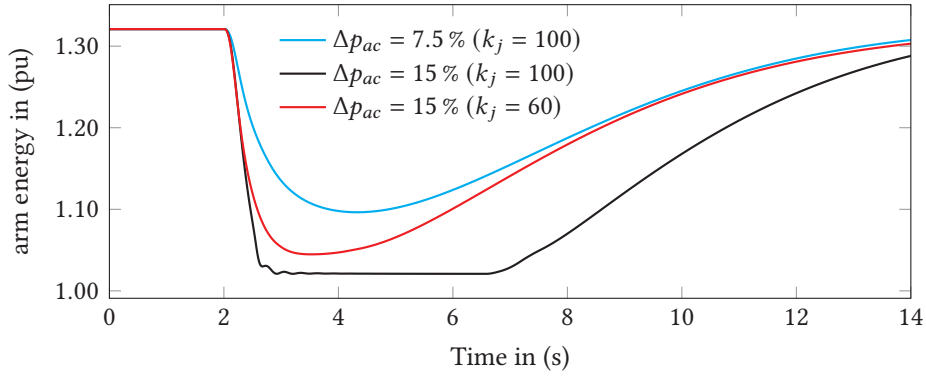

Figure 7.39: Energy variation due to a sudden 15% loss of generation at converter 2 with VCS.

ure shows the dc voltage with a reduced VCS gain. It can be noted that the rate of change is not as good as the original one, but the support is not interrupted. Fig. 7.39 shows the energy variation for the two cases and one more case with a reduced gain. The lower energy variation limit is exceeded in the case of the 15% power change with $k_j = 100$ as discussed earlier. One important aspect here is that the energy changes for this application are significantly higher than the other applications discussed in this chapter. Reducing the gain, like in Fig. 7.39, is not desirable because it also reduces the gain for the other applications. The filter stage in VCS can be designed such that there is less sensitivity at lower frequencies while maintaining the higher gain values in the frequency range for the other applications.

7.4.3 Summary

Two methods of utilizing the MMC energy storage capability to provide active power-based services were explored in the previous few sections. Both methods work effectively in diverting power disturbances associated with services into the arm capacitors of the MMC. This is important because these disturbances can propagate into other connected ac systems causing further problems like power quality issues and electromechanical oscillations. Different philosophies were adopted in the development of the two methods. The power cancellation method aims to cancel the disturbance at the source by removing the effect of the disturbance from the feedback signal of the energy controller. By doing so, the energy control does not transfer the disturbance to the dc side. The Virtual Capacitance Support (VCS), on the other hand, allows the disturbance to be transferred to the dc side, but its effect on the dc voltage is minimized since the VCS increases the effective dc grid capacitance. Thus, the power disturbance transferred to other connected ac grid is also minimized.

Unlike the power cancellation method, VCS is an inherently distributed approach where any terminal which has some reserve energy storage capacity and a dc voltage measurement can participate. This increases the capability of the system in absorbing larger disturbances because the total reserve energy is the sum of available energy in all the participating nodes. Furthermore, VCS can be readily applied to a wider range of applications as opposed to the power cancellation method, which needs to be fine-tuned for each application. This was demonstrated with the simulation case studies, where the VCS method was applied in applications involving POD, wind power smoothening, and dc voltage support. Its versatility makes the VCS method more attractive because it can also handle unforeseen events that cause power disturbance. More detailed analysis and experimental validation of the VCS method are presented in Chapter 8.

One requirement common to both methods is the need for a reserve energy storage capability. It was shown in the case studies that applications with lower frequency content lead to increased storage requirement. The next section discusses topics related to sizing and realization of such reserve energy storage capability with a focus on POD application.

7.5 Energy storage requirement

It has been established in the last few sections that the arm energy exhibits variations when the MMC is providing active power-based services using its energy storage capability. The maximum magnitudes of these variations are determined by the amount of available energy which can be used without affecting *normal* operation. Normal operation is disturbed when the insertion indexes exceed one, which happens when the arm energy (voltage) goes lower than the desired inserted voltage reference. When this takes place, the converter is said to be in over-modulation. Under such conditions, the inserted voltage is constant irrespective of the reference voltage. This means that converter can no longer control its output current. Additionally, the flat-top signal that results from over-modulation can distort the output voltage causing further disturbance to the system.

A first step in avoiding over-modulation is setting the nominal (average) arm voltage with enough headroom above the maximum expected inserted voltage reference. Once the headroom is established, the variations in the arm energy have to be limited to avoid over-modulation. Both the power cancellation and VCS methods enforce the limits by the saturation blocks at their outputs. The upper limit, Δw_{max}, is placed to avoid exceeding the voltage rating of the arms (the submodules), and the lower limit, Δw_{min}, is there to avoid over-modulation. A discussion on how these limits are quantified with a focus on POD application is presented in this section. This is followed by the analysis of two ways of realizing the extra energy storage capacity needed for the service.

7.5.1 Relation between arm energy and active power

The arm energy variations associated with active power variations are quantified by using (7.24), which relates, in per-unit, the arm energy w to the arm power p and the arm capacitance c_a.

$$\frac{\mathrm{d}}{\mathrm{d}t}w = \frac{2}{c_a}p \tag{7.24}$$

The change in the arm energy Δw due to active power imbalance, Δp, is thus given by (7.25), which is obtained by integrating (7.24).

$$\Delta w = \frac{2}{c_a}\int \Delta p \,\mathrm{d}t \tag{7.25}$$

Fig. 7.40 is a simplified depiction of the power injected by a POD controller when an electromechanical oscillation is excited. The resulting energy deviation, as given by (7.25), is the area under the curve. It is assumed that the oscillation mode, on which the POD is applied, is stable. This implies that the area under subsequent half-cycles diminishes with time. Therefore, the worst-case energy deviation is caused by the first swing, which is indicated by the gray area in Fig. 7.40. In practical cases the maximum swing might be the second or third one because of the effect of the washout filter in a POD controller. Nonetheless, the area under the first swing in Fig. 7.40 will give the worst-case estimate because the attenuation due to the washout filter is neglected. The maximum energy deviation, Δw_{max}, can be computed using (7.26). This area is the maximum possible since any phase shift in the waveform results in a smaller area.

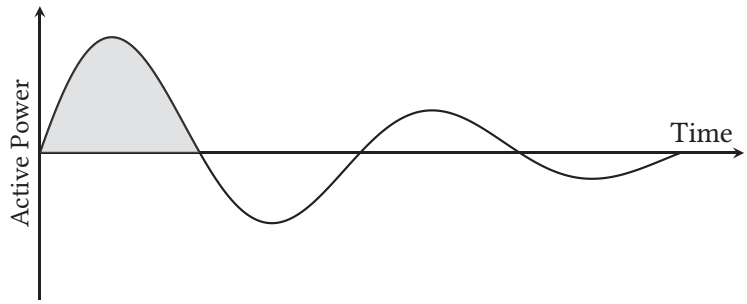

Figure 7.40: An example waveform of power injected by a POD controller.

$$\Delta w_{max} = \frac{2}{c_a} \frac{2\hat{p}}{\omega_{osc}} \tag{7.26}$$

where $\hat{p}$ is peak value of the oscillation. Equation (7.26) over-estimates the deviation since it ignores the effect of damping. This is justified because the damping is not constant, and the intention here is to consider the worst possible case, which is when the damping is zero. The corresponding deviation in arm voltage, Δv_{max}, can be computed, from the fact that $w = v^2$ in per-unit, using (7.27).

$$\Delta w_{max} = \Delta v_{max} \left(\Delta v_{max} + 2v_0\right) \tag{7.27}$$

where v_0 is the nominal arm voltage. Having defined the maximum voltage deviation, the requirement for the extra energy storage can now be defined. The main constraint is that the arm voltages have to be more than the peak of the inserted voltage reference in order to avoid over-modulation. The peak of the inserted voltage reference for both the upper and lower arms ($\hat{v}^r_{u,l}$) is given by (7.28).

$$\hat{v}^r_{u,l} = \frac{1}{2}\left(\hat{v}^r_{ac} + v^r_{dc}\right) \tag{7.28}$$

where $\hat{v}_{ac}^{r}$ is peak of the ac voltage reference and v_{dc}^{r} is the dc voltage reference. Taking the maximum reference $\hat{v}_{ac}^{r}$ into account and considering the fact that v_{max} can have both positive and negative polarity, the constraint that the arm voltage v_0 should satisfy is given in (7.29).

$$\hat{v}_{u,l}^{r} + |\Delta v_{max}| \leq v_0 \leq V_{rated} - |\Delta v_{max}| \tag{7.29}$$

where V_{rated} is the sum of the maximum operating voltages of all the submodules in the same arm. From (7.29), it can be seen that the arm voltage has to be greater than 1 pu in order to provide the required headroom for the service, since $\hat{v}_{u,l}^{r}$ is typically close to 1 pu.

Equations (7.26) to (7.29) can be used to determine the nominal arm voltage v_0 and the associated extra energy storage capacity starting with the desired maximum active power swing for a POD application. This calculation can be adapted to the other applications by modifying (7.26). For example, in the case of the wind power smoothening application, the energy deviation can be calculated by taking into account the statistical properties of the expected wind power variation. Once the energy deviation is determined, the remaining steps are common to any of the applications. The next step after calculating the required extra energy storage capacity is identifying options to realize it. This is discussed in the next section.

7.5.2 Realization of the extra energy storage capacity

The additional energy storage capacity needed to provide energy-based services using the MMC can be realized in two different ways. In order to analyze these options, the relationship between the arm energy and the submodule parameters in physical units, given by (7.30), is used.

$$W = \frac{1}{2}\frac{C_{SM}}{N}\left(N \cdot V_{SM}\right)^2 \tag{7.30}$$

where C_{SM} is the submodule capacitance, N is the number of submodules per arm, V_{SM} is the submodule voltage, and W is the average arm energy. In a typical design, the arm voltage is chosen to be equal to the dc voltage ($NV_{sm} = V_{dc}$). In order to provide the energy-based services, the arm voltage has to be increased above V_{dc}. This can be achieved by increasing either the number of submodules, N, or the submodule voltage, V_{SM}. The two options are discussed in the following sections.

7.5.2.1 Increasing the number of submodules

The effect of introducing additional submodules will be investigated by replacing N by $(1+\alpha)\,N$ in (7.30), where α is a number between 0 and 1. The additional

energy due to α, ΔW^{α}, is given by (7.31).

$$\Delta W^{\alpha} = \alpha W \tag{7.31}$$

where W is the nominal energy calculated using (7.30). The maximum available POD power can be calculated by combining (7.31) with (7.26) as shown in (7.32).

$$\hat{P}_{max} = \frac{1}{4}\Delta W_{max} \cdot \omega_{osc} \cdot \alpha \cdot 6 \tag{7.32}$$

where $\Delta W_{max} = W_b \cdot \Delta w_{max}$ is the maximum energy deviation in joules. The factor 6 is included because the ac power oscillation is assumed to be shared equally by the six arms of the MMC. The average energy is set to $1 + \alpha/2$ times the nominal energy so that it can accommodate swing of both $\alpha/2$ and $-\alpha/2$ times the nominal energy without going below 1 pu. $\hat{P}_{max}$ is calculated for combinations of ω_{osc} and α using the parameters of the 900 MW converter in the four-terminal test system given in Table 7.1. The result is shown in Fig. 7.41, where it can be seen that the amount of extra storage gained is linearly proportional to α. The maximum available POD power is very limited at low frequencies. At 1 Hz, a peak POD swing of up to only 14 MW can be absorbed without affecting normal operation given that 25% additional submodules are used. The amount of available power can be improved by increasing the capacitance. This option can be more attractive in cases where there are some extra submodules that are added for redundancy. These submodules can be utilized for the POD service.

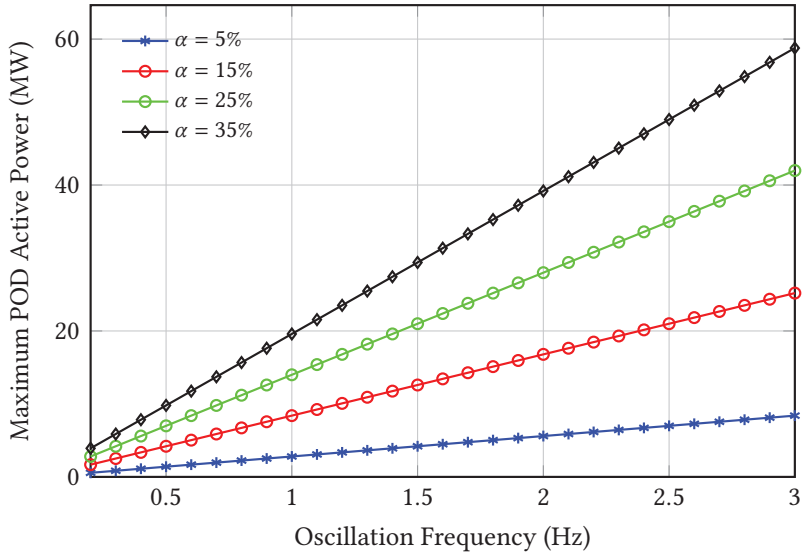

Figure 7.41: Maximum POD power as a function of oscillation frequency for different values of α.

7.5.2.2 Increasing the rated voltage of submodules

In this section an increase in the submodule voltage from V_{SM} to $(1+\beta)V_{SM}$ is considered, where β is a number between 0 and 1. By following a similar approach to the previous section, the maximum POD power can be calculated as shown in (7.33). A plot of $\hat{P}_{max}$ for different values of β as a function of frequency is depicted in Fig. 7.42.

$$\hat{P}_{max} = \frac{1}{4}\Delta W_{max} \cdot \omega_{osc} \cdot \left(\beta^2 + 2\beta\right) \cdot 6 \tag{7.33}$$

It can be observed that more POD power can be obtained by increasing β compared to α. A peak POD power of 31 MW can be obtained at 1 Hz when $\beta = 0.25$, which is approximately double the power obtained when $\beta = 0.25$. This option can, however, be more expensive since it requires the upgrade of all submodules.

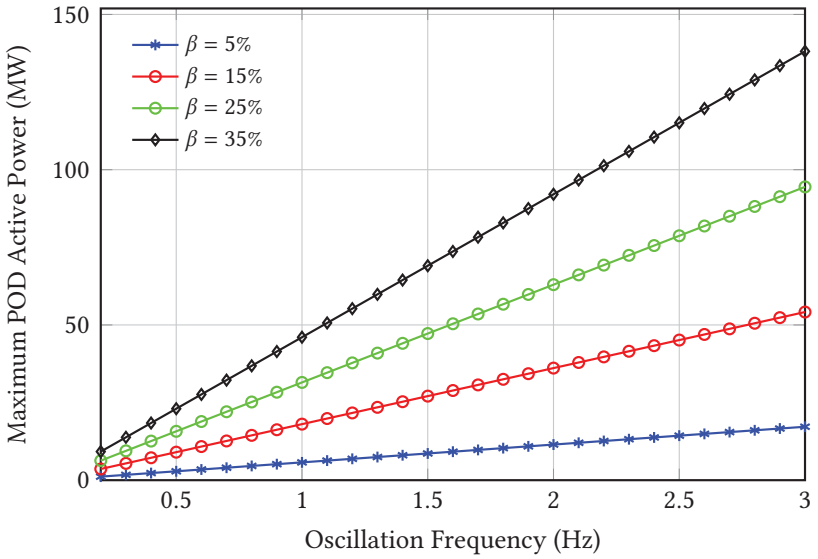

Figure 7.42: Maximum POD power as a function of oscillation frequency for different values of β.

7.5.2.3 Discussion

Two options to obtain the extra energy required to provide active power-based services were discussed in the last two sections. An important observation is that the amount of power available for the services is limited, especially at low frequencies. This is true even under drastic upgrades with $\alpha = 0.35$ or $\beta = 0.35$. This can be improved to some degree by increasing the submodule capacitance, which gives more power for the same ΔW_{max}.

The two options give different trade-offs between size and cost. Therefore, an optimal solution can be obtained by combining the two options and increasing the capacitance. However, even with the optimal choice, the amount of power that can be obtained from a single converter can be heavily constrained at low frequencies. This has implications for the feasibility of the power cancellation method, which is implemented on a single converter. The VCS method has an advantage in this case because multiple converters can share the power. Thus, the energy storage requirement is reduced when VCS is used across multiple converters.

7.6 Conclusion

Two methods to utilize the energy storage capability of the MMC for ancillary services were proposed in this chapter. The methods were analyzed in detail using a simplified aggregate dc grid model. The analysis showed that conventional implementations of active power-based services cause disturbances that propagate through dc grids and into other connected ac power systems causing power quality issues and electromechanical oscillations. The proposed methods prevent such propagations of active power disturbances by taking the active power needed for the services from the MMC capacitors instead of the dc grid.

The first method, *power cancellation*, is a solution that works at the source of the disturbance, where the converter generating the disturbance locally compensates for it. This approach was shown to be effective and easy to implement. Its main limitation is that it relies on one converter to provide the energy storage capability, which can be especially high when the frequency of the disturbance is low. The second approach, *VCS*, is a distributed approach, where all the capable converters in a dc grid can support the service by providing a portion of the required energy storage. Moreover, VCS is more versatile in the sense that it can be applied to different applications without modification. The effectiveness of the VCS method was demonstrated by using simplified analyses and detailed simulations for POD, wind power smoothening, and dc voltage support applications.

It was highlighted that the MMC needs to be upgraded in order to provide the required energy storage without affecting its normal function. The upgrade can be in the form of increasing the number of submodules or increasing the voltage rating of each module. The first option can lead to an increased overall size because of the extra submodules, while the second option might be more expensive because it applies the modification to all the submodules. A combination of these two options can be adopted to optimize for cost and size. The capacitance can also be increased in combination with either of the options in order to increase the amount of energy gained from the modification. The VCS has a clear

advantage in this case because the energy storage requirement is shared by multiple converters, thus leading to a reduced modification, and potentially a lower cost and size for a given application. This makes the VCS a promising option for practical implementations.

8

Power Oscillation Damping Using the MMC

This chapter presents a detailed analysis and experimental validation of the Virtual Capacitance Support (VCS) method, proposed in the previous chapter, in a Power Oscillation Damping (POD) application. The method increases the effective dc grid capacitance by using the stored energy of multiple MMCs connected in the same grid. The virtual capacitance is designed to be significantly larger than the effective dc grid capacitance, which means that it can absorb most of the power oscillation generated by a POD controller. Consequently, the oscillation is diverted into the MMCs because the extra virtual capacitance creates a low impedance path for the oscillation. The experiments, which were carried-out using a power hardware in the loop setup, demonstrated the effectiveness of the method. The discussion in this chapter is supported by the following contribution by the author.

> A. A. Taffese, A. G. Endegnanew, S. D'Arco, *et al.*, "Power oscillation damping with virtual capacitance support from modular multilevel converters," eng, *IET Renewable Power Generation*, 2019, Accepted: 2020-01-28T12:53:16Z, ISSN: 1752-1416

Chapter Outline

8.1 Introduction

As the number of HVDC interconnections in the power system is growing, system operators are requiring HVDC converters to have the capability to provide ancillary services such as Power Oscillation Damping (POD) to connected ac networks. [55]. Such services were traditionally delivered by equipment such as synchronous generators. A number of studies on POD using power electronic converters can be found in the recent literature [106], [111]–[115]. The main goal of a POD controller is to improve damping of electromechanical modes (usually in the range 0.2 Hz to 2 Hz [47]) by modulating either active or reactive power [112]. It was highlighted in Chapter 7 that the provision of such services leads to the propagation of active power disturbances (oscillations) into other connected ac power systems. This can be avoided by utilizing the energy storage capability of the MMC using the methods proposed in Chapter 7. Among the proposed methods, Virtual Capacitance Support (VCS) is chosen for further analysis because it is the most promising one.

A formulation of the VCS method, together with a preliminary analysis, was presented in Chapter 7 [12]. The analysis in Chapter 7 represents the ac grids by ideal voltage sources with the POD controller effect emulated by an oscillating active power injection. This can be used to show the basic principle of the method. However, the results in Chapter 7 are not sufficient to show the feasibility of the method under practical conditions. This chapter presents extensive analyses and validation of the VCS method using modal analysis, and time-domain simulations under more realistic conditions. Modal analysis is used to identify poorly damped modes and later to show the effectiveness of the POD controller in damping the identified mode. Furthermore, observability is used to highlight propagation of the oscillation into other connected ac systems. The findings from the modal analysis are complemented by waveforms obtained from time-domain simulations, which further underpin the observations. The case study in this chapter uses a multi-machine system with proper representation of the POD effects. Moreover, the method is experimentally validated on an 18 level MMC using a Power Hardware In The Loop (PHIL) approach.

8.2 Case study system

The system used for the case studies in this chapter is shown in Fig. 8.1. It is composed of three isolated ac grids that are interconnected by a three terminal MMC-based MTDC network. Two of the ac grids are onshore ac networks (labeled AC Grid 1 and 2 in Fig. 8.1), while the third ac grid is an offshore wind farm represented by a single equivalent generator, G4. AC Grid 2 has two areas that are 110 km apart: Area 1 with G2 and G3, and Area 2 with G5.

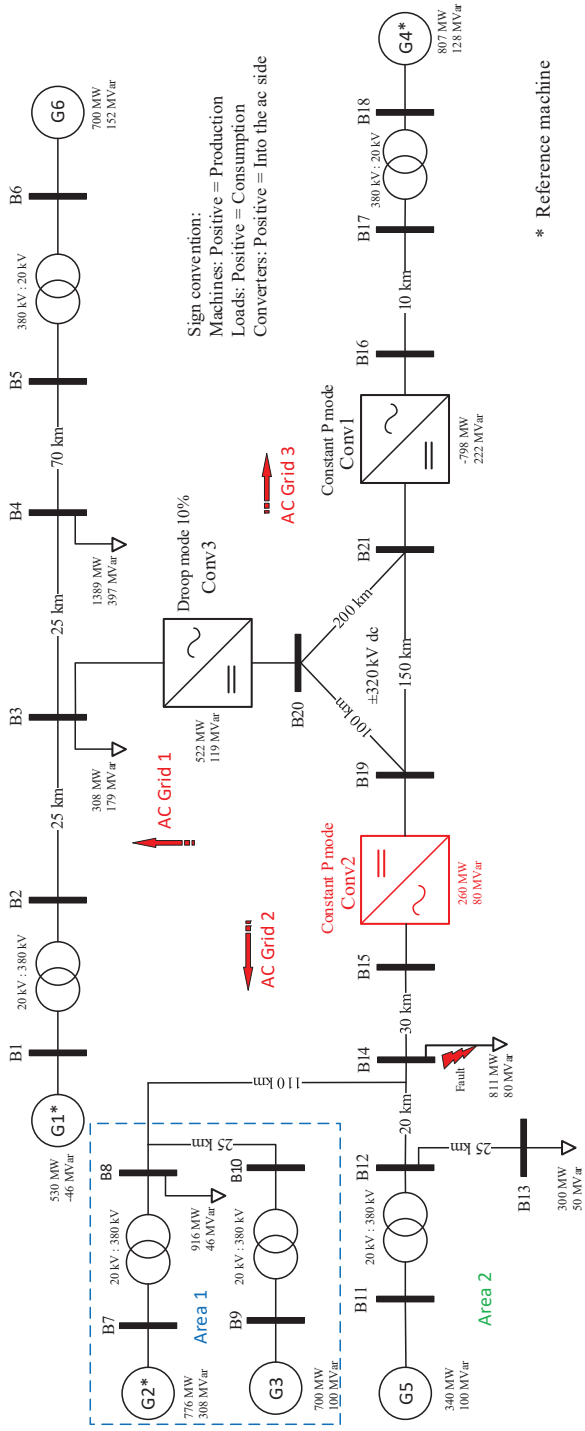

Figure 8.1: Case study system.

The model of the case study system was built using custom library components developed using Simscape Language from MathWorks [69] as described in Chapter 5. All component models are in *dq* domain with constant values in steady state so that it is possible to use the same models for linear analysis. The generators are represented using a detailed sixth-order machine model and were validated against DigSilent PowerFactory [116]. The MMC is represented by a simplified fifth-order model presented in Chapter 3. All converters are equipped with active and reactive power controllers. Conv1 is controlled in droop mode, while Conv2 and Conv3 are controlled in constant power mode. Conv2 (shown in red in Fig. 8.1) is replaced by a physical converter for Power Hardware In The Loop (PHIL) testing as explained in Section 8.5.1. Component parameters for the test system, adopted from literature [47], [102], are given in the following.

8.2.1 Per-unit base values

The base values used for per-unit calculations for the converters are depicted in (8.1) (see Chapter 3). The base values for both simulated and physical converters are given in the next section.

$$
\begin{aligned}
&I_b^{ac} = \frac{2}{3}\frac{S_b}{V_b^{ac}} \quad Z_b^{ac} = \frac{V_b^{ac}}{I_b^{ac}} \quad I_b^{dc} = \frac{S_b}{V_b^{dc}} \quad Z_b^{dc} = \frac{V_b^{dc}}{I_b^{dc}} \\
&L_b^{ac} = Z_b^{ac} \quad C_b^{ac} = \frac{1}{Z_b^{ac}} \quad L_b^{dc} = Z_b^{dc} \quad C_b^{dc} = \frac{1}{Z_b^{dc}} \\
&V_b^{ac} = \tfrac{1}{2}V_b^{dc} \qquad\qquad W_b = \frac{1}{2}C_{arm}\left(V_b^{dc}\right)^2
\end{aligned}
\tag{8.1}
$$

8.2.2 Converter and dc cable parameters

Parameters for the simulated and physical converters are shown in Tables 8.1 and 8.2, respectively. The dc cables are rated for 900 MW at ±320 kV (total voltage 640 kV). They are represented by a π-equivalent model with resistance per km of 0.0001 pu and shunt capacitance per km of 0.02 µF. The converter controllers are implemented as presented in [11], [12]. The MMC variables are grouped into ac and dc sides for per-unit conversion. The ac side includes ac currents and voltages. The remaining variables, such as arm voltages and currents, are considered as dc.

8.2.3 Synchronous machine parameters

The generators in this chapter are represented by a detailed sixth-order model [47] with parameters shown in Table 8.3. All generators are rated for 900 MW and

Table 8.1: HVDC Converter Parameters [102].

Parameter	Value
Base apparent power, S_b	900 MVA
Base dc voltage, V_b^{dc}	640 kV
Frequency, ω	$2\pi 50$ rad/s
Arm capacitance, $C_{arm} = C_{SM}/N$	29 μF
Arm inductance, L_{arm}	84 mH
Arm resistance, R_{arm}	0.885 Ω
Transformer reactance, X_t	17.7 Ω
Transformer resistance, R_t	1.77 Ω

Table 8.2: Scaled Prototype Converter Parameters.

Parameter	Value
Base apparent power, S_b	60 kVA
Base dc voltage, V_b^{dc}	600 V
Frequency, ω	$2\pi 50$ rad/s
Arm capacitance, $C_{arm} = C_{SM}/N$	1250 µF
Arm inductance, L_{arm}	1.4 mH
Arm resistance, R_{arm}	0.1 Ω
Transformer reactance, X_t	0.22 Ω
Transformer resistance, R_t	0.01 Ω

have the same parameters except inertia time constant, H. The value of H is 6 s for G1, G2, and G3, while G4, G5, and G6 have 6.75 s. The Automatic Voltage Regulator (AVR) used with all the generators is of the Simplified Excitation System (SEXS) type. Hydro governor, HYGOV1, is used for G2, G3, and G5. The remaining generators are gas turbine type (TGOV1). The transmission lines are represented by π-equivalent model with the $r = 0.0001\,pu/km$ and $x = 0.001\,pu/km$ with power and voltage rating of 100 MW and 380 kV, respectively. The transformers are rated for 900 MW and have per-unit impedance of 0 + 0.15i.

The case study system will be analyzed in this section using modal analysis and time domain simulations in order to identify poorly damped electromechanical

Table 8.3: Generator parameters [47].

Parameter	Value	Parameter	Value	Parameter	Value
X_d	1.8	X_q	1.7	X_l	0.2
X'_d	0.3	X'_q	0.55	X''_d	0.25
X''_q	0.25	R_a	0.0025	T'_{d0}	8 s
T'_{q0}	0.4 s	T''_{d0}	0.03 s	T''_{q0}	0.05 s

modes that will be damped using POD on one of the MMC converters in the MTDC grid.

8.2.4 Modal analysis

The case study system has 138 states that are associated with the generators, converters, controllers, and measurement filters. The system is linearized around an operating point shown by the load-flow condition depicted in Fig. 8.1. A detailed discussion on modal analysis is given in Chapter 5.

Two poorly damped electromechanical modes, listed in Table 8.4, are identified in the study system using modal analysis. Poorly damped electromechanical modes are defined in this work to have damping below 5% and frequency in the range 0.2 Hz to 2 Hz. From the observability/mode shapes of speed states variables, Mode 1 is found to be a local mode between G2 and G3. On the other hand, Mode 2 is an inter-area mode with G2 and G3 oscillating together and G5 on the other side, as shown in Fig. 8.2. The inter-area mode, Mode 2, is chosen for further analysis to study the performance of POD with VCS.

Table 8.4: Poorly damped electromechanical modes.

No.	Mode	damping [%]	Frequency [Hz]
1	−0.1948 + 5.8377i	3.34	0.93
2	−0.0814 + 3.3027i	2.46	0.525

8.2.5 Time-domain analysis

The time domain simulation results shown in Fig. 8.3 support the modal analysis presented in the previous section. A fault at bus B14 creates a disturbance in the system and excites the inter-area mode (Mode 2). It can be seen from the generator speeds that an oscillation at approximately 0.53 Hz is visible in the response

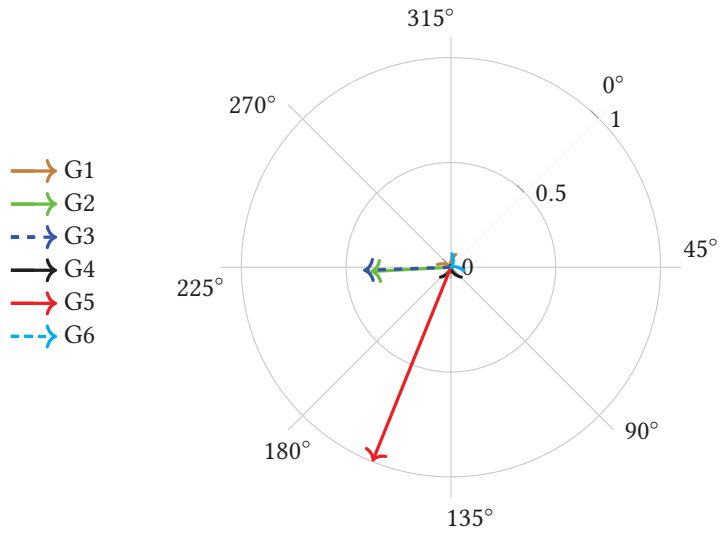

Figure 8.2: Observability of Mode 2 in rotor speeds states of the generators.

plots. This frequency is the same as the damped natural frequency of Mode 2 in Table 8.4. The damping is also consistent with the modal analysis result. It can also be observed that G2 and G3 oscillate together while the oscillation in G5 is shifted by approximately 60° with respect to the other generators. This is an indication of an inter-area mode since G2 and G3 are in Area 1, and G5 is in Area 2.

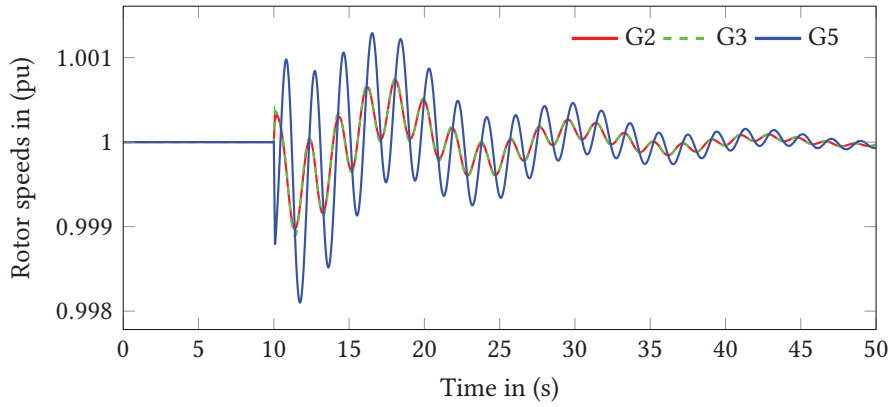

Figure 8.3: Rotor speed of generators in AC Grid 2.

8.3 Power oscillation damping controller

This section presents the design of a POD controller integrated with control of Conv2 to improve the damping ratio of Mode 2 to be above 5%. The input-output pairing for the POD controller is chosen so that the input gives high observability and the output gives high controllability of the selected mode [117]. Using this approach, the input is chosen to be the PLL angle (θ_{PLL}) while the output is active power (Δp) [5]. The basic structure of the controllers is shown in Fig. 8.4. It includes a washout filter, a lead-lag compensation, and a gain with limiter. The washout filter removes any dc offset from θ_{PLL}, and the lead-lag block provides phase angle adjustment. There can be multiple lead-lag blocks in series depending on the amount of angle compensation needed. The design of the POD controller parameters is done using the root-locus method [118].

First, root-locus plots are made for the system with active power reference as input and the output of the washout filter as output. Then, the departure angle of the mode of interest is calculated from the plot. The required compensation angle is computed to be the angle required to rotate the departure angle towards 180° so that the maximum possible damping improvement for a given gain is obtained. The gain is chosen to achieve the desired level of damping. For the case study system, the washout filter time-constant is chosen to be 5 s, the mode of interest has frequency of 0.53 Hz, and the desired level of damping is greater than 5%. Taking these values into consideration, the resulting design is to have two stages of lead-lag each one providing 48° angle boost, and the gain is set to be $k_{pod} = -0.06$. Another possibility to achieve the same effect on Mode 2 is to use a positive gain and two lead-lag blocks each providing −42°. However, these values are not adopted because, for this particular case, they cause the other modes to be unstable. As one of the goal of the chapter is the experimental validation of

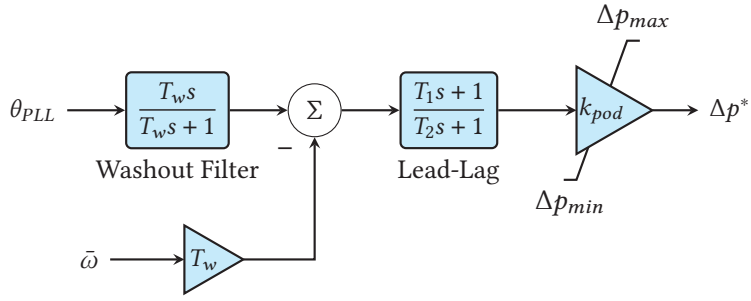

Subtraction of $\bar{\omega} T_w$ is not needed in phasor (dq) simulation.

Figure 8.4: Power Oscillation Damping controller.

the VCS method with POD, it should be noted that there is a difference between

the simulation and the experimental setup representation of the angles. Since the simulation is in the *dq* domain, every angle is measured with respect to the reference machine, which results in constant angle values in steady state. However, this is not true in practical systems which are in the *abc* domain since there is no reference machine and all the angles are linear functions of time and fundamental frequency. Therefore, a washout filter is not sufficient to remove the linear time variation. After passing through the washout, the PLL angle still has a dc offset equal to $\bar{\omega}T_w$, where $\bar{\omega}$ is the steady-state grid frequency. The solution used in this work is to subtract $\bar{\omega}T_w$ from the output of the washout filter (Fig. 8.4). $\bar{\omega}$ can be calculated by applying filtering or averaging to the PLL frequency over a few tens of seconds so that the electromechanical range is not affected. It should be noted that this subtraction of $\bar{\omega}T_w$ is not necessary for the phasor simulation.

8.4 Simulation results

This section presents the performance of the VCS method using simulations. To this end, three case studies are considered. The first case is a base case where both the POD and VCS are disabled. In the second case, the POD controller is enabled to improve damping of Mode 2, while in the last case both the POD and VCS controllers are enabled. These three cases are labelled Base, POD, and POD + VCS, respectively. Each case is studied using modal analysis and time domain simulations. The arm voltages of all the MMCs, including the physical one, are set to be 10% above the nominal dc voltage. As will be shown, this 10% headroom is more than what is required for VCS. The VCS gain is set to have a value $k_v = 125$.

8.4.1 Modal analysis results

The values of Mode 2 under the three case studies are shown in Table 8.5. It can be seen that the POD controller moves the mode to the left with only a minor shift in frequency, which results in the maximum possible damping improvement for the given gain. Note that the VCS does not affect the location of the mode in the complex plane, (Table 8.5).

Table 8.5: Mode 2 under different case studies.

Case	Mode	damping [%]	Frequency [Hz]
Base	−0.0814 + 3.30i	2.46	0.525
POD	−0.225 + 3.34i	6.76	0.53
POD + VCS	−0.225 + 3.34i	6.76	0.53

Observability of Mode 2 in the speed states of the generators in the system is

shown in Table 8.6. The magnitudes are normalized by the maximum values in each column and presented as percentages. Mode 2 is most observable from the states of G5, as can be seen from the speed in Table 8.6 and the rotor angles in Table 8.7. As discussed in Section 8.2, the mode is an inter-area mode in Grid 2, where G2 and G3 oscillate against G5. This is evident from the observability angles in Table 8.6. It can be noted that the mode is slightly observable in Grid 1 (0.4% in G1, and 0.6% in G6, for the rotor speeds) even in the base case. This is because the oscillation in the grid appears as a disturbance to the active power controller, which tries to reject it. However, complete rejection of disturbance using a PI controller is only possible at dc. This creates a residual oscillation in active power which is transferred to the dc side by the energy controller. This is then picked-up by converters participating in dc voltage regulation. Converters controlled in constant power mode, such as Conv3, do not pass this oscillation into their ac sides [5]. When POD is enabled the mode becomes more observable

Table 8.6: Normalized observability of Mode 2 in rotor speeds.

Element	Base		POD		POD + VCS	
	Mag [%]	Angle	Mag [%]	Angle	Mag [%]	Angle
G1	0.4	106°	7.6	101°	1.9	122°
G2	38.6	222°	37.5	125°	37.5	198°
G3	41.5	223°	40.4	126°	40.4	199°
G4	0	110°	0	112°	0	196°
G5	100	157°	100	65°	100	138°
G6	0.6	190°	9.5	183°	2.4	204°

in AC Grid 1 (see G1 and G6 in Table 8.6). The observability in the speed of G1 increased from 0.4% to 7.6%, and from 0.6% to 9.5% for G6. The same pattern can be observed from Table 8.7, where the observability of Mode 2 in the rotor angles of G6 increased from 0.8% to 13%. This is in accordance with the discussion in Chapter 7 that POD propagates the oscillation to other connected grids via the dc grid.

When VCS is enabled, the observability of Mode 2 in AC Grid 1 decreased by a factor of more than 3 (Table 8.6). The same can be seen from the rotor angle in Table 8.7. Another interesting plot is the observability mode phasor plot of Mode 2 in the MMC energy states of the three converters in Fig. 8.5. The figure compares the POD case with the POD+VCS case to highlight the changes when the support function is enabled. In the POD case the three energy states are oscillating in dif-

Table 8.7: Normalized observability of Mode 2 in rotor angles

Element	Base		POD		POD + VCS	
	Mag [%]	Angle	Mag [%]	Angle	Mag [%]	Angle
G3	3.2	145°	3.4	49°	3.4	122°
G5	100	42°	100	310°	100	23°
G6	0.8	135°	13	131°	3.3	152°

ferent directions (with different phase shifts). In this case the energy controllers are working to keep the MMC energy states constant irrespective of disturbances. They cannot completely reject the oscillations in power because they have a PI structure. Therefore, there is a residual oscillation in the energy states. The phase angle of the observability in Conv2 is close to 90° because there is an integral relation between active power and energy. For Conv1, the disturbance comes from the dc voltage droop controller, which tries to oppose the oscillating power injected by Conv2. Hence, the observability of Mode 2 in Conv1 energy appears almost opposite to that of Conv2. Since Conv3 is not participating in dc voltage control, observability of the mode in energy state of Conv3 is significantly lower than the others. When VCS is enabled, the three energy states are more closely aligned with each other and also with the mode (i.e. the observability angles are close to 0°), which means that they are collaborating effectively in absorbing the oscillation. This will be more evident from time domain results in the next sections.

8.4.2 Time-domain simulation

Simulation studies were performed based on the three case studies used in this chapter. A fault at bus 14, which is applied at 10 s and cleared after 75 ms, is used to excite the inter-area mode in AC Grid 2. The fault is cleared without changing the grid topology, which means that the system dynamic properties before and after the fault are the same. Fig. 8.7 shows rotor angles of G5 (AC Grid 2) and G6 (AC Grid 1) under the three case studies. The rotor angle of G5 shows that the POD improves the damping of Mode 2. Moreover, by looking at the same figure, it can be noted that there is no visible difference in the damping and frequency of Mode 2 when energy support is enabled, which is in line with the modal analysis results. The same effect can be seen from the rotor speed of G5 in Fig. 8.8. By looking at the measurements from G6, it can be noted that the machine starts oscillating when POD is activated. The frequency and damping of the oscillation are the same as those of Mode 2 in Table 8.5. Once VCS is enabled, the oscillation

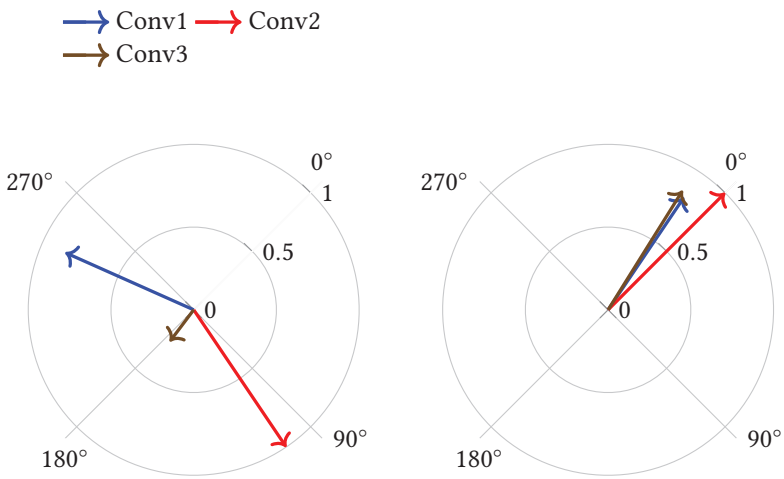

Figure 8.5: Observability of Mode 2 in converter energy states: POD Case (left) and POD+VCS Case (right).

in AC Grid 1 shows a significant reduction (by a factor of 3.4 taking the peak-to-peak ratio).

Fig. 8.9 shows that the energy states start oscillating when VCS is enabled. This confirms that the oscillation is being diverted into the arm capacitors. The variations in arm energy are proportional to the variations in active power when VCS is enabled.

8.5 Experimental results

This section presents experimental results using a PHIL approach. The test cases are the same as those used in the simulation results. A description of the PHIL setup is presented first, followed by the experimental results.

8.5.1 PHIL setup

The purpose of PHIL in this work is to validate the VCS and POD control schemes on a physical converter under realistic conditions. Components of the PHIL setup are presented in Section 5.4.2 and reiterated here for quick reference. In the setup, *Conv2*, a 900 MW converter, is replaced by a scaled down 60 kVA, 18 level MMC. The scaling is such that the Per-unit power, voltages, and currents are the same between the simulation and the physical system. This is achieved by exchanging Per-unit currents and voltages between the two systems. Fig. 8.6 shows the test setup including a real-time simulator (from OPAL-RT [119]), a power amplifier (from EGSTON Power [120]), and the MMC (built by SINTEF Energy Research

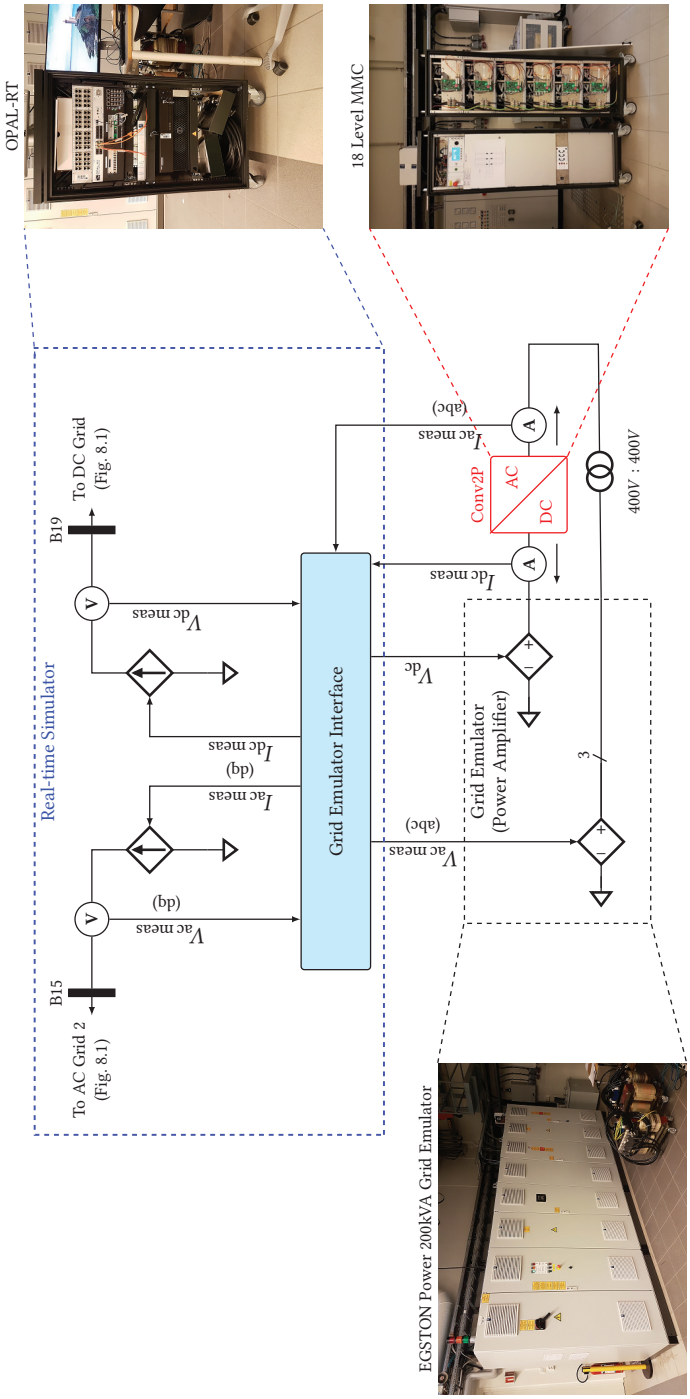

Figure 8.6: Power Hardware In The Loop setup.

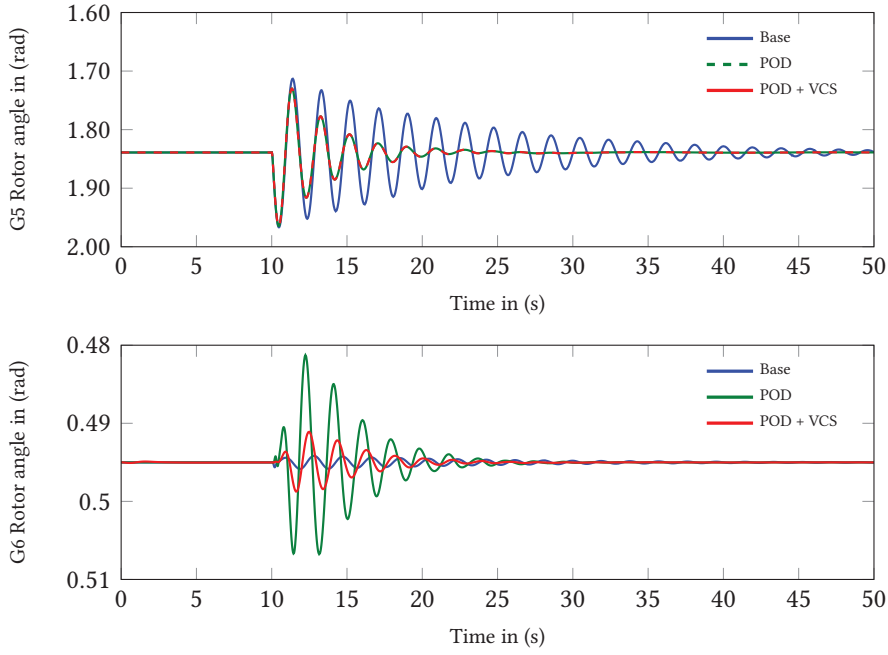

Figure 8.7: Rotor angles of G5 and G6 (simulation).

[121]). The simulator is responsible for running the simulated system and interfacing with the power amplifier. The interface is where the scaling, and transformations between *abc* and *dq* domain are performed. The transformation is necessary because the ac system is modeled in *dq* domain in the simulation. The references to the controlled current sources are obtained from physical current measurements ($I_{ac\,meas}$ and $I_{dc\,meas}$ in Fig. 8.6). Similarly, the references to the grid emulator come from voltage measurements in the simulation ($V_{ac\,meas}$ and $V_{dc\,meas}$ in Fig. 8.6). This creates a virtual connection between the physical converter and the simulated system. The test setup should be started by following a sequence of steps in order for the setup to start from steady state and run properly. The simulation is started first with constant power injections obtained from load-flow at Buses 15 and 19 in order to avoid transients during start-up. Then the grid emulator is started by setting its voltage references to bus voltages measured at buses 15 and 19 from the simulation. Once the grid emulator is ready, the physical converter is energized from the dc side so that it pre-charges the arm capacitor. When pre-charging is done, the converter is connected to the ac side after the PLL synchronizes. Then, the current injection into the simulation are enabled. Finally, the power is transferred from the constant injections at Buses 15 and 19 to the converter without causing transients in the simulation. At this point the setup is ready for running the tests.

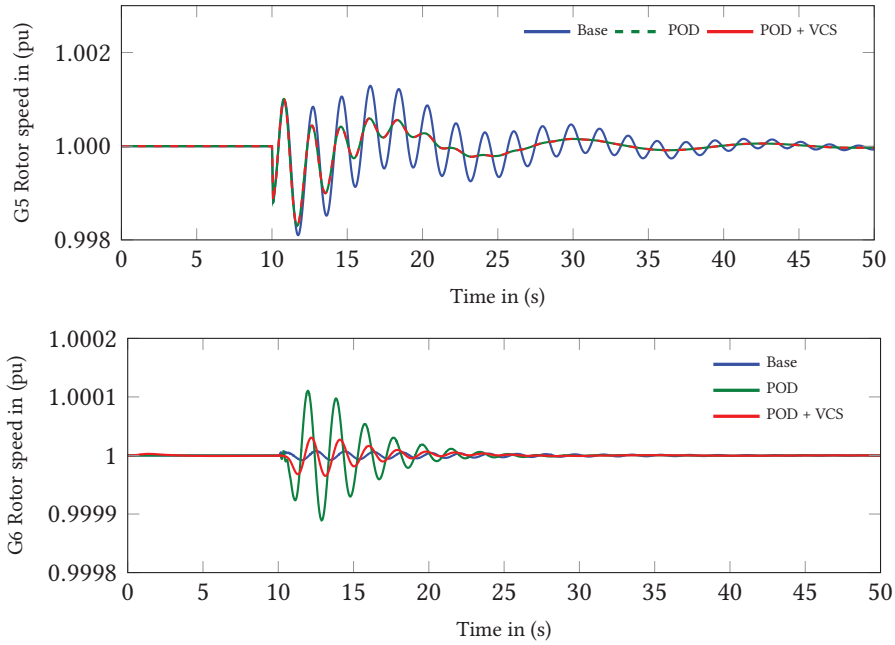

Figure 8.8: Rotor speeds of G5 and G6 (simulation).

8.5.2 PHIL test results

The experiments were conducted at 450 V dc, which is 75% of the base voltage of Conv2P (600 V). Hence, the voltages are scaled such that a 1 pu voltage in simulation results in a 0.75 pu in the physical system. In order to preserve the per-unit value of power between the simulated and physical systems, the same scaling of 0.75 is applied to the physical current measurements before they are sent to the simulation. The arm voltage is 10% above the dc voltage 0.75 pu, i.e. 0.825 pu. The corresponding arm energy is the square of the arm voltage ($0.825^2 = 0.6805$ in pu). Figs. 8.10 and 8.11 show the rotor angles and speeds of G5 and G6 from the PHIL tests. The same pattern as the results from Section 8.4.2 is observed, where the POD causes the oscillations to propagate to AC Grid 1, and the energy support reduces the propagation by more than a factor of 3. Active power injected by Conv2P due to the POD action is shown in Fig. 8.12, which shows a significant amount of distortion due to noise. The noise is not reflected in the rotor angles and speeds because the ac system has a large inertia which filters fast variations. Arm energy of the Conv2P is shown in Fig. 8.12 for the three cases. The findings are once again similar to the simulation cases. From Fig. 8.12, it can be seen the maximum variation in active power is ≈0.005 pu and the resulting variation in energy is ≈0.02 pu.

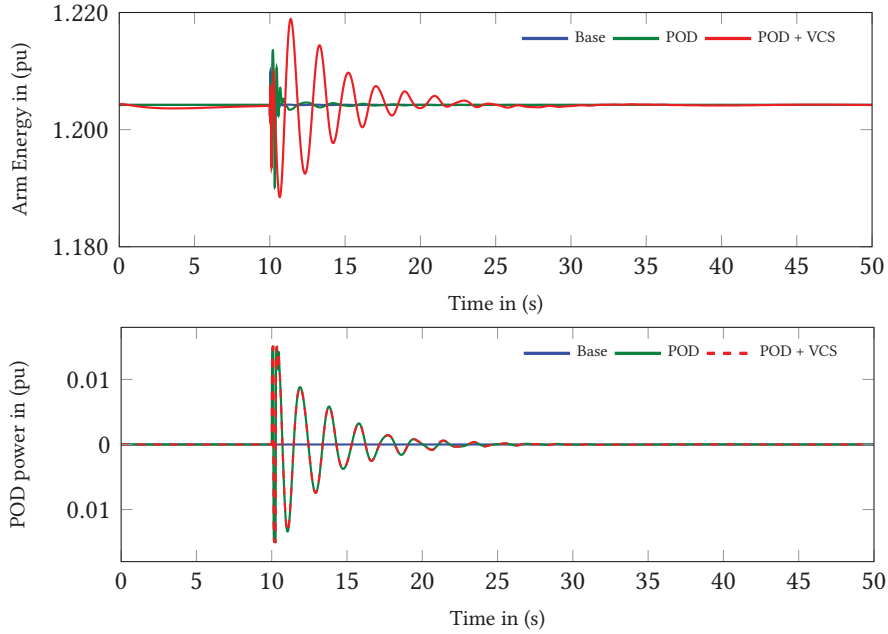

Figure 8.9: Active power and energy measurements of Conv2 (simulation).

The experimental results show the same general trend as the simulation cases. However, when closely inspecting Figs. 8.8 and 8.10, it can be noted that the damping of the inter-area mode (Mode 2) is lower in the experimental case. This is primarily due to the time delays in the PHIL setup, i.e. the time elapsed from the measurement of the currents (or voltages) to the time when they are applied in the simulation (or power amplifier). These delays are principally caused by the bandwidth of the power amplifier and the one step time delays introduced to avoid algebraic loops in the simulation. In order to confirm the source of the mismatch between the simulation and PHIL results, the simulation was repeated taking into account the PHIL delays. Fig. 8.13 shows that there is a very good match between the simulation and the PHIL results when the time delays are considered (Sim + Delay).

8.6 Discussion

The results presented in the previous sections showed that AC Grid 2 in the system under test has a poorly damped (2.46%) electromechanical mode which was excited when a fault was applied to the system. The damping was then improved to 6.76% when POD was enabled on converter 2(Conv2), the converter interfacing to AC Grid 2. However, this resulted in oscillation of G6 (see Fig. 8.8), a generator in AC Grid 1. Later, this effect was reduced by using the VCS method. The same

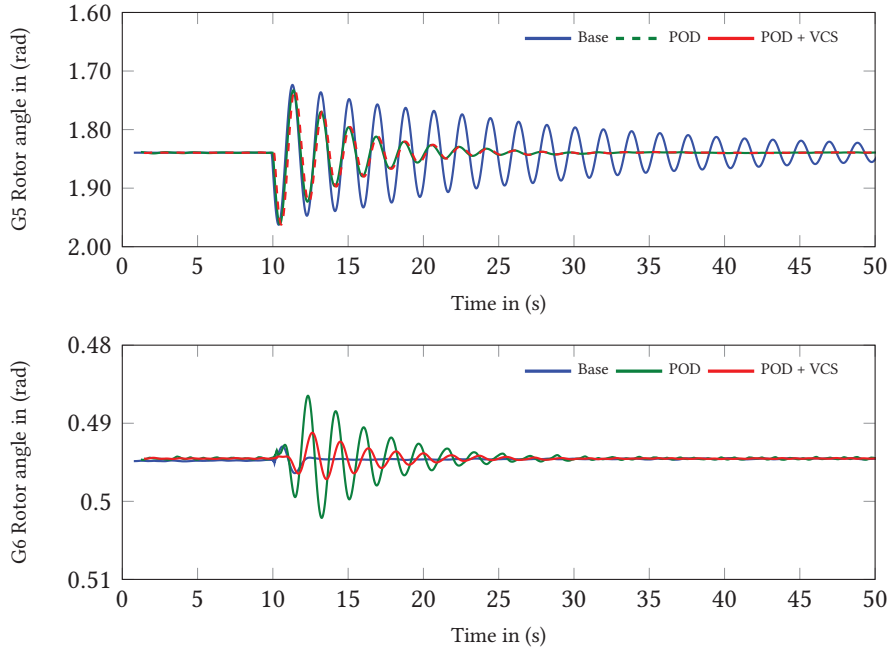

Figure 8.10: Rotor angles of G5 and G6 (experimental).

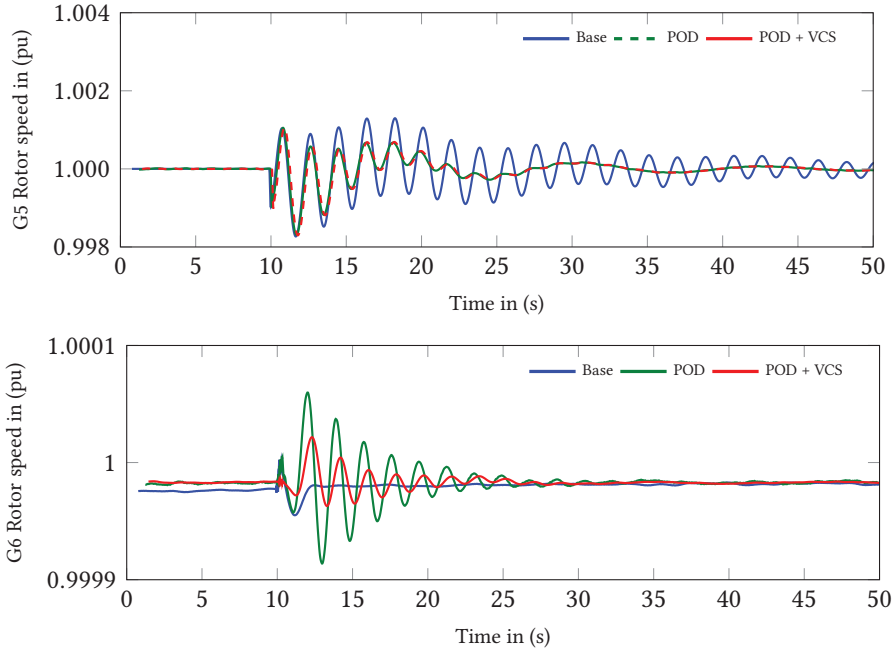

Figure 8.11: Rotor speeds of G5 and G6 (experimental).

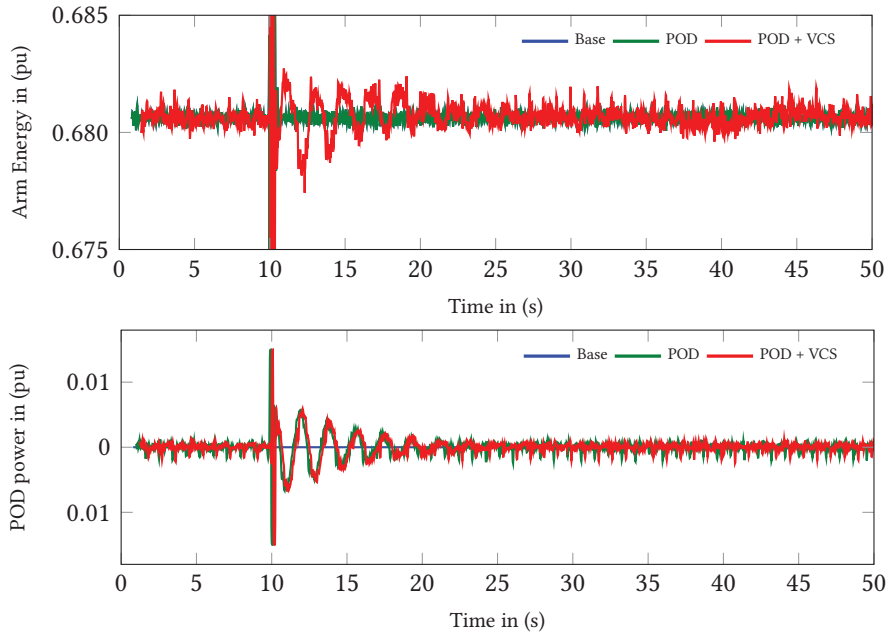

Figure 8.12: Active power and energy measurements of Conv2 (experimental).

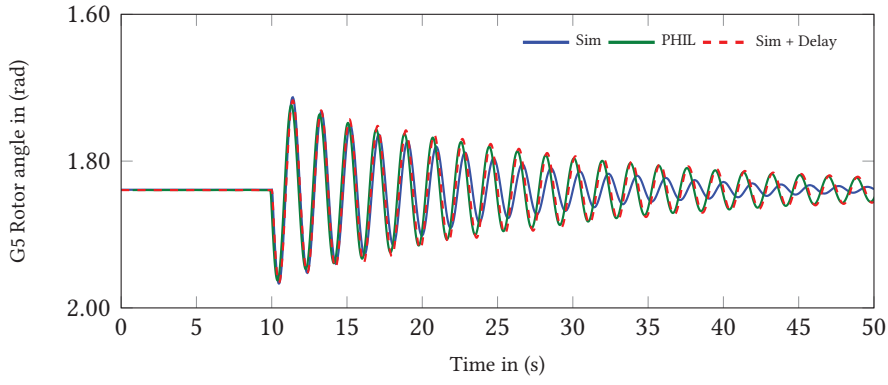

Figure 8.13: Comparison of simulation and experimental results.

effect was observed from the experimental results.

The amount of energy storage required for such a service can be calculated as discussed in Section 7.5. The method presented in Section 7.5 for calculating the extra energy requirement can be used in two ways. The first way is to define the maximum active power required by the POD service and then use this value to calculate the extra energy required. The second way is to define the maximum possible energy deviation and then specify the available POD power. The first approach is more challenging because the POD power can vary depending on a number of factors such as damping of the mode, magnitude and location of the disturbance, and inertia in the system. In this chapter, the maximum energy deviation is specified to be 20% (10% maximum voltage deviation), which gives around 75 MW peak power (25 MW from each converter according to Section 7.5). This extra energy is obtained by either adding a few sub-modules or by increasing the operating voltage of each of the sub-modules. Increasing the sub-module capacitance reduces the voltage (energy) deviation for a given peak power, which means that there will be fewer modules required or the voltage increase can be lowered. This action can be combined with the other two to obtain an optimal solution for a given application.

8.7 Conclusion

The chapter presents a detailed analysis and validation of a scheme to provide virtual capacitance support to a dc grid. Since the virtual capacitance can be designed to be significantly larger that the equivalent dc grid capacitance, it provides a low impedance path for oscillating dc current. This action diverts the oscillations into the arm capacitors of the MMC instead of propagating them to the other ac grids.

A 21-bus system is used to investigate the effectiveness of the scheme using modal analysis, time-domain simulation, and PHIL tests. There is a strong correlation between the results from the three studies, and they all show that the scheme can effectively divert the oscillation into the arm capacitors. It was shown that the VCS method affects only the observability of the mode in other grids, not the damping or frequency, as expected. Additionally, the PHIL tests show that the scheme is practically applicable since it was implemented using a scaled MMC prototype.

A requirement for the scheme is that the converter be designed with a slightly higher storage capacity compared to nominal design, for example 15% increase in sub-module voltage was used in this study. The amount of additional capacity can be chosen depending on the desired level of participation of the converters

in providing the service. Optimization of such extra energy storage requirement can be taken as future work.

9
Conclusions and Future Work

The main findings in this thesis together with recommendations for future work are presented in this chapter.

9.1 Conclusions

This thesis has demonstrated that the energy storage capability of MMC-based HVDC converters can be utilized for active power-based services to the power system. This not only prevents unwanted disturbances from propagating into the ac grids connected via the multi-terminal/meshed dc grid, but also reduces the risk of negative interaction among system level controllers, such as Power System Stabilizers (PSSs), found in different ac grids. The thesis proposes modeling and analysis tools, and control methods to enable these energy-based services. The main original contributions are summarized in the following sections.

9.1.1 Modeling and analysis

MMC models of varying levels of detail have been presented and compared in Chapter 3. They are grouped into voltage-based and energy-based models, as described in the literature. Energy-based models result in simplifications when compensated modulation is employed. These simplified models are suitable for large-scale systems studies. Energy-based models can also be used with other types of control when the effect of the circulating current ripple is not relevant in the desired case study. Additionally, phasor models are used in order to obtain a model which gives constant values in steady state with sinusoidal excitations. Such models are useful when performing small-signal (modal) analysis, where the response of the system to small disturbance around a steady-state operating point is evaluated.

A new simplified model of the MMC-based Front-to-Front (F2F) dc-dc converter is also proposed in this thesis. The model aggregates the arm energy states of the converter into one in order to reduce the number of states, which is desired when performing large-scale studies. A second alternative including the effect of the circulating current ripple is also proposed to cover the cases where compensated modulation is not used. In both cases, the models show good agreement with a more detailed average arm model.

Furthermore, aggregate modeling of a dc grid was used to analyze response of the grid to active power disturbance by using simplified calculations. This type

of model is important when comparing different methods of utilizing the MMC stored energy. It has been shown in Chapter 7 that these simple calculations can predict the system response with good accuracy compared to simulations with detailed models.

9.1.2 Control method

Control-related aspects are addressed in two different levels in the thesis. The first one is at the arm energy control level where an improved arm energy controller is proposed in Chapter 6. The other is at a higher level where different implementations of methods to utilize the arm energy are proposed and analyzed in Chapters 7 and 8. The arm energy controller is instrumental for the effective implementation of the high-level controllers.

The proposed arm energy control is a complete approach for implementing closed-loop compensated modulation without accurate knowledge of system parameters. The arm capacitance and the time delay between the controller and the converter are the parameters which are not known accurately or are assumed to change throughout the lifetime of the converter. The detailed derivation has shown that these quantities are related to the first and second harmonic ripples in the circulating current. The corrections are implemented using two PI controllers per leg that are enabled on-demand. Moreover, the controllers are designed to be slower than higher level controllers, which results in time-scale separation. This enables removal of the circulating current ripple without potential negative interactions with the higher level controllers because of the time-scale separation.

The proposed method has been tested using both simulation and experimental tests with a strong correlation between the two results. The experimental tests have shown that the method can work in cases that are not ideal where the number of modules is as low as 18. The tests have also demonstrated that the method works well in the presence of noise and unsymmetrical capacitance changes. In summary, the proposed method provides a complete solution for implementing compensated modulation under changing system parameters. Moreover, the application of the method is not limited to the correction of parameter changes due to environmental conditions; it can also be used to identify the parameters during commissioning where they are not accurately known.

At a higher level, the thesis proposes two methods for utilizing the MMC energy for grid services. These are the power cancellation method and Virtual Capacitance Support (VCS). The power cancellation method is a local implementation where active power disturbance due to the grid service being diverted into the arm energy. This method is local because it relies on the availability of the active

power disturbance measurement. On the other hand, VCS requires measurement of the dc voltage variations which can be accessed by multiple converters. This enables a distributed implementation where the energy storage capability of multiple converters can be utilized. The methods have been shown to be effective in three applications: Power Oscillation Damping (POD), wind farm active power smoothening, and dc voltage dynamic support (*"inertia support"*).

A detailed analysis and validation of a scheme in a POD application is also presented. A 21-bus system is used to investigate the effectiveness of the scheme using modal analysis, time-domain simulation, and PHIL tests. There is a strong correlation between the results from the three studies, and they all show that the scheme can effectively divert the oscillation into the arm capacitors. It was shown that the VCS method only affects the observability of the mode in other grids, not the damping or frequency, as expected. Additionally, the PHIL tests show that the scheme is practically applicable since it was implemented using a scaled 18-level MMC prototype under realistic conditions.

A requirement for the scheme is that the converter be designed with a slightly higher storage capacity compared to nominal design, for example 15% increase in sub-module voltage was used in this study. The amount of additional capacity can be chosen depending on the desired level of participation of the converters in providing the service. Optimization of such extra energy storage requirement can be undertaken as future work.

9.2 Future work

The following are potential topics for further research in the area of this thesis.

Improved implementation of VCS: The basic VCS implementation presented in Chapter 7 has limitations with regard to filtering of the dc voltage to extract variations in the desired frequency range. The current implementation is a first-order washout filter, which does not provide good blocking at low frequencies without affecting the desired range, which makes the overall service less effective. Another aspect that can be considered is the possibility to use dynamic gain for the VCS in order to avoid saturating the output, which is not desired because the converter stops providing the capacitance support as soon as the VCS goes into saturation.

Optimization the storage requirement: As previously highlighted, the implementation of VCS requires the converter to be slightly over-designed. This thesis has shown that this can be achieved by increasing the number of submodules, the voltage rating of each submodules, or the submodule capacitance (Chapter 7). A

combination of these options can give an optimal solution in terms of cost and size. This can be taken as a possible topic for further work.

Quantifying the effect of VCS on controller interaction: It was mentioned that VCS decouples system-level controllers located in different ac grids. Such a decoupling can be analyzed and quantified by using interaction analysis techniques like relative gain arrays [5]. Interaction between VCS and other controllers in the MMC can also be investigated.

Implementation of VCS on dc-dc converters: The energy-based services can also be implemented in dc-dc converters in HVDC grids. In such applications the dc-dc converter can be equipped with battery storage in order to achieve both short-term and long-term dc voltage support. The combination of VCS and battery storage can provide a topic for further research.

Application to embedded HVDC links: Application of the VCS method to an embedded HVDC links providing a POD service presents a unique advantages. This is because the same ac grid is present on both sides of the link, which makes damping the oscillation without VCS impractical.

Application to offshore platforms: Another application space for the services is the electrification of offshore oil and gas platforms. An attractive option considered for such electrification is a scenario with a few gas turbine generators complemented by renewable generation from wind power [122]. The control methods proposed in this thesis can be applied to provide both active power smoothening and POD.

Bibliography

[1] D. Van Hertem, O. Gomis-Bellmunt, and J. Liang, "Drivers for the development of HVDC grids," in *HVDC Grids: For Offshore and Supergrid of the Future*, IEEE, 2016, pp. 3–24, ISBN: 978-1-119-11522-9.

[2] P. Rodriguez and K. Rouzbehi, "Multi-terminal DC grids: Challenges and prospects," *J. Mod. Power Syst. Clean Energy*, vol. 5, no. 4, pp. 515–523, Jul. 2017, ISSN: 2196-5625, 2196-5420.

[3] T. An, G. Tang, and W. Wang, "Research and application on multi-terminal and DC grids based on VSC-HVDC technology in China," *High Voltage*, vol. 2, no. 1, pp. 1–10, 2017, ISSN: 2397-7264.

[4] D. Jovcic and K. Ahmed, *High Voltage Direct Current Transmission: Converters, Systems and DC Grids*. John Wiley & Sons, 2015, OCLC: 942387454, ISBN: 978-1-118-84666-7.

[5] A. G. Endegnanew, "Stability Analysis of High Voltage Hybrid AC/DC Power Systems," PhD Dissertation, NTNU, Trondheim, Norway, 2017.

[6] R. H. Renner and D. V. Hertem, "Ancillary services in electric power systems with HVDC grids," *Transmission Distribution IET Generation*, vol. 9, no. 11, pp. 1179–1185, 2015, ISSN: 1751-8687.

[7] O. Lavoine, F. Regairaz, T. Baker, *et al.*, "Ancillary Services: An overview of International Practices," CIGRE C5.06, Technical Brochure 435, Oct. 2010.

[8] A. A. Taffese, E. de Jong, and E. Tedeschi, "Modelling of DC-DC Converter for System Level Studies," in *Proceedings of the 8th IEEE Benelux Young Researchers Symposium in Electrical Power Engineering: YRS2016*, Eindhoven, The Netherlands: Technische Universiteit Eindhoven, May 2016, p. 6.

[9] A. A. Taffese, E. Tedeschi, and E. C. W. de Jong, "Modelling of DC-DC converters based on front-to-front connected MMC for small signal studies," in *2016 IEEE 17th Workshop on Control and Modeling for Power Electronics (COMPEL)*, Jun. 2016, pp. 1–7.

[10] A. A. Taffese, E. Tedeschi, and E. de Jong, "Arm voltage estimation method for compensated modulation of modular multilevel converters," in *2017 IEEE Manchester PowerTech*, Jun. 2017, pp. 1–6.

[11] A. A. Taffese, E. Tedeschi, and E. de Jong, "A control scheme for utilizing energy storage of the modular multilevel converter for power oscillation damping," in *2017 IEEE 18th Workshop on Control and Modeling for Power Electronics (COMPEL)*, Stanford, CA, USA: IEEE, Jul. 2017, pp. 1–8.

[12] A. A. Taffese and E. Tedeschi, "Coordination of Modular Multilevel Converter Based HVDC Terminals for Ancillary Services," in *2018 Power Systems Computation Conference (PSCC)*, Dublin, Ireland: IEEE, Jun. 2018, pp. 1–7.

[13] A. A. Taffese and E. Tedeschi, "Simplified Modelling of the F2F MMC-Based High Power DC-DC Converter Including the Effect of Circulating Current Dynamics," in *2018 IEEE 19th Workshop on Control and Modeling for Power Electronics (COMPEL)*, Jun. 2018, pp. 1–6.

[14] E. Tedeschi and A. A. Taffese, "Electrical power transmission and grid integration," *Renewable Energy from the Oceans: From wave, tidal and gradient systems to offshore wind and solar*, pp. 321–343, Jul. 2019.

[15] A. A. Taffese, E. de Jong, S. D'Arco, and E. Tedeschi, "Online Parameter Adjustment Method for Arm Voltage Estimation of the Modular Multilevel Converter," *IEEE Transactions on Power Electronics*, vol. 34, no. 12, pp. 12 491–12 503, Dec. 2019, ISSN: 1941-0107.

[16] A. A. Taffese, A. G. Endegnanew, S. D'Arco, and E. Tedeschi, "Power oscillation damping with virtual capacitance support from modular multilevel converters," *IET Renewable Power Generation*, 2019, Accepted: 2020-01-28T12:53:16Z, ISSN: 1752-1416.

[17] L. V. Costanzo, I. Zubimendi, A. A. Taffese, and E. Tedeschi, "Parallelization of Medium Voltage generator-side converters for Multi-MW wind turbines: Comparison of two topological alternatives," in *2015 International Conference on Renewable Energy Research and Applications (ICRERA)*, Nov. 2015, pp. 917–922.

[18] A. A. Taffese and E. Tedeschi, "Harmonic Resonance Mode Analysis in dq Domain," *Renewable Energy and Power Quality Journal*, vol. 15, 2017, Accepted: 2017-11-30T09:56:15Z, ISSN: 2172-038X.

[19] S. Sanchez, D. T. Duong, A. A. Taffese, K. Uhlen, and E. Tedeschi, "Performance Evaluation of the Empirical Method for Online Detection of Power Oscillations: A Multiterminal HVDC Application," in *IECON 2018 - 44th Annual Conference of the IEEE Industrial Electronics Society*, Oct. 2018, pp. 6021–6025.

[20] H. Akagi, "Classification, Terminology, and Application of the Modular Multilevel Cascade Converter (MMCC)," *IEEE Transactions on Power Electronics*, vol. 26, no. 11, pp. 3119–3130, Nov. 2011, ISSN: 0885-8993.

[21] K. Sharifabadi, L. Harnefors, H.-P. Nee, S. Norrga, and R. Teodorescu, *Design, Control and Application of Modular Multilevel Converters for HVDC Transmission Systems*. Chichester, UK: John Wiley & Sons, Ltd, Aug. 2016, ISBN: 978-1-118-85155-5.

[22] J. Qin, M. Saeedifard, A. Rockhill, and R. Zhou, "Hybrid Design of Modular Multilevel Converters for HVDC Systems Based on Various Submodule Circuits," *IEEE Transactions on Power Delivery*, vol. 30, no. 1, pp. 385–394, Feb. 2015, ISSN: 1937-4208.

[23] A. Lesnicar and R. Marquardt, "An innovative modular multilevel converter topology suitable for a wide power range," in *2003 IEEE Bologna Power Tech Conference Proceedings,*, vol. 3, Jun. 2003, pp. 1–6.

[24] C. Oates, "Modular Multilevel Converter Design for VSC HVDC Applications," *IEEE Journal of Emerging and Selected Topics in Power Electronics*, vol. 3, no. 2, pp. 505–515, Jun. 2015, ISSN: 2168-6777.

[25] R. Irnawan, F. M. F. da Silva, C. L. Bak, and T. C. Bregnhøj, "An Initial Topology of Multiterminal HVDC Transmission System in Europe: A Case Study of the North-Sea Region," in *Ieee International Energy Conference (Enrgycon) 2016*, 2016.

[26] C. Barker, C. Davidson, D. Trainer, and R. Whitehouse, "Requirements of DC-DC Converters to facilitate large DC Grids," *Cigre Session 2012*, 2012.

[27] G. P. Adam, I. A. Gowaid, S. J. Finney, D. Holliday, and B. W. Williams, "Review of dc–dc converters for multi-terminal HVDC transmission networks," *IET Power Electronics*, vol. 9, no. 2, pp. 281–296, 2016.

[28] J. A. Ferreira, "The Multilevel Modular DC Converter," *IEEE Transactions on Power Electronics*, vol. 28, no. 10, pp. 4460–4465, Oct. 2013, ISSN: 1941-0107.

[29] G. Kish and P. Lehn, "Modeling Techniques for Dynamic and Steady-State Analysis of Modular Multilevel DC/DC Converters," 2015.

[30] R. Vidal, D. Soto, I. Andrade, *et al.*, "A multilevel modular DC–DC converter topology," *Mathematics and Computers in Simulation*, 11th International Conference on Modeling and Simulation of Electric Machines, Converters and Systems, vol. 131, pp. 128–141, Jan. 2017, ISSN: 0378-4754.

[31] T. Lüth, M. M. C. Merlin, T. C. Green, F. Hassan, and C. D. Barker, "High-Frequency Operation of a DC/AC/DC System for HVDC Applications," *IEEE Transactions on Power Electronics*, vol. 29, no. 8, pp. 4107–4115, Aug. 2014, ISSN: 0885-8993.

[32] N. Soltau, R. U. Lenke, and R. W. De Doncker, "High-Power DC-DC Converter," E.ON Energy Research Center Series, vol. 5, no. 5, Jul. 2013.

[33] G. Bergna Diaz, J. A. Suul, and S. D'Arco, "Small-signal state-space modeling of modular multilevel converters for system stability analysis," in *Energy Conversion Congress and Exposition (ECCE), 2015 IEEE*, Montreal, QC, Canada: IEEE, 2015, pp. 5822–5829.

[34] L. Harnefors, A. Antonopoulos, S. Norrga, L. Angquist, and H. P. Nee, "Dynamic Analysis of Modular Multilevel Converters," *IEEE Transactions on Industrial Electronics*, vol. 60, no. 7, pp. 2526–2537, Jul. 2013, ISSN: 0278-0046.

[35] D. Jovcic and A. A. Jamshidifar, "Phasor Model of Modular Multilevel Converter With Circulating Current Suppression Control," *IEEE Transactions on Power Delivery*, vol. 30, no. 4, pp. 1889–1897, Aug. 2015, ISSN: 0885-8977.

[36] J. Freytes, L. Papangelis, H. Saad, *et al.*, "On the modeling of MMC for use in large scale dynamic simulations," in *2016 Power Systems Computation Conference (PSCC)*, Jun. 2016, pp. 1–7.

[37] U. N. Gnanarathna, A. M. Gole, and R. P. Jayasinghe, "Efficient Modeling of Modular Multilevel HVDC Converters (MMC) on Electromagnetic Transient Simulation Programs," *IEEE Transactions on Power Delivery*, vol. 26, no. 1, pp. 316–324, Jan. 2011, ISSN: 0885-8977.

[38] H. Saad, J. Peralta, S. Dennetière, *et al.*, "Dynamic Averaged and Simplified Models for MMC-Based HVDC Transmission Systems," *IEEE Transactions on Power Delivery*, vol. 28, no. 3, pp. 1723–1730, Jul. 2013, ISSN: 0885-8977.

[39] G. Bergna-Diaz, J. A. Suul, and S. D'Arco, "Energy-Based State-Space Representation of Modular Multilevel Converters with a Constant Equilibrium Point in Steady-State Operation," *IEEE Transactions on Power Electronics*, vol. PP, no. 99, pp. 1–19, 2017, ISSN: 0885-8993.

[40] G. Bergna-Diaz, J. Freytes, X. Guillaud, S. D'Arco, and J. A. Suul, "Generalized Voltage-based State-Space Modelling of Modular Multilevel Converters with Constant Equilibrium in Steady-State," *IEEE Journal of Emerging and Selected Topics in Power Electronics*, pp. 1–18, 2018, ISSN: 2168-6777.

[41] S. S. Khan and E. Tedeschi, "Modeling of MMC for Fast and Accurate Simulation of Electromagnetic Transients: A Review," *Energies*, vol. 10, no. 8, p. 1161, Aug. 2017.

[42] A. Ferreira, C. Collados, O. Gomis-Bellmunt, and M. Teixido, "Modular multilevel converter electrical circuit model for HVdc applications," in *2015 17th European Conference on Power Electronics and Applications (EPE'15 ECCE-Europe)*, Sep. 2015, pp. 1–10.

[43] N. T. Trinh, M. Zeller, K. Wuerflinger, and I. Erlich, "Generic Model of MMC-VSC-HVDC for Interaction Study With AC Power System," *IEEE Transactions on Power Systems*, vol. 31, no. 1, pp. 27–34, Jan. 2016, ISSN: 0885-8950.

[44] R. Wachal *et al.*, "Guide for the development of models for HVDC converters in a HVDC grid," Technical Brochure TB-604, 2014.

[45] J. Freytes, G. Bergna, J. A. Suul, *et al.*, "Improving Small-Signal Stability of an MMC with CCSC by Control of the Internally Stored Energy," *IEEE Transactions on Power Delivery*, vol. PP, no. 99, pp. 1–10, 2017, ISSN: 0885-8977.

[46] A. a. J. Far and D. Jovcic, "Circulating current suppression control dynamics and impact on MMC converter dynamics," in *2015 IEEE Eindhoven PowerTech*, Jun. 2015, pp. 1–6.

[47] P. Kundur, N. J. Balu, and M. G. Lauby, *Power System Stability and Control*. New York: McGraw-Hill, 1994, OCLC: 28929603, ISBN: 978-0-07-035958-1.

[48] J. A. Martinez-Velasco, *Power System Transients: Parameter Determination*. Boca Raton: CRC Press/Taylor & Francis Group, 2010, OCLC: 751259234, ISBN: 978-1-4200-6529-9.

[49] A. Morched, B. Gustavsen, and M. Tartibi, "A universal model for accurate calculation of electromagnetic transients on overhead lines and underground cables," *IEEE Transactions on Power Delivery*, vol. 14, no. 3, pp. 1032–1038, Jul. 1999.

[50] B. Gustavsen and A. Semlyen, "Rational approximation of frequency domain responses by vector fitting," *IEEE Transactions on Power Delivery*, vol. 14, no. 3, pp. 1052–1061, Jul. 1999, ISSN: 1937-4208.

[51] J. Beerten, S. D'Arco, and J. A. Suul, "Frequency-dependent cable modelling for small-signal stability analysis of VSC-HVDC systems," *Transmission Distribution IET Generation*, vol. 10, no. 6, pp. 1370–1381, 2016, ISSN: 1751-8687.

[52] S. D'Arco, J. A. Suul, and J. Beerten, "Analysis of accuracy versus model order for frequency-dependent Pi-model of HVDC cables," in *2016 IEEE 17th Workshop on Control and Modeling for Power Electronics (COMPEL)*, Jun. 2016, pp. 1–8.

[53] J. Beerten, S. D'Arco, and J. Suul, "Cable Model Order Reduction for HVDC Systems Interoperability Analysis," in *11th IET International Conference on AC and DC Power Transmission*, Feb. 2015, pp. 1–10.

[54] S. Skogestad and I. Postlethwaite, *Multivariable Feedback Control: Analysis and Design*. Hoboken, NJ: Wiley, 2007, OCLC: 970532185, ISBN: 978-0-470-01167-6.

[55] *Commission Regulation (EU) 2016/1447 of 26 August 2016 establishing a network code on requirements for grid connection of high voltage direct current systems and direct current-connected power park modules (Text with EEA relevance)*, Sep. 2016.

[56] J. W. Umland and M. Safiuddin, "Magnitude and symmetric optimum criterion for the design of linear control systems: What is it and how does it compare with the others?" *IEEE Transactions on Industry Applications*, vol. 26, no. 3, pp. 489–497, May 1990, ISSN: 0093-9994.

[57] C. Bajracharya, M. Molinas, J. A. Suul, T. M. Undeland, *et al.*, "Understanding of tuning techniques of converter controllers for VSC-HVDC," in *Nordic Workshop on Power and Industrial Electronics (NORPIE/2008), June 9-11, 2008, Espoo, Finland*, Helsinki University of Technology, 2008.

[58] A. Antonopoulos, L. Angquist, and H. P. Nee, "On dynamics and voltage control of the Modular Multilevel Converter," in *2009 13th European Conference on Power Electronics and Applications*, Sep. 2009, pp. 1–10.

[59] S. Debnath, J. Qin, B. Bahrani, M. Saeedifard, and P. Barbosa, "Operation, Control, and Applications of the Modular Multilevel Converter: A Review," *IEEE Transactions on Power Electronics*, vol. 30, no. 1, pp. 37–53, Jan. 2015, ISSN: 0885-8993.

[60] Y. Zhou, D. Jiang, J. Guo, P. Hu, and Y. Liang, "Analysis and Control of Modular Multilevel Converters Under Unbalanced Conditions," *IEEE Transactions on Power Delivery*, vol. 28, no. 4, pp. 1986–1995, Oct. 2013, ISSN: 1937-4208.

[61] Q. Tu, Z. Xu, and J. Zhang, "Circulating current suppressing controller in modular multilevel converter," in *IECON 2010 - 36th Annual Conference on IEEE Industrial Electronics Society*, Nov. 2010, pp. 3198–3202.

[62] L. Ängquist, A. Haider, H. P. Nee, and H. Jiang, "Open-loop approach to control a Modular Multilevel Frequency Converter," in *Proc. 2011-14th European Conf. Power Electronics and Applications (EPE 2011)*, Aug. 2011, pp. 1–10.

[63] L. Ängquist, A. Antonopoulos, D. Siemaszko, *et al.*, "Inner control of Modular Multilevel Converters - An approach using open-loop estimation of stored energy," in *Proc. Int. Power Electronics Conf. (IPEC)*, Jun. 2010, pp. 1579–1585.

[64] A. Antonopoulos, L. Ängquist, L. Harnefors, K. Ilves, and H. P. Nee, "Global Asymptotic Stability of Modular Multilevel Converters," *IEEE_J_IE*, vol. 61, no. 2, pp. 603–612, Feb. 2014, ISSN: 0278-0046.

[65] L. Harnefors, A. Antonopoulos, K. Ilves, and H. P. Nee, "Global Asymptotic Stability of Current-Controlled Modular Multilevel Converters," *IEEE Transactions on Power Electronics*, vol. 30, no. 1, pp. 249–258, Jan. 2015, ISSN: 0885-8993.

[66] S. Kavungal Kolparambath, "DC/DC Converters for Multi-terminal HVDC system for Integrating Offshore Wind Farms," *126*, 2015, Accepted: 2015-12-17T08:02:22Z.

[67] M. Tiller, *Introduction to Physical Modeling with Modelica*. Boston; Dordrecht: Kluwer Academic Publishers, 2001, OCLC: 906957312, ISBN: 978-0-7923-7367-4.

[68] P. A. Fritzson, *Introduction to Modeling and Simulation of Technical and Physical Systems with Modelica*. 2012, OCLC: 1141128533, ISBN: 978-1-118-09425-9.

[69] *Simscape Documentation - MathWorks*, https://se.mathworks.com/help/physmod/simscape/.

[70] *PowerFactory - DIgSILENT*, https://www.digsilent.de/en/powerfactory.html, Apr. 2019.

[71] R. D. Zimmerman, C. E. Murillo-Sánchez, and R. J. Thomas, "MATPOWER: Steady-State Operations, Planning, and Analysis Tools for Power Systems Research and Education," *IEEE Transactions on Power Systems*, vol. 26, no. 1, pp. 12–19, Feb. 2011, ISSN: 1558-0679.

[72] J. Beerten and R. Belmans, "Development of an open source power flow software for high voltage direct current grids and hybrid AC/DC systems: MATACDC," *IET Generation, Transmission & Distribution*, vol. 9, no. 10, pp. 966–974, 2015.

[73] J. Beerten and R. Belmans, "MatACDC - an open source software tool for steady-state analysis and operation of HVDC grids," in *AC and DC Power Transmission, 11\textsuperscriptth IET International Conference On*, 2015, pp. 1–9.

[74] P. W. Sauer and M. A. Pai, *Power System Dynamics and Stability*, 1 edition. Champaign, IL.: Stipes Publishing Co., Jan. 2007, ISBN: 978-1-58874-673-3.

[75] J. Machowski, J. Bialek, and J. Bumby, *Power System Dynamics: Stability and Control*. John Wiley & Sons, 2011.

[76] K. Ogata and Pearson, *Modern Control Engineering*. Delhi: Pearson, 2016, OCLC: 971421460, ISBN: 978-93-325-5016-2.

[77] G. Strang, *Introduction to Linear Algebra*. Wellesley (Mass.): Wellesley-Cambridge Press, 2009, OCLC: 495353687, ISBN: 978-0-9802327-1-4.

[78] I. J. Perez-arriaga, G. C. Verghese, and F. C. Schweppe, "Selective Modal Analysis with Applications to Electric Power Systems, PART I: Heuristic Introduction," *IEEE Transactions on Power Apparatus and Systems*, vol. PAS-101, no. 9, pp. 3117–3125, Sep. 1982, ISSN: 0018-9510.

[79] F. Zhang, *The Schur Complement and Its Applications*. New York: Springer, 2010, OCLC: 909832861, ISBN: 978-1-4419-3712-4.

[80] M. I. García Planas and J. L. Domínguez García, "A general approach for computing residues of partial-fraction expansion of transfer matrices," *WSEAS transactions on mathematics*, vol. 12, no. 7, pp. 647–756, 2013.

[81] H. K. Khalil, *Nonlinear Systems*. Upper Saddle River, NJ: Prentice Hall, 2002, OCLC: 314091496, ISBN: 978-0-13-067389-3.

[82] A. Meurer, C. P. Smith, M. Paprocki, *et al.*, "SymPy: Symbolic computing in Python," *PeerJ Comput. Sci.*, vol. 3, e103, Jan. 2017, ISSN: 2376-5992.

[83] Wolfram Research, *Mathematica: A System for Doing Mathematics by Computer : Version 2.2 : User's Guide for Microsoft Windows*. Champaign, 1994, OCLC: 475039202.

[84] L. M. Wedepohl, H. V. Nguyen, and G. D. Irwin, "Frequency-dependent transformation matrices for untransposed transmission lines using Newton-Raphson method," *IEEE Transactions on Power Systems*, vol. 11, no. 3, pp. 1538–1546, Aug. 1996.

[85] W. Ren, M. Steurer, and T. L. Baldwin, "Improve the Stability and the Accuracy of Power Hardware-in-the-Loop Simulation by Selecting Appropriate Interface Algorithms," in *2007 IEEE/IAS Industrial Commercial Power Systems Technical Conference*, Edmonton, Alta., Canada: IEEE, May 2007, pp. 1–7.

[86] A. Viehweider, G. Lauss, and L. Felix, "Stabilization of Power Hardware-in-the-Loop simulations of electric energy systems," *Simulation Modelling Practice and Theory*, vol. 19, no. 7, pp. 1699–1708, Aug. 2011, ISSN: 1569-190X.

[87] O. B. Fosso, M. Molinas, K. Sand, and G. H. Coldevin, "Moving towards the Smart Grid: The Norwegian case," in *2014 International Power Electronics Conference (IPEC-Hiroshima 2014 - ECCE ASIA)*, May 2014, pp. 1861–1867.

[88] M. A. Perez, S. Bernet, J. Rodriguez, S. Kouro, and R. Lizana, "Circuit Topologies, Modeling, Control Schemes, and Applications of Modular Multilevel Converters," *IEEE Transactions on Power Electronics*, vol. 30, no. 1, pp. 4–17, Jan. 2015, ISSN: 0885-8993.

[89] M. Barnes and A. Beddard, "Voltage Source Converter HVDC Links – The State of the Art and Issues Going Forward," *Energy Procedia*, Selected Papers from Deep Sea Offshore Wind R&D Conference, Trondheim, Norway, 19-20 January 2012, vol. 24, pp. 108–122, Jan. 2012, ISSN: 1876-6102.

[90] M. Sleiman, K. Al-Haddad, H. F. Blanchette, and H. Y. Kanaan, "Insertion Index Generation Method Using Available Leg-Average Voltage to Control Modular Multilevel Converters," *IEEE Transactions on Industrial Electronics*, vol. PP, no. 99, pp. 1–11, 2017, ISSN: 0278-0046.

[91] D. Siemaszko, A. Antonopoulos, K. Ilves, *et al.*, "Evaluation of control and modulation methods for modular multilevel converters," in *The 2010 International Power Electronics Conference - ECCE ASIA -*, Jun. 2010, pp. 746–753.

[92] B. Bahrani, S. Debnath, and M. Saeedifard, "Circulating Current Suppression of the Modular Multilevel Converter in a Double-Frequency Rotating Reference Frame," *IEEE Transactions on Power Electronics*, vol. 31, no. 1, pp. 783–792, Jan. 2016, ISSN: 0885-8993.

[93] X. She, A. Huang, X. Ni, and R. Burgos, "AC circulating currents suppression in modular multilevel converter," in *IECON 2012 - 38th Annual Conference on IEEE Industrial Electronics Society*, Oct. 2012, pp. 191–196.

[94] Q. Tu, Z. Xu, and L. Xu, "Reduced Switching-Frequency Modulation and Circulating Current Suppression for Modular Multilevel Converters," *IEEE Transactions on Power Delivery*, vol. 26, no. 3, pp. 2009–2017, Jul. 2011, ISSN: 0885-8977.

[95] Z. Li, P. Wang, Z. Chu, *et al.*, "An Inner Current Suppressing Method for Modular Multilevel Converters," *IEEE Transactions on Power Electronics*, vol. 28, no. 11, pp. 4873–4879, Nov. 2013, ISSN: 0885-8993.

[96] L. Ängquist, A. Antonopoulos, D. Siemaszko, *et al.*, "Inner control of Modular Multilevel Converters - An approach using open-loop estimation of stored energy," in *The 2010 International Power Electronics Conference - ECCE ASIA -*, Jun. 2010, pp. 1579–1585.

[97] C. S. Kulkarni, J. R. Celaya, G. Biswas, and K. Goebel, "Accelerated aging experiments for capacitor health monitoring and prognostics," in *2012 IEEE AUTOTESTCON Proceedings*, Sep. 2012, pp. 356–361.

[98] Y.-J. Jo, T. H. Nguyen, and D.-C. Lee, "Capacitance Estimation of the Submodule Capacitors in Modular Multilevel Converters for HVDC Applications," *Journal of Power Electronics*, vol. 16, no. 5, pp. 1752–1762, 2016, ISSN: 2093-4718.

[99] H. R. Wickramasinghe, G. Konstantinou, S. Ceballos, and J. Pou, "Alternate Arm Converter Energy Balancing under Parameter Variation," *IEEE Transactions on Power Electronics*, pp. 1–1, 2018, ISSN: 0885-8993.

[100] M. Vasiladiotis, N. Cherix, and A. Rufer, "Accurate Capacitor Voltage Ripple Estimation and Current Control Considerations for Grid-Connected Modular Multilevel Converters," *IEEE Transactions on Power Electronics*, vol. 29, no. 9, pp. 4568–4579, Sep. 2014, ISSN: 0885-8993.

[101] "IEEE Recommended Practice and Requirements for Harmonic Control in Electric Power Systems," *IEEE Std 519-2014 (Revision of IEEE Std 519-1992)*, pp. 1–29, Jun. 2014.

[102] W. Leterme, N. Ahmed, J. Beerten, *et al.*, "A new HVDC grid test system for HVDC grid dynamics and protection studies in EMT-type software," in *11th IET International Conference on AC and DC Power Transmission*, Birmingham, UK, Feb. 2015, pp. 1–7.

[103] L. Angquist and C. Gama, "Damping algorithm based on phasor estimation," in *2001 IEEE Power Engineering Society Winter Meeting. Conference Proceedings (Cat. No.01CH37194)*, vol. 3, 2001, 1160–1165 vol.3.

[104] "Establishing a network code on requirements for grid connection of high voltage direct current systems and direct current-connected power park modules," *Commission Regulation (EU) 2016/ 1447*, vol. 59, no. L 241, Sep. 2016.

[105] T. M. Haileselassie, R. E. Torres-Olguin, T. K. Vrana, K. Uhlen, and T. Undeland, "Main grid frequency support strategy for VSC-HVDC connected wind farms with variable speed wind turbines," in *2011 IEEE Trondheim PowerTech*, Jun. 2011, pp. 1–6.

[106] L. Harnefors, N. Johansson, L. Zhang, and B. Berggren, "Interarea oscillation damping using active-power modulation of multiterminal HVDC transmissions," *IEEE Transactions on Power Systems*, vol. 29, no. 5, pp. 2529–2538, 2014.

[107] S. Samimi, F. Gruson, P. Delarue, *et al.*, "MMC Stored Energy Participation to the DC Bus Voltage Control in an HVDC Link," *IEEE Transactions on Power Delivery*, vol. 31, no. 4, pp. 1710–1718, Aug. 2016, ISSN: 0885-8977.

[108] P. Sorensen, N. A. Cutululis, A. Vigueras-Rodriguez, *et al.*, "Power Fluctuations From Large Wind Farms," *IEEE Transactions on Power Systems*, vol. 22, no. 3, pp. 958–965, Aug. 2007, ISSN: 0885-8950.

[109] Y. H. Wan, "Long-Term Wind Power Variability," National Renewable Energy Laboratory (NREL), Golden, CO., Tech. Rep. NREL/TP-5500-53637, Jan. 2012.

[110] *ABB to supply battery energy storage for Dong's 90MW UK wind farm | Energy Storage News*, https://www.energy-storage.news/news/abb-to-supply-battery-energy-storage-for-dongs-90mw-uk-wind-farm, 2017.

[111] R. Preece and J. V. Milanović, "Power Oscillation Damping using VSC-based Multi-terminal HVDC Grids," *IFAC Proceedings Volumes*, 8th Power Plant and Power System Control Symposium, vol. 45, no. 21, pp. 20–25, Jan. 2012, ISSN: 1474-6670.

[112] M. Ndreko, A. van der Meer, M. Gibescu, M. van der Meijden, and B. Rawn, "Damping Power System Oscillations by VSC-Based HVDC Networks: A North Sea Grid Case Study," in *12th International Workshop on Large-Scale Integration of Wind Power into Power Systems as Well as on Transmission Networks for Offshore Wind Power Plants*, London, Oct. 2013.

[113] N. T. Trinh, I. Erlich, and S. P. Teeuwsen, "Methods for utilization of MMC-VSC- HVDC for power oscillation damping," in *2014 IEEE PES General Meeting | Conference Exposition*, National Harbor, MD, USA: IEEE, Jul. 2014, pp. 1–5.

[114] L. Zeni, R. Eriksson, S. Goumalatsos, *et al.*, "Power Oscillation Damping From VSC HVDC Connected Offshore Wind Power Plants," *IEEE Transactions on Power Delivery*, vol. 31, no. 2, pp. 829–838, Apr. 2016, ISSN: 0885-8977.

[115] D. V. Hertem, O. Gomis-Bellmunt, and J. Liang, "Power system oscillation damping by means of VSC-HVDC systems," in *HVDC Grids: For Offshore and Supergrid of the Future*, Wiley-IEEE Press, 2016, ISBN: 978-1-119-11524-3.

[116] F. Gonzalez-Longatt and J. L. Rueda, Eds., *PowerFactory Applications for Power System Analysis*, ser. Power Systems. Springer International Publishing, 2014, ISBN: 978-3-319-12957-0.

[117] J. L. Domínguez-García, C. E. Ugalde-Loo, F. Bianchi, and O. Gomis-Bellmunt, "Input–output signal selection for damping of power system oscillations using wind power plants," *International Journal of Electrical Power & Energy Systems*, vol. 58, pp. 75–84, Jun. 2014, ISSN: 0142-0615.

[118] J. Chow, G. Boukarim, and A. Murdoch, "Power System Stabilizers as Undergraduate Control Design Projects," *IEEE Transactions on Power Systems*, vol. 19, no. 1, pp. 144–151, Feb. 2004.

[119] *Real-Time simulation*, https://www.opal-rt.com/, Online, 2019.

[120] *EGSTON POWER | Hardware in the Loop Testing*, 2019.

[121] S. D'Arco, A. G. Endegnanew, G. Guidi, and J. A. Suul, "Interoperability of Modular Multilevel Converters and 2-level Voltage Source Converters in a Laboratory-Scale Multi-Terminal DC Grid," in *2018 International Power Electronics Conference (IPEC-Niigata 2018 -ECCE Asia)*, Niigata, Japan: IEEE, May 2018, pp. 2003–2010.

[122] W. He, G. Jacobsen, T. Anderson, *et al.*, "The Potential of Integrating Wind Power with Offshore Oil and Gas Platforms," *Wind Engineering*, vol. 34, no. 2, pp. 125–137, Mar. 2010, ISSN: 0309-524X.

ISBN 978-82-326-5425-3 (printed ver.)
ISBN 978-82-326-5262-4 (electronic ver.)
ISSN 1503-8181 (printed ver.)
ISSN 2703-8084 (online ver.)

NTNU

Norwegian University of
Science and Technology